ONSET OF IGNITION IN SOLID FUELS AND MODELLING THE NATURAL CONVECTION

A thesis submitted to the University of Manchester
for the degree of Doctor of Philosophy
in the Faculty of Engineering and Physical Sciences

2013

Imran Khan
School of Mathematics

Contents

Word count 31,903

The University of Manchester

Imran Khan
Doctor of Philosophy
Onset of ignition in solid fuels and modelling the natural convection
December 6, 2013

This thesis examines two important physical phenomena that occur when solid fuels are exposed to external radiative heating: (1) the pyrolysis process in reaching ignition conditions and (2) the natural convection around one or more radiatively heated fuel samples. A vegetation fire (bushfire, wildfire, or forest fire) preheating the vegetation which is in its path is a particular example which occurs in nature. However there are many more applications where modelling the pyrolysis process and/or the natural convection is of practical use.

For the pyrolysis phenomena, a one-dimensional time dependent pyrolysis model is proposed. The mathematical model is solved numerically and results are used to analyse the influence of the size of a wood-based fuel sample, the heating rate it is exposed to, and its initial moisture content in the process of the sample reaching the conditions where it can produce enough pyrolysate vapour to support a flame (flash point). In many pyrolysis models in the open literature it is assumed that the fuel samples are dry. In the present study it is found that the initial moisture content has a marked effect for a fuel sample reaching its flash point.

For the convection phenomena, a two-dimensional steady model, which explores the natural convection around one or more solid fuels, is also presented. The flame front is represented by a radiating panel. This means that the solid fuels receive a non-uniform heating rate depending on their geometry and location in relation to the panel. Changes in temperature and velocity profiles are monitored for varying heating rates and sample sizes (or, equivalently, the Rayleigh number Ra). Additionally, in the case of multiple fuel samples, changes in the distance between the fuels is also taken into account. For multiple fuels in arbitrary locations it is possible that one sample will block some of the radiation from the panel from reaching another sample. This means that the fuel sample will receive a reduced heating rate. This reduction in heating is also incorporated in the natural convection model.

Both the pyrolysis and natural convection models are solved numerically using the finite element software package COMSOL Multiphysics. A comparison of COMSOL is performed with benchmark solutions provided by the open literature. A good agreement in the numerical results is observed.

Declaration

No portion of the work referred to in the thesis has been submitted in support of an application for another degree or qualification of this or any other university or other institute of learning.

Copyright Statement

i. The author of this thesis (including any appendices and/or schedules to this thesis) owns certain copyright or related rights in it (the "Copyright") and s/he has given The University of Manchester certain rights to use such Copyright, including for administrative purposes.

ii. Copies of this thesis, either in full or in extracts and whether in hard or electronic copy, may be made **only** in accordance with the Copyright, Designs and Patents Act 1988 (as amended) and regulations issued under it or, where appropriate, in accordance with licensing agreements which the University has from time to time. This page must form part of any such copies made.

iii. The ownership of certain Copyright, patents, designs, trade marks and other intellectual property (the "Intellectual Property") and any reproductions of copyright works in the thesis, for example graphs and tables ("Reproductions"), which may be described in this thesis, may not be owned by the author and may be owned by third parties. Such Intellectual Property and Reproductions cannot and must not be made available for use without the prior written permission of the owner(s) of the relevant Intellectual Property and/or Reproductions.

iv. Further information on the conditions under which disclosure, publication and commercialisation of this thesis, the Copyright and any Intellectual Property and/or Reproductions described in it may take place is available in the University IP Policy (see http://documents.manchester.ac.uk/DocuInfo.aspx?DocID=487), in any relevant Thesis restriction declarations deposited in the University Library, The University Library's regulations (see http://www.manchester.ac.uk/library/aboutus/regulations) and in The University's Policy on Presentation of Theses.

Acknowledgements

I would like to thank my supervisor Prof. John Dold for his support during the past four years. This thesis would not have been possible without his expert advise and insight into mathematics and physics. I have learnt a lot from him.

I would also like to thank Dr. Joel Daou for his support in the final year of my PhD and taking the time to understand what I had been working on. I am also indebted to the IT support provided by Chris Paul. Without Chris's help I would probably still be running simulations.

I have been fortunate to befriend a fantastic mathematician, scientist, artist, poet, photographer, sportsman, cook, and raconteur in Dr. Vasileios Tsitsopoulos. He has been there for me all through the duration of my PhD and given me so much inspiration as a human being. I wish him, Nicola, and little Leonardo all the best and I hope we remain good friends for the foreseeable future.

Finally I'd like to thank my little brother Aman who has provided so much joy in my life. He means the world to me.

Chapter 1

Introduction

An understanding of the fundamentals of vegetation fires (bushfires, wildfires, and forest fires) is particularly important in terms of suppression efforts. These large scale fires can occur all over the world, in a variety of vegetal fuels, where the climate is moist enough to allow the growth of vegetation supplemented by extended periods of hot, dry weather. They can occur naturally (lightning strikes or following volcanic eruptions) or through human activity (arson, neglected camp fires, etc). Their effects are potentially fatal to nearby plants and animals, even humans. They can also have a significant economic impact [1].

Suppressing large scale fires is usually very difficult as access for fire-fighting machinery is limited. An effective strategy is to create firebreaks (gaps in vegetation which limits the fuel supply to the fire). These can be created by cutting down the vegetation or even burning it well before the large fire arrives. Using these suppression techniques requires good predictions of how a fire front will develop. Understanding the physical and chemical processes involved, and analysing fire related phenomena, can lead to accurate physical fire spread models [2].

Fire spread models based on the physics and chemistry of combustion and heat transfer [3, 4] involve finding the solution of a system of partial differential equations. These models give an insight into a number of vegetation fire variables such as spread rates, fuel consumption, volatile gas production, and ignition estimates [5–11].

The aim of this thesis is to model two physical phenomena that occur during a vegetation fire: (1) the pyrolysis process of vegetation reaching the point of ignition conditions and (2) the natural convection around the vegetation due to radiant heating.

The pyrolysis and natural convection models are described in Chapters 2 and 4 respectively.

Numerical results for the pyrolysis model are analysed in Chapter 3. In Chapter 5, the numerical method for solving natural convection problems is compared with literature for isothermal and uniformly heated bodies. The natural convection model, which incorporates a non-uniform heating rate, is solved and the results are analysed in Chapter 6.

The pyrolysis model involves the uniform heating of a vegetal fuel sample which leads to the thermal degradation of the fuel. This degradation leads to moisture evaporation and to pyrolysis processes which produce flammable vapour. Ignition conditions are met when the external gaseous mixture is composed of a certain amount of flammable vapour which allows piloted ignition (e.g. a lit match, lightning strike, ember, etc). Estimating the when a flammable mixture is obtained for various initial fuel moisture contents, sample sizes, and heating rates is of interest.

The natural convection model involves the study of flow around two-dimensional bodies subjected to a non-uniform heating rate. A flame approaching vegetation in its path will heat one side of the vegetation more than the other. The heating rate around the vegetation can be calculated based on geometric consideration. In the natural convection study, the interaction between multiple fuel samples will be considered. The flow and temperature fields are analysed for various sample sizes, heating rates, sample distances, and arrays.

Before describing the pyrolysis and natural convection processes in more detail it is worth introducing the fundamentals of heat transfer.

1.1 Heat transfer

Heat transfer is the transfer of thermal energy from one physical system to another. There are many texts describing the fundamentals of heat transfer [12, 13]. The three main modes of heat transfer are conduction, convection, and radiation. These forms of heat transfer will be present for both the pyrolysis and natural convection models. Phase-change heat transfer [14] will be incorporated in the pyrolysis model.

Heat transfer through conduction is the transfer of thermal energy between solids due to a temperature gradient. This can be described by

$$\mathbf{q} = -k\nabla T \tag{1.1}$$

where $\mathbf{q}$ [W/m^2] is the heat flux, k [W/m K] is the thermal conductivity, and T [K] represents the temperature. Equation 1.1 is Fourier's law for the conduction of heat. This is an empirical law which states that the heat transfer through a material is proportional to the change in temperature and to the area along the path of the heat flow. There is a minus sign in the equation because heat flows from a higher temperature to a lower temperature. The thermal conductivity, k, is a material property and in general varies in temperature and pressure so that $k = k(T, P)$. The heat conduction taking place within the vegetal fuel sample will be modelled for both the pyrolysis and natural convection studies. The sample will receive heat on its surface which will be conducted through the solid. The surrounding air will also conduct some heat although heat transfer in the air is dominated by convection.

Heat transfer through convection is the movement of molecules in fluids (i.e. liquid and gas states), it cannot occur in solids since motion can not take place. Heat convection takes place through the net displacement of a fluid, which transports the heat content in a fluid through the fluid's own velocity. The term convection is also used for the heat dissipation from a solid surface to a fluid where the temperature difference across a boundary layer [15] describes the flux. Convection can be described as either forced or natural (or a mixture of both). In forced convection the fluid movement results from external surface forces (e.g. wind). However in natural convection the temperature differences in the fluid result in density differences. The heavier (more dense) fluid will fall whereas the lighter (less dense) fluid will rise resulting in a buoyant flow. Forced convection effects are neglected in this thesis with the emphasis on modelling the natural convection flow (section 1.3).

Radiation is the heat transfer mechanism which allows bodies to exchange heat from a distance without making contact. It takes place in the form of electromagnetic waves which are mainly in the infrared region. Heat transfer by radiation does not require the presence of a medium as the electromagnetic waves will also transfer energy in a vacuum. If radiation reaches a surface then part of it is reflected from the body and the other part penetrates into the body [16]. Let ρ be the ratio of the reflected radiation and the incident radiation which represents the reflectivity. Similarly let α

be the ratio of the absorbed radiation and the incident radiation which represents the absorptivity. Finally let τ be the ratio of the transmitted radiation and the incident radiation which represents the transmissivity. Then

$$\rho + \alpha + \tau = 1.$$

Most solids and liquids absorb almost all the heat radiation which penetrates the surface so that τ is negligible. In this case

$$\rho + \alpha = 1.$$

An object which absorbs all the radiation which falls on to its surface is known as a black body so that

$$\alpha = 1.$$

Now consider the walls of a hollow space with a solid body situated within this space. The temperature at the walls of the hollow space and the body temperature may be the same. Then the heat which is radiated by the body must be equal to the heat which is radiated from the wall and absorbed by the body. If this was not the case then the second law of thermodynamics would be violated since heat would be created or lost in an isolated system. Let e denote the heat radiated per unit time from a unit surface [W/m^2]. This is called the emissive power. If the body in question was a black body with $e = e_b$ then the heat radiated from the walls and impinging the black body must be e_b as well. If we consider a general body with absorptivity $\alpha \neq 1$ (i.e. not a black body) then the body will absorb αe_b. The emissive power must be the same so that

$$e = \alpha \, e_b.$$

This is known as the Kirchhoff law. The ratio of the emissive power e and the emissive power of a black body e_b is known as the emissivity ϵ so that

$$\frac{e}{e_b} = \epsilon = \alpha.$$

For a black body the radiative heat flux q [W/m^2] is proportional to the fourth power of absolute temperature of the body T [K] so that

$$q = \varsigma \, T^4 \tag{1.2}$$

where $\varsigma = 5.6703 \times 10^{-8}$ [W/(m^{2}K^4)]. Equation (1.2) is the Stefan-Boltzmann equation and ς is the Stefan-Boltzmann constant of proportionality. However, a black body does not exist in the real world (that is, a body will never absorb all the radiation that falls on its surface) which is why we introduce the emissivity $0 \leq \epsilon \leq 1$. The Stefan-Boltzmann equation for variable emissivities is

$$q = \epsilon \varsigma T^4.$$

Phase-change heat transfer occurs when a substance changes its state in a system. In the pyrolysis model, a liquid-vapour phase-change occurs when moisture within the vegetal fuel sample will evaporate. This means that liquid water will change to water vapour (gas) when the vegetal fuel sample receives external heating. This form of heat transfer will be neglected in the natural convection model but will be incorporated in the pyrolysis model.

1.2 Pyrolysis in vegetal fuels

Pyrolysis is the decomposition of organic material at high temperatures relative to the ambient. As the vegetal fuel is heated, endothermic reactions take place before the ignition stage. Very few reactions occur as the temperature is increased from the ambient up to 100°C. At approximately 100°C, any moisture in the fuel is evaporated into the ambient air. Significant pyrolysis begins to take place at higher temperatures (about 200°C) when chemical bonds of the fuel begin to break. Solid char is produced as well as volatile gases. Significant char production can create a char layer which acts as a thermal insulator for the vegetal fuel. The char layer can reach high surface temperatures allowing the surface to react with oxygen in the air which can lead to glowing ignition [17]. Flaming combustion occurs when enough flammable volatile gases are released to form a mixture that can pilot ignite (e.g. with the aid of a lit match or contact with any nearby flame).

In most pyrolysis models the full reaction scheme is replaced by a few dominant overall reactions [18]. This approach simplifies the model and although this will not capture the exact processes by which pyrolysis occurs, when good reaction schemes are chosen, the model can be used to predict the main features of pyrolysis. In a mathematical model of pyrolysis of vegetal fuels, solutions to conservation equations are required. These partial differential equations have the form

$$\frac{\partial c}{\partial t} + \nabla \cdot (D \nabla c) = N_R$$

where c is the variable of interest, D is the diffusivity, and N_R is the net rate of production. The conservation equations are applied to mass, momentum, energy, and species which gives rise to a system of coupled partial differential equations which usually require numerical methods for their solution. In the pyrolysis of vegetal fuels the net rate of production/consumption is due to the chemical reactions creating or consuming mass, momentum, or energy. These chemical reactions occur when molecules collide with enough kinetic energy to overcome the repulsive forces and break up the molecular structure of the fuel. This gives rise to an activation energy, E_A, which is a threshold value below which the molecules do not have enough energy for reactions to occur. The Arrhenius law can be used to model the chemical reactions. This temperature dependant law makes use of the activation energy in order to predict the reaction rate so that

$$\omega = A\, e^{-(E_A/RT)}$$

where ω is the reaction rate, A is the pre-exponential factor which incorporates the frequency of molecular collisions, R is the gas constant, and T is the temperature. The Arrhenius law is widely used as it has been verified to have good accuracy for most chemical reactions which are temperature dependant [19].

The vegetal fuel is usually modelled as a porous medium, that is, a material consisting of solid matrix with interconnected empty sites or pores [20]. The porosity, φ say, is defined as the fraction of the total volume of the medium that is occupied by the pores so that the fraction that is occupied by the solid is $1 - \varphi$.

In this thesis, a pyrolysis model is presented (Chapter 2) which incorporates evaporation, charring, and fast pyrolysis processes in the external radiant heating of a vegetal fuel sample. The aim is to analyse and provide an estimate of when a flammable mixture, capable of piloted ignition, forms for various geometries, fuel sample sizes, heating rates, and initial moisture contents.

A natural convection model for the non-uniform heating of multiple fuel samples is presented in addition to this pyrolysis model (Chapter 4).

1.3 Natural convection around solid vegetal fuel samples

Natural convection is the buoyancy-induced fluid motion which results from the fluid density differences interacting with gravity. These density differences may be a result of temperate gradients, differences in the concentration of chemical species, phase changes, and other effects. In the present natural convection study, it is the temperature gradient which will result in the fluid (air) density differences. There are many different kinds of buoyancy-induced flows as they depend on the geometry and boundary conditions [21].

The fluid motion and temperature fields coupled so that they must be considered together. Motion of the fluid is initially laminar at short distances from, say, a heated body (e.g. external radiant heating of a vegetal fuel). However, the flow will transition to turbulence at larger distances from the body and eventually become turbulent. The surrounding flow field is of interest in the present study since ignition will occur near the vegetal fuel body. Therefore it is assumed that the flow will be laminar [15].

Assuming that the fluid density ρ depends on the fluid temperature T and a gravitational field $\mathbf{g}$ (a vector) exists then a local region of lower density will produce an upward force $\mathbf{B}$. This buoyancy force results in the motion of the fluid. In two dimensional space (x, y), gravity is assumed to act vertically downwards so that $\mathbf{g} = -g\mathbf{j}$, where $\mathbf{j}$ is the unit vector in the positive y-direction and g is the acceleration due to gravity.

The main dimensionless parameters that arise in natural convection problems are the Prandtl number Pr and Rayleigh number Ra [15]. The Prandtl number is the ratio of kinematic viscosity ν to thermal diffusivity κ

$$\mathrm{Pr} = \frac{\nu}{\kappa}.$$

Values of Pr will vary depending on the type of fluid and its ambient temperature. Typical values of Pr are about 0.015 for mercury, 7 for water, and 0.7 for air. In the present study, the fluid under consideration will be air so that Pr will be 0.7 unless otherwise stated. The Raleigh number gives a measure of how much the heat transfer is dominated by convection. When Ra is below a critical value, $\mathrm{Ra}_{\mathrm{cr}}$ say, for the fluid then heat transfer is said to be dominated by conduction from the body into the fluid.

For $\mathrm{Ra} > \mathrm{Ra}_{\mathrm{cr}}$, heat transfer is dominated by convection. The Raleigh number can be defined as

$$\mathrm{Ra} = \frac{g\beta l^3}{\nu\kappa}\left(T - T_0\right)$$

where T is the fluid temperature, T_0 is the ambient temperature, β is the thermal expansion coefficient ($1/T$ for ideal gases), and l is the length scale (e.g. diameter of the body). The Rayleigh number is the key parameter in the present natural convection problem as it will vary for different sample sizes and heating rates.

In the natural convection part of the thesis (Chapter 4 onwards), it is assumed that vegetal fuels will receive non-uniform external radiative heating. This approach models a flame front preheating a fuel sample of particular shape and size. The heating rate around a fuel sample will depend on the view factor [22]. This is the proportion of thermal radiation which leaves the flame and impinges the surface of the fuel. The view factor will vary depending on how much of the flame a point on the fuel surface can ‘see’. Incorporating this non-uniform radiative heating in the natural convection model will give a more realistic representation of the temperature and flow field around vegetal fuel sample in forest fire conditions.

1.4 Numerical solution procedure

The pyrolysis and natural convection models are solved using the commercial software package COMSOL Multiphysics. This software is based on the finite element method which includes packages to model topics of fluid dynamics coupled with heat transfer [23].

The geometry of the problem can be specified using the in-built drawing capabilities of COMSOL. Simple objects (squares, circles, rectangles, . . .), lines, and points can be specified. Within the geometry, coupled partial differential equations and appropriate boundary and initial conditions are specified. A mesh is generated based on the geometry which can be tuned to be finer on certain boundaries by specifying the ‘maximum element size’ option. This is a key feature in obtaining convergence, particularly for natural convection problems, as the mesh needs to be sufficiently fine around the solid in order to resolve the temperature gradients. Adjustments can also be made in the solver settings in order to solve the nonlinear Navier-Stokes equations coupled with heat transfer. The choice of solver, relative and absolute tolerance values, and initial solution have a significant effect on whether the solution will converge. It may be necessary to use numerical continuation [24] by solving a simplified problem (e.g. reduced heating rate) in order to provide a good initial solution when simulating the full problem.

In-built post-processing tools exist in COMSOL which allow point, line, and surface plots. In analysing results for various parameters, it is useful to export relevant data to software which is designed to deal with its numerical analysis (e.g. Matlab [25]).

1.5 Overview of thesis

- Chapter 1 - Introduction - The motivation for investigating pyrolysis and natural convection phenomena, particularly for gaining an insight into fire dynamics, is discussed. Also, the basics of pyrolysis, chemical reactions, heat and mass transfer, and natural convection are explained.

- Chapter 2 - Onset of ignition in vegetal fuels - The literature relevant to the pyrolysis phenomenon is reviewed. A pyrolysis model is presented which incorporates evaporation, charring, and fast pyrolysis processes. An estimate of the time taken to reach flammable mixture is also presented.

- Chapter 3 - Numerical results for pyrolysis model - Numerical results, using COMSOL Multiphysics, are presented. Variations in geometry, heating rate, fuel sample size, and initial fuel moisture content are explored.

- Chapter 4 - Natural convection with radiative heating - The literature relevant to the natural convection phenomenon is reviewed. Nondimensional governing equations are presented. The non-uniform radiative heating rate is derived along with an approach to deal with shadowing effects.

- Chapter 5 - Natural convection test problems - Natural convection test problems are solved using COMSOL Multiphysics. The numerical results are compared with the relevant literature in order to test COMSOL's suitability in accurately solving natural convection flow problems.

- Chapter 6 - Steady solutions are obtained for the natural convection around fuel samples subjected to nonuniform radiative heating. Problem parameters are the sample size, heating rate, and the distance between the samples. Temperature and velocity profiles are presented.

- Chapter 7 - Steady solutions are obtained for the natural convection around fuel samples for configurations where shadowing effects are present.

- Chapter 8 - Conclusions of both the pyrolysis and natural convection studies are discussed and the possibilities for further study.

Chapter 2

Onset of ignition in vegetal fuels

In this chapter, literature which is relevant to the pyrolysis process for vegetal fuels is reviewed (section 2.1), the governing equations for the pyrolysis model are presented (section 2.2), and a method for estimating the time taken to reach a flammable mixture is suggested (section 2.3).

In producing a good pyrolysis model a suitable chemical kinetic scheme must be chosen. A variety of schemes from the literature are summarised and existing pyrolysis models are reviewed. Typical model equations are also outlined. Various vapourisation models are outlined with particular emphasis on Di Blasi's relatively comprehensive model [26].

After the literature review, a one-dimensional time dependant model for the pyrolysis of an external radiatively heated vegetal fuel sample is presented. This model incorporates evaporation, charring, and fast pyrolysis chemical reactions. The model allows flake-like, cylindrical, and spherical vegetal fuels as the geometry. The fuel sample size, heating rate, and initial fuel moisture content are parameters of the problem. A simple approach is taken in estimating when a flammable mixture is formed in the external gas phase. The aim of the model is to obtain general results and not to delve into specialised chemical kinetics, vegetation orientation, and thermal shrinkage effects [27].

2.1 Pyrolysis literature

A large amount of experimental and theoretical research of the pyrolysis of vegetation-based fuels has been carried out in the literature [27]. A variety of theoretical approaches to pyrolysis modelling exist. Algebraic and analytical models usually ignore most of the chemical and physical processes involved in pyrolysis in order to reduce the complexity of the problem with the goal of obtaining a closed form solution for the rate of fuel pyrolysis [28]. The solutions provided to these models usually have a limited range of applicability. There are also integral based models which utilise numerical procedures to obtain temperature profiles and fuel pyrolysis rates [29]. These models include many of the chemical and physical processes which are ignored in most algebraic and analytical models. However, they assume a critical pyrolysis temperature criterion which means that the role of chemical kinetics in the overall thermal degradation process is neglected. When modelling the transient heating of a vegetal fuel the temperature ranges from ambient (300 K) to around 1000 K.

For relatively low temperatures (300–600 K) the pyrolysis process in the sample depends mainly on the chemical kinetics. However for larger temperatures the process depends less on the chemical kinetics and more on the diffusion of species within the sample [18]. Therefore, in a comprehensive model, it is important to account for the chemical kinetics as well as the diffusion processes.

2.1.1 Chemical kinetic schemes

Vegetal fuels are composed of cellulose, hemicellulose, lignin, and other extractives with cellulose making up around half of most vegetation species [30]. There is large diversity in vegetal fuels but, generally, more than half of the mass of the fuel species is composed of cellulose. Therefore many of the chemical kinetics of cellulose pyrolysis are applicable to all vegetal fuel types [31].

The first chemical kinetic model that managed to take into account some of the complexity of cellulose pyrolysis was developed in the seminal papers by Broido and his collegues [32–34]. Later, the generally accepted kinetic model of Bradbury et al. [35] simplified Broido's reaction network by omitting some of the solid forming reactions. This simplified reaction scheme is known as the Broido-Shafizadeh model (Figure

2.1) and is frequently used in pyrolysis models. In this kinetic model, the pyrolysis

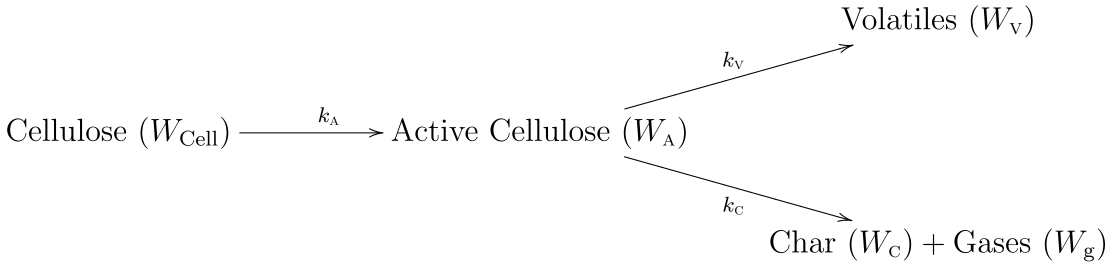

Figure 2.1: Three reaction Broido-Shafizadeh model proposed by Bradbury et al. [35].

reactions that take place at relatively low temperatures (less than 300°C) are assumed to lead to the formation of an 'active cellulose' (W_{A}). Upon further heating the active cellulose then decomposes by two competitive reactions, one which produces volatile species (W_{V}) and the other producing solid char (W_{C}) and other gases (e.g. CO, CO_2 and H_2O). The charring reaction is dominant at low temperatures with the reaction producing volatiles being dominant at higher temperatures. The chemical reaction rates k_i with $i \in \{\mathrm{A}, \mathrm{V}, \mathrm{C}\}$ are modelled by applying the Arrhenius law

$$k_i = A_i e^{-E_i/RT}$$

where R is the universal gas constant. The pre-exponential factor A_i and activation energy E_i are constants which are chosen based on experimental observations [36].

Varhegyi and Jakab [37] simplified the Broido-Shafizadeh scheme by omitting the Cellulose → Active Cellulose reaction. Their experimental results were better represented when this reaction was omitted in the kinetic scheme.

2.1.2 Pyrolysis models

The pyrolysis of vegetal fuels involves many physical phenomena. These include heat transfer through conduction, heat due to chemical reactions, convection of gaseous species, build-up of gaseous species within the fuel and the increase in pressure within, and vaporisation of moisture. Certain assumptions need to be made on computational grounds and also for keeping the generality of the model's applicability.

Velocity and pressure

The velocity $\mathbf{u} = (u, v, w)$ and pressure P of gaseous species within a heated vegetal fuel sample can be described by Darcy's law and the ideal gas law respectively [20].

Assuming the vegetal fuel can be modelled using one spatial dimension, r, so that there is only one nonzero component of the velocity $\mathbf{u} = (u, 0, 0)$, then Darcy's equation is reduced to [38]

$$u = -\frac{K}{\mu}\frac{\partial P}{\partial r}.$$

The permeability, K, of the fuel sample is a measure of the sample's ability to allow a fluid to flow through it under a total pressure gradient [39]. The viscosity of the fluid within the fuel sample, μ, is a measure of the fluid's resistance to deformation (e.g. water is considerably more viscous than air). Darcy's law can be used to calculate the mass flux of a gaseous mixture g since

$$\begin{aligned} m_g &= -\rho_g \frac{K}{\mu}\frac{\partial P}{\partial r} \\ &= \rho_g u \end{aligned}$$

where m_g is the mass flux and ρ_g is the density of the gaseous mixture g respectively [40].

The ideal gas law is an equation of state

$$P = \frac{\rho_g R T}{M_g}$$

where R is the gas constant and T is the temperature. The mean molecular weight of a gaseous mixture can be calculated as

$$\frac{1}{M_g} = \sum_i \frac{y_i}{M_i}$$

where y_i and M_i are the mass fraction and molecular weight of gaseous species i respectively.

Moisture evaporation

The vegetal fuel moisture content affects the vegetal temperature history due to the evaporation process [41]. It has been noted [42] that if moisture evaporation is not accounted for then the temperature results are overestimated. There are a few basic ways to model the evaporation of water from a heated vegetal fuels sample. Saastamoinen and Richard [43] use a relatively simple model where the drying front of the fuel is assumed to be infinitely thin and the phase change between liquid water to steam occurs at a constant temperature (100°C). Chan et al. [42] model the drying as an additional reaction using an Arrhenius expression with a suitable choice of the activation energy and pre-exponential factor based on experimental results. Alves and Figueiredo [44] and Bilbao et al. [45] use an algebraic expression for the temperature as a function of moisture content.

Di Blasi [26] applies a more detailed model of the drying process. The transport of bound and capillary water in the porous sample is taken into account. Her model focuses on the drying process. Therefore it is assumed that there is no thermal degradation of the solid at the temperatures needed for driving out the moisture in the fuel samples. Moisture in vegetal fuels can exist as bound water in the solid, free (liquid state) water in the pores, and water vapour in the pores [46]. Di Blasi formulates conservation equations for bound water, free water, and water vapour. The flow of gas and liquid are described by Darcy's law. For moisture contents greater than the fibre saturation point (typically around 30% for vegetal fuels) the Clausius-Clapeyron equation characterises the transition of water in its liquid state to its gaseous state. For moisture contents below the fibre saturation point, experimental studies show the vapour pressure is reduced which depends on the temperature and moisture content. The latent heat of vapourisation of capillary water (liquid water which exists within the pores of the sample) is constant (2260 kJ/kg). Bound water is the very thin layer of water which is chemically bound to the sample. Experiments by Siau [46] suggest that the latent heat of vaporisation of bound water depends on the moisture content. An iterative method for calculating the water vapour density is used in the numerical solution [26].

Typical conservation equations and model assumptions

Pyrolysis models are described by a number of conservation equations which include mass (solid, liquid, and gas), momentum (liquid and gas), and energy. The conservation equations depend on the the modelled species and chemical reactions. For example, by applying the Broido-Shafizadeh chemical kinetic model for cellulose pyrolysis (Figure 2.1) the solid species conservation equations are

$$\frac{\partial W_{\mathrm{Cell}}}{\partial t} = -k_{\mathrm{A}} \tag{2.1}$$

$$\frac{\partial W_{\mathrm{A}}}{\partial t} = k_{\mathrm{A}} - (k_{\mathrm{V}} + k_{\mathrm{C}}) \tag{2.2}$$

$$\frac{\partial W_{\mathrm{C}}}{\partial t} = \mu_{\mathrm{C}} k_{\mathrm{C}} \tag{2.3}$$

where μ_{C} is the mass-ratio between char and cellulose in the slow pyrolysis reaction k_{C} (about 0.35 [47]). The cellulose is consumed in order to produce an 'activated cellulose' which means that the temporal evolution of cellulose is driven by the activation reaction k_{A} (Equation 2.1). The activated cellulose is produced according to the activation reaction k_{A} and consumed by both the volatile species reaction k_{V} and the charring reaction k_{C} (Equation 2.2). Finally, char is produced by a fraction μ_{C} of the slow pyrolysis reaction k_{C} (Equation 2.3).

In deriving a typical comprehensive one-dimensional pyrolysis model, the following assumptions are made:

- The fuel sample is modelled as a porous medium but changes in its structure (e.g. thermal swelling/shrinkage, formation of cracks, etc) during the pyrolysis process are ignored.
- For each component of the fuel sample, pyrolysis follows a first-order Arrhenius law.
- The temperature of the fuel sample is in thermal equilibrium with the liquids and gases within the sample.
- Movement of liquids and gases in the fuel sample is governed by Darcy's law.

Based on the considerations highlighted in this section, a one-dimensional pyrolysis model, which incorporates drying, charring, and fast pyrolysis reaction, can be formulated. This model can also give an estimate of when a flammable mixture forms around the vegetal fuel sample.

2.2 Pyrolysis model

A model for the thermal degradation of vegetal fuel samples is developed in this chapter. Understanding this phase of a forest fire is important when attempting to provide good physical fire spread models [2]. The aim of the model is to include drying, charring, and fast pyrolysis processes for a given external radiant heat flux and fuel sample size in order to estimate when a flammable mixture is formed.

A vegetal fuel sample is considered to be subjected to a uniform constant external radiant heat flux at its surface resulting in the vaporisation of the moisture within the sample and the production of solid char and flammable vapour. The gaseous species convect through the fuel sample, which acts as a porous medium, and escape into an external gas phase. For this time dependent model, with one symmetrical spatial dimension, the emerging fuel and water vapour are considered to mix by diffusion with the surrounding air. If the concentration of the flammable vapour becomes high enough to exceed its lean flammability limit then any nearby flame is able to initiate a piloted ignition of a flame around the vegetation. That is, the vegetation reaches a form of flash point. For flammable liquids, the flash point is the temperature at which the air around the evaporating surface of the liquid contains fuel vapour that exceeds the lean flammability limit so that a premixed flame would be able to travel through it. This concept is extended in this study to flammable vapour emerging from the solid and mixing symmetrically with the surrounding air. This is modelled in a simplified way in order to capture the essence of the processes involved in the phenomenon.

A time dependant model is presented in this chapter which examines the nature of the flash point in a typical vegetal fuel sample. The geometry of the sample takes the form of either a solid slab of thickness $2a$ (e.g. disc-like objects such as a leaf), a cylinder of radius a (e.g. a stalk of grass) or a spherical sample of radius a (e.g. a seed) (see Figure 2.2). There is one independent spatial variable r so that the vegetal sample receives a uniform heating rate of J kW/m^2 on its surface at $r = a$. The parameters for dimension, radius, heating rate, and moisture content all affect the progress towards the flash point. Results are obtained for variations in these parameters. A nomenclature for this problem is presented in Table 2.1 due to the number of solid and gaseous species, and chemical reactions that are modelled.

There are various constants in the current heat and mass transfer problem many of which relate to the material and thermal properties of the solid vegetation and its products following pyrolysis. Table 2.2 shows the approximate values of the constants used in the model [48, 49]. The latent heat of vaporisation can be approximated as $L_{\mathrm{w}} \approx 2260$ J/g however a more accurate expression for the latent heat of vapourisation which depends on the moisture content w of the solid vegetation sample is [44]

$$L_{\mathrm{w}} \approx 2260 \times \max\left\{1, 1.48 - 5.79w + 26.7w^2 - 42.4w^3\right\} \text{ J/g}.$$

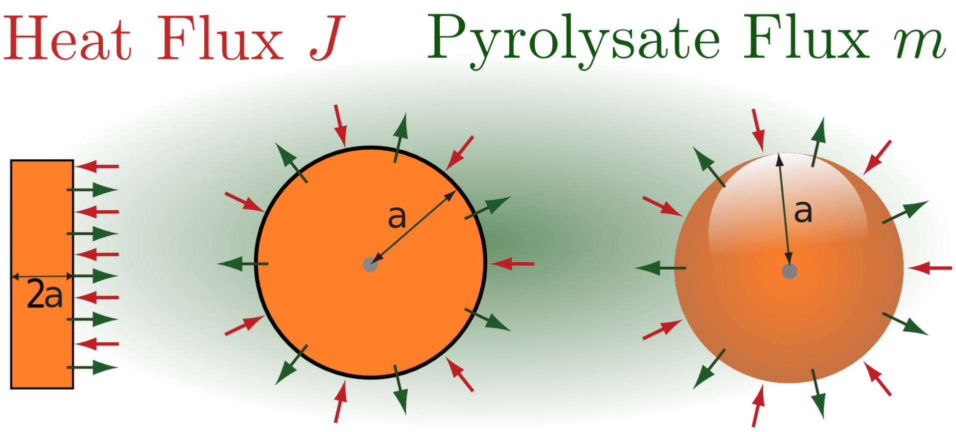

Figure 2.2: Pyrolysate vapour generated by the heating of vegetation with radius a. Sample is subjected to constant heat flux J kW/m^2 and the pyrolysate mass flux is m kg/(m^{2}s). Vegetal geometry can take the form of a slab, cylinder, or sphere.

2.2.1 Chemical reactions

There are many reactions which take place in the pyrolysis and combustion of vegetation. However the reactions which produce flammable fuel vapour and water vapour are of particular interest. When a sufficient amount of fuel vapour is released then a flame is produced subject to an ignition source (lean flammability limit). The role of the moisture in the sample of vegetation in reaching the lean flammability limit will be explored. Hence the model will consist of three main reactions which are of interest: solid vegetal fuel producing flammable fuel vapour (fast pyrolysis), vegetation producing solid char and some water vapour (slow pyrolysis or charring), and water evaporating into water vapour in the gas phase. The pyrolysis and water evaporation rates are given by the following relations

$$\begin{aligned}
&\text{Fast pyrolysis:} && \mathrm{G} \to \mathrm{F} && : \quad \omega_{\mathrm{F}} = \rho_{\mathrm{G}} \tau_{\mathrm{c}}^{-1} \exp\big(\beta_{\mathrm{F}}(1 - T_{\mathrm{c}}/T)\big) \\
&\text{Charring:} && \mathrm{G} \to \mathrm{C} + \mathrm{V} && : \quad \omega_{\mathrm{C}} = \rho_{\mathrm{C}} \tau_{\mathrm{c}}^{-1} \exp\big(\beta_{\mathrm{C}}(1 - T_{\mathrm{c}}/T)\big) \\
&\text{Vapourisation:} && \mathrm{W} \to \mathrm{V} && : \quad \omega_{\mathrm{V}} = \rho_{\mathrm{W}} \tau_{\mathrm{W}}^{-1} \left(1 - \frac{R T \rho_{\mathrm{V}}}{M_{\mathrm{V}} \varphi P_{\mathrm{Vb}}}\right)
\end{aligned}$$

where, as a rough estimate for modelling purposes, it can be taken that $\tau_{\mathrm{c}} \approx 30$ mins, $T_{\mathrm{c}} \approx 553$ K (290°C), $\beta_{\mathrm{F}} \approx 52$, $\beta_{\mathrm{C}} \approx 32$ and $\tau_{\mathrm{W}} \approx \frac{1}{8}$ s. Here τ_{c} is a typical time scale for both pyrolysis reactions at the crossover temperature $T = T_{\mathrm{c}}$. The exponential factor of the charring reaction is less than the exponential factor for the fast pyrolysis reaction (Table 2.2) because the fast pyrolysis reaction is dominant over the charring

G	dry vegetation	F	fuel vapour
W	absorbed water	V	water vapour
C	char	A	air
φ	porosity	ϱ_i	intrinsic density of species i
$\rho_i = (1-\varphi)\varrho_i$: overall density of solid i		$\rho_i = \varphi\varrho_i$: overall density of pore gas i	
$\mathbf{v} = \varphi\mathbf{u}$: 'Darcy' or mean flux velocity		$\hat{\varrho}_i$	'pure' density of condensed phase i
$\mathbf{u}$	mean gas velocity	$\rho_\mathrm{S} = \rho_\mathrm{G} + \rho_\mathrm{C} + \rho_\mathrm{W}$: overall solid density	
$\mathbf{u}_i$	velocity of species i	$\rho_\mathrm{g} = \rho_\mathrm{F} + \rho_\mathrm{V} + \rho_\mathrm{A}$: overall pore-gas density	
$\mathbf{u}'_i = \mathbf{u}_i - \mathbf{u}$: diffusive velocity of i		$\rho = \rho_\mathrm{S} + \rho_\mathrm{g}$: overall density	
$m = \rho_\mathrm{g} u$: mass flux in porous-medium		$\mathsf{m} = \varrho_\mathrm{g} v$: mass flux in external gas	
d_i	porous-medium diffusivity of $i \in \{\mathrm{F},\ \mathrm{V}\}$	$y_i = \rho_i/\rho_\mathrm{g}$: mass-fraction of pore gas i	
D_i	mass-diffusivity of external gas i	$\mathsf{y}_i = \varrho_i/\varrho_\mathrm{g}$: mass-fraction of external gas i	
K	permeability	M_i	molar mass of species i
l	grain scale	$n_i = M_\mathrm{A}/M_i - 1$: molar mass difference of i	
T	gas absolute temperature	P	absolute pressure
θ	solid absolute temperature	R	universal gas constant
T	porous medium absolute temperature	P_Vb	saturated water-vapour pressure in wood
ω_F	fast pyrolysis rate G → F	ω_V	water vapourisation rate W → V
ω_C	slow pyrolysis rate G → C + V	μ_C	mass-ratio (C : G) in slow pyrolysis
β_F	thermal sensitivity of fast pyrolysis	β_C	thermal sensitivity of slow pyrolysis
T_c	pyrolysis crossover temperature	τ_c	pyrolysis time scale at crossover
E_g	energy density of gaseous species	E_S	energy density of condensed species
c_{P_i}	specific heat of gas i	c_i	specific heat of solid i
L_W	latent heat of water vapourisation	T_b	boiling point of water (373.15 K)
$-Q_\mathrm{F}$	energy of fast-pyrolysis reaction	T_P	pyrolysis reference temperature ≈ 600 K
h_i	specific enthalpy of species i	$\mathbf{q}$	overall energy flux
$\mathbf{q}_\mathrm{g}$	total energy flux in the gas phase	$\mathbf{q}'_\mathrm{S}$	condensed-phase conductive energy flux
$\mathbf{q}'_\mathrm{g}$	gas-phase conductive energy flux	λ	overall thermal conductivity
λ_g	overall gas thermal conductivity	λ_S	overall condensed thermal conductivity
κ_i	thermal diffusivity of species i	ν_i	kinematic viscosity of gas i
h_X	gas-solid heat-exchange factor	$w = \rho_\mathrm{W}/\rho_\mathrm{G}$: moisture content	
ς	Stefan-Bolztmann radiative constant	J	heat received radially by sample

Table 2.1: Nomenclature for pyrolysis study.

reaction for temperatures greater than T_c. Also $\partial/\partial t$ is the partial derivative with respect to time. It is assumed that water will evaporate to reach its saturated water vapour pressure P_Vb over the time scale τ_W, which is set to be a reasonable value for numerical convergence. The fast pyrolysis and charring reactions follow the Arrhenius law where τ_c^{-1} is the pre-exponential factor.

The porosity of the vegetal fuel sample is defined as

$$\varphi = 1 - \rho_\mathrm{G}/\hat{\varrho}_\mathrm{G} - \rho_\mathrm{C}/\hat{\varrho}_\mathrm{C} - \rho_\mathrm{W}/\hat{\varrho}_\mathrm{W} \tag{2.4}$$

where $\hat{\varrho}_i$ represents the pure density of species $i \in \{\mathrm{G}, \mathrm{C}, \mathrm{W}\}$ (object made up of species i only). Equation (2.4) represents the fact that the porosity of the vegetal fuel sample will change depending on how much the densities of the vegetation, char, and water vary from their pure densities. Hence the porosity will change as the vegetation is pyrolysed and the water is being evaporated.

c_{G}	$=$	2.5 J/g K	c_{C}	$=$	1 J/g K	c_{W}	$=$	4.2 J/g K
$c_{\mathrm{P_F}}$	$=$	1 J/g K	$c_{\mathrm{P_V}}$	$=$	1.9 J/g K	$c_{\mathrm{P_A}}$	$=$	1 J/g K
κ_{G}	$=$	10^{-3} cm^2/s	κ_{C}	$=$	10^{-3} cm^2/s	κ_{G}	$=$	$1/700$ cm^2/s
κ_{F}	$=$	0.2 cm^2/s	κ_{V}	$=$	$3/13$ cm^2/s	κ_{A}	$=$	$2/9$ cm^2/s
M_{F}	$=$	50 g/mol	M_{V}	$=$	18 g/mol	M_{A}	$=$	29 g/mol
$\hat{\varrho}_{\mathrm{G}}$	$=$	1 g/cm^3	$\hat{\varrho}_{\mathrm{C}}$	$=$	2.2 g/cm^3	$\hat{\varrho}_{\mathrm{W}}$	$=$	1 g/cm^3
d_{F}	$=$	0.2 cm^2/s	d_{V}	$=$	$3/13$ cm^2/s	R	$=$	8.3145 J/K mol
β_{C}	$=$	32	β_{F}	$=$	52	Q_{F}	$=$	340 J/g
τ_{C}	$=$	3000 s	τ_{W}	$=$	$1/100$ s	μ_{C}	$=$	$1/3$
T_{C}	$=$	553 K	κ_{g}	$=$	$2/9$ cm^2/s	L_{W}	$=$	2260 J/g

Table 2.2: Approximate values of constants and their units of measurement for the current pyrolysis study.

The model for the vapourisation of water is based on the saturated water vapour pressure (measured in pascals Pa) in wood with a moisture content w [26]

$$P_{\mathrm{vb}} \approx P_{\mathrm{vs}} \times \exp\left(\min\left\{0, \left[\left(\frac{T-301}{65}\right)^2 - 3.54\right]\left(1+\frac{48.5-T}{1484}\right)^{92w}\right\}\right)$$

having a saturated water vapour pressure of free water of P_{vs}. A simple formula for the latter is

$$P_{\mathrm{vs}} \approx P_a \exp\left(13.336\left(1-\frac{T_{\mathrm{b}}}{T}\right) - 1.75\left(1-\frac{T_{\mathrm{b}}}{T}\right)^2\right)$$

where P_a is the standard atmospheric pressure at sea level of $P_a = 101325$ Pa and T_{b} is the boiling point of water (about 373 K). This simple formula was fitted using MAPLE and found to provide a close fit to the Goff-Gratch formula [50]. The relative difference is below 0.5% for a temperature range of 0°C - 230°C and below 1/100 % for the temperature range 18°C to 110°C. P_{vb} represents the saturated water vapour pressure of the water which is bound to the solid and is used by Di Blasi [26] and w is the moisture content of the vegetal fuel sample. The ratio of the vapour pressure of bound water and water vapour $P_{\mathrm{vb}}/P_{\mathrm{vs}}$ is plotted against the temperature T for various moisture contents w in Figure 2.3. An increase in the moisture content in the sample gives $P_{\mathrm{vb}} \approx P_{\mathrm{vs}}$ at lower temperatures.

2.2.2 Governing equations

The governing equations for modelling the heat and mass transport for a radially heated sample are the conservation equations for mass, energy, and species. A basic form of a

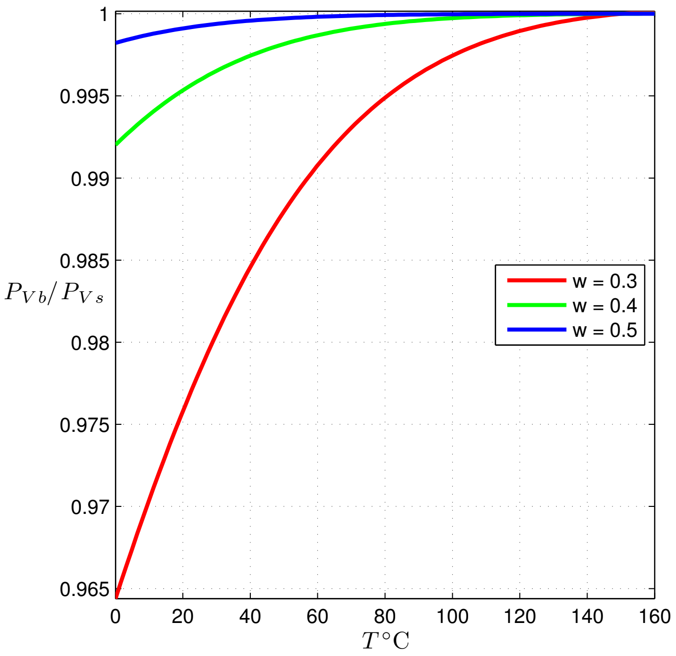

Figure 2.3: Plot of the vapour pressure $(P_{\mathrm{Vb}}/P_{\mathrm{VS}})$ when $P_{\mathrm{Vb}} \neq P_{\mathrm{VS}}$ against the temperature T for various moisture contents w.

conservation equation of any property, $\psi(\mathbf{x}, t)$ say, which is measured as a quantity per unit volume and varies with space $\mathbf{x} = (x, y, z)$ and time t is

$$\frac{\partial \psi}{\partial t} + \nabla \cdot (\text{flux of } \psi) = (\text{net rate of production per unit volume})$$

where the 'flux of ψ' is the amount of quantity which flows through a unit area per unit time.

Porous vegetation model equations

The mass and species conservation equations within the fuel sample are (using a subscript t to denote $\partial/\partial t$)

$$\rho_{\mathrm{G}_t} = -\omega_{\mathrm{F}} - \omega_{\mathrm{C}} \tag{2.5}$$

$$\rho_{\mathrm{C}_t} = \mu_{\mathrm{C}} \omega_{\mathrm{C}} \tag{2.6}$$

$$\rho_{\mathrm{W}_t} = -\omega_{\mathrm{V}} \tag{2.7}$$

$$\rho_{\mathrm{F}_t} + \nabla \cdot \rho_{\mathrm{F}} \mathbf{u} = \nabla \cdot \rho_{\mathrm{F}}\, d_{\mathrm{F}} \nabla y_{\mathrm{F}} + \omega_{\mathrm{F}} \tag{2.8}$$

$$\rho_{\mathrm{V}_t} + \nabla \cdot \rho_{\mathrm{V}} \mathbf{u} = \nabla \cdot \rho_{\mathrm{V}}\, d_{\mathrm{V}} \nabla y_{\mathrm{V}} + \omega_{\mathrm{V}} + (1 - \mu_{\mathrm{C}})\, \omega_{\mathrm{C}} \tag{2.9}$$

$$\rho_{\mathrm{g}_t} + \nabla \cdot \rho_{\mathrm{g}} \mathbf{u} = \omega_{\mathrm{F}} + \omega_{\mathrm{V}} + (1 - \mu_{\mathrm{C}})\, \omega_{\mathrm{C}} \tag{2.10}$$

where μ_{C} is the fraction of the solid vegetation which is converted to char in the charring reaction; the rest is converted to water vapour. The gas densities, mass fractions, and mass diffusivities are defined as $\rho_{\mathrm{g}} = \rho_{\mathrm{F}} + \rho_{\mathrm{V}} + \rho_{\mathrm{A}}$, $y_i = \rho_i/\rho_{\mathrm{g}}$ and d_i respectively. Here y_i is the mass fraction of gas $i \in \{\mathrm{F}, \mathrm{V}\}$ in the porous vegetation and d_i is the mass diffusivity of species $i \in \{\mathrm{F}, \mathrm{V}\}$. The mean gas velocity is $\mathbf{u}$ so that

$$(\rho_{\mathrm{F}} + \rho_{\mathrm{V}} + \rho_{\mathrm{A}})\,\mathbf{u} = \rho_{\mathrm{F}}\mathbf{u}_{\mathrm{F}} + \rho_{\mathrm{V}}\mathbf{u}_{\mathrm{V}} + \rho_{\mathrm{A}}\mathbf{u}_{\mathrm{A}}$$

where $\mathbf{u}_i$ represents the velocity of species $i \in \{\mathrm{F}, \mathrm{V}, \mathrm{A}\}$. Equations (2.5)–(2.7) represent conservation equations for the non-gaseous species of vegetation, char, and water (in its liquid state which is assumed to be bound to the solid vegetation as in [26]) whereas Equations (2.8)–(2.10) represent conservation equations for the gaseous species of pyrolysate vapour, water vapour, and air. In the case of the gaseous species, Fick's law of diffusion is applied [3] which states that the flux of species $i \in \{\mathrm{F}, \mathrm{V}, \mathrm{A}\}$ moves from regions of high concentration to regions of lower concentration with a magnitude which is proportional to the spatial gradient of the mass fraction. That is

$$F_i = -d_i \nabla y_i,\ i \in \{\mathrm{F}, \mathrm{V}, \mathrm{A}\}$$

where F_i is the flux of species $i \in \{\mathrm{F}, \mathrm{V}, \mathrm{A}\}$. The constant diffusion coefficient d_i depends on the properties of the gaseous species. Substituting $\rho_{\mathrm{F}} = y_{\mathrm{F}}\rho_{\mathrm{g}}$, $\rho_{\mathrm{V}} = y_{\mathrm{V}}\rho_{\mathrm{g}}$, and $\rho_{\mathrm{A}} = (1 - y_{\mathrm{F}} - y_{\mathrm{V}})\,\rho_{\mathrm{g}}$ into the pore gas equations will make them independent of the individual species densities ρ_{F} and ρ_{V} so that Equation (2.8) and Equation (2.9) become

$$\rho_{\mathrm{g}}\, y_{\mathrm{F}_t} + \rho_{\mathrm{g}}\mathbf{u} \cdot \nabla y_{\mathrm{F}} = \nabla \cdot \rho_{\mathrm{g}}\, d_{\mathrm{F}} \nabla y_{\mathrm{F}} + (1 - y_{\mathrm{F}})\,\omega_{\mathrm{F}} - y_{\mathrm{F}}\left(\omega_{\mathrm{V}} + (1 - \mu_{\mathrm{C}})\,\omega_{\mathrm{C}}\right)$$

$$\rho_{\mathrm{g}}\, y_{\mathrm{V}_t} + \rho_{\mathrm{g}}\mathbf{u} \cdot \nabla y_{\mathrm{V}} = \nabla \cdot \rho_{\mathrm{g}}\, d_{\mathrm{V}} \nabla y_{\mathrm{V}} + (1 - y_{\mathrm{V}})\left(\omega_{\mathrm{V}} + (1 - \mu_{\mathrm{C}})\,\omega_{\mathrm{C}}\right) - y_{\mathrm{V}}\omega_{\mathrm{F}}$$

respectively. The problem under consideration consists of a single sample of vegetation (Figure 2.2) in the form of either a solid slab of thickness $2a$ (e.g. a leaf), a cylinder of radius a (e.g. a stalk of grass), or a sphere of radius a (e.g. a seed). Hence the equations can be simplified further since the gradient and divergence operators can be reduced to

$$\nabla f = f_r$$

$$\nabla \cdot \mathbf{F} = \frac{1}{r^N}\left(r^N f\right)_r = \frac{N}{r} f + f_r$$

with $\mathbf{F} = f(r)\hat{\mathbf{r}}$ being an arbitrary function where r is the radial spatial coordinate and $\hat{\mathbf{r}}$ is a unit vector in the radial direction. The subscript r denotes differentiation with respect to r. Values of N determine the geometry of the sample with $N = 0$ representing the case of an infinite slab, $N = 1$ represents an infinite cylindrical sample, and $N = 2$ represents a spherical sample [3]. The gaseous mass flux can be defined as $m = \rho_{\mathrm{g}} u$. It is assumed that the fuel vapour, water vapour, and air have the same diffusion coefficient. That is they diffuse in a similar manner so that $d_{\mathrm{F}} = d_{\mathrm{V}} = d_{\mathrm{A}} = d$. Hence the conservation equations for the gaseous species reduce to

$$\rho_{\mathrm{g}}\, \rho_{\mathrm{F}_t} + m\, y_{\mathrm{F}_r} = \frac{d}{r^N}\left(r^N \rho_{\mathrm{g}}\, y_{\mathrm{F}_r}\right)_r + (1 - y_{\mathrm{F}})\,\omega_{\mathrm{F}} - y_{\mathrm{F}}\left(\omega_{\mathrm{V}} + (1 - \mu_{\mathrm{C}})\,\omega_{\mathrm{C}}\right)$$

$$\rho_{\mathrm{g}}\, \rho_{\mathrm{V}_t} + m\, y_{\mathrm{V}_r} = \frac{d}{r^N}\left(r^N \rho_{\mathrm{g}}\, y_{\mathrm{V}_r}\right)_r + (1 - y_{\mathrm{V}})\left(\omega_{\mathrm{V}} + (1 - \mu_{\mathrm{C}})\,\omega_{\mathrm{C}}\right) - y_{\mathrm{V}}\omega_{\mathrm{F}}$$

$$\rho_{\mathrm{g}_t} + \frac{1}{r^N}\left(r^N m\right)_r = \omega_{\mathrm{F}} + \omega_{\mathrm{V}} + (1 - \mu_{\mathrm{C}})\,\omega_{\mathrm{C}}.$$

In the latter equation, it will be assumed that gases are driven out of the porous vegetal fuel almost immediately as they are formed (due to the chemical reactions). Therefore the term ρ_{g_t} will be negligible.

The equation of state in the porous vegetation is

$$\rho_{\mathrm{g}} = \frac{\varphi\, M_{\mathrm{A}} P}{R\,T\,(1 + y_{\mathrm{F}} n_{\mathrm{F}} + y_{\mathrm{V}} n_{\mathrm{V}})} \tag{2.11}$$

where M_{A} is the molar mass of air, $n_i = M_{\mathrm{A}}/M_i - 1$ represents the molar mass difference of species $i \in \{\mathrm{F}, \mathrm{V}\}$ from that of air, and T is the porous medium absolute temperature. This is the ideal gas law

$$P = \frac{\varrho_{\mathrm{g}} R T}{M_{\mathrm{g}}}$$

where ϱ_{g} is the pure density of the gaseous species. The ideal gas law has been rearranged in the form of Equation (2.11) so that it is independent of the mass fraction of air y_{A} by applying the relations

$$y_{\mathrm{F}} + y_{\mathrm{V}} + y_{\mathrm{A}} = 1,$$

$$\frac{1}{M_{\mathrm{g}}} = \frac{y_{\mathrm{F}}}{M_{\mathrm{F}}} + \frac{y_{\mathrm{V}}}{M_{\mathrm{V}}} + \frac{y_{\mathrm{A}}}{M_{\mathrm{A}}}$$

and

$$\rho_{\mathrm{g}} = \varphi \varrho_{\mathrm{g}}.$$

The conservation of energy equation is given by

$$\frac{\partial E_{\mathrm{S}}}{\partial t} + \frac{\partial E_{\mathrm{g}}}{\partial t} + \nabla \cdot \mathbf{q} = 0 \tag{2.12}$$

where $E_{\mathrm{S}} = \rho_{\mathrm{G}} h_{\mathrm{G}} + \rho_{\mathrm{C}} h_{\mathrm{C}} + \rho_{\mathrm{W}} h_{\mathrm{W}}$ is the energy density of the condensed species (solid vegetation, char, and water) and $E_{\mathrm{g}} = \rho_{\mathrm{F}} h_{\mathrm{F}} + \rho_{\mathrm{V}} h_{\mathrm{V}} + \rho_{\mathrm{A}} h_{\mathrm{A}}$ is the energy density of the gaseous species (fuel vapour, water vapour, and air). The specific enthalpy of species $i \in \{\mathrm{G}, \mathrm{C}, \mathrm{W}, \mathrm{F}, \mathrm{V}, \mathrm{A}\}$ is denoted by h_i. Finally $\mathbf{q}$ is the overall energy flux. The specific enthalpies are defined to be

$$h_{\mathrm{G}} = c_{\mathrm{G}} \left(\theta - T_{\mathrm{P}}\right) \tag{2.13}$$

$$h_{\mathrm{C}} = c_{\mathrm{C}} \theta - h_{\mathrm{C}0} \tag{2.14}$$

$$h_{\mathrm{W}} = c_{\mathrm{W}} \left(\theta - T_{\mathrm{b}}\right) - L_{\mathrm{W}} \tag{2.15}$$

$$h_{\mathrm{F}} = c_{\mathrm{P_F}} \left(\mathsf{T} - T_{\mathrm{P}}\right) + Q_{\mathrm{F}} \tag{2.16}$$

$$h_{\mathrm{V}} = c_{\mathrm{P_V}} \left(\mathsf{T} - T_{\mathrm{b}}\right) \tag{2.17}$$

$$h_{\mathrm{A}} = c_{\mathrm{P_A}} \mathsf{T} \tag{2.18}$$

where c_i is the specific heat capacity of the condensed species $i \in \{\mathrm{G}, \mathrm{C}, \mathrm{W}\}$ and c_{p_i} is the specific heat capacity of the gaseous species $i \in \{\mathrm{F}, \mathrm{V}, \mathrm{A}\}$. The gas absolute temperature is denoted by T and θ is the solid absolute temperature. Also T_{b} is the standard boiling point of water (100°C or 373 K) at sea level and T_{P} is chosen to represent a pyrolysis reference temperature ($\approx$ 300°C or 573 K). The heat absorbed due to the fast pyrolysis reaction G $\rightarrow$ F, at the temperature T_{P}, is denoted by Q_{F}. The charring reaction is treated as thermally neutral. The energy flux $\mathbf{q} = \mathbf{q}_{\mathrm{S}}' + \mathbf{q}_{\mathrm{g}}$ can be split up into the condensed phase conductive energy flux $\mathbf{q}_{\mathrm{S}}'$ and the total gas phase energy flux $\mathbf{q}_{\mathrm{g}}$ so that

$$\mathbf{q}_{\mathrm{S}}' = -\lambda_{\mathrm{S}} \nabla \theta$$

$$\mathbf{q}_{\mathrm{g}} = \rho_{\mathrm{F}} h_{\mathrm{F}} \mathbf{u}_{\mathrm{F}} + \rho_{\mathrm{V}} h_{\mathrm{V}} \mathbf{u}_{\mathrm{V}} + \rho_{\mathrm{A}} h_{\mathrm{A}} \mathbf{u}_{\mathrm{A}} + \mathbf{q}_{\mathrm{g}}'$$

where $\mathbf{q}_{\mathrm{g}}' = -\lambda_{\mathrm{g}} \nabla T$ is the gas phase conductive energy flux. The overall thermal conductivities of the condensed phase and gas phase are λ_{S} and λ_{g} respectively with $\mathbf{u}_i$ representing the velocity of species $i \in \{\mathrm{F}, \mathrm{V}, \mathrm{A}\}$. Equation (2.12) can be split into an energy equation for the condensed species

$$E_{\mathrm{S}_t} + \nabla \cdot \mathbf{q}_{\mathrm{S}}' = h_{\mathrm{X}} \left(\mathsf{T} - \theta\right) \tag{2.19}$$

and an energy equation for the gaseous species

$$E_{\mathrm{g}_t} + \nabla \cdot \mathbf{q}_{\mathrm{g}} = h_{\mathrm{X}} \left(\theta - \mathsf{T}\right) \tag{2.20}$$

where h_{X} is the gas-solid heat-exchange factor. Equation (2.19) can be written as

$$\begin{aligned} &\left[\rho_{\mathrm{G}} c_{\mathrm{g}} \left(\theta - T_{\mathrm{P}}\right) + \rho_{\mathrm{C}} \left(c_{\mathrm{C}} \theta + h_{\mathrm{C}0}\right) + \rho_{\mathrm{W}} \left(c_{\mathrm{W}} \left(\theta - T_{\mathrm{b}}\right) - L_{\mathrm{W}}\right)\right]_t \\ &\qquad\qquad\qquad\qquad + \nabla \cdot \mathbf{q}_{\mathrm{S}}' = h_{\mathrm{X}} \left(\mathsf{T} - \theta\right) \end{aligned}$$

and applying the product rule for differentiation reduces the energy equation for the condensed species to

$$\begin{aligned} &\rho_{\mathrm{G}} c_{\mathrm{G}} \frac{\partial \theta}{\partial t} + \rho_{\mathrm{C}} c_{\mathrm{C}} \frac{\partial \theta}{\partial t} + \rho_{\mathrm{W}} c_{\mathrm{W}} \frac{\partial \theta}{\partial t} + h_{\mathrm{G}} \frac{\partial \rho_{\mathrm{G}}}{\partial t} + h_{\mathrm{C}} \frac{\partial \rho_{\mathrm{C}}}{\partial t} + h_{\mathrm{W}} \frac{\partial \rho_{\mathrm{W}}}{\partial t} \\ &\qquad\qquad\qquad\qquad + \nabla \cdot \mathbf{q}_{\mathrm{S}}' = h_{\mathrm{X}} \left(\mathsf{T} - \theta\right). \end{aligned}$$

The mass conservation equations can be applied to give

$$\begin{aligned} &\left(\rho_{\mathrm{G}} c_{\mathrm{G}} + \rho_{\mathrm{C}} c_{\mathrm{C}} + \rho_{\mathrm{W}} c_{\mathrm{W}}\right) \frac{\partial \theta}{\partial t} - h_{\mathrm{G}} \omega_{\mathrm{F}} - h_{\mathrm{W}} \omega_{\mathrm{V}} + \left(\mu_{\mathrm{C}} h_{\mathrm{C}} - h_{\mathrm{G}}\right) \omega_{\mathrm{C}} \\ &\qquad\qquad\qquad\qquad + \nabla \cdot \mathbf{q}_{\mathrm{S}}' = h_{\mathrm{X}} \left(\mathsf{T} - \theta\right). \end{aligned} \tag{2.21}$$

Similarly Equation (2.20) can be written as

$$\begin{aligned} &\left[\rho_{\mathrm{F}} \left(c_{\mathrm{P_F}} \left(\mathsf{T} - T_{\mathrm{P}}\right) + Q_{\mathrm{F}}\right) + \rho_{\mathrm{V}} c_{\mathrm{P_V}} \left(\mathsf{T} + T_{\mathrm{b}}\right) + \rho_{\mathrm{A}} \left(c_{\mathrm{P_A}} \mathsf{T}\right)\right]_t \\ &+ \nabla \cdot \left(\rho_{\mathrm{F}} \left(c_{\mathrm{P_F}} \left(\mathsf{T} - T_{\mathrm{P}}\right) + Q_{\mathrm{F}}\right) \mathbf{u}_{\mathrm{F}} + \rho_{\mathrm{V}} c_{\mathrm{P_V}} \left(\mathsf{T} - T_{\mathrm{b}}\right) \mathbf{u}_{\mathrm{V}} + \rho_{\mathrm{A}} c_{\mathrm{P_A}} \mathsf{T}\, \mathbf{u}_{\mathrm{A}}\right) \\ &\qquad\qquad\qquad\qquad + \nabla \cdot \mathbf{q}_{\mathrm{g}}' = h_{\mathrm{X}} \left(\theta - \mathsf{T}\right) \end{aligned}$$

and applying the product rule of differentiation reduces the energy equation for the gaseous species to

$$\begin{aligned} &\rho_{\mathrm{F}} c_{\mathrm{P_F}} \frac{\partial \mathsf{T}}{\partial t} + \rho_{\mathrm{V}} c_{\mathrm{P_C}} \frac{\partial \mathsf{T}}{\partial t} + \rho_{\mathrm{A}} c_{\mathrm{P_W}} \frac{\partial \mathsf{T}}{\partial t} + h_{\mathrm{F}} \frac{\partial \rho_{\mathrm{F}}}{\partial t} + h_{\mathrm{V}} \frac{\partial \rho_{\mathrm{V}}}{\partial t} + h_{\mathrm{A}} \frac{\partial \rho_{\mathrm{A}}}{\partial t} \\ &+ h_{\mathrm{F}} \nabla \cdot \rho_{\mathrm{F}} \mathbf{u}_{\mathrm{F}} + h_{\mathrm{V}} \nabla \cdot \rho_{\mathrm{V}} \mathbf{u}_{\mathrm{V}} + h_{\mathrm{A}} \nabla \cdot \rho_{\mathrm{A}} \mathbf{u}_{\mathrm{A}} + \rho_{\mathrm{F}} c_{\mathrm{P_F}} \mathbf{u}_{\mathrm{F}} \cdot \nabla \mathsf{T} + \rho_{\mathrm{V}} c_{\mathrm{P_V}} \mathbf{u}_{\mathrm{V}} \cdot \nabla \mathsf{T} + \rho_{\mathrm{A}} c_{\mathrm{P_A}} \mathbf{u}_{\mathrm{A}} \cdot \nabla \mathsf{T} \\ &\qquad\qquad\qquad\qquad + \nabla \cdot \mathbf{q}_{\mathrm{g}}' = h_{\mathrm{X}} \left(\theta - \mathsf{T}\right). \end{aligned}$$

Defining the diffusive velocity of species $i \in \{\mathrm{F}, \mathrm{V}, \mathrm{A}\}$ as $\mathbf{u}_i' = \mathbf{u_i} + \mathbf{u}$ and applying the mass conservation equations gives the energy conservation equation for gaseous species as

$$\begin{aligned}
\left(\rho_{\mathrm{F}} c_{\mathrm{P_F}} + \rho_{\mathrm{V}} c_{\mathrm{P_C}} + \rho_{\mathrm{A}} c_{\mathrm{P_A}}\right) \frac{\partial \mathsf{T}}{\partial t} &+ \left(\rho_{\mathrm{F}} c_{\mathrm{P_F}} + \rho_{\mathrm{V}} c_{\mathrm{P_C}} + \rho_{\mathrm{A}} c_{\mathrm{P_W}}\right) \mathbf{u} \cdot \nabla \mathsf{T} \\
&+ \left(\rho_{\mathrm{F}} c_{\mathrm{P_F}} \mathbf{u}'_{\mathrm{F}} + \rho_{\mathrm{V}} c_{\mathrm{P_C}} \mathbf{u}'_{\mathrm{V}} + \rho_{\mathrm{A}} c_{\mathrm{P_A}} \mathbf{u}'_{\mathrm{A}}\right) \cdot \nabla \mathsf{T} \\
&+ h_{\mathrm{V}} \omega_{\mathrm{V}} + h_{\mathrm{F}} \omega_{\mathrm{F}} + (1 - \mu_{\mathrm{C}}) h_{\mathrm{C}} \omega_{\mathrm{C}} \\
&+ \nabla \cdot \mathbf{q}'_{\mathrm{g}} = h_{\mathrm{X}} \left(\theta - \mathsf{T}\right). \qquad (2.22)
\end{aligned}$$

In order to simplify Equations (2.21) and (2.22) it is necessary to make certain assumptions about the physics of this particular heat and mass transfer problem. It is expected that the temperature difference between the solid absolute temperature and the gas absolute temperature will be small. That is the solid phase and gas phase are in thermal equilibrium so that

$$\theta \approx \mathsf{T} \approx T$$

everywhere in the porous fuel sample [20]. This assumption is reasonable for small and samples with low porosity (i.e. almost solid). From this assumption the change in the specific enthalpy of water and water vapour is simplified

$$\begin{aligned}
h_{\mathrm{V}} - h_{\mathrm{W}} &= c_{\mathrm{P_V}} \left(\mathsf{T} - T_{\mathrm{b}}\right) - c_{\mathrm{W}} \left(\theta - T_{\mathrm{b}}\right) + L_{\mathrm{W}} \\
&\approx \left(c_{\mathrm{P_V}} - c_{\mathrm{W}}\right) \left(T - T_{\mathrm{b}}\right) + L_{\mathrm{W}}.
\end{aligned}$$

Further assuming that nearly all the vapourisation of water takes place near the boiling point (i.e. $T \approx T_{\mathrm{b}}$) then

$$\left(h_{\mathrm{V}} - h_{\mathrm{W}}\right) \omega_{\mathrm{V}} \approx L_{\mathrm{W}} \omega_{\mathrm{V}}.$$

Again this is a reasonable assumption if the heating rate is sufficient to heat the sample to the boiling point quickly. Similarly

$$\begin{aligned}
h_{\mathrm{F}} - h_{\mathrm{G}} &= c_{\mathrm{P_F}} \left(\mathsf{T} - T_{\mathrm{P}}\right) - c_{\mathrm{G}} \left(\theta - T_{\mathrm{P}}\right) + Q_{\mathrm{F}} \\
&\approx \left(c_{\mathrm{P_F}} - c_{\mathrm{G}}\right) \left(T - T_{\mathrm{P}}\right) + Q_{\mathrm{F}}.
\end{aligned}$$

and assuming that pyrolysis occurs mainly around the temperature T_{P}, then

$$\left(h_{\mathrm{F}} - h_{\mathrm{G}}\right) \omega_{\mathrm{F}} \approx Q_{\mathrm{F}} \omega_{\mathrm{F}}.$$

It is also fair to assume that the contribution to the energy equation from the charring reaction, ω_{C}, will be small compared to the other reactions so that

$$\left(h_{\mathrm{V}} - h_{\mathrm{G}} + \mu_{\mathrm{C}} \left(h_{\mathrm{C}} - h_{\mathrm{V}}\right)\right) \omega_{\mathrm{C}} \approx 0.$$

The overall energy flux can be simplified to

$$\begin{aligned}\mathbf{q} = \mathbf{q}'_{\mathrm{S}} + \mathbf{q}_{\mathrm{g}} &= -\left(\lambda_{\mathrm{S}}\nabla\theta + \lambda_{\mathrm{g}}\nabla \mathsf{T}\right)\\ &\approx -\left(\lambda_{\mathrm{S}}\nabla T + \lambda_{\mathrm{g}}\nabla T\right) = -\lambda\nabla T.\end{aligned}$$

Recall that

$$\left(\rho_{\mathrm{F}} + \rho_{\mathrm{V}} + \rho_{\mathrm{A}}\right)\mathbf{u} = \rho_{\mathrm{F}}\mathbf{u}_{\mathrm{F}} + \rho_{\mathrm{V}}\mathbf{u}_{\mathrm{V}} + \rho_{\mathrm{A}}\mathbf{u}_{\mathrm{A}}.$$

It follows that the mass-weighted diffusion velocity $\rho_{\mathrm{F}}\mathbf{u}'_{\mathrm{F}} + \rho_{\mathrm{V}}\mathbf{u}'_{\mathrm{V}} + \rho_{\mathrm{A}}\mathbf{u}'_{\mathrm{A}}$ is zero by definition. If the gaseous specific heats are not very different then it is fair to assume that

$$\rho_{\mathrm{F}}c_{\mathrm{P_F}}\mathbf{u}'_{\mathrm{F}} + \rho_{\mathrm{V}}c_{\mathrm{P_C}}\mathbf{u}'_{\mathrm{V}} + \rho_{\mathrm{A}}c_{\mathrm{P_A}}\mathbf{u}'_{\mathrm{A}} \approx 0,$$

or at least we assume that the contribution of these diffusive velocities to energy flow is small compared with the other contributions. Applying these assumptions and using the fact that the density of the condensed species is much larger than the density of the gaseous species [20]

$$\rho_{\mathrm{F}}c_{\mathrm{P_F}} + \rho_{\mathrm{V}}c_{\mathrm{P_C}} + \rho_{\mathrm{A}}c_{\mathrm{P_A}} \ll \rho_{\mathrm{G}}c_{\mathrm{G}} + \rho_{\mathrm{C}}c_{\mathrm{C}} + \rho_{\mathrm{W}}c_{\mathrm{W}}.$$

gives the much simplified energy conservation equation in the porous medium as

$$\begin{aligned}\left(\rho_{\mathrm{G}}c_{\mathrm{G}} + \rho_{\mathrm{C}}c_{\mathrm{C}} + \rho_{\mathrm{W}}c_{\mathrm{W}}\right)\frac{\partial T}{\partial t} + \left(\rho_{\mathrm{F}}c_{\mathrm{PF}} + \rho_{\mathrm{V}}c_{\mathrm{PV}} + \rho_{\mathrm{A}}c_{\mathrm{PA}}\right)\mathbf{u}\cdot\nabla T + L_{\mathrm{W}}\omega_{\mathrm{V}} + Q_{\mathrm{F}}\omega_{\mathrm{F}}&\\ = \nabla\cdot\lambda\nabla T.& \qquad (2.23)\end{aligned}$$

To summarise, the model equations applicable in the porous medium are the mass conservation equations

$$\begin{aligned}\partial_t\rho_{\mathrm{G}} &= -\omega_{\mathrm{F}} - \omega_{\mathrm{C}}\\ \partial_t\rho_{\mathrm{C}} &= \mu_{\mathrm{C}}\omega_{\mathrm{C}}\\ \partial_t\rho_{\mathrm{W}} &= -\omega_{\mathrm{V}}\\ \rho_{\mathrm{g}}\partial_t y_{\mathrm{F}} + m y_{\mathrm{F}_r} &= \left(1 - y_{\mathrm{F}}\right)\omega_{\mathrm{F}} - y_{\mathrm{F}}\left(\omega_{\mathrm{V}} + \left(1 - \mu_{\mathrm{C}}\right)\omega_{\mathrm{C}}\right)\\ \rho_{\mathrm{g}}\partial_t y_{\mathrm{V}} + m y_{\mathrm{V}_r} &= \left(1 - y_{\mathrm{V}}\right)\left(\omega_{\mathrm{V}} + \left(1 - \mu_{\mathrm{C}}\right)\omega_{\mathrm{C}}\right) - y_{\mathrm{V}}\omega_{\mathrm{F}}\\ \left(r^N m\right)_r &= r^N\left(\omega_{\mathrm{F}} + \omega_{\mathrm{V}} + \left(1 - \mu_{\mathrm{C}}\right)\omega_{\mathrm{C}}\right),\end{aligned}$$

and energy conservation

$$r\overline{\rho c}\frac{\partial T}{\partial t} + \left(r\bar{c}_{\mathrm{g}}m + (1 - N)\lambda\right)T_r = \left(r\lambda T_r\right)_r - rL_{\mathrm{W}}\omega_{\mathrm{V}} - rQ_{\mathrm{F}}\omega_{\mathrm{F}}$$

with

$$\overline{\rho c} = \rho_{\mathrm{G}} c_{\mathrm{G}} + \rho_{\mathrm{C}} c_{\mathrm{C}} + \rho_{\mathrm{W}} c_{\mathrm{W}} + \rho_{\mathrm{g}} \overline{c}_{\mathrm{g}} \quad \text{and} \quad \overline{c}_{\mathrm{g}} = y_{\mathrm{F}} c_{\mathrm{P_F}} + y_{\mathrm{V}} c_{\mathrm{P_V}} + y_{\mathrm{A}} c_{\mathrm{P_A}}.$$

The ideal gas law can be written as

$$\rho_{\mathrm{g}} = \frac{\varphi P M_{\mathrm{A}}}{RT\left(1 + y_{\mathrm{F}} n_{\mathrm{F}} + y_{\mathrm{V}} n_{\mathrm{V}}\right)}$$

and the mean gas velocity is

$$u = \frac{m}{\rho_{\mathrm{g}}}.$$

The chemical reaction rates for fast pyrolysis, slow pyrolysis, and vapourisation of water are modelled as

$$\omega_{\mathrm{F}} = \rho_{\mathrm{G}} \tau_{\mathrm{C}}^{-1} \exp\left(\beta_{\mathrm{F}}(1 - T_{\mathrm{C}}/T)\right)$$

$$\omega_{\mathrm{C}} = \rho_{\mathrm{G}} \tau_{\mathrm{C}}^{-1} \exp\left(\beta_{\mathrm{C}}(1 - T_{\mathrm{C}}/T)\right)$$

$$\omega_{\mathrm{V}} \approx \tau_{\mathrm{W}}^{-1} \rho_{\mathrm{W}} \left(1 - \frac{RT\rho_{\mathrm{V}}}{M_{\mathrm{V}} \varphi P_{\mathrm{V_b}}}\right)$$

respectively.

The governing equations in the porous medium of the solid fuel sample have been presented. The external gas equations with boundary and initial conditions also need to be determined for a complete pyrolysis model.

External gas equations

In the external gas phase, model equations for ϱ_{F}, ϱ_{V}, ϱ_{g}, v, and T are applicable, where ϱ_i is the intrinsic density of species $i \in \{\mathrm{F}, \mathrm{V}, \mathrm{g}\}$, v is the velocity, and T is the temperature in the external gas phase. It is assumed that there are no condensed species in the external gas phase, only air, water vapour, and pyrolysis vapour.

The model equations in the external gas phase includes the mass conservation equations

$$\varrho_{\mathrm{g}} \frac{\partial \mathsf{y}_{\mathrm{F}}}{\partial t} + \left(\mathsf{m} - \frac{N}{r} \varrho_{\mathrm{g}} D_{\mathrm{F}}\right) \mathsf{y}_{\mathrm{F}_r} = \left(\varrho_{\mathrm{g}} D_{\mathrm{F}} \mathsf{y}_{\mathrm{F}_r}\right)_r$$

$$\varrho_{\mathrm{g}} \frac{\partial \mathsf{y}_{\mathrm{V}}}{\partial t} + \left(\mathsf{m} - \frac{N}{r} \varrho_{\mathrm{g}} D_{\mathrm{V}}\right) \mathsf{y}_{\mathrm{V}_r} = \left(\varrho_{\mathrm{g}} D_{\mathrm{V}} \mathsf{y}_{\mathrm{V}_r}\right)_r$$

$$\left(r^N \mathsf{m}\right)_r = 0,$$

in which the term $\partial \varrho_{\mathrm{g}} / \partial t$ is neglected in the continuity equation, in comparison with flow divergence. This would also be the result of a constant density assumption as it is often found to provide good results in combustion theory, even when density changes are small. The energy conservation equation in the external gas phase is

$$\varrho_{\mathrm{g}}\bar{c}_{\mathrm{g}}\frac{\partial \mathsf{T}}{\partial t} + \left(\bar{c}_{\mathrm{g}}\mathsf{m} - \frac{N}{r}\lambda_{\mathrm{g}}\right)\mathsf{T}_r = \left(\lambda_{\mathrm{g}}\mathsf{T}_r\right)_r$$

with

$$\lambda_{\mathrm{g}} = \varrho_{\mathrm{g}}\left(\mathsf{y}_{\mathrm{F}}c_{\mathsf{p}_{\mathrm{F}}}\kappa_{\mathrm{F}} + \mathsf{y}_{\mathrm{V}}c_{\mathrm{P_V}}\kappa_{\mathrm{V}} + \mathsf{y}_{\mathrm{A}}c_{\mathrm{P_A}}\kappa_{\mathrm{A}}\right)$$

$$\bar{c}_{\mathrm{g}} = \mathsf{y}_{\mathrm{F}}c_{\mathrm{P_F}} + \mathsf{y}_{\mathrm{V}}c_{\mathrm{P_V}} + \mathsf{y}_{\mathrm{A}}c_{\mathrm{P_A}}.$$

The equation of state is again the ideal gas law

$$\varrho_{\mathrm{g}} = \frac{PM_{\mathrm{A}}}{R\,\mathsf{T}\left(1 + \mathsf{y}_{\mathrm{F}}n_{\mathrm{F}} + \mathsf{y}_{\mathrm{V}}n_{\mathrm{V}}\right)}$$

and the mass flux of the external gas is

$$\mathsf{m} = \varrho_{\mathrm{g}}v.$$

The governing equations for the combustion of a vegetal fuel sample and the convection of the gaseous species have been presented for both the porous medium and external gas phase. It is necessary to apply relevant boundary and initial conditions before the problem can be solved numerically.

Boundary and initial conditions

Initially ($t = 0$) the vegetal sample and its surrounding air are at ambient temperature

$$T = \mathsf{T} = T_0 \approx 300 \text{ K}.$$

The vegetal sample will be made up of dry vegetation G and some initial fuel moisture content w_0 so that

$$\rho_{\mathrm{g}} = \rho_{\mathrm{g}_0} \approx 500 \text{ kg/m}^3 \qquad \rho_{\mathrm{W}} = w_0\,\rho_{\mathrm{G}_0} \approx 500\,w_0 \text{ kg/m}^3$$

$$\rho_{\mathrm{C}} = \rho_{\mathrm{C}_0} = 0 \text{ kg/m}^3 \qquad \rho_{\mathrm{F}} = \rho_{\mathrm{F}_0} = 0 \text{ kg/m}^3$$

$$\varphi = \varphi_0 = 1 - \frac{\rho_{\mathrm{G}_0}}{\hat{\varrho}_{\mathrm{G}}} - \frac{\rho_{\mathrm{W}_0}}{\hat{\varrho}_{\mathrm{W}}}.$$

Initial saturated water vapour pressure in the vegetal sample will be evaluated at $T = T_0$ and $w = w_0$ so that

$$P_{\mathrm{vb}} = P_{\mathrm{vb}_0} \approx P_{\mathrm{VS}_0} \times \exp\left(\left[\left(\frac{T_0 - 301}{65}\right)^2 - 3.54\right]\left(1 + \frac{48.5 - T_0}{1484}\right)^{92w_0}\right) \text{ Pa}$$

with

$$P_{\mathrm{VS}} = P_{\mathrm{VS}_0} \approx P_a \exp\left(13.336\left(1-\frac{T_{\mathrm{b}}}{T_0}\right) - 1.75\left(1-\frac{T_{\mathrm{b}}}{T_0}\right)^2\right)\ \mathrm{Pa}.$$

Initially there is no flammable vapour within the porous medium or in the external gas

$$y_{\mathrm{F}} = y_{\mathrm{F}_0} = 0 \qquad\qquad \mathsf{y}_{\mathrm{F}} = \mathsf{y}_{\mathrm{F}_0} = 0.$$

The initial mass fraction of water vapour in the porous medium and in the external gas, assuming it is in equilibrium with the solid, can be calculated from the ideal gas law so that

$$y_{\mathrm{V}} = y_{\mathrm{V}_0} = \frac{M_{\mathrm{V}}\, \varphi_0\, P_{\mathrm{Vb}_0}}{R\, T_0\, \rho_{\mathrm{g}_0}}$$

$$\mathsf{y}_{\mathrm{V}} = \mathsf{y}_{\mathrm{V}_0} = \frac{M_{\mathrm{V}}\, P_{\mathrm{VS}_0}}{R\, T_0\, \varrho_{\mathrm{g}_0}}.$$

In reality, at ambient temperatures, the values of y_{V_0} and $\mathsf{y}_{\mathrm{V}_0}$ are very small.

The centre of an infinite slab of thickness $2a$ $(N = 0)$, infinite cylinder of radius a $(N = 1)$ or a sphere of radius a is located at $r = 0$. At this point, symmetry conditions apply so that

$$T_r = \rho_{\mathrm{G}_r} = \rho_{\mathrm{C}_r} = \rho_{\mathrm{W}_r} = y_{\mathrm{F}_r} = y_{\mathrm{V}_r} = 0.$$

Also the mass flux at the point $r = 0$ must be zero

$$m = 0.$$

As $r \to \infty$ it is expected that the external gas temperature reaches the ambient temperature

$$\mathsf{T} = T_0 \approx 300\ \mathrm{K}$$

and the gaseous mixture is composed of air only so that, in the far field

$$\mathsf{y}_{\mathrm{F}} = \mathsf{y}_{\mathrm{V}} = 0.$$

Interface conditions between the solid vegetation phase and the external gas phase of the flow $(r = a)$ are necessary to close the pyrolysis model. Continuity conditions are applicable for temperature

$$T = \mathsf{T}$$

mass flux

$$m = \mathsf{m}$$

energy flux

$$\bar{c}_{\mathrm{g}} m T - \lambda T_r + J - \varsigma T^4 = \bar{c}_{\mathrm{g}} \mathsf{m} \mathsf{T} - \lambda_{\mathrm{g}} \mathsf{T}_r$$

flammable vapour flux

$$m\, y_{\mathrm{F}} = \mathsf{m}\, \mathsf{y}_{\mathrm{F}} - \varrho D_{\mathrm{F}} \mathsf{y}_{\mathrm{F}_r}$$

and water vapour flux

$$m\, y_{\mathrm{V}} = \mathsf{m}\, \mathsf{y}_{\mathrm{V}} - \varrho D_{\mathrm{V}} \mathsf{y}_{\mathrm{V}_r}.$$

The radiation heat flux at the surface of the sample is denoted as J and ς is the Stefan-Bolztmann radiative constant.

The boundary and initial conditions have been presented for the governing equations. This time dependant problem can now be solved numerically, however, in order to estimate a flash point in the external gas phase, it is important to approximate when a mixture of flammable vapour, water vapour, and air is capable of supporting a flame.

2.3 Finding the flash point

As the sample of vegetation is degraded and pyrolysed it releases fuel and water vapour into the external gas phase which is initially made up of air. However the fuel vapour and water vapour will mix with the air which consists mainly of nitrogen (N_2) and oxygen (O_2). The conditions at which this mixture is capable of supporting a flame need to be estimated. The mass of air is mainly made up of the sum of the mass of O_2 and N_2 in the air with ratio $O_2 : N_2 \approx 7 : 23$. Any carbon dioxide (CO_2) produced by burning needs to be considered along with the fuel vapour (F), water vapour (V), oxygen (X), and nitrogen.

The lean flammability limit for a mixture of cellulose flammable vapour and air is not known at the present time. However, it can be estimated that the flame temperature would need to exceed a minimum value of about $\mathsf{T}_{\mathrm{X}} \approx 1150$ K (as for methanol) in order for oxidation reactions to sustain a flame.

The specific enthalpy h_i in the external gas phase for species $i \in \{\mathrm{F}, \mathrm{V}, \mathrm{X}, \mathrm{N}, \mathrm{CO}_2\}$ are given by

$$\mathsf{h}_{\mathrm{F}} = \mathsf{h}_{\mathrm{F}0} + \mathsf{c}_{\mathrm{P}_{\mathrm{F}}} \mathsf{T}$$

$$\mathsf{h}_{\mathrm{V}} = \mathsf{h}_{\mathrm{V}0} + \mathsf{c}_{\mathrm{P}_{\mathrm{V}}} \mathsf{T}$$

$$\mathsf{h}_{\mathrm{X}} = \mathsf{h}_{\mathrm{X}0} + \mathsf{c}_{\mathrm{P_X}}\mathsf{T}$$

$$\mathsf{h}_{\mathrm{N}} = \mathsf{h}_{\mathrm{N}0} + \mathsf{c}_{\mathrm{P_N}}\mathsf{T}$$

$$\mathsf{h}_{\mathrm{CO_2}} = \mathsf{h}_{\mathrm{CO_2}0} + \mathsf{c}_{\mathrm{P_{CO_2}}}\mathsf{T}$$

where specific heat estimates for high temperatures are [51]

$$\mathsf{c}_{\mathrm{P_F}} \approx 1 \text{ J g}^{-1} \text{ K}^{-1}$$

$$\mathsf{c}_{\mathrm{P_X}} \approx 1.05 \text{ J g}^{-1} \text{ K}^{-1}$$

$$\mathsf{c}_{\mathrm{P_N}} \approx 1.15 \text{ J g}^{-1} \text{ K}^{-1}$$

$$\mathsf{c}_{\mathrm{P_V}} \approx 2.28 \text{ J g}^{-1} \text{ K}^{-1}$$

$$\mathsf{c}_{\mathrm{P_{CO_2}}} \approx 1.19 \text{ J g}^{-1} \text{ K}^{-1}.$$

The latter four estimates agree with those provided in the NIST-JANAF tables [51] while the value of $\mathsf{c}_{\mathrm{P_F}}$ is a rough estimate, consistant with the values for $\mathsf{c}_{\mathrm{P_X}}, \mathsf{c}_{\mathrm{P_N}}$, and $\mathsf{c}_{\mathrm{P_{CO_2}}}$. In keeping with approximating the fuel vapour as simply CH_2O and taking the threshold flammability temperature to be that of alcohol, results are expected to provide reasonably good estimates rather than being precise.

The oxidation of typical carbohydrate fuel vapour (CH_2O say) produces CO_2 and H_2O, i.e. $CH_2O(30) + O_2(32) \rightarrow CO_2(44) + H_2O(18)$ where the numbers in the brackets denote the molecular mass of the preceding object.

When there is an excess of air in the air-fuel stoichiometric ratio the oxidation is said to be fuel lean [19]. Similarly, when there is an excess of fuel in the stoichiometric ratio the oxidation is said to be fuel rich. Hence for fuel lean (excess of air) oxidation, the energy content before and after the reaction is [52]

$$\begin{aligned}\left(\mathsf{y}_{\mathrm{F}}\mathsf{c}_{\mathrm{P_F}} + \mathsf{y}_{\mathrm{V}}\mathsf{c}_{\mathrm{P_V}} + \mathsf{y}_{\mathrm{A}}\left(\frac{7}{30}\mathsf{c}_{\mathrm{P_X}} + \frac{23}{30}\mathsf{c}_{\mathrm{P_N}}\right)\right)\mathsf{T} + \mathsf{y}_{\mathrm{F}}\left(\mathsf{h}_{\mathrm{F}0} + \frac{16}{15}\mathsf{h}_{\mathrm{X}0} - \frac{3}{5}\mathsf{h}_{\mathrm{V}0} - \frac{22}{15}\mathsf{h}_{\mathrm{CO_2}0}\right) \\ = \left(\left(\mathsf{y}_{\mathrm{V}} + \frac{3}{5}\mathsf{y}_{\mathrm{F}}\right)\mathsf{c}_{\mathrm{P_V}} + \frac{22}{15}\mathsf{y}_{\mathrm{F}}\mathsf{c}_{\mathrm{P_{CO_2}}} + \left(\frac{7}{30}\mathsf{y}_{\mathrm{A}} - \frac{16}{15}\mathsf{y}_{\mathrm{F}}\right)\mathsf{c}_{\mathrm{P_X}} + \frac{23}{30}\mathsf{y}_{\mathrm{A}}\mathsf{c}_{\mathrm{P_N}}\right)\mathsf{T}_{\mathrm{f}}\end{aligned} \tag{2.24}$$

and for fuel rich (excess of fuel) oxidation

$$\begin{aligned}\left(\mathsf{y}_{\mathrm{F}}\mathsf{c}_{\mathrm{P_F}} + \mathsf{y}_{\mathrm{V}}\mathsf{c}_{\mathrm{P_V}} + \mathsf{y}_{\mathrm{A}}\left(\frac{7}{30}\mathsf{c}_{\mathrm{P_X}} + \frac{23}{30}\mathsf{c}_{\mathrm{P_N}}\right)\right)\mathsf{T} + \frac{7}{32}\mathsf{y}_{\mathrm{A}}\left(\mathsf{h}_{\mathrm{F}0} + \frac{16}{15}\mathsf{h}_{\mathrm{X}0} - \frac{3}{5}\mathsf{h}_{\mathrm{V}0} - \frac{22}{15}\mathsf{h}_{\mathrm{CO_2}0}\right) \\ = \left(\left(\mathsf{y}_{\mathrm{F}} - \frac{7}{32}\mathsf{y}_{\mathrm{A}}\right)\mathsf{c}_{\mathrm{P_F}} + \left(\mathsf{y}_{\mathrm{V}} + \frac{21}{160}\mathsf{y}_{\mathrm{A}}\right)\mathsf{c}_{\mathrm{P_V}} + \frac{77}{240}\mathsf{y}_{\mathrm{A}}\mathsf{c}_{\mathrm{P_{CO_2}}} + \frac{23}{30}\mathsf{y}_{\mathrm{A}}\mathsf{c}_{\mathrm{P_N}}\right)\mathsf{T}_{\mathrm{f}}\end{aligned} \tag{2.25}$$

where T_{f} is the temperature after the adiabatic chemical reaction with T being the temperature before the chemical reaction. Rearranging Equation (2.24) gives

$$\mathsf{T}_{\mathrm{f}} = \frac{\left(\mathsf{y}_{\mathrm{F}}\mathsf{c}_{\mathrm{P}_{\mathrm{F}}} + \mathsf{y}_{\mathrm{V}}\mathsf{c}_{\mathrm{P}_{\mathrm{V}}} + \mathsf{y}_{\mathrm{A}}\left(\frac{7}{30}\mathsf{c}_{\mathrm{P}_{\mathrm{X}}} + \frac{23}{30}\mathsf{c}_{\mathrm{P}_{\mathrm{N}}}\right)\right)\mathsf{T} + \mathsf{y}_{\mathrm{F}}\left(\mathsf{h}_{\mathrm{F0}} + \frac{16}{15}\mathsf{h}_{\mathrm{X0}} - \frac{3}{5}\mathsf{h}_{\mathrm{V0}} - \frac{22}{15}\mathsf{h}_{\mathrm{CO_20}}\right)}{\mathsf{y}_{\mathrm{A}}\left(\frac{7}{30}\mathsf{c}_{\mathrm{P}_{\mathrm{X}}} + \frac{23}{30}\mathsf{c}_{\mathrm{P}_{\mathrm{N}}}\right) + \mathsf{y}_{\mathrm{V}}\mathsf{c}_{\mathrm{P}_{\mathrm{V}}} + \mathsf{y}_{\mathrm{F}}\left(\frac{3}{5}\mathsf{c}_{\mathrm{P}_{\mathrm{V}}} + \frac{22}{15}\mathsf{c}_{\mathrm{P}_{\mathrm{CO_2}}} - \frac{16}{15}\mathsf{c}_{\mathrm{P}_{\mathrm{N}}}\right)}$$

and Equation (2.25) gives

$$\mathsf{T}_{\mathrm{f}} = \frac{\left(\mathsf{y}_{\mathrm{F}}\mathsf{c}_{\mathrm{P}_{\mathrm{F}}} + \mathsf{y}_{\mathrm{V}}\mathsf{c}_{\mathrm{P}_{\mathrm{V}}} + \mathsf{y}_{\mathrm{A}}\left(\frac{7}{30}\mathsf{c}_{\mathrm{P}_{\mathrm{X}}} + \frac{23}{30}\mathsf{c}_{\mathrm{P}_{\mathrm{N}}}\right)\right)\mathsf{T} + \frac{7}{32}\mathsf{y}_{\mathrm{A}}\left(\mathsf{h}_{\mathrm{F0}} + \frac{16}{15}\mathsf{h}_{\mathrm{X0}} - \frac{3}{5}\mathsf{h}_{\mathrm{V0}} - \frac{22}{15}\mathsf{h}_{\mathrm{CO_20}}\right)}{\mathsf{y}_{\mathrm{F}}\mathsf{c}_{\mathrm{P}_{\mathrm{F}}} + \frac{23}{30}\mathsf{y}_{\mathrm{A}}\mathsf{c}_{\mathrm{P}_{\mathrm{N}}} + \mathsf{y}_{\mathrm{V}}\mathsf{c}_{\mathrm{P}_{\mathrm{V}}} + \mathsf{y}_{\mathrm{F}}\left(\frac{3}{5}\mathsf{c}_{\mathrm{P}_{\mathrm{V}}} + \frac{22}{15}\mathsf{c}_{\mathrm{P}_{\mathrm{CO_2}}} - \mathsf{c}_{\mathrm{P}_{\mathrm{F}}}\right)}.$$

It is estimated that the mixture reaches its flash point when $\mathsf{T}_{\mathrm{f}} > \mathsf{T}_{\mathrm{X}}$ where the 'crossover' temperature $\mathsf{T}_{\mathrm{X}} \approx 1150$ K.

Measuring heat of chemical reactions using oxygen calorimetry [3, 51] suggests that

$$\mathsf{h}_{\mathrm{F0}} + \frac{16}{15}\mathsf{h}_{\mathrm{X0}} - \frac{3}{5}\mathsf{h}_{\mathrm{V0}} - \frac{22}{15}\mathsf{h}_{\mathrm{CO_20}} \approx 14 \text{ kJ/g} \tag{2.26}$$

so that for fuel lean and fuel rich oxidation the mixture temperatures can be estimated to be

$$\mathsf{T}_{\mathrm{f_L}} \approx \frac{\left(\mathsf{y}_{\mathrm{F}}\mathsf{c}_{\mathrm{P}_{\mathrm{F}}} + \mathsf{y}_{\mathrm{V}}\mathsf{c}_{\mathrm{P}_{\mathrm{V}}} + \mathsf{y}_{\mathrm{A}}\left(\frac{7}{30}\mathsf{c}_{\mathrm{P}_{\mathrm{X}}} + \frac{23}{30}\mathsf{c}_{\mathrm{P}_{\mathrm{N}}}\right)\right)\mathsf{T} + 14\mathsf{y}_{\mathrm{F}}}{\mathsf{y}_{\mathrm{A}}\left(\frac{7}{30}\mathsf{c}_{\mathrm{P}_{\mathrm{X}}} + \frac{23}{30}\mathsf{c}_{\mathrm{P}_{\mathrm{N}}}\right) + \mathsf{y}_{\mathrm{V}}\mathsf{c}_{\mathrm{P}_{\mathrm{V}}} + \mathsf{y}_{\mathrm{F}}\left(\frac{3}{5}\mathsf{c}_{\mathrm{P}_{\mathrm{V}}} + \frac{22}{15}\mathsf{c}_{\mathrm{P}_{\mathrm{CO_2}}} - \frac{16}{15}\mathsf{c}_{\mathrm{P}_{\mathrm{N}}}\right)}$$

$$\mathsf{T}_{\mathrm{f_R}} \approx \frac{\left(\mathsf{y}_{\mathrm{F}}\mathsf{c}_{\mathrm{P}_{\mathrm{F}}} + \mathsf{y}_{\mathrm{V}}\mathsf{c}_{\mathrm{P}_{\mathrm{V}}} + \mathsf{y}_{\mathrm{A}}\left(\frac{7}{30}\mathsf{c}_{\mathrm{P}_{\mathrm{X}}} + \frac{23}{30}\mathsf{c}_{\mathrm{P}_{\mathrm{N}}}\right)\right)\mathsf{T} + \frac{49}{16}\mathsf{y}_{\mathrm{A}}}{\mathsf{y}_{\mathrm{F}}\mathsf{c}_{\mathrm{P}_{\mathrm{F}}} + \frac{23}{30}\mathsf{y}_{\mathrm{A}}\mathsf{c}_{\mathrm{P}_{\mathrm{N}}} + \mathsf{y}_{\mathrm{V}}\mathsf{c}_{\mathrm{P}_{\mathrm{V}}} + \mathsf{y}_{\mathrm{F}}\left(\frac{3}{5}\mathsf{c}_{\mathrm{P}_{\mathrm{V}}} + \frac{22}{15}\mathsf{c}_{\mathrm{P}_{\mathrm{CO_2}}} - \mathsf{c}_{\mathrm{P}_{\mathrm{F}}}\right)}$$

respectively. It can be noted that specific heats on the numerators of these formulae will be dominated by that of nitrogen. Hence the uncertainty in the value of $\mathsf{c}_{\mathrm{P}_{\mathrm{F}}}$ should change things in a relatively minor way.

2.4 Summary of the pyrolysis model

The pyrolysis model consists of chemical reactions for fast pyrolysis, charring (slow pyrolysis), and water evaporation

$$\omega_{\mathrm{F}} = \rho_{\mathrm{G}}\tau_{\mathrm{C}}^{-1}\exp\left(\beta_{\mathrm{F}}(1 - T_{\mathrm{C}}/T)\right), \tag{2.27}$$

$$\omega_{\mathrm{C}} = \rho_{\mathrm{G}}\tau_{\mathrm{C}}^{-1}\exp\left(\beta_{\mathrm{C}}(1 - T_{\mathrm{C}}/T)\right), \tag{2.28}$$

$$\omega_{\mathrm{V}} \approx \tau_{\mathrm{W}}^{-1}\rho_{\mathrm{W}}\left(1 - \frac{RT\rho_{\mathrm{V}}}{M_{\mathrm{V}}\varphi P_{\mathrm{V_b}}}\right), \tag{2.29}$$

conservation equations in the porous vegetation

$$\partial_t\rho_{\mathrm{G}} = -\omega_{\mathrm{F}} - \omega_{\mathrm{C}}, \tag{2.30}$$

$$\partial_t \rho_{\mathrm{C}} = \mu_{\mathrm{C}} \omega_{\mathrm{C}}, \tag{2.31}$$

$$\partial_t \rho_{\mathrm{W}} = -\omega_{\mathrm{V}}, \tag{2.32}$$

$$\rho_{\mathrm{g}} \partial_t y_{\mathrm{F}} + m y_{\mathrm{F}_r} = (1 - y_{\mathrm{F}})\, \omega_{\mathrm{F}} - y_{\mathrm{F}} \left(\omega_{\mathrm{V}} + (1 - \mu_{\mathrm{C}})\, \omega_{\mathrm{C}}\right), \tag{2.33}$$

$$\rho_{\mathrm{g}} \partial_t y_{\mathrm{V}} + m y_{\mathrm{V}_r} = (1 - y_{\mathrm{V}}) \left(\omega_{\mathrm{V}} + (1 - \mu_{\mathrm{C}})\, \omega_{\mathrm{C}}\right) - y_{\mathrm{V}} \omega_{\mathrm{F}}, \tag{2.34}$$

$$\left(r^N m\right)_r = r^N \left(\omega_{\mathrm{F}} + \omega_{\mathrm{V}} + (1 - \mu_{\mathrm{C}})\, \omega_{\mathrm{C}}\right), \tag{2.35}$$

$$r\overline{\rho c} \frac{\partial T}{\partial t} + \left(r \bar{c}_{\mathrm{g}} m + (1 - N)\, \lambda\right) T_r = \left(r \lambda T_r\right)_r - r L_{\mathrm{W}} \omega_{\mathrm{V}} - r Q_{\mathrm{F}} \omega_{\mathrm{F}}, \tag{2.36}$$

and conservation equations in the external gas

$$\varrho_{\mathrm{g}} \frac{\partial \mathsf{y}_{\mathrm{F}}}{\partial t} + \left(\mathsf{m} - \frac{N}{r} \varrho_{\mathrm{g}} D_{\mathrm{F}}\right) \mathsf{y}_{\mathrm{F}_r} = \left(\varrho_{\mathrm{g}} D_{\mathrm{F}} \mathsf{y}_{\mathrm{F}_r}\right)_r, \tag{2.37}$$

$$\varrho_{\mathrm{g}} \frac{\partial \mathsf{y}_{\mathrm{V}}}{\partial t} + \left(\mathsf{m} - \frac{N}{r} \varrho_{\mathrm{g}} D_{\mathrm{V}}\right) \mathsf{y}_{\mathrm{V}_r} = \left(\varrho_{\mathrm{g}} D_{\mathrm{V}} \mathsf{y}_{\mathrm{V}_r}\right)_r, \tag{2.38}$$

$$\left(r^N \mathsf{m}\right)_r = 0, \tag{2.39}$$

and

$$\varrho_{\mathrm{g}} \bar{c}_{\mathrm{g}} \frac{\partial \mathsf{T}}{\partial t} + \left(\bar{c}_{\mathrm{g}} \mathsf{m} - \frac{N}{r} \lambda_{\mathrm{g}}\right) \mathsf{T}_r = \left(\lambda_{\mathrm{g}} \mathsf{T}_r\right)_r. \tag{2.40}$$

The ideal gas law in the porous vegetation and external gas is

$$\rho_{\mathrm{g}} = \frac{\varphi P M_{\mathrm{A}}}{R T \left(1 + y_{\mathrm{F}} n_{\mathrm{F}} + y_{\mathrm{V}} n_{\mathrm{V}}\right)} \tag{2.41}$$

and

$$\varrho_{\mathrm{g}} = \frac{P M_{\mathrm{A}}}{R \mathsf{T} \left(1 + \mathsf{y}_{\mathrm{F}} n_{\mathrm{F}} + \mathsf{y}_{\mathrm{V}} n_{\mathrm{V}}\right)} \tag{2.42}$$

respectively.

Initial conditions ($t = 0$) are

$$T = \mathsf{T} = T_0 \approx 300 \text{ K},$$

$$\rho_{\mathrm{g}} = \rho_{\mathrm{g}_0} \approx 500 \text{ kg/m}^3, \qquad \rho_{\mathrm{W}} = w_0\, \rho_{\mathrm{G}_0} \approx 500\, w_0 \text{ kg/m}^3,$$

$$\rho_{\mathrm{C}} = \rho_{\mathrm{C}_0} = 0 \text{ kg/m}^3, \qquad \rho_{\mathrm{F}} = \rho_{\mathrm{F}_0} = 0 \text{ kg/m}^3,$$

$$\varphi = \varphi_0 = 1 - \frac{\rho_{\mathrm{G}_0}}{\hat{\varrho}_{\mathrm{G}}} - \frac{\rho_{\mathrm{W}_0}}{\hat{\varrho}_{\mathrm{W}}},$$

$$P_{\mathrm{vb}} = P_{\mathrm{vb}_0} \approx P_{\mathrm{vs}_0} \times \exp\left(\left[\left(\frac{T_0 - 301}{65}\right)^2 - 3.54\right] \left(1 + \frac{48.5 - T_0}{1484}\right)^{92 w_0}\right) \text{ Pa},$$

$$P_{\mathrm{VS}} = P_{\mathrm{VS}_0} \approx P_a \exp\left(13.336\left(1-\frac{T_{\mathrm{b}}}{T_0}\right) - 1.75\left(1-\frac{T_{\mathrm{b}}}{T_0}\right)^2\right)\ \mathrm{Pa},$$

$$y_{\mathrm{F}} = y_{\mathrm{F}0} = 0, \qquad \mathsf{y}_{\mathrm{F}} = \mathsf{y}_{\mathrm{F}0} = 0,$$

$$y_{\mathrm{V}} = y_{\mathrm{V}_0} = \frac{M_{\mathrm{V}}\,\varphi_0\,P_{\mathrm{vb}_0}}{R\,T_0\,\rho_{\mathrm{g}_0}},$$

$$\mathsf{y}_{\mathrm{V}} = \mathsf{y}_{\mathrm{V}_0} = \frac{M_{\mathrm{V}}\,P_{\mathrm{VS}_0}}{R\,T_0\,\varrho_{\mathrm{g}_0}}.$$

Conditions at the centre of the vegetation sample ($r = 0$) are

$$T_r = \rho_{\mathrm{G}_r} = \rho_{\mathrm{C}_r} = \rho_{\mathrm{W}_r} = y_{\mathrm{F}_r} = y_{\mathrm{V}_r} = m = 0.$$

Conditions at considerable distances from the vegetation sample $r \to \infty$ are

$$\mathsf{T} = T_0 \approx 300\ \mathrm{K}$$

and

$$\mathsf{y}_{\mathrm{F}} = \mathsf{y}_{\mathrm{V}} = 0.$$

Conditions on the surface of the vegetation sample ($r = a$) are

$$T = \mathsf{T},$$

$$m = \mathsf{m},$$

$$\bar{c}_{\mathrm{g}} m T - \lambda T_r + J - \varsigma T^4 = \bar{c}_{\mathrm{g}} \mathsf{m} \mathsf{T} - \lambda_{\mathrm{g}} \mathsf{T}_r,$$

$$m\, y_{\mathrm{F}} = \mathsf{m}\, \mathsf{y}_{\mathrm{F}} - \varrho D_{\mathrm{F}} \mathsf{y}_{\mathrm{F}_r},$$

and

$$m\, y_{\mathrm{V}} = \mathsf{m}\, \mathsf{y}_{\mathrm{V}} - \varrho D_{\mathrm{V}} \mathsf{y}_{\mathrm{V}_r}.$$

The parameters of the model are the vegetation sample geometry (N), sample size (a mm), heating rate (J kW/m^2), and initial fuel moisture content (w_0). The pyrolysis model is solved numerically for the a range of parameter values. The time evolution of vegetation and gas fractions, and temperature, are analysed. Additionally, an estimate of the time taken for a flammable mixture to form can be made by calculating the fuel lean and fuel rich oxidation temperatures

$$\mathsf{T}_{\mathrm{f_L}} \approx \frac{\left(\mathsf{y}_{\mathrm{F}}\mathsf{c}_{\mathrm{P_F}} + \mathsf{y}_{\mathrm{V}}\mathsf{c}_{\mathrm{P_V}} + \mathsf{y}_{\mathrm{A}}\left(\frac{7}{30}\mathsf{c}_{\mathrm{P_X}} + \frac{23}{30}\mathsf{c}_{\mathrm{P_N}}\right)\right)\mathsf{T} + 14\mathsf{y}_{\mathrm{F}}}{\mathsf{y}_{\mathrm{A}}\left(\frac{7}{30}\mathsf{c}_{\mathrm{P_X}} + \frac{23}{30}\mathsf{c}_{\mathrm{P_N}}\right) + \mathsf{y}_{\mathrm{V}}\mathsf{c}_{\mathrm{P_V}} + \mathsf{y}_{\mathrm{F}}\left(\frac{3}{5}\mathsf{c}_{\mathrm{P_V}} + \frac{22}{15}\mathsf{c}_{\mathrm{P_{CO_2}}} - \frac{16}{15}\mathsf{c}_{\mathrm{P_N}}\right)} \tag{2.43}$$

and

$$\mathsf{T}_{\mathrm{f_R}} \approx \frac{\left(\mathsf{y}_{\mathrm{F}}\mathsf{c}_{\mathrm{P_F}} + \mathsf{y}_{\mathrm{V}}\mathsf{c}_{\mathrm{P_V}} + \mathsf{y}_{\mathrm{A}}\left(\frac{7}{30}\mathsf{c}_{\mathrm{P_X}} + \frac{23}{30}\mathsf{c}_{\mathrm{P_N}}\right)\right)\mathsf{T} + \frac{49}{16}\mathsf{y}_{\mathrm{A}}}{\mathsf{y}_{\mathrm{F}}\mathsf{c}_{\mathrm{P_F}} + \frac{23}{30}\mathsf{y}_{\mathrm{A}}\mathsf{c}_{\mathrm{P_N}} + \mathsf{y}_{\mathrm{V}}\mathsf{c}_{\mathrm{P_V}} + \mathsf{y}_{\mathrm{F}}\left(\frac{3}{5}\mathsf{c}_{\mathrm{P_V}} + \frac{22}{15}\mathsf{c}_{\mathrm{P_{CO_2}}} - \mathsf{c}_{\mathrm{P_F}}\right)}. \tag{2.44}$$

respectively. If the minimum value of $\mathsf{T}_{\mathrm{f_L}}$ and $\mathsf{T}_{\mathrm{f_R}}$ is greater than the crossover temperature $\mathsf{T}_{\mathrm{X}} \approx 1150$ then it is assumed that a flammable mixture has formed in the external gas.

This pyrolysis model can now be solved numerically. The finite element software COMSOL Multiphysics is used to solve this problem. Governing equations, boundary and initial conditions, expressions, and constants are specified. After a mesh is generated, the model can be solved provided there are no convergence issues [23].

Chapter 3

Numerical results for pyrolysis model

The numerical results for surface temperature, solid and gas profiles, estimate of flash point location and time, and mass flow rates are presented in this section. The fuel sample size, fuel geometry, initial moisture content, and heating rate are parameters of the problem. The aim is to determine how these parameters affect the onset of ignition in vegetal fuels.

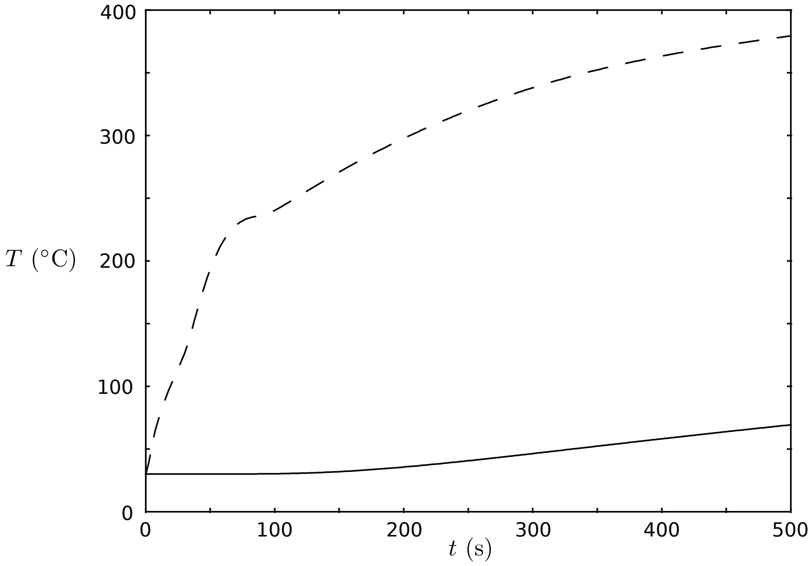

Figure 3.1: Temperature at depth 1 mm (dashed line) and 14 mm (solid line) for a slab ($N = 0$). Heating rate is 20 kW/m^2, sample size is 15 mm, and initial moisture content is 15.3%.

The model has been tested against the experiments of Shen et al. [53]. A slab of 15 mm thickness was exposed to a heating rate of 20 kW/m^2 at its surface. The initial fuel moisture content was calculated to be 15.3% of the mass of dry vegetation. Figure 3.1 shows the temperature at depths 1 mm (dashed line) and 14 mm (solid line). The depth is measured from the heated surface of the slab. These temperature results are found to be in good agreement with the experiments of Shen et al. [53].

3.1 Profiles for vegetation, water, char, fuel vapour, water vapour, and air

Figures 3.2–3.5 show the profiles, at the predicted flammability time, for vegetation, water, char, fuel vapour, water vapour, and air at fixed heating rates 20 kW/m^2, 40 kW/m^2, 60 kW/m^2, and 80 kW/m^2 respectively. These profiles are presented for the infinite slab, infinite cylinder, and spherical sample geometries. Initial fuel moisture contents (MC) of 0%, 30%, and 60% of the mass of dry vegetation are considered with each row of profiles being calculated at a specific value for MC. Fuel samples have a half-width/radius of 1 mm and 5 mm. The vertical scale range for the nondimensional profiles is $[0, 1]$. Vegetation, water (liquid), and char densities are normalised by the initial vegetation density. These profiles are plotted in the left segment of each profile plot which represents the porous vegetation phase. Mass fractions of fuel vapour, water vapour, and air are plotted, on a different, much larger scale, in the right segment of each profile plot which represents the external gas phase. The colours of each curve represent the species written below the figures.

Profiles in Figure 3.2 are for a heating rate of 20 kW/m^2. For the infinite slab geometry, all the liquid water in the sample is evaporated by the time that flammable conditions are reached, even with relatively large initial moisture contents. Very little vegetation is consumed in the formation of a flammable mixture when there is a negligible amount of moisture in the sample. At appreciable moisture contents, a good deal of the vegetation is consumed in order to form a flammable mixture. This mixture is located at some distance from the surface of the slab as its immediate surroundings are diluted by the water vapour which is mixed with the flammable vapour. The estimated time taken to reach the flash point increases for larger initial moisture contents and sample sizes. This is to be expected from the findings of pyrolysis models

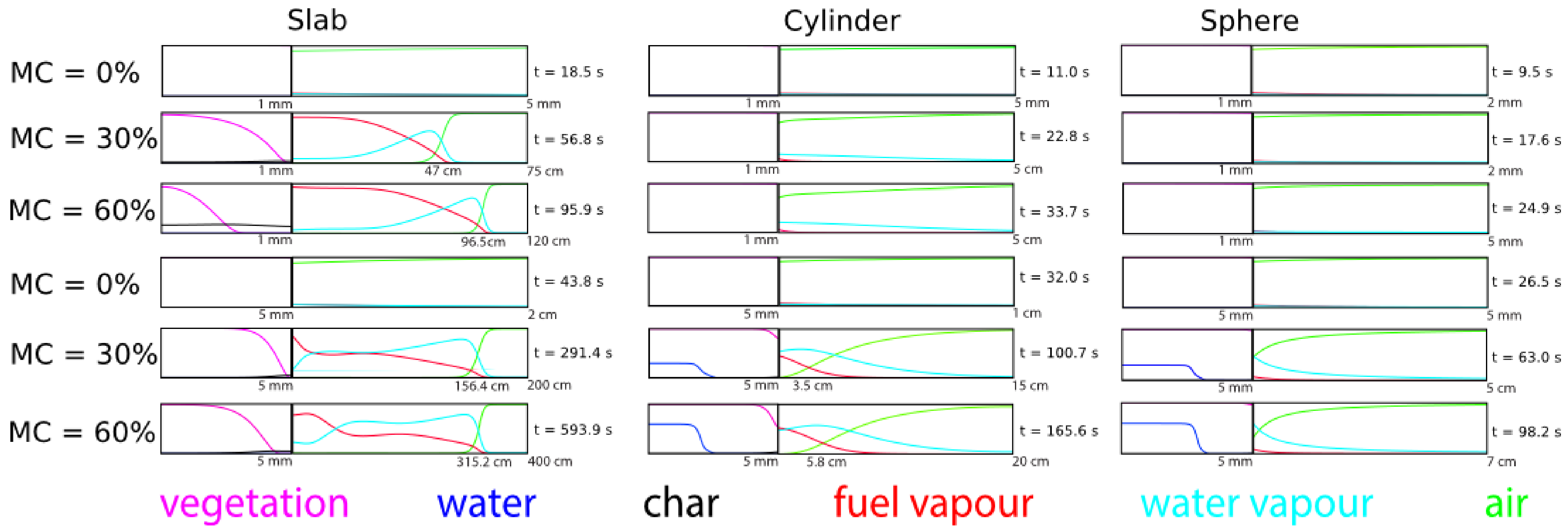

Figure 3.2: Condensed and gaseous profiles at flammability for the heating rate of 20 kW/m^2.

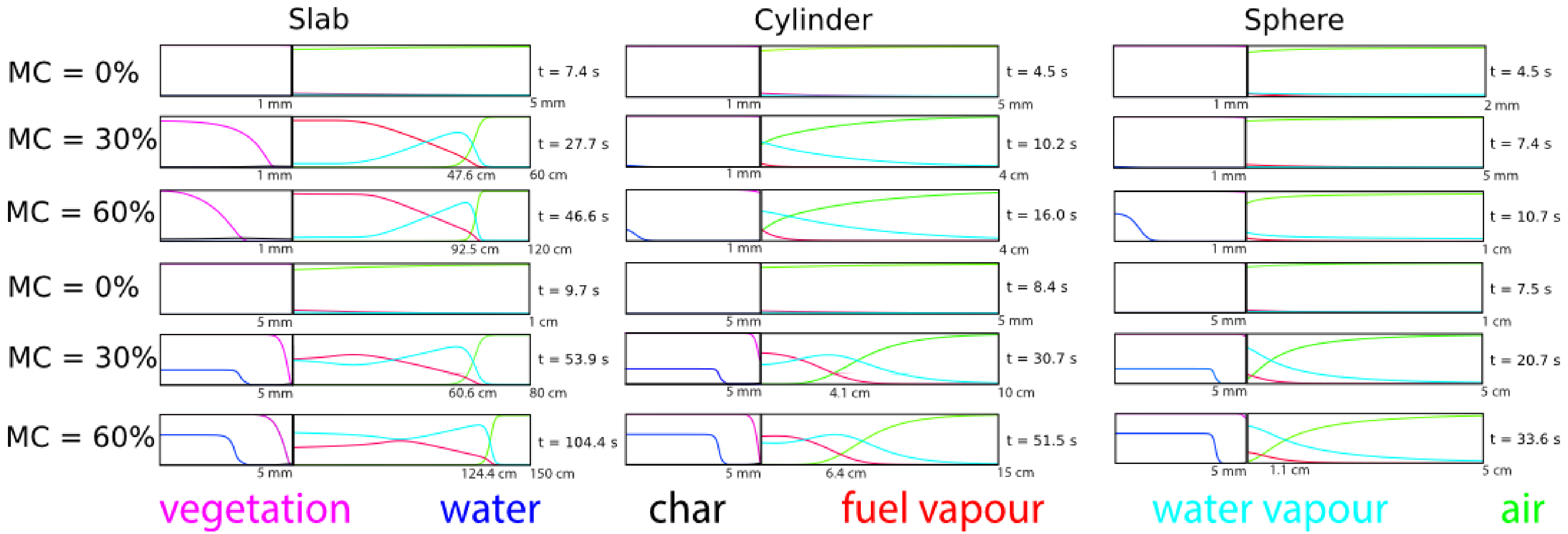

Figure 3.3: Condensed and gaseous profiles at flammability for the heating rate of 40 kW/m^2.

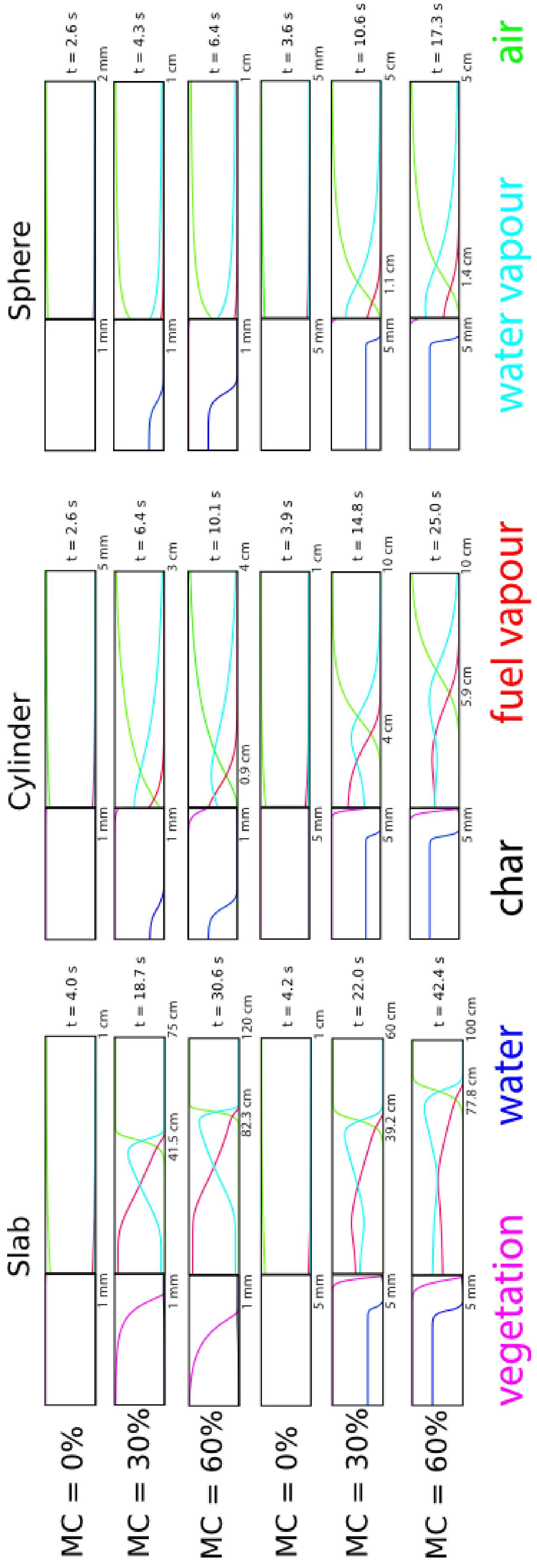

Figure 3.4: Condensed and gaseous profiles at flammability for the heating rate of 60 kW/m^2.

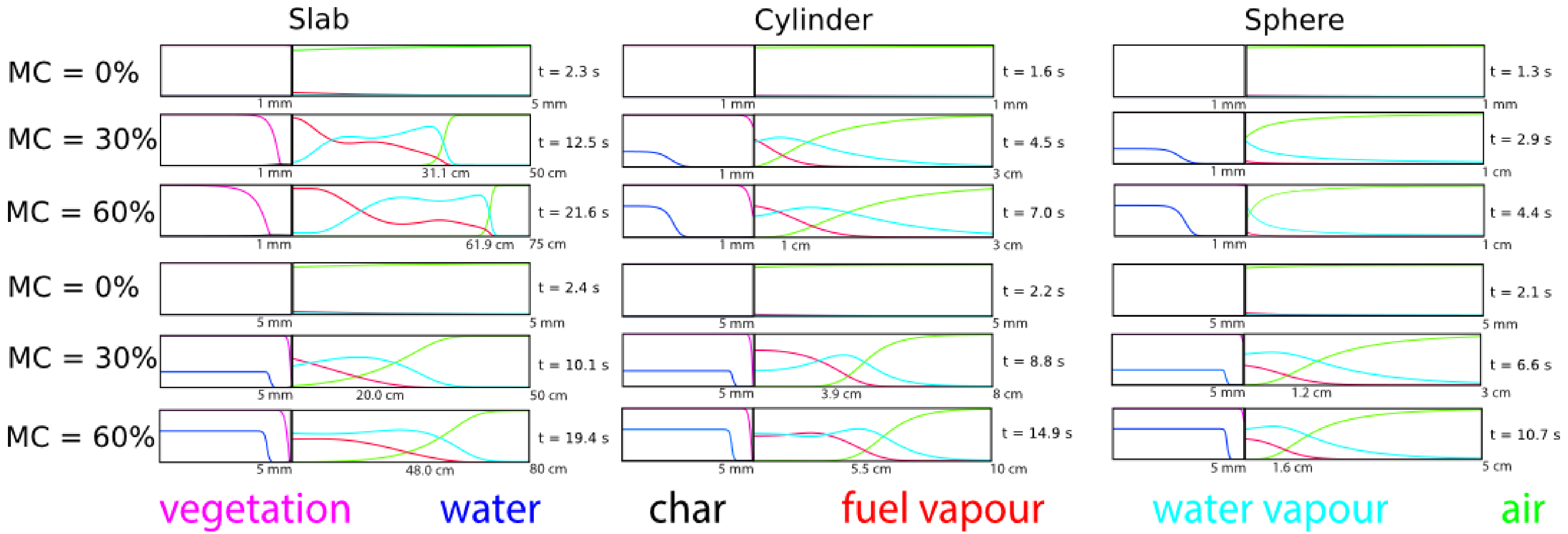

Figure 3.5: Condensed and gaseous profiles at flammability for the heating rate of 80 kW/m^2.

in the open literature where temperature profiles are found to decrease with large fuel moisture contents and sample sizes.

The cylindrical sample reaches its flash point sooner than the slab due to its larger surface area, allowing a greater capacity to receive heat, and the larger external volume in which gaseous mixing occurs. The flash point location remains relatively close to the cylinder for fine samples. The flash point location is pushed away from the surface of the cylinder for larger samples of nonzero initial moisture contents (this will be discussed later). For appreciable initial moisture contents the cylinder consumes less vegetation and produces less char than the slab before reaching its flash point. The larger cylinder also retains some liquid water at the estimated pyrolysis time. The spherical sample reaches the flash point earlier than the cylinder and retains the flash point location (where a flammable mixture forms) closer to its surface as well. Again this is consistent with experimental and numerical temperature profile results in the open literature. Compared to the cylinder, the sphere consumes less vegetation and retains more of its initial moisture. Vegetal fuel samples reach flammability conditions more readily at higher heating rates. Vegetation consumption and char production are reduced and the sample retains more of its initial moisture at the estimated flash point time.

Figures 3.6–3.8 show the char fraction, at the estimated flash point time, against the normalised half-width/radius for the slab, cylinder, and sphere geometries respectively. The char fraction is defined as the density of the char in the fuel normalised against the vegetation density. Sample sizes of 2 mm and 4 mm, heating rates of 20 kW/m^2 and 40 kW/m^2, and initial fuel moisture contents of 0%, 30%, and 60% are presented. The surface of a fuel sample, regardless of the geometry, is located at $r/a = 1$ with the centre located at $r/a = 0$.

The results show that more char is produced, at the estimated flash point time, for weaker heating rates and larger initial fuel moisture contents. This is to be expected from the pyrolysis modelling used here since char production is dominant over fast pyrolysis when the fuel sample is exposed to lower heating rates. The moisture in the fuel sample delays the onset of flammability and keeps the temperature down for longer allowing more char to be produced. For a 2 mm slab, with 60% initial fuel moisture content, exposed to a 20 kW/m^2 heating rate, char is produced throughout the sample.

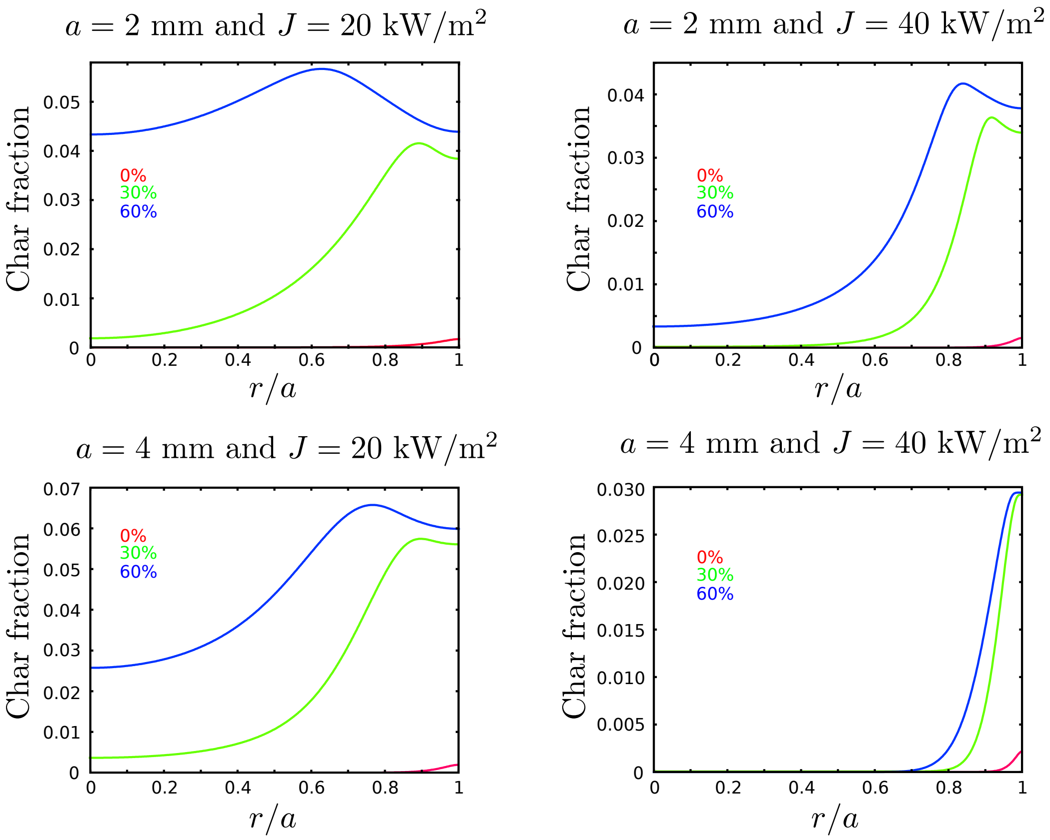

Figure 3.6: Slab ($N = 0$) char fraction at flammability.

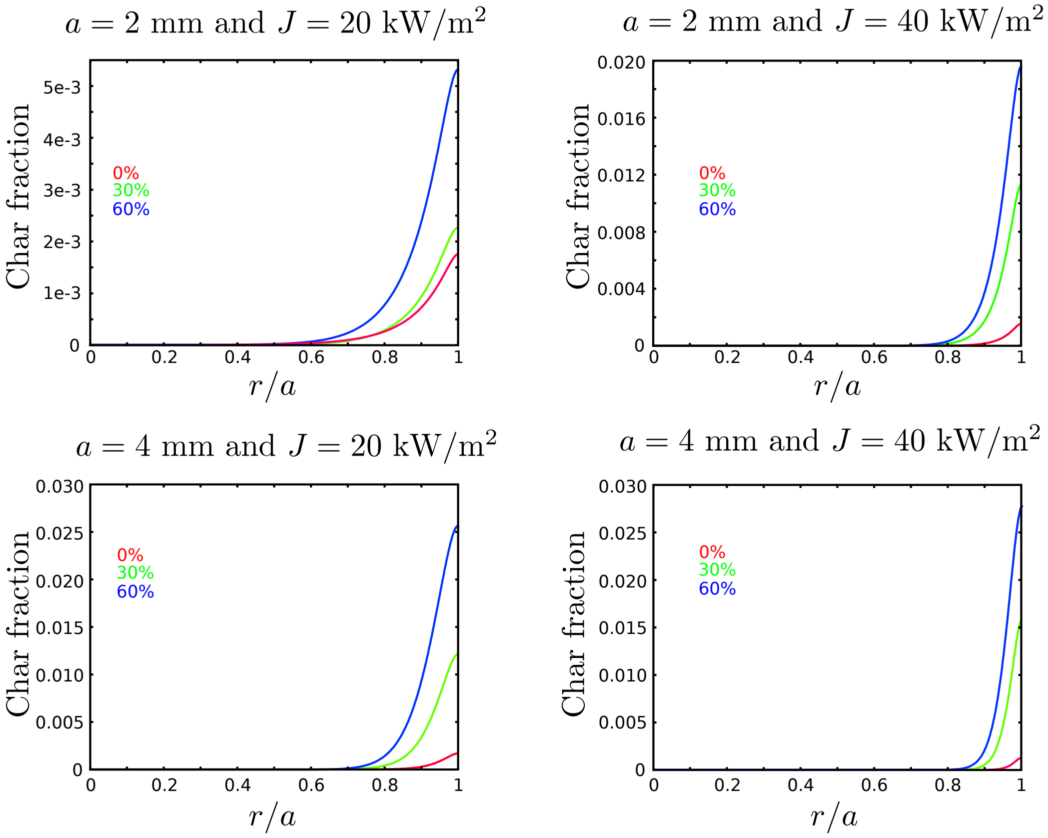

Figure 3.7: Cylinder ($N = 1$) char fraction at flammability.

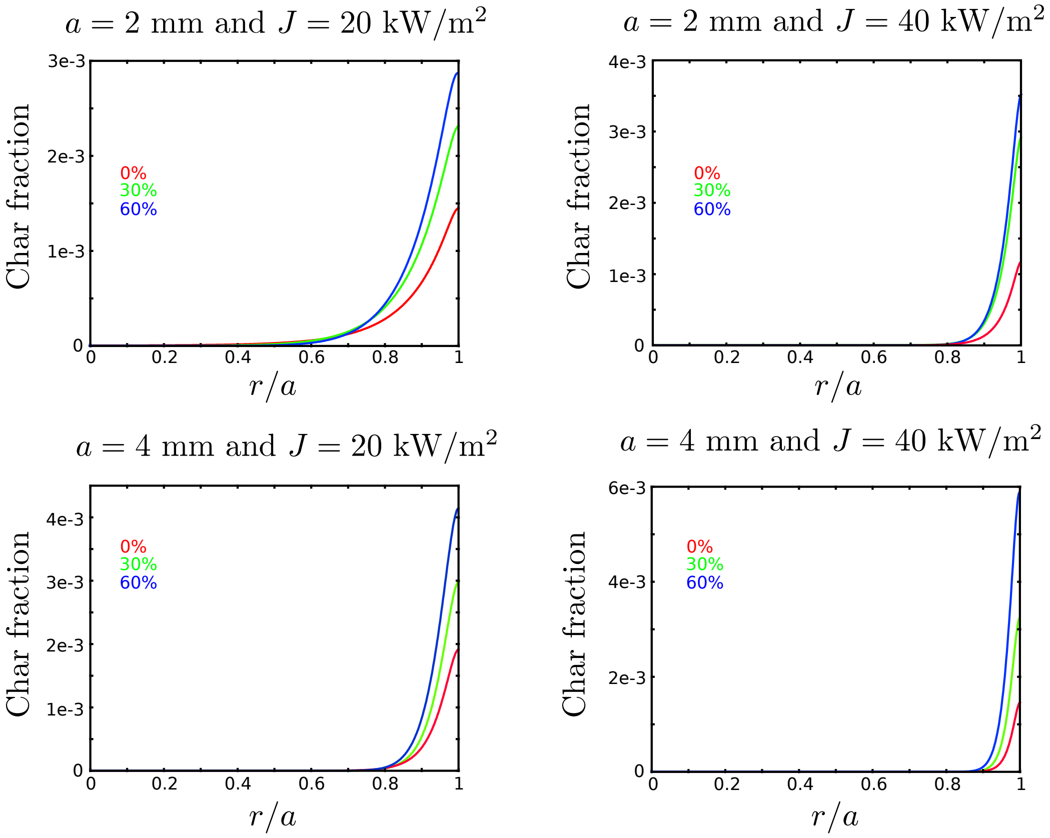

Figure 3.8: Sphere ($N = 2$) char fraction at flammability.

This is not the case with cylindrical and spherical fuels at the same heating rate as the time to flammability is shorter and the surface-area-to-volume ratio is larger compared to the slab geometry which allows thermal radiation to impinge a larger surface area. This means that the cylindrical sample will heat more rapidly than the slab with the spherical sample heating even quicker than the cylinder. Consequently the cylinder and sphere will form a flammable mixture sooner than a slab so that char production is reduced.

3.2 Fuel surface temperature

Figure 3.9 shows the surface temperature of slabs of different half-width a, subjected to various heating rates, with the moisture content assumed to be 15% of the dry vegetation. The surface temperature is plotted against the time from $t = 0$ up to the estimated flammability time which is the time taken to reach an estimated flammable mixture.

The surface temperature is increased more quickly for larger heating rates due to the higher temperature gradient. The temperature increases very quickly up to around 100°C when the moisture begins to evaporate. The surface temperature of the slab, at the estimated flash point time, is around 350°C–550°C depending on the heating rate. This is quite a large temperature range which suggests that the notion of a fixed ignition temperature is an oversimplification when predicting the ignition of vegetal fuels. Therefore integral based pyrolysis models [29] must restrict the range of the problem parameters (e.g. moisture content, sample size, heating rate, etc.) so that their model can produce satisfactory results.

Surface temperature plots for slab, cylinder, and sphere geometries are shown in Figure 3.10. The sample size is $a = 5$ mm and the heating rate is 40 kW/m^2 in all the plots. The initial fuel moisture content is fixed for each plot.

Cylindrical fuel samples heat more rapidly compared to slabs, and spherical samples heat still more quickly, due to the increased surface-area-to-volume ratio. Spherical fuels form a flammable mixture sooner, and at a lower surface temperature, than the cylinder and slab fuels.

An increase in the initial fuel moisture content results in larger surface temperatures

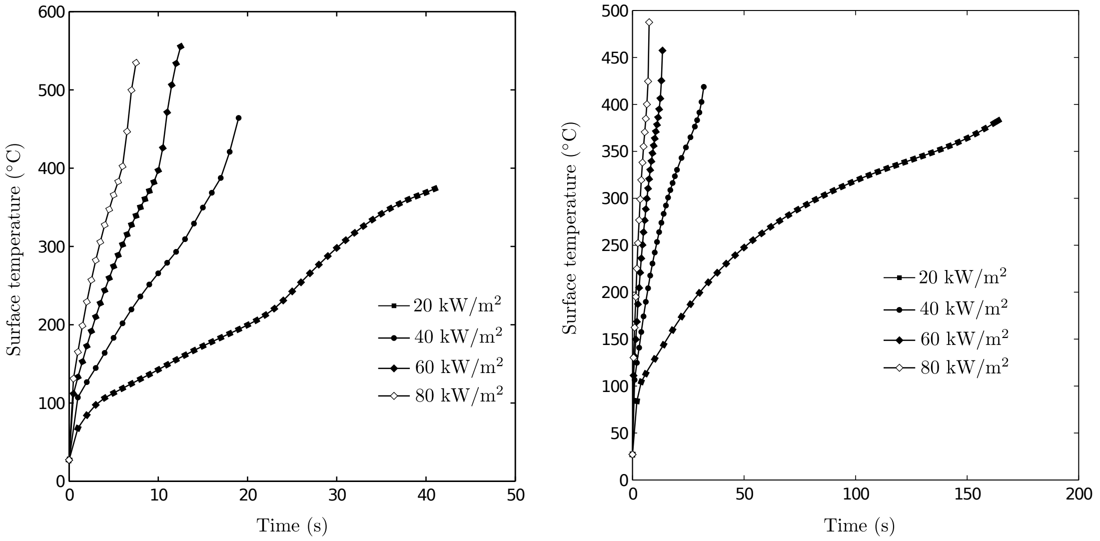

(a) $a = 1$ mm (b) $a = 5$ mm

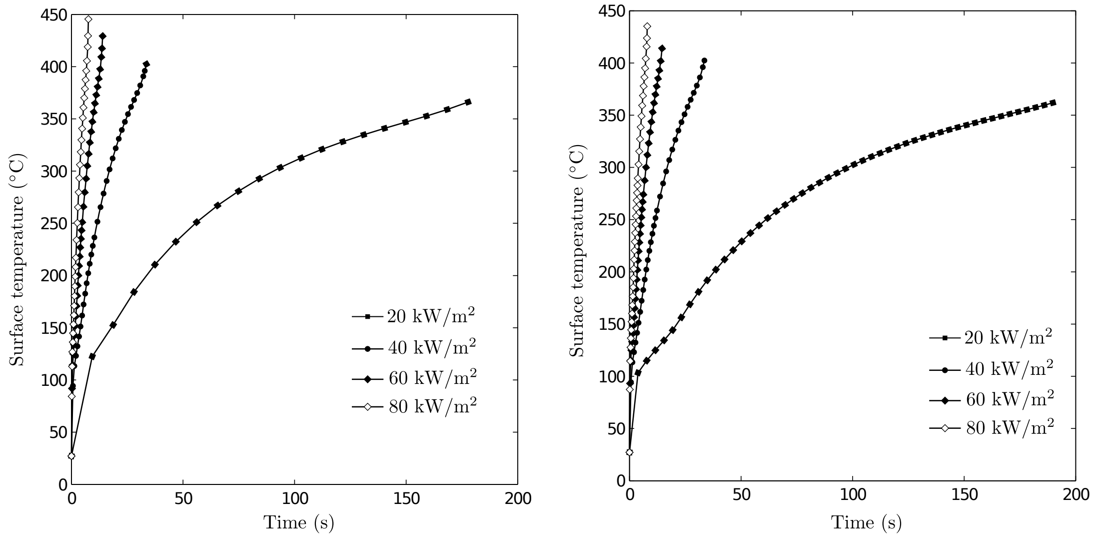

(c) $a = 10$ mm (d) $a = 15$ mm

Figure 3.9: Slab surface temperature up to the time of flammability, for various heating rates and half-width a, against time t. Moisture content set at 15% of dry vegetation.

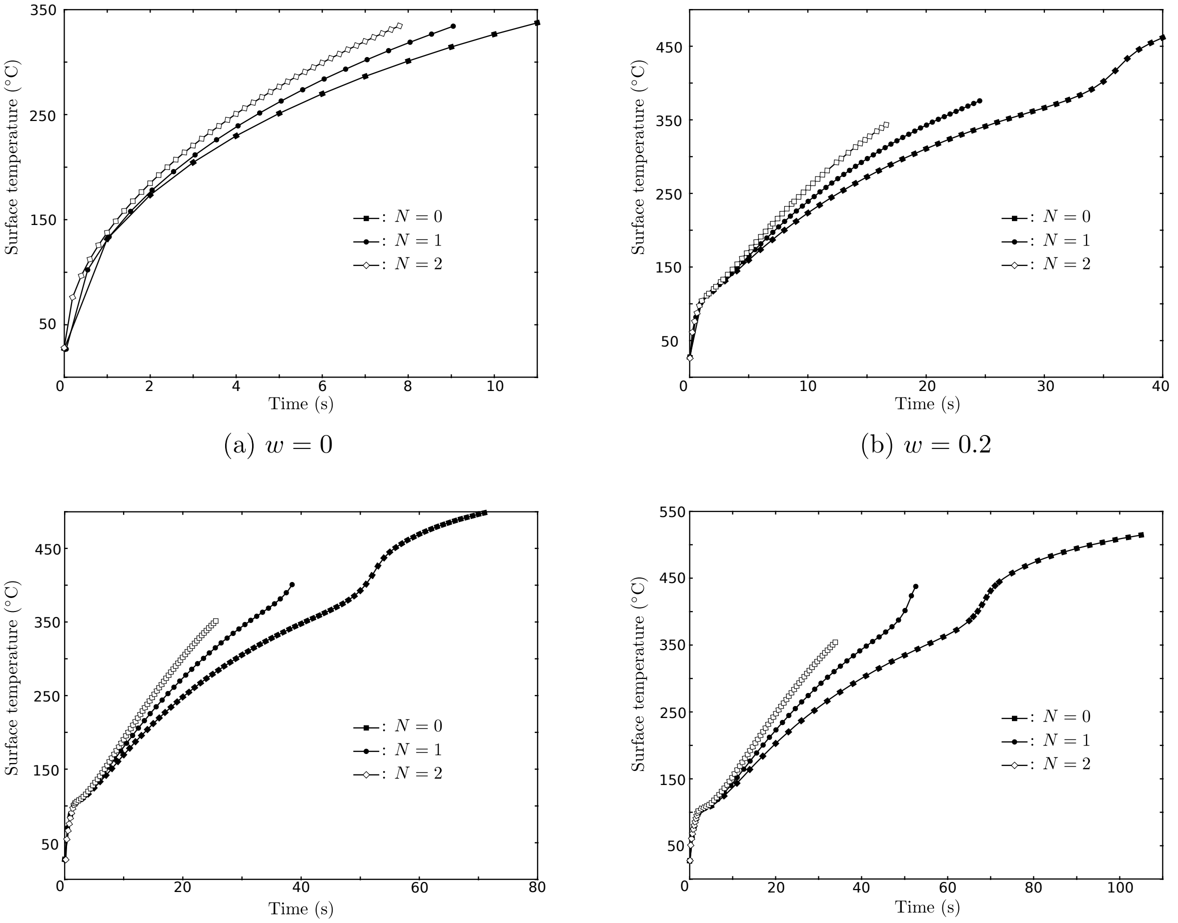

(a) $w = 0$

(b) $w = 0.2$

(c) $w = 0.4$

(d) $w = 0.6$

Figure 3.10: Surface temperature against time up to the time of flammability for slab, cylinder, and sphere geometries. Initial fuel moisture content is (a) 0%, (b) 20%, (c) 40%, and (d) 60%. The sample size is $a = 5$ mm and the heating rate is 40 kW/m^2 in all the plots.

at the flash point. This is due to the increased time taken to reach the flash point which means that the fuel sample is heated for a longer period of time resulting in larger surface temperatures.

3.3 Estimate of position and time of the flash point

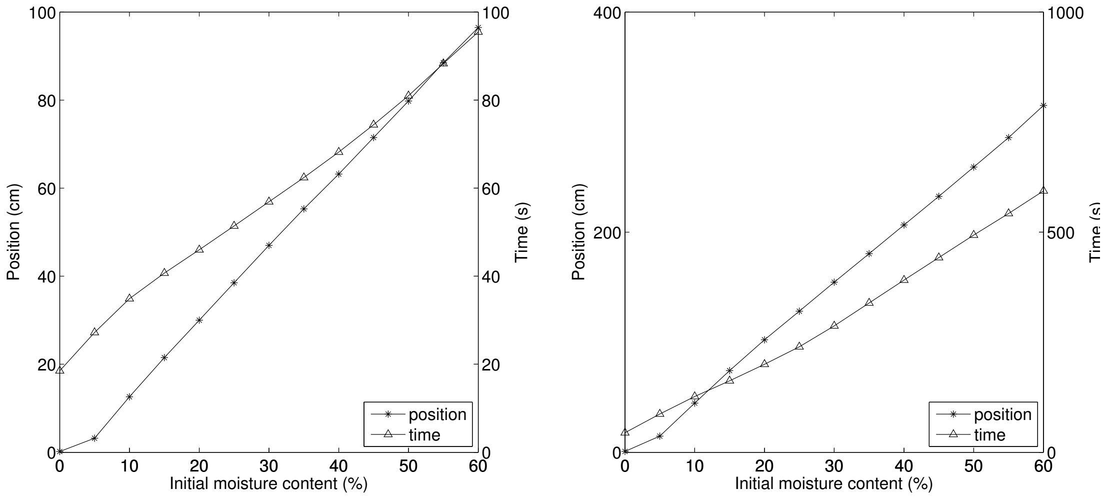

(a) $a = 1$ mm and $J = 20$ kW/m^2 (b) $a = 5$ mm and $J = 20$ kW/m^2

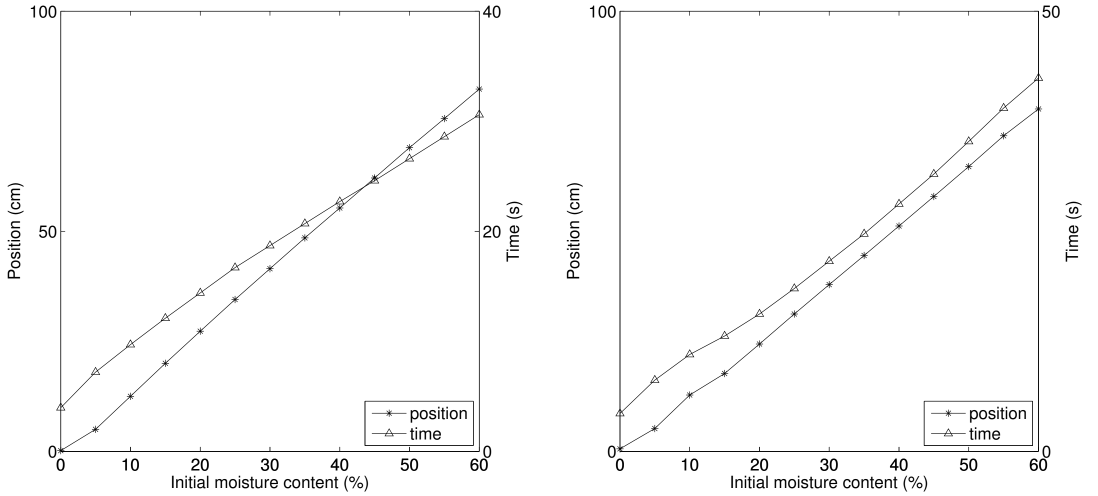

(c) $a = 1$ mm and $J = 60$ kW/m^2 (d) $a = 5$ mm and $J = 60$ kW/m^2

Figure 3.11: Estimate of position and time of the flash point for the slab ($N = 0$). Sample surface located at $r = a$.

Figures 3.11–3.13 show the estimated positions of, and time taken to reach, the flash point against the initial moisture content for slab, cylinder, and sphere geometries respectively. Heating rates of 20 kW/m^2 and 60 kW/m^2, and sample sizes of 1 mm and 5 mm are considered.

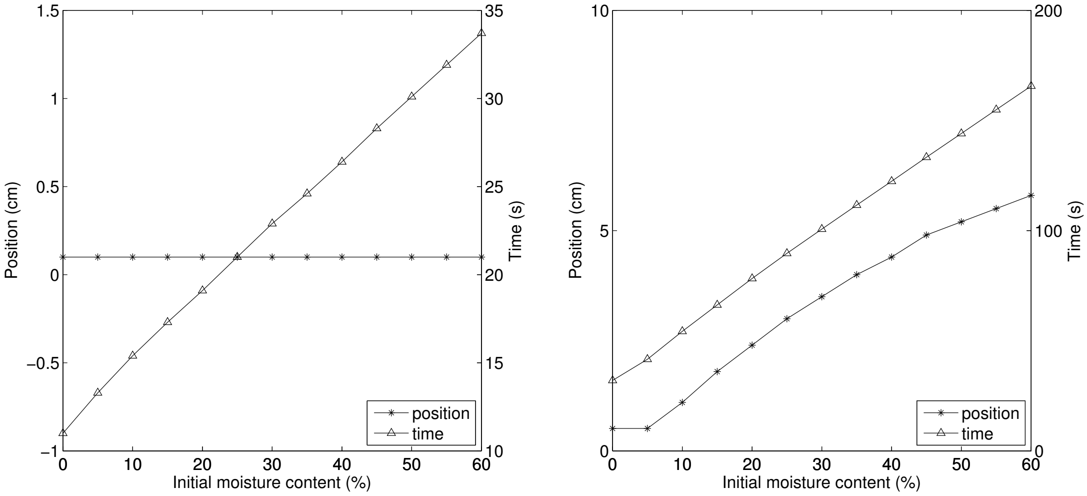

(a) $a = 1$ mm and $J = 20$ kW/m^2 (b) $a = 5$ mm and $J = 20$ kW/m^2

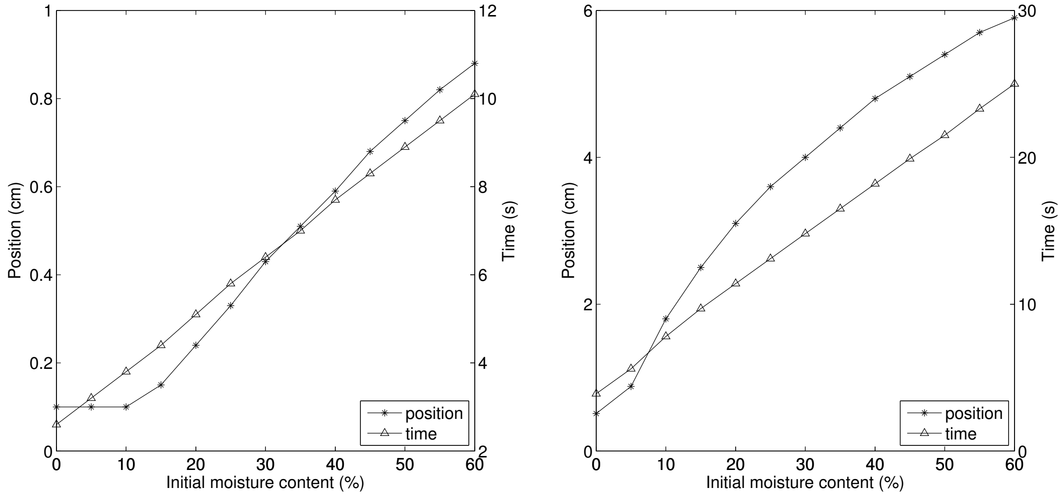

(c) $a = 1$ mm and $J = 60$ kW/m^2 (d) $a = 5$ mm and $J = 60$ kW/m^2

Figure 3.12: Estimate of position and time of the flash point for the cylinder ($N = 1$). Sample surface located at $r = a$.

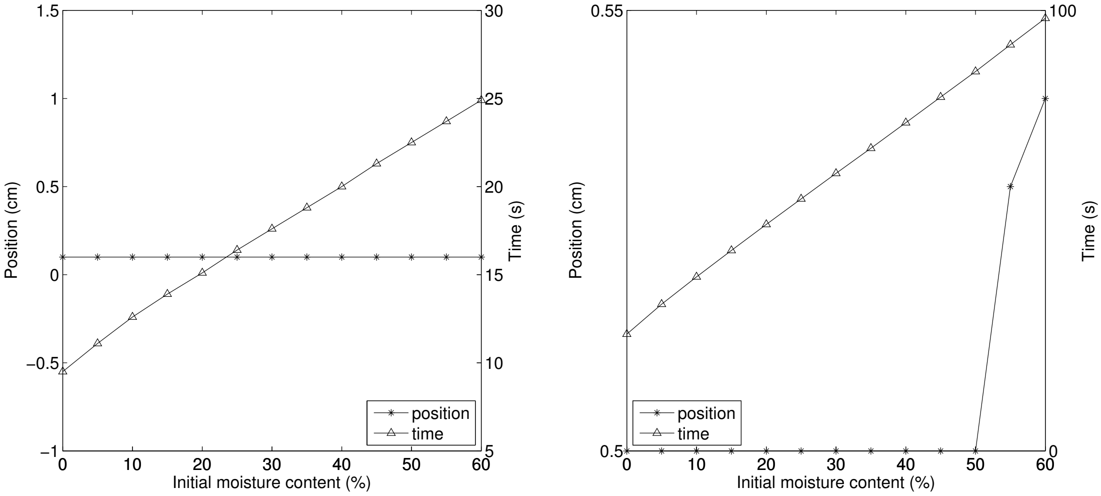

(a) $a = 1$ mm and $J = 20$ kW/m^2 (b) $a = 5$ mm and $J = 20$ kW/m^2

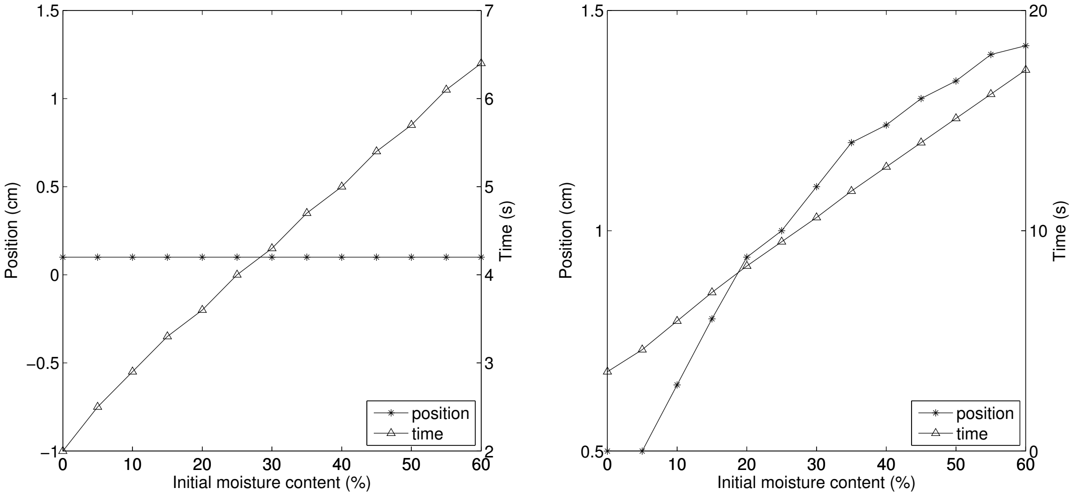

(c) $a = 1$ mm and $J = 60$ kW/m^2 (d) $a = 5$ mm and $J = 60$ kW/m^2

Figure 3.13: Estimate of position and time of the flash point for the sphere ($N = 2$). Sample surface located at $r = a$.

For the slab geometry, the estimated time taken to reach a flammable mixture increases monotonically with the moisture content as does the location, from the centre of the fuel sample, of the mixture. An increase in the sample size results in an increase in the flash point time and distance whereas increasing the heating rate results in a reduction in the flash point time and its distance from the centre of the fuel sample. Larger fuel samples contain more moisture so that an increased amount of water vapour is formed to dilute the pyrolysis vapour and air mixture, hence reducing the flammability.

For the cylindrical geometry, the flash point time continues to increase monotonically with an increase in initial moisture content. However, for relatively small heating rates and sample radii, the location of the flammable mixture remains close to the surface of the sample. When comparing results to the slab geometry, it is noticeable that the flash point time is reduced since the surface-are-to-volume ratio is larger for the cylinder and mixing takes place more readily in the external gases.

The time taken to reach a flammable mixture is further reduced in the spherical sample case relative to the cylinder since its surface-area-to-volume ratio is greater than even the cylinder and the external volume for gaseous mixing is further increased.

3.4 Mass flux at the surface

Figures 3.14–3.16 show both fuel and water vapour mass flow rates as a function of time for slab, cylinder, and sphere geometries respectively. These plots are not stopped at the time of flammability. Sample sizes are either 2 mm or 4 mm, heating rate is 20 kW/m^2 or 40 kW/m^2, and the initial moisture content is 0%, 30%, or 60% of the dry fuel mass. The results reveal that for appreciable sample sizes, heating rates, or initial moisture contents, the drying and pyrolysis processes overlap. This explains the difficulty in igniting wet vegetal fuels since the water vapour dilutes the pyrolysis products in the external gas phase.

Initial fuel moisture, if any, evaporates when the temperature of the fuel sample reaches about 100°C. For small fuel samples and low heating rates, the evaporation process can be dominant over pyrolysis so that hardly any pyrolysis products are formed until the fuel moisture is evaporated. This is evident from the slab fuel results

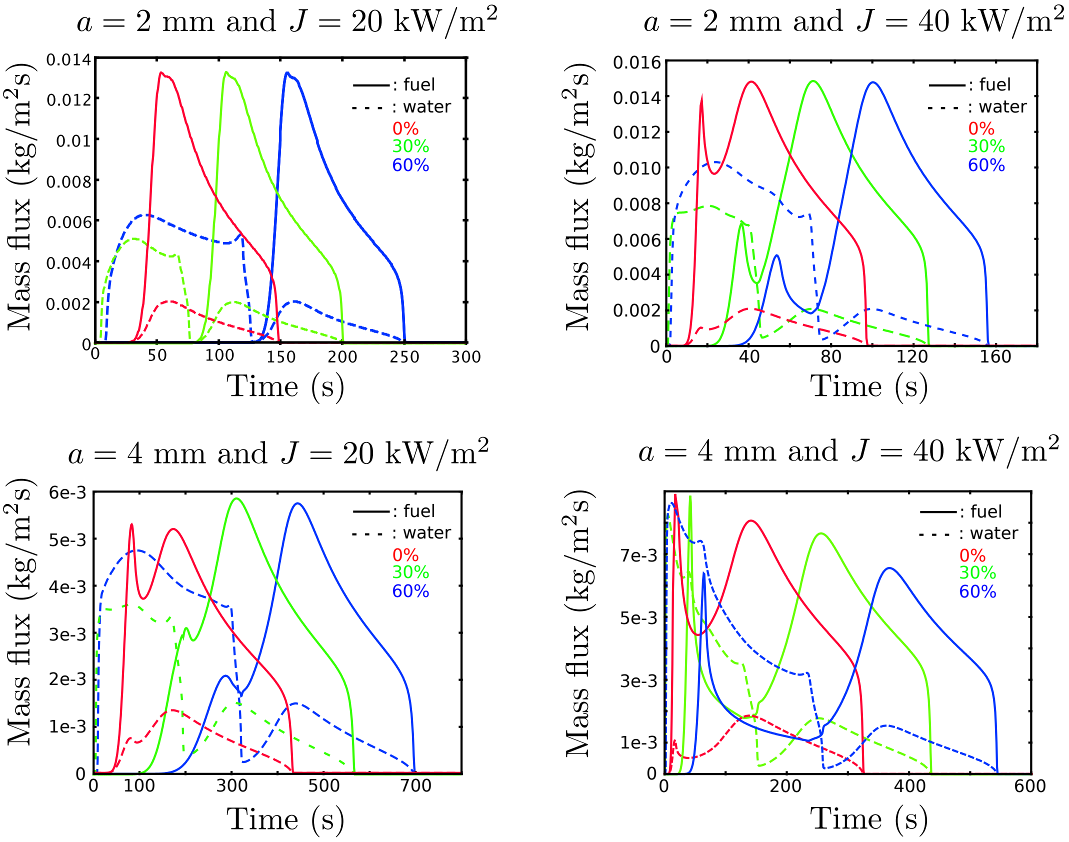

Figure 3.14: Mass flux for the fuel and water vapour at the surface of the slab ($N = 0$).

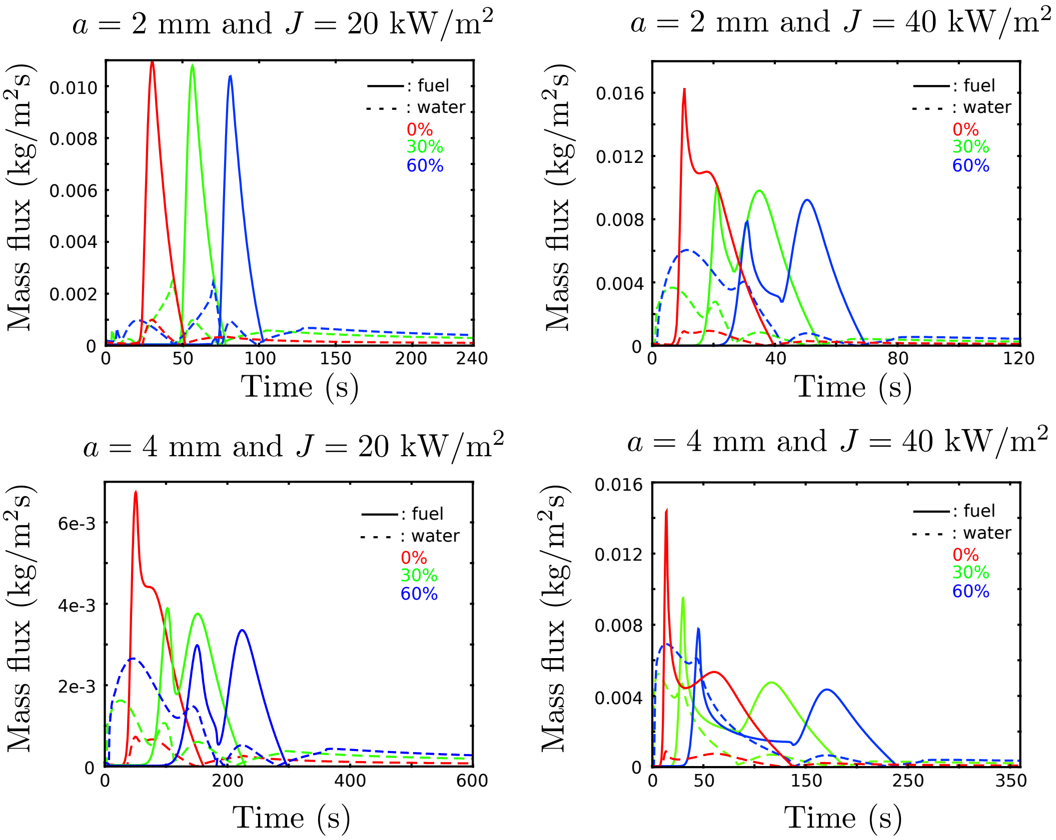

Figure 3.15: Mass flux for the fuel and water vapour at the surface of the cylinder ($N = 1$).

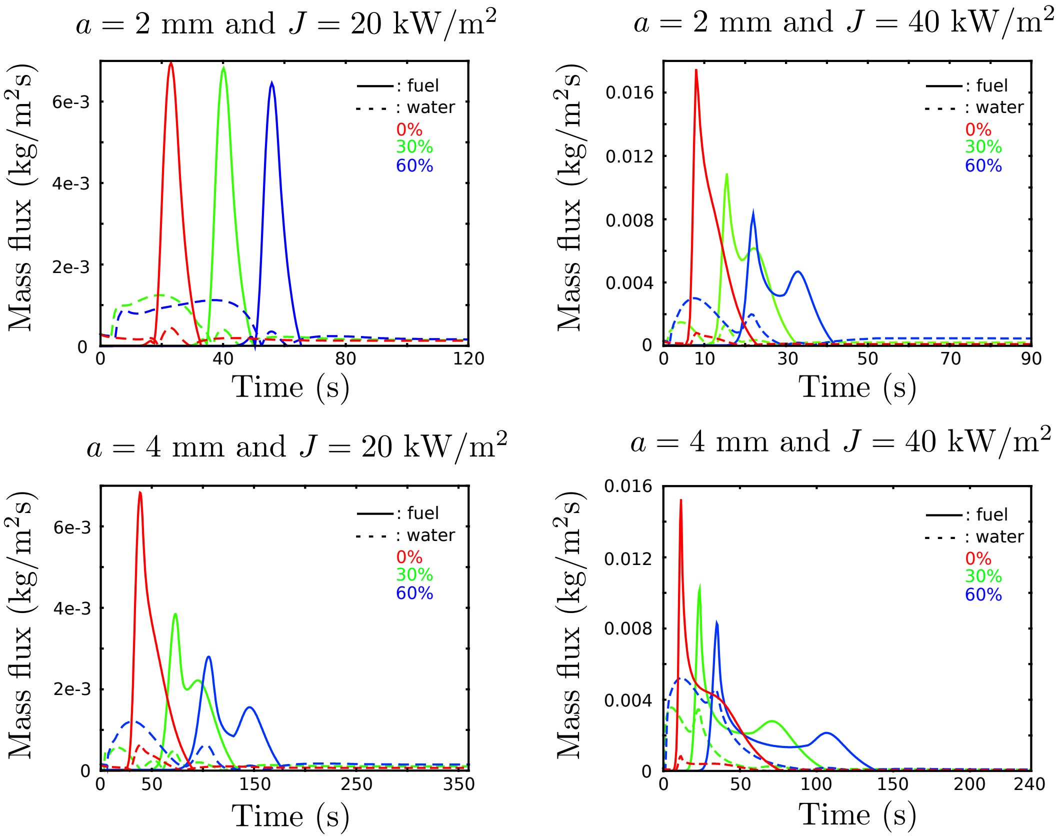
$a = 2$ mm and $J = 20$ kW/m^2

$a = 2$ mm and $J = 40$ kW/m^2

$a = 4$ mm and $J = 20$ kW/m^2

$a = 4$ mm and $J = 40$ kW/m^2

Figure 3.16: Mass flux for the fuel and water vapour at the surface of the sphere ($N = 2$).

(Figure 3.14) for $a = 2$ mm and $J = 20$ kW/m^2.

Evaporation and pyrolysis processes will occur simultaneously for stronger heating rates. Larger vegetal fuel samples will heat up more quickly as the heat impinges a larger surface area. Also the cylindrical and spherical fuels will heat more rapidly, even at the same heating rate, due to the increased surface-area-to-volume ratio compared to a slab of vegetal fuel. Therefore the overlap between pyrolysis and evaporation is more pronounced in large cylindrical and spherical fuel samples.

Water vapour is produced even when there is zero initial moisture content in the fuel sample. The reason for this is that the charring reaction produces gases which includes water in its vapour form. For appreciable initial fuel moisture contents, the production of pyrolysis vapour is delayed by the evaporation process.

3.5 Conclusions

Using a simplified model for the fuel pyrolysis, gaseous mixing, and conditions for flammability, the onset of ignition in vegetal fuels, of slab, cylinder, and sphere geometries, has been investigated for varying external radiant heating rates, fuel sample sizes, and initial fuel moisture contents. Drying, charring, and fast pyrolysis processes have been included in order to estimate when, and where, a flammable mixture is formed.

The geometry of the vegetal fuel plays a crucial role in its thermal degradation. Cylinder and sphere like fuels will heat up much more rapidly than slab like fuels due to their larger surface-area-to-volume ratio. The larger external volume in these cases also speeds up the process of gaseous mixing which leads to a flammable mixture. Initial fuel moisture content delays the flash point time. The evaporated moisture dilutes the external gas mixture which can push away the location of the flash point. Char production is dominant over lower temperatures/heating rates. The temperature at the flash point time is around 350°C–550°C. This large temperature range suggests that using a fixed value of ignition temperature is an oversimplification.

In nature, an isolated vegetal fuel would not be encountered. It is more common the have a line, or array, of fuels and vapour mixing from multiple sources would act together in a two or three dimensional flow field. The heating rate would not be uniform as it would depend on the geometry of the fuel sample and radiative source. In the next chapter, a two dimensional natural convection model is developed which will take into account the buoyant airflow from multiple fuel samples.

Chapter 4

Natural convection with radiative heating

The role of moisture content of a fuel particle in reaching the flash point was explored in Chapter 2. A one dimensional time-dependent model was introduced which incorporated vapourisation, charring, and fast pyrolysis reactions. Although this reveals some issues related to the onset of flaming in heated vegetation the model is too simple to capture all of the processes that must occur in reality. A two dimensional natural convection around vegetal fuel bodies model is presented in this chapter which will allow for a more realistic interaction of the flow around a solid fuel sample in either reducing or enhancing the heating of the vegetation.

Cylindrical fuel samples are taken to be exposed to radiant heat from an external panel. Heat conduction within the solid and the resulting natural convection are modelled. The model consists of Navier-Stokes and conservation of energy equations with the ideal gas law as the equation of state in the air domain. The conduction equation is applicable in the solid domain.

The radiating panel, which mimics the characteristics of a nearby radiating flame front, is assumed to be positioned sufficiently far way from the solid fuel so that the flow around the panel does not affect the solid. That is, the solid fuels will not receive any convective, or conductive, heat from the panel source. The heat received by a point on a fuel sample from the panel can be approximated using geometrical arguments based on view factors [22].

For multiple fuel samples in arbitrary locations, it is possible that some of the radiation from the panel will be blocked by one sample from reaching another. This shadowing contribution can also be approximated using geometrical arguments based on the calculation of view factors (section 4.3).

Although vapourisation and pyrolysis reactions are not included in this part of the work, the model does provide insight into the role of natural convection in modifying the heating process that would lead to these reactions.

4.1 Natural convection literature

The study of natural convection flow around two-dimensional bodies in an infinite domain has been studied, under steady-state conditions, experimentally, analytically, and numerically for over 50 years [54, 55]. In recent years, such flows around cylindrical geometries have been studied due to their range of industrial applications [56].

At moderately large values of the Rayleigh number ($10^4 < \mathrm{Ra} < 10^8$), the flow is laminar and forms a boundary layer around the cylinder [57–60]. Boundary-layer equations can be solved for this problem by assuming that curvature effects and the pressure difference across the boundary layer are negligible [61, 62]. However, the assumption of negligible curvature effects is valid for large Ra when the boundary layer thickness is much smaller than the radius of curvature of the body [63]. For moderate values of Ra (e.g. of order 10^2) the assumption of negligible curvature effects produces appreciable errors.

Kuehn and Goldstein [57] numerically solved the complete Navier-Stokes and energy equation for laminar natural convection around a solitary horizontal cylinder which is maintained at a constant surface temperature (isothermal). Wang et al. [58] solved the same problem using a different numerical method. They also solved the case when the cylinder is maintained at a constant heating rate. The steady dimensionless equations were derived using the Boussinesq approximation [15]. This assumes that density differences in the governing equations are small except in the buoyancy term of the momentum equation. Saitoh et al. [59] attempted to obtain benchmark solutions for the steady natural convection problem around an isothermal horizontal circular cylinder for the Rayleigh number range $10^3 \leq \mathrm{Ra} \leq 10^5$.

In the present natural convection model, fluid density will be assumed to vary with temperature. A non-uniform heating rate, based on the geometric considerations, will be incorporated in the model. The fuel samples will receive heat from a radiating rectangular heat source which represents a fire front. This approach is based on the experimental study by Cohen and Finney [64] where wood-based fuel samples were exposed to heat from a radiating panel at a rate of 41 kW/m^2. Fuel samples of 1 mm and 12 mm width were considered and the radiating panel was 486 mm wide and 375 mm high. The fuel sample was placed 10 cm from the panel which was deemed to be a sufficient distance from buoyant flow around the panel.

The governing equations for the natural convection around horizontal cylindrical fuels sample will be presented in the next section. The non-uniform heating rate will be calculated based on the a setup similar to that presented in the experiments of Cohen and Finney [64].

4.2 Governing equations for the natural convection flow around a horizontal fuel sample subjected to non-uniform radiative heating

The model will incorporate the flow around the solid fuel sample and the heat conduction taking place within the solid. It is assumed that the fuel sample is sufficiently far away from the radiating panel so that the natural convection taking place around the panel does not affect the solid [64]. That is, the heat transfer from the panel to the solid is dominated by radiation from the panel being absorbed by the fuel sample. This overcomes the problem of having to model the flow around the radiating panel. In the experiments of Cohen and Finney [64] a panel radiating 41 kW/m^2 of heat was placed 10 cm away from the solid. This distance was deemed sufficiently far away from the solid so that the flow around the panel did not interfere with the solid fuel sample. The heat conduction equation will model the heat transfer taking place in the solid sample. For the air flow the conservation equations for mass, momentum, and energy hold. The boundary conditions will include radiative heat transfer from the panel and the conductive heat exchange with the sample's surroundings.

For the solid domain the heat conduction equation is

$$\rho_s c_s \frac{\partial \Theta}{\partial t} = \nabla \cdot \lambda_s \nabla \Theta \tag{4.1}$$

where ρ_s [kg/m^3][1] is the density of the solid, c_s [J/(kg K)] is the specific heat capacity of the solid, Θ [K] is the solid temperature, t [s] is time, and λ_s [W/(K m)] is the solid thermal conductivity. For the air domain the mass balance is

$$\frac{\partial \rho}{\partial t} + \nabla \cdot \rho \mathbf{u} = 0 \tag{4.2}$$

where $\rho = \rho(T)$ [kg/m^3] is the density of the air (T [K] is the air temperature) and $\mathbf{u}$ [m/s] is the flow velocity. The density varies with temperature in general. The momentum balance is

$$\rho \left(\frac{\partial \mathbf{u}}{\partial t} + \mathbf{u} \cdot \nabla \mathbf{u} \right) = \mathbf{F} - \nabla P + \nabla \cdot \boldsymbol{\tau}$$

where P [N/m^2] is the pressure and $\mathbf{F}$ [N/m^3] is the body force. The viscous stress tensor $\boldsymbol{\tau}$ [N/m^2] can be written as

$$\boldsymbol{\tau} = \eta \left(\nabla \mathbf{u} + \nabla \mathbf{u}^{\mathsf{T}} - \tfrac{2}{3} (\nabla \cdot \mathbf{u}) \mathbb{I} \right)$$

where η [N·s/m^2] is the dynamic viscosity [65]. The pressure P may be broken down into the hydrostatic pressure P_h and the dynamic pressure, which is the pressure due to the motion of the fluid, P_d so that

$$P = P_h + P_d$$

where $P_h = -\rho_0 \, g y$ and ρ_0 is the density of the ambient air. The body force $\mathbf{F}$ is just the force due to gravity so that

$$\mathbf{F} = -\rho g \, \mathbf{j}$$

where $\mathbf{j}$ is the unit vector pointing in the vertical or positive y-direction. Hence the momentum equation may be written as

$$\rho \left(\frac{\partial \mathbf{u}}{\partial t} + \mathbf{u} \cdot \nabla \mathbf{u} \right) + \nabla P_d = \nabla \cdot \boldsymbol{\tau} + g \left(\rho_0 - \rho \right) \mathbf{j}.$$

The energy equation is

$$\rho c_p \left(\frac{\partial T}{\partial t} + \mathbf{u} \cdot \nabla T \right) = \nabla \cdot \lambda \nabla T \tag{4.3}$$

---

[1] Contents of the square brackets [.] give the units of the preceding quantity.

where c_p [J/(kg K)] is the specific heat capacity at constant pressure of the air and λ [W/(K m)] is the thermal conductivity of the air. Finally the equation of state is the ideal gas law

$$P = \rho R_{\mathrm{A}} T$$

where $R_{\mathrm{A}} = R/M_{\mathrm{A}} \approx 287$ J/(kg K) is the specific gas constant and the mean molecular mass of air is $M_{\mathrm{A}} \approx 29$ g/mol. If it is assumed that the pressure variations about the ambient pressure of $\rho_0 R_{\mathrm{A}} T_0$ are negligibly small (Boussinesq approximation), then the density difference term in the momentum equation can be written independently of the pressure as [21]

$$\rho_0 - \rho \quad = \quad \frac{P}{R_{\mathrm{A}} T_0} - \frac{P}{R_{\mathrm{A}} T} \quad = \quad \frac{P}{R_{\mathrm{A}} T}\left(\frac{T}{T_0} - 1\right) \quad = \quad \frac{\rho}{T_0}\left(T - T_0\right).$$

Rearranging this equation gives the density as

$$\rho = \frac{\rho_0}{1 + \frac{T - T_0}{T_0}} \tag{4.4}$$

and the momentum equation can be rewritten as

$$\rho\left(\frac{\partial \mathbf{u}}{\partial t} + \mathbf{u} \cdot \nabla \mathbf{u}\right) + \nabla P_d = \nabla \cdot \boldsymbol{\tau} + \frac{g\rho\left(T - T_0\right)}{T_0}\mathbf{j}. \tag{4.5}$$

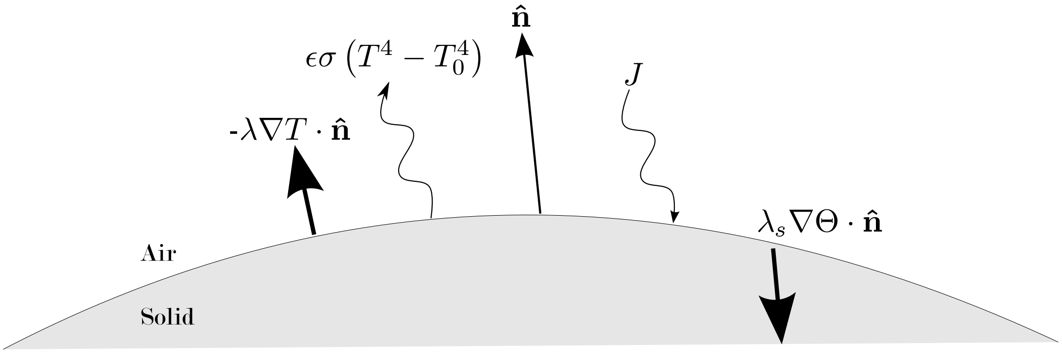

Figure 4.1: Solid sample receives incident heat flux of J [kW/m^2] on the boundary. Part of this heat is conducted by the solid and part of it is conducted in the air. The solid will also reradiated some of the heat it receives. Directions of arrows indicate directions of heat transfer, either towards or away from the interface.

There are six unknown quantities ($\mathbf{u} = (u, v), P_d, \rho, T$, and Θ) and six equations (Equations (4.1)-(4.5) where the momentum equation is composed of x and y components and uniformity in the z-direction means that the velocity in this direction is $w = 0$). Initially ($t = 0$) it is assumed that $u = v = P_d = 0$ and $T = \Theta = T_0$. Far away from the cylinder ($r \to \infty$) $u = v = P_d = 0$, and $T = T_0$. On the solid boundary the no slip

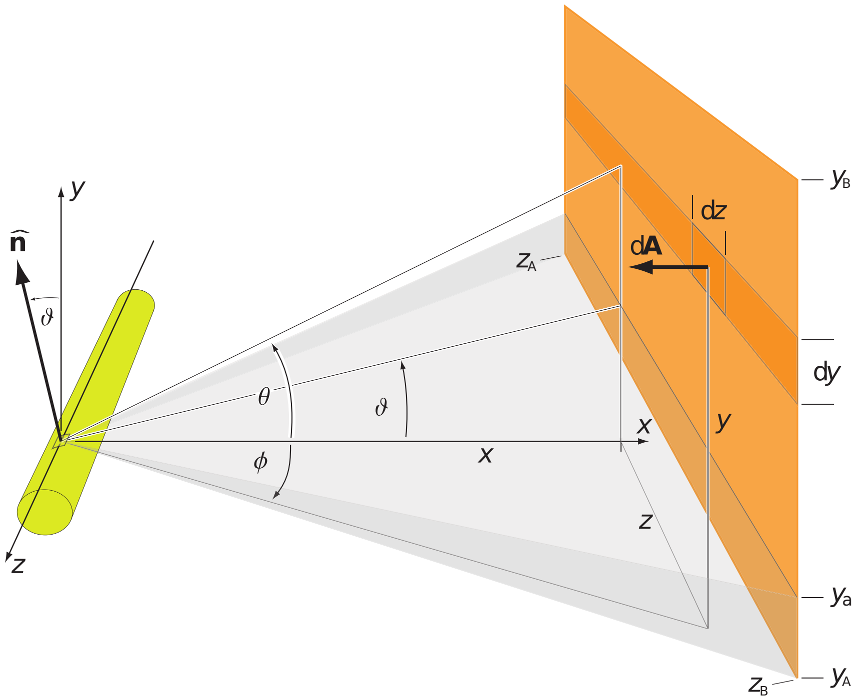

Figure 4.2: Geometric properties of the solid sample being heated by the radiation from the parallel rectangular panel. The unit vector $\hat{\mathbf{n}} = (-\sin\vartheta, \cos\vartheta, 0)$ is the outward normal at a particular point on the rod surface and the angle ϑ represents the angle between the tangent plane at the point on the rod with outward normal $\hat{\mathbf{n}}$ and the x-axis.

condition is applicable so that $\mathbf{u} = \mathbf{0}$ and continuity of temperature implies $T = \Theta$. Also the solid body is exposed to a radiant heat flux from a parallel heating panel so that the conservation of energy on the cylinder surface (Figure 4.1) gives

$$\lambda \nabla T \cdot \hat{\mathbf{n}} + J = \lambda_s \nabla \Theta \cdot \hat{\mathbf{n}} + \epsilon \varsigma \left(T^4 - T_0^4 \right)$$

where the outward pointing normal at a point on the rod surface is $\hat{\mathbf{n}}$ (Figure 4.2) where

$$\hat{\mathbf{n}} = \left(\cos\left(\vartheta + \pi/2\right), \sin\left(\vartheta + \pi/2\right), 0\right) = \left(-\sin\vartheta, \cos\vartheta, 0\right).$$

Also J_0 $\left[\mathrm{W/m^2}\right]$ is the incident heat flux, ϵ is the emissivity, and ς $\left[\mathrm{W/m^2K^4}\right]$ is the Stefan-Boltzmann constant. The air and solid thermal conductivities are $\lambda = \rho c_{\mathrm{p}} \kappa$ and $\lambda_s = \rho_s c \kappa_s$ respectively. The angle ϑ represents the angle between the tangent plane at a point on the rod and the x-axis. This angle determines whether the point on the surface of the fuel sample is visible from the radiating panel as only objects above the tangent plane are visible from the point. There is an isotropic radiant heat flux J_0 emitted by a vertical rectangular panel (486 mm × 375 mm in the experiments of Cohen and Finney [64]) which is parallel to the fuel sample at a distance x_{B}. A visible element $\mathrm{d}\mathbf{A} = (-1, 0, 0)\,\mathrm{d}y\,\mathrm{d}z$ at a position $\mathbf{r} = (x_\mathrm{B}, y, z)$ on the panel (as measured from a point on the fuel sample with normal vector $\hat{\mathbf{n}}$) subtends the solid angle $\mathrm{d}A = -\mathrm{d}\mathbf{A}\cdot\mathbf{r}/4\pi r^3$ about the point. The solid angle is the fractional surface area of a sphere of unit radius. This gives the energy flux per unit surface area arriving at the point as

$$\mathrm{d}J = 4J_0\frac{\hat{\mathbf{n}}\cdot\mathbf{r}}{r}\,\mathrm{d}A = \frac{J_0}{\pi}\,x_\mathrm{B}\,\frac{y\cos\vartheta - x_\mathrm{B}\sin\vartheta}{(x_\mathrm{B}^2 + y^2 + z^2)^2}\,\mathrm{d}y\,\mathrm{d}z.$$

If the visible panel runs from $z = z_\mathrm{A}$ to $z = z_\mathrm{B}$ and $y = y_\mathrm{A}$ to $y = y_\mathrm{B}$ then the radiative power per unit area received at the point on the fuel sample is

$$J = \frac{J_0}{\pi}\,x_\mathrm{B}\int_{y_\mathrm{A}}^{y_\mathrm{B}}\int_{z_\mathrm{A}}^{z_\mathrm{B}}\frac{y\cos\vartheta - x_\mathrm{B}\sin\vartheta}{(x_\mathrm{B}^2 + y^2 + z^2)^2}\,\mathrm{d}z\,\mathrm{d}y.$$

Assuming that the panel is very long (relative to its height) effectively means that $z_\mathrm{A} \to -\infty$ and $z_\mathrm{B} \to +\infty$. Introducing the parameter ζ so that

$$\zeta^2 = \frac{z^2}{x_\mathrm{B}^2 + y^2} \;\Rightarrow\; \mathrm{d}\zeta = \frac{\mathrm{d}z}{\sqrt{x_\mathrm{B}^2 + y^2}}$$

then the power received is

$$J = \frac{J_0}{\pi}\,x_\mathrm{B}\int_{y_\mathrm{A}}^{y_\mathrm{B}}\frac{y\cos\vartheta - x_\mathrm{B}\sin\vartheta}{(x_\mathrm{B}^2 + y^2)^{3/2}}\int_{-\infty}^{\infty}\frac{\mathrm{d}\zeta}{(1+\zeta^2)^2}\,\mathrm{d}y = \frac{J_0}{2}\,x_\mathrm{B}\int_{y_\mathrm{A}}^{y_\mathrm{B}}\frac{y\cos\vartheta - x_\mathrm{B}\sin\vartheta}{(x_\mathrm{B}^2 + y^2)^{3/2}}\,\mathrm{d}y$$

using the fact that the value of the infinite integral with respect to ζ is $\pi/2$. Introducing another parameter $\eta = y/x_\mathrm{B}$ gives

$$J = \frac{J_0}{2}\int_{y_\mathrm{A}/x_\mathrm{B}}^{y_\mathrm{B}/x_\mathrm{B}}\frac{\eta\cos\vartheta - \sin\vartheta}{(1+\eta^2)^{3/2}}\,\mathrm{d}\eta.$$

Let the angles θ_A and θ_B represent the lowest and highest visible points on the panel as seen from the point on the fuel sample where the tangent angle is ϑ (Figure 4.2), then $\tan\theta_\mathrm{A} = y_\mathrm{A}/x_\mathrm{B}$ and $\tan\theta_\mathrm{B} = y_\mathrm{B}/x_\mathrm{B}$. Hence,

$$J = \frac{J_0}{2}\left[\frac{\eta\sin\vartheta + \cos\vartheta}{(1+\eta^2)^{1/2}}\right]_{\tan\theta_\mathrm{B}}^{\tan\theta_\mathrm{A}}$$

where the limits have been switched to account for the minus sign. Using trigonometric identities for $\tan\alpha$ and $\cos\alpha$ for some angle α gives

$$J = \frac{J_0}{2}\left(\cos(\theta_\mathrm{A} - \vartheta) - \cos(\theta_\mathrm{B} - \vartheta)\right).$$

This formula is based on assuming that the angles θ_{A} and θ_{B} are between zero and π so that the bottom and top of the panel are both visible. When this is not the case the values of $\theta_{\mathrm{A}} - \vartheta$ and $\theta_{\mathrm{B}} - \vartheta$ can be replaced as follows

$$\theta_{\mathrm{A}} - \vartheta \to \min\{\pi, \max[0, \theta_{\mathrm{A}} - \vartheta]\} \qquad \text{and} \qquad \theta_{\mathrm{B}} - \vartheta \to \max\{0, \min[\pi, \theta_{\mathrm{B}} - \vartheta]\}$$

so that $J = J_0 \times \psi(\vartheta)$ with

$$\psi(\vartheta) = \frac{1}{2}\left[\cos(\min\{\pi, \max[0, \theta_{\mathrm{A}} - \vartheta]\}) - \cos(\max\{0, \min[\pi, \theta_{\mathrm{B}} - \vartheta]\})\right].$$

This formula is now valid for any value of ϑ whether or not any part of the panel is visible. If the fuel sample is very thin in relation to the size of the panel and its distance from the sample, then the angles θ_{A} and θ_{B} do not vary significantly between the different points on the surface of the rod. The heat flux boundary condition becomes

$$\lambda \nabla T \cdot \hat{\mathbf{n}} + J_0\, \psi(\vartheta) = \lambda_s \nabla \Theta \cdot \hat{\mathbf{n}} + \epsilon\varsigma\left(T^4 - T_0^4\right). \tag{4.6}$$

4.2.1 Nondimensionalisation

Equations (4.1)–(4.6) are in dimensional form. The following scalings are applied for the nondimensionalisation

$$t = t_c\,\overline{t}, \qquad \mathbf{r} = l\,\overline{\mathbf{r}}, \qquad \mathbf{u} = \frac{l}{t_c}\,\overline{\mathbf{u}}, \qquad \boldsymbol{\tau} = \frac{\eta_0}{t_c}\overline{\boldsymbol{\tau}}$$

$$P_d = \frac{\rho_0\, l^2}{t_c^2}\,\overline{P}, \qquad \rho = \rho_0\,\overline{\rho}, \qquad c_p = c_{p0}\,\overline{c}_p$$

$$\eta = \eta_0\,\overline{\eta}, \qquad \lambda = \lambda_0\,\overline{\lambda}, \qquad \lambda_s = \lambda_{s0}\,\overline{\lambda}_s$$

$$T = T_0 + (T_c - T_0)\,\overline{T}, \qquad \Theta = T_0 + (T_c - T_0)\,\overline{\Theta}.$$

After substituting the above scales into Equations (4.1)–(4.6), rearranging the equations, and dropping the bar notation, the following nondimensional governing equations, with the heat flux boundary condition, are obtained

$$\frac{\partial \Theta}{\partial t} = \left[\frac{\kappa_{s0} t_c}{l^2}\right] \nabla \cdot \lambda_s \nabla \Theta$$

$$\frac{\partial \rho}{\partial t} + \nabla \cdot \rho \mathbf{u} = 0$$

$$\rho c_p \left(\frac{\partial T}{\partial t} + \mathbf{u} \cdot \nabla T\right) = \left[\frac{\kappa_0 t_c}{l^2}\right] \nabla \cdot \lambda \nabla T$$

$$\rho\left(\frac{\partial \mathbf{u}}{\partial t}+\mathbf{u}\cdot\nabla\mathbf{u}\right)+\nabla P=\left[\frac{\nu_0 t_c}{l^2}\right]\left(\nabla\cdot\left(\nabla\mathbf{u}+\nabla\mathbf{u}^{\intercal}-\tfrac{2}{3}\left(\nabla\cdot\mathbf{u}\right)\mathbb{I}\right)+\left[\frac{glt_c}{\nu_0}\frac{\left(T_c-T_0\right)}{T_0}\right]\rho T\,\mathbf{j}\right)$$

$$\left[\frac{\lambda_{s0}}{\lambda_0}\right]\lambda_s\nabla\Theta\cdot\mathbf{n}-\lambda\nabla T\cdot\hat{\mathbf{n}}=$$

$$\left[\frac{lJ_0}{\lambda_0\left(T_c-T_0\right)}\right]\left(\psi(\vartheta)-\left[\frac{\epsilon\varsigma T_0^4}{J_0}\right]\left(\left(1+\left[\frac{T_c-T_0}{T_0}\right]T\right)^4-1\right)\right)$$

where $\kappa_0=\lambda_0/\rho_0 c_{\mathrm{p}0}$ and $\kappa_{s0}=\lambda_{s0}/\rho_s c_s$ [m^2/s] are air and solid thermal diffusivities respectively, and ν_0 [m^2/s] is the viscosity of ambient air. Nondimensionalising the equation of state and dropping the bar notation gives

$$\rho=\frac{1}{1+\left(\frac{T_c-T_0}{T_0}\right)T}.$$

It is useful to select values for the characteristic temperature T_c and characteristic time scale t_c such that

$$\left[\frac{lJ_0}{\lambda_0\left(T_c-T_0\right)}\right]=1\implies T_c=\frac{lJ_0}{\lambda_0}+T_0,$$

$$\left[\frac{\kappa_0 t_c}{l^2}\right]=1\implies t_c=\frac{l^2}{\kappa_0},$$

and to define the nondimensional parameters as

$$\mathrm{Pr}=\left[\frac{\nu_0 t_c}{l^2}\right]=\frac{\nu_0}{\kappa_0}$$

$$\mathrm{Ra}=\left[\frac{glt_c\left(T_c-T_0\right)}{\nu_0 T_0}\right]=\frac{gl^3}{\nu_0\kappa_0}\frac{\left(T_c-T_0\right)}{T_0}$$

$$A_T=\left[\frac{T_c-T_0}{T_0}\right]$$

$$B_\lambda=\left[\frac{\lambda_{s0}}{\lambda_0}\right]=\frac{\rho_s c_s\kappa_{s0}}{\rho_0 c_{p0}\kappa_0}$$

$$C_\kappa=\left[\frac{\kappa_{s0}t_c}{l^2}\right]=\frac{\kappa_{s0}}{\kappa_0}$$

$$D_R=\left[\frac{\epsilon\varsigma T_0^4}{J_0}\right]$$

where Pr and Ra are the Prandtl and Rayleigh numbers respectively. Using the fact that $T_c=T_0+lJ_0/\lambda_0$ the Rayleigh number can be rewritten as

$$\mathrm{Ra}=\frac{gJ_0 l^4}{\nu_0\lambda_0\kappa_0 T_0}.$$

The nondimensional governing equations for the natural convection around a fuel sample exposed to radiative heating can now be written as

$$\frac{\partial \Theta}{\partial t} = C_\kappa \nabla \cdot \lambda_s \nabla \Theta \tag{4.7}$$

$$\frac{\partial \rho}{\partial t} + \nabla \cdot \rho \mathbf{u} = 0 \tag{4.8}$$

$$\rho c_p \left(\frac{\partial T}{\partial t} + \mathbf{u} \cdot \nabla T \right) = \nabla \cdot \lambda \nabla T \tag{4.9}$$

$$\rho = \frac{1}{1 + A_T T} \tag{4.10}$$

$$\rho \left(\frac{\partial \mathbf{u}}{\partial t} + \mathbf{u} \cdot \nabla \mathbf{u} \right) + \nabla P = \Pr \left(\nabla \cdot \left(\nabla \mathbf{u} + \nabla \mathbf{u}^\intercal - \tfrac{2}{3} \left(\nabla \cdot \mathbf{u} \right) \mathbb{I} \right) + \mathrm{Ra}\, \rho T \mathbf{j} \right) \tag{4.11}$$

with the heat flux boundary condition

$$B_\lambda \, \lambda_s \nabla \Theta \cdot \hat{\mathbf{n}} - \lambda \nabla T \cdot \hat{\mathbf{n}} = \psi(\vartheta) + D_R \left(1 - (1 + A_T T)^4 \right). \tag{4.12}$$

The approximate physical properties of solid wood and air at ambient temperature (300 K) are [18, 46, 66]

$$\begin{array}{ccc} c_{s0} \approx 2{,}500 \text{ J/(kg K)} & \rho_{s0} \approx 1{,}000 \text{ kg/m}^3 & \kappa_{s0} \approx 10^{-7} \text{ m}^2\text{/s} \\ \lambda_{s0} \approx 1/4 \text{ W/(m K)} & c_{p0} \approx 1{,}000 \text{ J/ (kg K)} & \rho_0 \approx 1.2 \text{ kg/m}^3 \\ \kappa_0 \approx 2.2 \times 10^{-5} \text{ m}^2 \text{ s}^{-1} & \lambda_0 \approx 1/40 \text{ W/(m K)} & \nu_0 \approx 1.6 \times 10^{-5} \text{ m}^2\text{/s} \\ \eta_0 \approx 1.8 \times 10^{-5} \text{ Pa s} & \epsilon \approx 6/7 & \varsigma \approx 5.67 \times 10^{-8} \text{ J/(m}^2 \text{ K}^4 \text{ s).} \end{array}$$

Applying the above approximations allows an estimate for the nondimensional parameters

$$\Pr = \left[\frac{\nu_0 t_c}{l^2} \right] = \frac{\nu_0}{\kappa_0} \approx 0.7$$

$$A_T = \left[\frac{T_c - T_0}{T_0} \right] = \beta \left(T_c - T_0 \right) = \frac{l J_0}{\lambda_0 T_0} \approx \frac{40\, l J_0}{T_0}$$

$$\mathrm{Ra} = \left[\frac{g l t_c \beta \left(T_c - T_0 \right)}{\nu_0} \right] = \frac{g \beta l^3 \left(T_c - T_0 \right)}{\nu_0 \kappa_0} = \frac{g l^3}{\nu_0 \kappa_0} A_T \approx \left(3000\, l \right)^3 A_T$$

$$B_\lambda = \left[\frac{\lambda_{s0}}{\lambda_0} \right] = \frac{\rho_{s0} c_{s0} \kappa_{s0}}{\rho_0 c_{p0} \kappa_0} \approx 10$$

$$C_\kappa = \left[\frac{\kappa_{s0} t_c}{l^2} \right] = \frac{\kappa_{s0}}{\kappa_0} \approx 1/222$$

$$D_R = \left[\frac{\epsilon \varsigma T_0^4}{J_0} \right] \approx \frac{400}{J_0}$$

where l is measured in metres [m], T_0 is in kelvin [K], and J_0 is in watts per square metre [W/m^2].

The nondimensional governing equations for mass, momentum, and energy conservation, together with the ideal gas law, have been presented (Equations (4.7)–(4.11)). The model equation include the solid conduction process as well as the natural convection around the fuel sample. The heat flux boundary condition (Equations (4.12)) includes the radiative heat received from a hot panel with heat loss due to reradiation and conduction also addressed.

The radiating panel has been assumed to be infinitely long, with the justification that the flame front in a forest fire is likely to be much larger than the vegetation in its path. A view factor based on a finite radiating panel can be calculated for when the large flame front approximation is unrealistic.

4.2.2 Finite radiating panel

For a panel with finite length (i.e. finite z_A and z_B), an approximate approach is to use the same formula as before but with an effective value for J_0 that is reduced as a result of the smaller solid angle subtended by the panel. Though the panel is assumed to be finite it is, in reality, much larger than the fuel sample. The panel is being considered as finite in order to better represent the heat received by the fuel sample. For the case that is symmetric in z, such that $z_\mathrm{B} = -z_\mathrm{A} = x\zeta_\mathrm{B}$ say, the radiative power is

$$J = \frac{J_0}{\pi} \int_{y_\mathrm{A}/x}^{y_\mathrm{B}/x} \frac{\eta\cos\vartheta - \sin\vartheta}{(1+\eta^2)^{3/2}} \int_0^{\zeta_\mathrm{B}/\sqrt{1+\eta^2}} \frac{2\,\mathrm{d}\zeta}{(1+\zeta^2)^2}\,\mathrm{d}\eta.$$

The double integral cannot be calculated directly but it can be envisaged that the radiating panel is split into n segments and a mean inclination angle is calculated for each segment. There is a radiative contribution from each segment so that if the radiating panel is composed of N segments then the heat received at a point (x, y) on the surface of the cylinder is approximately

$$J \approx J_1 + J_2 + \cdots + J_n + \cdots + J_N$$

where

$$J_n = \frac{2J_0}{\pi} \int_{y_{n-1}/x_\mathrm{B}}^{y_n/x_\mathrm{B}} \frac{\eta\cos\vartheta - \sin\vartheta}{(1+\eta^2)^{3/2}} \int_0^{\bar{\zeta}_n} \frac{\mathrm{d}\zeta}{(1+\zeta^2)^2}\,\mathrm{d}\eta.$$

Here y_n is the value of y at the top of the n^th radiating panel segment and y_{n-1} is the bottom. The mean inclination angle in the n^th segment may be approximated by

$$\bar{\zeta}_n \approx \frac{1}{6}\left(\frac{z_\mathrm{B}/x_\mathrm{B}}{(1+\tan^2\theta_n)^{1/2}} + \frac{4z_\mathrm{B}/x_\mathrm{B}}{(1+\tan^2((\theta_n+\theta_{n-1})/2))^{1/2}} + \frac{z_\mathrm{B}/x_\mathrm{B}}{(1+\tan^2\theta_{n-1})^{1/2}}\right)$$

where z_{B} and x_{B} are constant, and θ_{n-1} and θ_n are angles from the x-axis to the lowest and highest points on the n^{th} panel segment respectively so that $\tan\theta_{n-1} = y_{n-1}/x_{\mathrm{B}}$ and $\tan\theta_n = y_n/x_{\mathrm{B}}$. This formula is analogous to the weighted mean value of the quadratic fit of a function $f(t)$

$$f(t) = f_1 + \frac{1}{2}(f_2 - f_0)\,t + \frac{1}{2}(f_2 + f_0 - 2f_1)\,t^2$$

to the points $f(-1) = f_0$, $f(0) = f_1$, and $f(1) = f_2$ which is

$$\frac{1}{2}\int_{-1}^{1} f(t)\mathrm{d}t = \frac{1}{6}(f_0 + 4f_1 + f_2)$$

over the interval $t \in [-1, 1]$ (Simpson's rule [67]). Applying such a mean inclination angle gives the heat received from the n^{th} panel segment as

$$J_n = \frac{J_0}{\pi}\left[\frac{\eta\sin\vartheta + \cos\vartheta}{(1+\eta^2)^{1/2}}\right]_{\tan\theta_n}^{\tan\theta_{n-1}} \left[\frac{\zeta}{1+\zeta^2} + \arctan\zeta\right]_0^{\overline{\zeta}_n}.$$

Applying trigonometric identities for $\tan\alpha$ and $\cos\alpha$ for some angle α gives the power received as

$$J_n = \frac{J_0}{\pi}K_n\left[\cos(\theta_{n-1} - \vartheta) - \cos(\theta_n - \vartheta)\right]$$

with the constant

$$K_n = \frac{\overline{\zeta}_n}{1 + \overline{\zeta}_n^2} + \arctan\overline{\zeta}_n.$$

Taking into account all the possible conditions when the edges are either visible or not visible from the point on the fuel sample, the following replacements can be applied, as before,

$$\theta_{n-1} - \vartheta \to \min\{\pi, \max[0, \theta_{n-1} - \vartheta]\} \qquad \text{and} \qquad \theta_n - \vartheta \to \max\{0, \min[\pi, \theta_n - \vartheta]\}$$

so that

$$J_n = \frac{2J_0K_n}{\pi}\,\psi_n(\vartheta)$$

where

$$\psi_n(\vartheta) = \frac{1}{2}\left[\cos(\min\{\pi, \max[0, \theta_{n-1} - \vartheta]\}) - \cos(\max\{0, \min[\pi, \theta_n - \vartheta]\})\right].$$

If the fuel sample is very thin in relation to the size of the panel and its distance from the sample is sufficiently large then the angles θ_{n-1} and θ_n do not vary significantly between the different points on the surface of the fuel sample. Let us consider the case when the inclination angle is approximated using only one panel segment so that

$$J \approx J_1$$

where

$$J_1 = \frac{2J_0K_1}{\pi}\,\psi_1(\vartheta).$$

The constant K_1 is defined to be

$$\frac{\overline{\zeta}_1}{1+\overline{\zeta}_1^2} + \arctan\overline{\zeta}_1,$$

where the mean inclination angle is

$$\overline{\zeta}_1 \approx \frac{1}{6}\left(\frac{z_{\mathrm{B}}/x_{\mathrm{B}}}{\left(1+\tan^2\theta_1\right)^{1/2}} + \frac{4z_{\mathrm{B}}/x_{\mathrm{B}}}{\left(1+\tan^2\left(\left(\theta_1+\theta_0\right)/2\right)\right)^{1/2}} + \frac{z_{\mathrm{B}}/x_{\mathrm{B}}}{\left(1+\tan^2\theta_0\right)^{1/2}}\right)$$

and

$$\psi_1(\vartheta) = \frac{1}{2}\left[\cos(\min\{\pi, \max[0, \theta_0 - \vartheta]\}) - \cos(\max\{0, \min[\pi, \theta_1 - \vartheta]\})\right]$$

where $\theta_0 = \arctan(y_0/x_{\mathrm{B}})$ and $\theta_1 = \arctan(y_1/x_{\mathrm{B}})$. Here y_0 and y_1 are the values of y at the bottom and top of the radiating panel respectively and z_{B} is the half-width of the panel. The length x_{B} is the horizontal distance of the panel from the fuel sample (constant). In order to calculate the radiant heat flux the dimensions of the radiating panel (y_0, y_1, x_{B}, and z_{B}) need to be known. In most of the calculations carried out, the panel dimension is such that $y_0 = -200$ mm, $y_1 = 200$ mm, $x_{\mathrm{B}} = 100$ mm, and $z_{\mathrm{B}} = 250$ mm (this panel has similar dimensions to that of Cohen and Finney [64])[2]. It follows that $\theta_0 = \arctan(-2) \approx -63°$ and $\theta_1 = \arctan(2) \approx 63°$. The nondimensional radiant heat flux can be plotted against the angle ϑ (Figure 4.3). The two segment case will give a better approximation for the radiative power

$$J \approx J_1 + J_2$$

where

$$J_1 = \frac{2J_0K_1}{\pi}\,\psi_1(\vartheta)$$
$$J_2 = \frac{2J_0K_2}{\pi}\,\psi_2(\vartheta).$$

---

[2] The same results would arise if all of y_0, y_1, x_{B}, and z_{B} were to be increased or decreased by exactly the same factor.

The panel height spans from $y = y_0$ to $y = y_2$ with the midpoint $y_1 = (y_0 + y_2)/2$. Also

$$K_1 = \frac{\overline{\zeta}_1}{1+\overline{\zeta}_1^2} + \arctan \overline{\zeta}_1$$

$$K_2 = \frac{\overline{\zeta}_2}{1+\overline{\zeta}_2^2} + \arctan \overline{\zeta}_2$$

where

$$\overline{\zeta}_1 \approx \frac{1}{6}\left(\frac{z_{\mathrm{B}}/x_{\mathrm{B}}}{\left(1+\tan^2\theta_1\right)^{1/2}} + \frac{4z_{\mathrm{B}}/x_{\mathrm{B}}}{\left(1+\tan^2\left(\left(\theta_1+\theta_0\right)/2\right)\right)^{1/2}} + \frac{z_{\mathrm{B}}/x_{\mathrm{B}}}{\left(1+\tan^2\theta_0\right)^{1/2}}\right)$$

$$\overline{\zeta}_2 \approx \frac{1}{6}\left(\frac{z_{\mathrm{B}}/x_{\mathrm{B}}}{\left(1+\tan^2\theta_2\right)^{1/2}} + \frac{4z_{\mathrm{B}}/x_{\mathrm{B}}}{\left(1+\tan^2\left(\left(\theta_2+\theta_1\right)/2\right)\right)^{1/2}} + \frac{z_{\mathrm{B}}/x_{\mathrm{B}}}{\left(1+\tan^2\theta_1\right)^{1/2}}\right).$$

The functions

$$\psi_1(\vartheta) = \frac{1}{2}\left[\cos(\min\{\pi, \max[0, \theta_0 - \vartheta]\}) - \cos(\max\{0, \min[\pi, \theta_1 - \vartheta]\})\right]$$

$$\psi_2(\vartheta) = \frac{1}{2}\left[\cos(\min\{\pi, \max[0, \theta_1 - \vartheta]\}) - \cos(\max\{0, \min[\pi, \theta_2 - \vartheta]\})\right]$$

where

$$\theta_0 = \arctan(y_0/x_{\mathrm{B}}) \qquad \theta_1 = \arctan(y_1/x_{\mathrm{B}}) \qquad \theta_2 = \arctan(y_2/x_{\mathrm{B}}).$$

Again if the dimensions of the radiating panel and its location are known (i.e. y_0, y_2, z_{B}, and x_{B} are given) then the radiant heat flux can be plotted against ϑ. This method can be extended to any number of panel segments n.

The radiant heat flux J_n is plotted against the angle ϑ for $n = 1, 2, 4, 8$ in Figure 4.3 for a panel spanning $-200 \leq y \leq 200$ and $-250 \leq z \leq 250$, in mm, and located 100 mm away from the solid fuel ($x_{\mathrm{B}} = 100$ mm). Figure 4.3 also shows the absolute relative percentage change between J_n and J_8 as

$$100 \times \left|\frac{J_n - J_8}{\max\left(J_8\right)}\right|$$

for $n = 1, 2, 3$. Using just a single panel to approximate the inclination angle still gives good accuracy ($< 1\%$ relative difference with J_8) although a marked increase in accuracy is observed when using four panel segments to approximate the inclination angle (about 0.1% relative difference with J_8). Therefore, for the numerical simulations (Chapters 6 and 7), four panel segments will be applied when determining the radiant heat flux received by the solid sample.

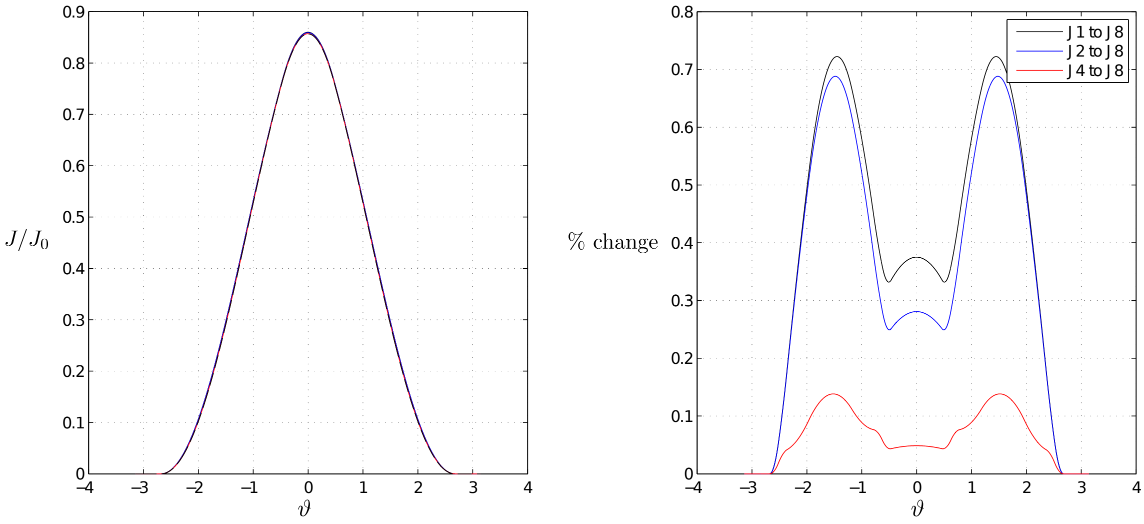

(a) (b)

Figure 4.3: (*a*) Radiant heat flux against the angle ϑ from the x-axis to the tangent at a point on the rod where the panel is split into 1, 2, 4, and 8 segments. The dimensions of the panel are $y_0 = -200$ mm, $y_n = 200$ mm, $x_{\rm B} = 100$ mm, and $z_{\rm B} = 250$ in all cases. (*b*) Absolute relative error from successive increase in panel segments.

4.3 Multiple fuel samples

The governing equations already derived will be valid for the case when multiple fuel samples are heated radiatively so that the following equations hold in the air domain

$$\rho c_p \left(\frac{\partial T}{\partial t} + \mathbf{u} \cdot \nabla T \right) = \nabla \cdot \lambda \nabla T$$

$$\rho \left(\frac{\partial \mathbf{u}}{\partial t} + \mathbf{u} \cdot \nabla \mathbf{u} \right) + \nabla P = \mathrm{Pr} \left(\nabla \cdot \left(\nabla \mathbf{u} + \nabla \mathbf{u}^{\intercal} - \tfrac{2}{3} \left(\nabla \cdot \mathbf{u} \right) \mathbb{I} \right) + \mathrm{Ra}\, \rho\, T\, \mathbf{j} \right)$$

$$\frac{\partial \rho}{\partial t} + \nabla \cdot \rho \mathbf{u} = 0$$

$$\rho = \frac{1}{1 + A_T T}$$

and in the solid domain the heat conduction equation is

$$\frac{\partial \Theta}{\partial t} = C_\kappa \nabla \cdot \lambda_s \nabla \Theta$$

Initially there is no flow and the temperature is ambient so that $\mathbf{u} = \mathbf{0}$ and $T = \Theta = 0$. At distances much further away from the fuel samples there will also be no flow and ambient temperature so that $\mathbf{u} = \mathbf{0}$ and $T = 0$. The heat flux boundary condition is

$$B_\lambda \, \lambda_s \nabla \Theta \cdot \hat{\mathbf{n}} - \lambda \nabla T \cdot \hat{\mathbf{n}} = \psi(\vartheta) + D_R \left(1 - \left(1 + A_T T \right)^4 \right).$$

However, for horizontally aligned fuel samples, it is possible that a sample will block some of the radiation from the panel from reaching another. This reduction in the heating rate can be calculated using the geometry of the fuel samples. For the present study, it will be assumed that the fuel samples are circular cylinders in order to simplify the calculation of the reduction in heating due to the shadowing effects.

4.3.1 Reduced heating due to shadowing effects

For multiple cylindrical fuel samples in arbitrary locations it is possible that one cylinder might block some of the radiation from the panel from reaching another cylinder. Any point (x, y) on a cylinder, for which the tangent angle is ϑ, needs to be considered in relation to any other cylinder $\mathcal{C}_k$ with centre (x_k, y_k) and radius a (Figure 7.1). Let the distance between the point (x, y) and the centre of $\mathcal{C}_k$ be $S(x, y)$ so that

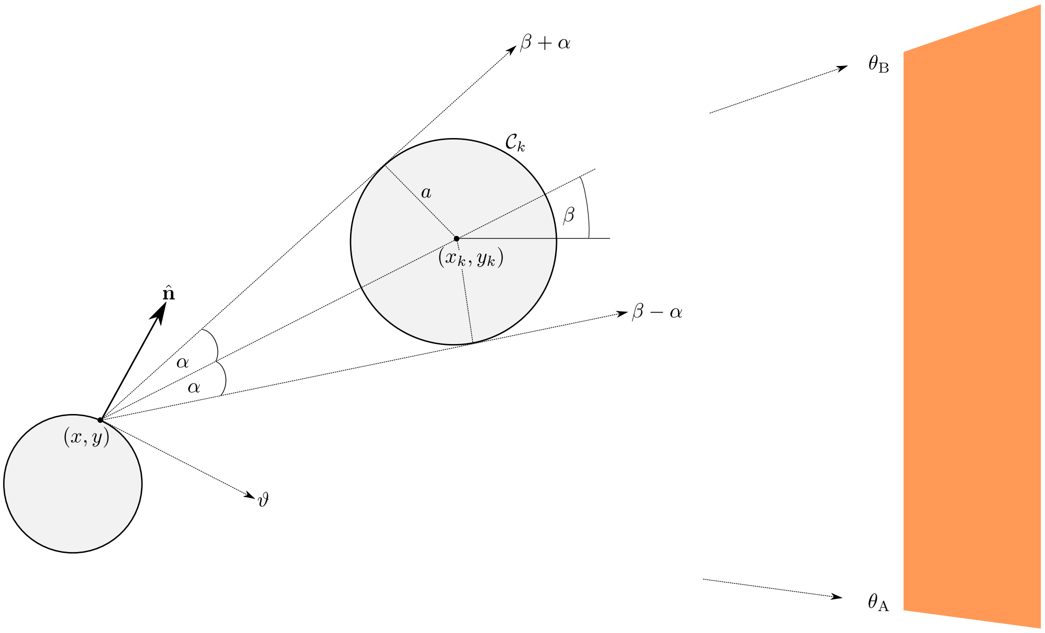

Figure 4.4: Shadowing effect for a point (x, y) on a cylinder due to the presence of cylinder $\mathcal{C}_k$ which blocks some of the radiation from the panel. Figure is not to scale as the radiating panel is assumed to be much further away than cylinder $\mathcal{C}_k$ when modelling the heat transfer.

$$S^2 = (x_k - x)^2 + (y_k - y)^2 .$$

If α is the angle subtended between the line from (x, y) to (x_k, y_k) and from (x, y) to a point on $\mathcal{C}_k$ where the line is tangential then from basic trigonometry

$$\sin \alpha = a/S.$$

The angle β between the horizontal and the line joining the centres of the cylinders satisfies

$$\tan\beta = \frac{y_k - y}{x_k - x}.$$

With θ_{A} and θ_{B} marking the angles to the lowest and highest points on the distant radiating panel respectively, the cylinder $\mathcal{C}_k$ blocks radiation from the panel between the angles

$$\gamma_{\mathrm{A}} = \min\left\{\theta_{\mathrm{B}}, \max\left[\theta_{\mathrm{A}}, \beta - \alpha\right]\right\} \quad \text{and} \quad \gamma_{\mathrm{B}} = \max\left\{\theta_{\mathrm{A}}, \min\left[\theta_{\mathrm{B}}, \beta + \alpha\right]\right\}$$

for which the angles γ_{A} and γ_{B} are equal if there is no shadowing. The shadowing may be considered as representing a panel of negative radiative intensity $-J_0$ which would cancel out the shielded part of the original radiation from the panel.

Treated as a single radiating panel, the negative radiative contribution arriving at the point (x, y) can therefore be expressed as

$$\tilde{J}_k = -J_0 \times \frac{2}{\pi}\left(\frac{\tilde{\zeta}_k}{1+\tilde{\zeta}_k} + \arctan(\tilde{\zeta}_k)\right) \times \tilde{\psi}_k(\vartheta)$$

with

$$\tilde{\zeta}_k \approx \frac{1}{6}\left(\frac{z_{\mathrm{B}}/x_{\mathrm{B}}}{\left(1+\tan^2\gamma_{\mathrm{A}}\right)^{1/2}} + \frac{4z_{\mathrm{B}}/x_{\mathrm{B}}}{\left(1+\tan^2\left(\left(\gamma_{\mathrm{A}}+\gamma_{\mathrm{B}}\right)/2\right)\right)^{1/2}} + \frac{z_{\mathrm{B}}/x_{\mathrm{B}}}{\left(1+\tan^2\gamma_{B}\right)^{1/2}}\right)$$

and

$$\tilde{\psi}_k(\vartheta) = \frac{1}{2}\left[\cos\left(\min\left\{\pi, \max\left[0, \gamma_{\mathrm{A}} - \vartheta\right]\right\}\right) - \cos\left(\max\left\{0, \min\left[\pi, \gamma_{\mathrm{B}} - \vartheta\right]\right\}\right)\right).$$

The terms γ_{A} and γ_{B}, as well as ϑ will, in general, vary for different points (x, y) on the surface of the cylinder.

If there is blocking by multiple cylinders (for, say, $k = 1, 2$, etc.) then additional contributions will arise for each corresponding value of k. However particular care must be taken not to double up the effect when one of these cylinders already partly falls within the shadow of another. It is worth exploring whether this approach of taking the blocking of radiation into account gives results significantly different to when shadowing effects are neglected. The most simple case of shadowing is when only one cylinder blocks some of the radiation from the panel from reaching another.

4.3.2 Single cylinder shadowing

Consider the case of a cylinder $\mathcal{C}$ receiving a reduced heating rate from a radiating panel due to the presence of cylinder $\mathcal{C}_1$. The cylinders, with equal nondimensional radii a, are assumed to be aligned at the same vertical height with a centre-to-centre distance of D (Figure 7.2). Recall that $l = 2a$ mm is the cylinder diameter. Let $S_D = D/l$ be the nondimensional centre-to-centre distance between the two cylinders $\mathcal{C}$ and $\mathcal{C}_1$. Varying the parameter S_D would alter the degree of radiation which is blocked by $\mathcal{C}_1$ from reaching cylinder $\mathcal{C}$ as described by the mean inclination angle $\tilde{\zeta}_1$ and the view factor $\tilde{\psi}_1(\vartheta)$. Let x_B, y_B, and z_B be the lengths, in mm, of the cylinder $\mathcal{C}$ to the radiating panel, the radiating panel half-height, and the cylinder half-width respectively. For now, let $x_\mathrm{B} = 100$ mm, $y_\mathrm{B} = 200$ mm, and $z_\mathrm{B} = 250$ mm, dimensions which are similar to the panel used in the experiments of Cohen and Finney [64]. Any panel in which all of the lengths $x_\mathrm{B}, y_\mathrm{B}$, and z_B increase by the same factor generates the same radiative field around the cylinders. The radiating panel is assumed to be composed of four segments as before but the negative contribution due to the shadowing is modelled as a single segment. This approach is favoured in order to simplify the reconciliation of the overlap between the shadowing angles and the panel angles.

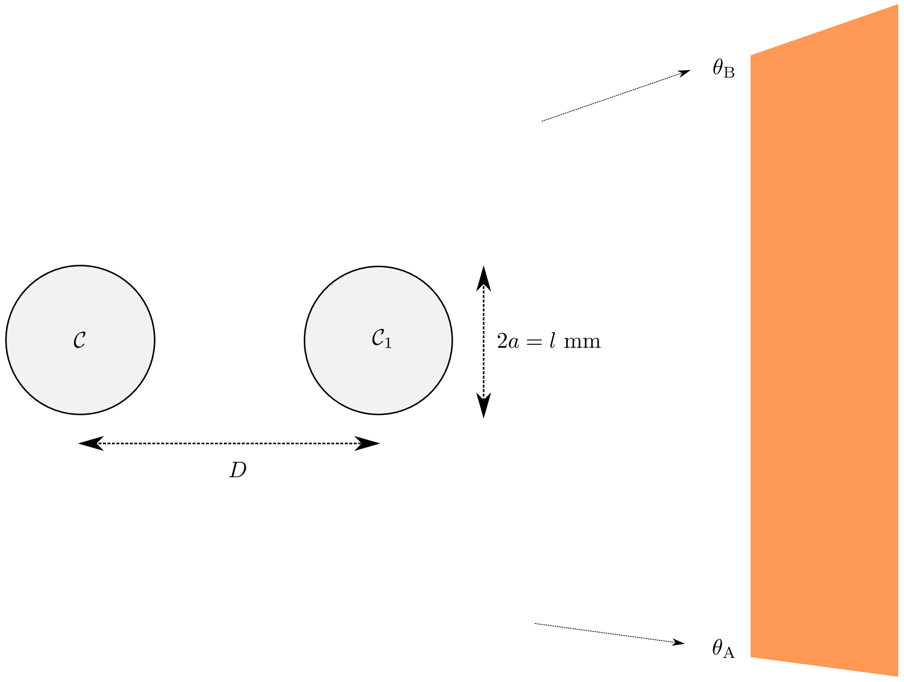

Figure 4.5: Cylinder $\mathcal{C}_1$ blocks some of the radiation from the panel from reaching cylinder $\mathcal{C}$. The centre-to-centre distance between the cylinders is D and the diameter is $2a = l$ mm.

The total radiation received at a point (x, y) on the surface of cylinder $\mathcal{C}$ is

$$J_{\text{Total}} = J + \tilde{J}_1$$

where J denotes radiation received as though cylinder $\mathcal{C}_1$ does not shadow $\mathcal{C}$ and $\tilde{J}_1$ is the negative contribution due to the presence of $\mathcal{C}_1$ which blocks some of the radiation reaching $\mathcal{C}$.

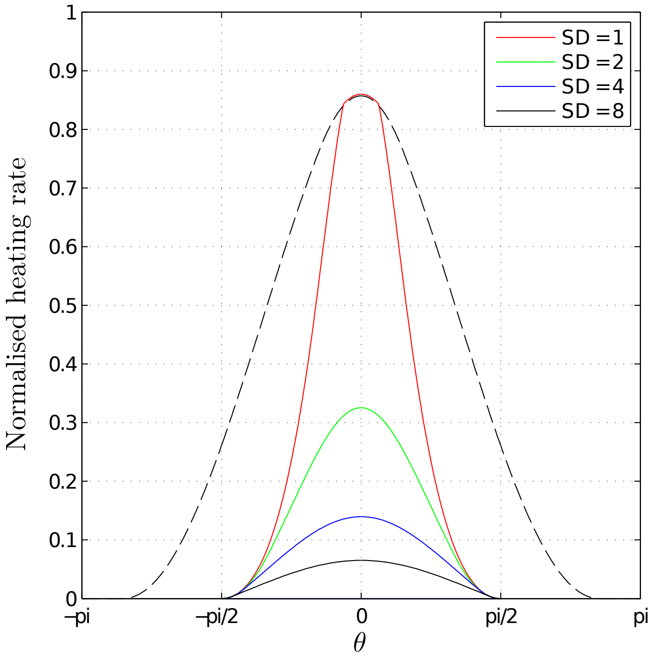

Figure 4.6: Full radiation J (*dashed line*) and negative radiation $-\tilde{J}_1$ normalised with incident heat flux J_0 kW/m^2 around cylinder $\mathcal{C}$ for various nondimensional centre-to-centre distances S_D. In polar coordinates, $r = a$ and θ varies.

Figure 4.6 is a plot of the functions J and $-\tilde{J}_1$ which shows the significance of the shadowing contribution for the nondimensional centre-to-centre distances S_D. These two functions quantify the amount of heat received and radiation blocked on the surface of cylinder $\mathcal{C}$ respectively. The surface of the cylinder can be described in polar coordinates so that $(r, \theta) = (a, \theta)$ where $\pi \leq \theta \leq \pi$ and $\theta = 0$ represents the rightmost point of cylinder $\mathcal{C}$ as shown on Figure 7.2. For large values of S_D the shadowing effects become negligible. However as $S_D \to 1$ the shadowing becomes more pronounced. Therefore shadowing effects will be taken into account as the current model assumes that the centre-to-centre distance S_D is small compared to the distance between the panel and fuel samples x_{B}. It would be realistic to take order one values for S_D.

4.3.3 Shadowing from multiple cylinders

When there are more than two cylinders being heated, it is possible that more than one cylinder will block the radiation from the panel reaching another cylinder. It is also possible that there could be an overlap in the negative radiation contribution. In this case it is important to avoid doubling up the shadowing effect.

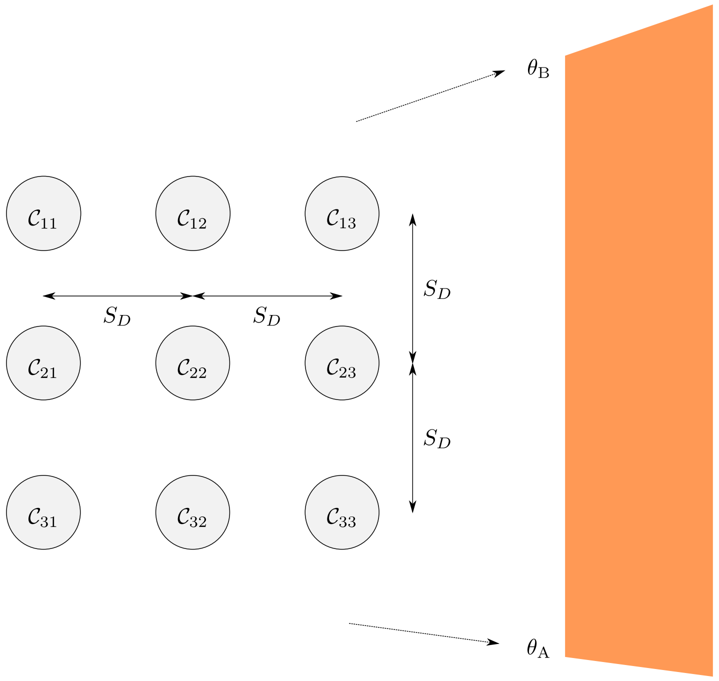

Figure 4.7: 3 × 3 square array of cylinders. The cylinders are labelled analogously to the entries of a matrix.

Consider a 3×3 regular square array of cylinders with a nondimensional centre-to-centre distance of S_D between orthogonally adjacent cylinders (Figure 7.16). The cylinders have been labelled analogously to the entries of a matrix so that cylinder $\mathcal{C}_{ij}$ is located in the i^{th} row and j^{th} column. In this scenario, there could be as many as five cylinders blocking radiation from the panel and potentially a doubling up effect when one of the cylinders already falls within the shadow of another.

Cylinders $\mathcal{C}_{i3}$, for $i = 1, 2, 3$, will receive the full radiation from the panel as there are no cylinders blocking the path from the panel to the cylinders. Cylinders $\mathcal{C}_{i2}$ will receive a reduced heating rate because of the presence of cylinders $\mathcal{C}_{i3}$ which is analogous to the 2×3 array case. However, for cylinders $\mathcal{C}_{i1}$ there will be some overlap of radiation contributions.

Again, applying $x_\mathrm{B} = 100$ mm, $y_\mathrm{B} = 200$ mm, and $z_\mathrm{B} = 250$ mm, dimensions which

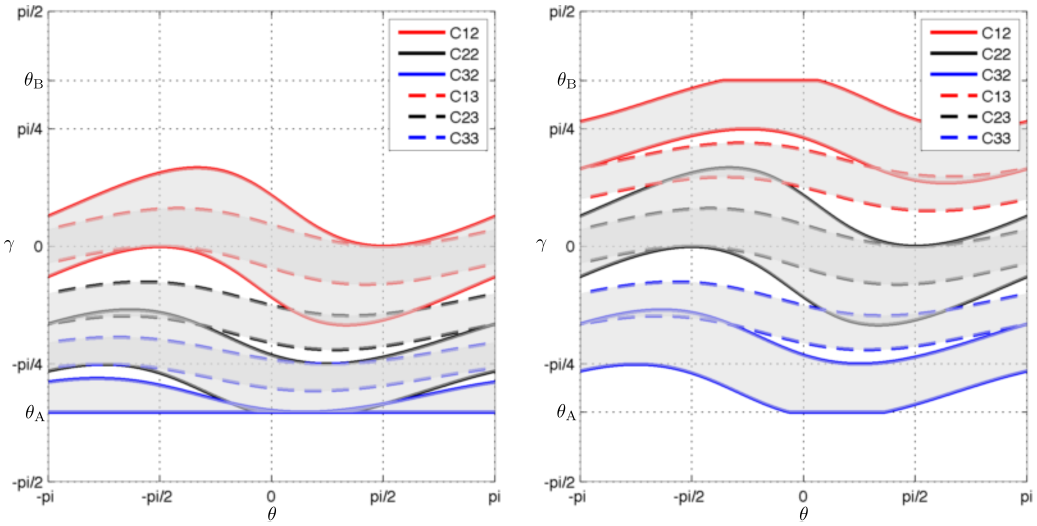

(a) $\mathcal{C}_{11}$ (b) $\mathcal{C}_{21}$

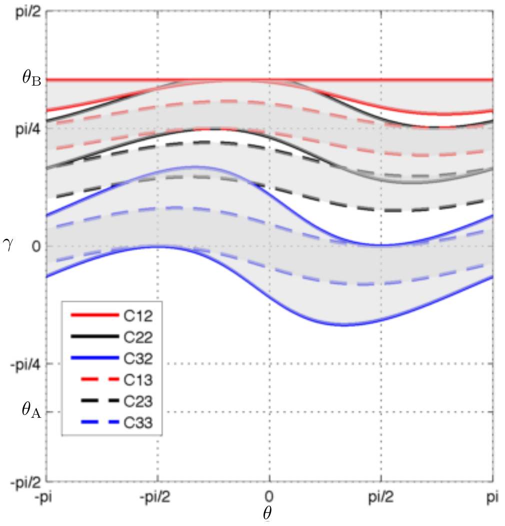

(c) $\mathcal{C}_{31}$

Figure 4.8: Shadowed regions for cylinders $\mathcal{C}_{i1}$ with $i = 1, 2, 3$ with $S_D = 2$ against the points on the cylinder surface located at an angle θ to the horizontal. The blocking contribution is from cylinders $\mathcal{C}_{1j}$, $\mathcal{C}_{2j}$, and $\mathcal{C}_{3j}$ with $j = 1, 2$ are denoted by the red, black, and blue lines respectively. Solid lines denote cylinders $\mathcal{C}_{i2}$ and dashed lines are for cylinders $\mathcal{C}_{i3}$. There is partial overlapping in the shadowing.

are similar to the panel used in the experiments of Cohen and Finney [64], the shadowed regions are shown in Figure 4.8 for cylinders $\mathcal{C}_{i1}$ and a centre-to-centre distance of $S_D = 2$. The cylinder in the final column and the same row as $\mathcal{C}_{i1}$, which happens to be cylinder $\mathcal{C}_{i3}$, will not contribute to the blocking of the radiation as cylinder $\mathcal{C}_{i2}$ will supersede it in terms of its contribution towards blocking the radiation from the panel. It would be cumbersome to calculate the heating rate around cylinders $\mathcal{C}_{i1}$ in this manner as for $S_D \leq 2$ there will be regions of overlap in the shadowing.

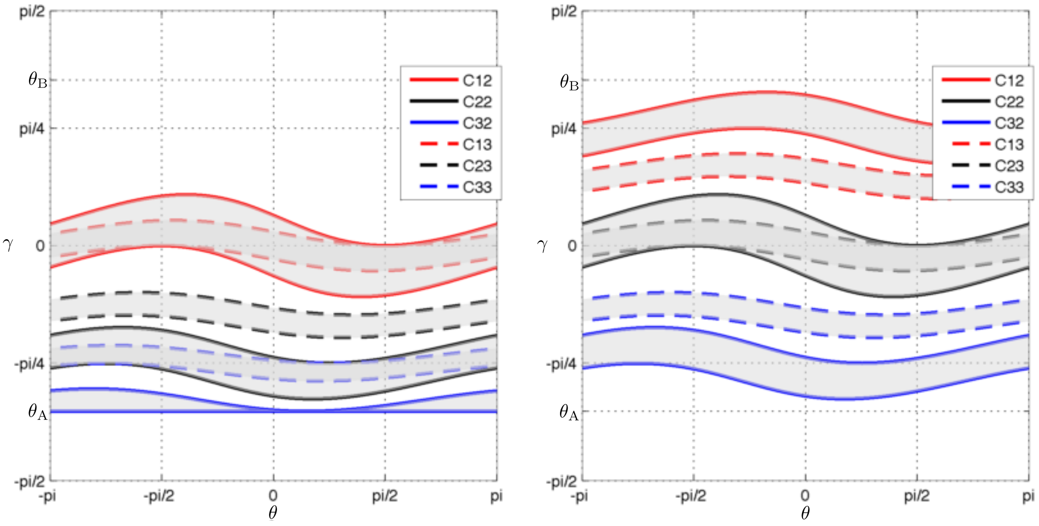

(a) $\mathcal{C}_{11}$ (b) $\mathcal{C}_{21}$

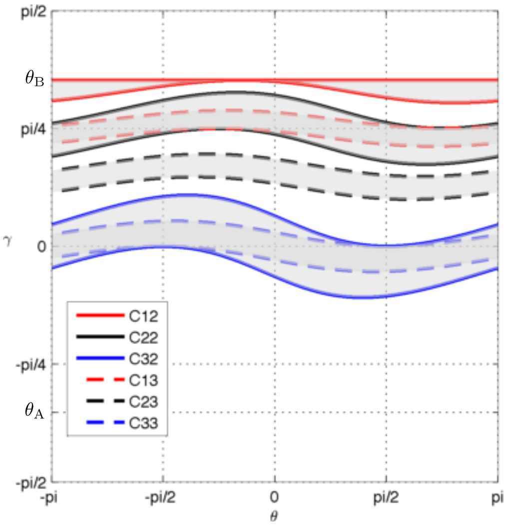

(c) $\mathcal{C}_{31}$

Figure 4.9: Shadowed regions for cylinders $\mathcal{C}_{i1}$ with $i = 1, 2, 3$ with $S_D = 3$ against the points on the cylinder surface located at an angle θ to the horizontal. The blocking contribution is from cylinders $\mathcal{C}_{1j}$, $\mathcal{C}_{2j}$, and $\mathcal{C}_{3j}$ with $j = 1, 2$ are denoted by the red, black, and blue lines respectively. Solid lines denote cylinders $\mathcal{C}_{i2}$ and dashed lines are for cylinders $\mathcal{C}_{i3}$. There is no partial overlapping in the shadowing.

Figure 4.9 shows the shadowed regions on cylinders $\mathcal{C}_{i1}$ with $i = 1, 2, 3$ but this time with $S_D = 3$. This is much easier to implement as the overlap regions are complete (there is no partial overlapping) so that it is easy to simply omit the blocking contribution of a cylinder.

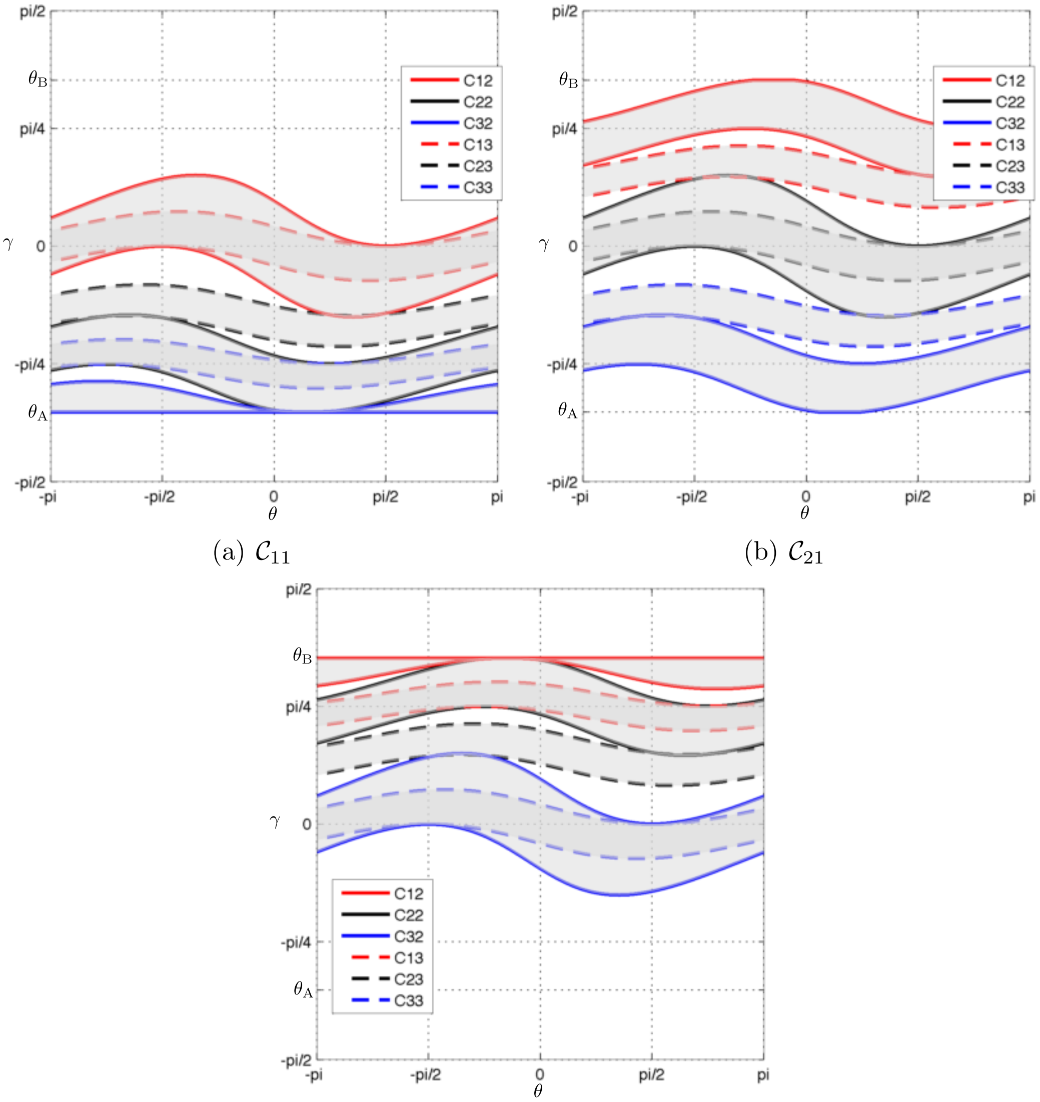

(a) $\mathcal{C}_{11}$

(b) $\mathcal{C}_{21}$

(c) $\mathcal{C}_{31}$

Figure 4.10: Shadowed regions for cylinders $\mathcal{C}_{i1}$ with $i = 1, 2, 3$ with $S_D = 2.2 \approx S_{D_c}$ against the points on the cylinder surface located at an angle θ to the horizontal. The blocking contribution is from cylinders $\mathcal{C}_{1j}$, $\mathcal{C}_{2j}$, and $\mathcal{C}_{3j}$ with $j = 1, 2$ are denoted by the red, black, and blue lines respectively. Solid lines denote cylinders $\mathcal{C}_{i2}$ and dashed lines are for cylinders $\mathcal{C}_{i3}$. There is very little partial overlapping in the shadowing.

Since partial overlapping occurs for smaller nondimensional spacings S_D, and it has been shown that partial overlapping occurs for $S_D = 2$ but not for $S_D = 3$, then it is expected that there will be a critical spacing, S_{D_c} with $2 < S_{D_c} < 3$, which is the minimum cylinder spacing for which there is no partial overlapping. This critical value of S_D for which there is no partial overlapping in the blocking has been calculated to be $S_{D\mathrm{c}} \approx 2.2$ (2 significant figures) for a 3×3 regular square array. Very little partial overlapping in the shadowing is observed with $S_D = 2.2$ (see Figure 4.10). When solving the numerical simulations for multiple fuel samples (Chapter 6) the nondimensional critical centre-to-centre distance S_{D_c} will be calculated and results will be obtained only for values of S_D greater than S_{D_c}.

4.4 Summary of natural convection model

Governing equations have been presented for the natural convection around radiatively heated fuel samples. These equations consist of the Navier-Stokes, energy balance, and ideal gas law equations in the air domain

$$\frac{\partial \rho}{\partial t} + \nabla \cdot \rho \mathbf{u} = 0$$

$$\rho \left(\frac{\partial \mathbf{u}}{\partial t} + \mathbf{u} \cdot \nabla \mathbf{u} \right) + \nabla P = \mathrm{Pr} \left(\nabla \cdot \left(\nabla \mathbf{u} + \nabla \mathbf{u}^{\intercal} - \tfrac{2}{3} \left(\nabla \cdot \mathbf{u} \right) \mathbb{I} \right) + \mathrm{Ra}\, \rho T \, \mathbf{j} \right)$$

$$\rho c_p \left(\frac{\partial T}{\partial t} + \mathbf{u} \cdot \nabla T \right) = \nabla \cdot \lambda \nabla T$$

The nondimensional ideal gas law is

$$\rho = \frac{1}{1 + A_T T}$$

and the heat conduction equation in the solid domain(s) is

$$\frac{\partial \Theta}{\partial t} = C_\kappa \nabla \cdot \lambda_s \nabla \Theta.$$

Initially there is no flow and ambient temperature in the solid and air domains. Far away from the solid fuel samples the temperature is again ambient and there is no flow. On the surface of the fuel samples there is continuity of temperature and the no slip condition holds as well as the heat flux boundary condition

$$B_\lambda \, \lambda_s \nabla \Theta \cdot \hat{\mathbf{n}} - \lambda \nabla T \cdot \hat{\mathbf{n}} = \psi(\vartheta) + D_R \left(1 - (1 + A_T T)^4 \right).$$

This condition incorporates the heat received from the radiating panel, reradiation of the heat, and the conduction into the air and solid(s). A closed analytical form of the heat received from the panel is not achieved for a finite radiating panel. Therefore, the panel is partitioned into segments where a mean inclination angle is calculated in each segment in order to approximate the heat received by a sample from the radiating panel. Using four panel segments to approximate this heating rate results in a relative difference below about 1% compared with partitioning the panel into eight segments.

Nondimensionalising the governing equations gives rise to a Prandtl number Pr, Rayleigh number Ra, heating intensity A_T, ratio of solid and air thermal conductivities B_λ, and a reradiation factor D_R. The Prandtl number for the present study will remain constant with $\text{Pr} = 0.7$ corresponding to the case when the fluid is air. Parameters Ra and A_T vary with sample size and heating rate whereas D_R only varies with a change in the heating rate. The parameter B_λ does not vary with sample size or the heating rate, and for wood-based samples it has a value of about 10.

The governing equations are valid for the heating of multiple fuel samples as well as for a single sample. However, for samples in arbitrary locations, it is possible that a sample might block some of the radiation from the panel from reaching another fuel sample. In this case, a negative radiation contribution can be calculated from the geometry of the array of circular cylinders. This negative contribution cancels out an appropriate part of the original radiation to calculate the heat received by a shadowed sample. When more than one cylinder is blocking the radiation from reaching another, it is possible that there will be a partial overlap in the shadowing contributions towards a point on the surface of a cylinder. A critical cylinder spacing S_{D_c} can be calculated which will be the minimum spacing for which there is no partial overlapping in the shadowing contributions.

In Chapters 6 and 7, these governing equations will be solved for varying sample sizes, heating rates, and, for multiple fuel samples, distances between the solids. For simplicity however, situations with partial overlapping will be avoided. Before that though, test problems for natural convection flows will be solved using COMSOL Multiphysics in order to verify the accuracy of the finite element software (Chapter 5). These test problems will include the natural convection around an isothermal cylinder study [57] and the uniform heating case [58]. Results obtained from COMSOL Multiphysics are compared with the literature.

Chapter 5

Natural convection test problems

Natural convection test problems are solved using COMSOL Multiphysics. In section 5.2, numerical results are verified by comparing the available results from literature for constant temperature (isothermal) [57] and uniform heat flux [58] boundary conditions for the natural convection around a circular cylinder. A test problem for the case when solid conduction is incorporated with the natural convection flow [68] is also solved using COMSOL. In the first test case, the natural convection around an isothermal horizontal circular cylinder in an infinite domain is explored and the results are compared with the benchmark solutions obtained by Saitoh et al. [59]. The second test problem is the same as the first except that the cylinder is not isothermal but is subjected to a constant heat flux. This problem is more relevant to the present study as the cylinder is subjected to a radiant heat flux from a panel. However, the heat received from the panel is non-uniform (Chapter 4). Heat transfer rates for the uniform heating problem will be compared with [58]. Finally the third test problem explores the case of a conducting cylinder where it is assumed that the cylinder is in an enclosure. This problem was studied by House et al. [68] and it is a useful problem in that it will test the continuity conditions in the solid phase (cylinder) with the fluid phase.

In section 5.3, natural convection test problem involving multiple bodies are solved, again using COMSOL Multiphysics. The first test problem deals with two vertically aligned isothermal cylinders [69]. Numerical results for more than two vertically aligned cylinders are also presented [70]. Finally, numerical results for horizontally aligned isothermal cylinders are presented [71].

In section 5.1, the nondimensional Nusselt number [72] is introduced. This number can be calculated at the end of a simulation and compared with the literature to test the accuracy of the numerical solution. Once heat transfer rates are shown to be in good agreement with the test problems then solving the problem of natural convection around a conducting cylinder subjected to radiant heating can be undertaken in confidence. All the test problems in this section use a steady state analysis and apply the Boussinesq approximation [15, 21].

5.1 Nusselt number

In natural convection problems, information for the heat transfer characteristics is usually presented using the Nusselt number Nu [72]. This nondimensional number is the ratio of convective and conductive heat transfer across a boundary. For small value of Nu (i.e. $\mathrm{Nu} \sim \mathcal{O}(10^0)$) the flow is laminar with turbulence usually associated with $\mathrm{Nu} \sim \mathcal{O}(10^2)$. It is common to compare local and average Nusselt number values when solving natural convection test problems [59].

The local Nusselt number is defined to be the ratio of the convective heat transfer to the conductive heat transfer at a point on a boundary. This can be written as

$$\mathrm{Nu} = \frac{hl}{\lambda_0}$$

with l and λ_0 the characteristic length scale and thermal conductivity of the fluid respectively. The SI units are [m] for l and [W/(m K)] for λ_0. The convective heat transfer coefficient h [W/(m^2 K)] is defined to be

$$h = \frac{Q}{A(T - T_0)}$$

with heat flow Q [W], heat transfer surface area A [m^2], fluid temperature T [K] and ambient fluid temperature T_0 [K]. The heat flow per unit area on a heated surface will be $Q/A = -\lambda_0 \nabla T \cdot \hat{\mathbf{n}}$ (the minus sign is due to the convention that the normal vector is pointing outwards from the body) or, an average value of this quantity so that the heat transfer coefficient on the isothermal boundary is

$$h = -\frac{\lambda_0 \nabla T \cdot \hat{\mathbf{n}}}{T - T_0}.$$

Nondimensionalising with $T = T_0 + (T_c - T_0)\bar{T}$, where T_c is a characteristic temperature and defining $\nabla = \bar{\nabla}/l$, reduces the Nusselt number to

$$\begin{aligned}\mathrm{Nu} &= -\frac{\lambda_0}{l}\frac{(T_c - T_0)\overline{\nabla}\,\overline{T}\cdot\hat{\mathbf{n}}}{(T_c - T_0)\overline{T}}\frac{l}{\lambda_0} \\ &= -\frac{\overline{\nabla}\,\overline{T}\cdot\hat{\mathbf{n}}}{\overline{T}}.\end{aligned}$$

Finally, by dropping the bar notation, the nondimensional local Nusselt number on the surface of a heated body is

$$\mathrm{Nu} = -\frac{\nabla T\cdot\hat{\mathbf{n}}}{T}.$$

For an isothermal body, the temperature is constant. Therefore, without loss of generality, the temperature can be taken as $T = 1$. Then, the local Nusselt number on the surface of an isothermal body is

$$\mathrm{Nu}_T = -\nabla T\cdot\hat{\mathbf{n}}$$

which can provide a local value at any point on the surface. Averaging over the surface produces the averaged Nusselt number $\overline{\mathrm{Nu}}_T$.

For a uniform heat flux boundary, the gradient of temperature will be constant. Again, without loss of generality, this gradient can be taken as $-\nabla T\cdot\hat{\mathbf{n}} = 1$. The local Nusselt number on the surface of a uniformly heated boundary is

$$\mathrm{Nu}_J = \frac{1}{T}$$

which again can be averaged over the surface to give the averaged Nusselt number $\overline{\mathrm{Nu}}_J$.

Finally, recall that the heat flux boundary condition in Chapter 4 was

$$B_\lambda\,\lambda_s\nabla\Theta\cdot\hat{\mathbf{n}} - \lambda\nabla T\cdot\hat{\mathbf{n}} = \psi(\vartheta) + D_R\left(1 - (1 + A_T T)^4\right).$$

Rearranging this equation gives the local Nusselt number on the surface of the cylinder as

$$\begin{aligned}\mathrm{Nu}_\psi &= -\frac{\nabla T\cdot\hat{\mathbf{n}}}{T} \\ &= \frac{\psi(\vartheta) + D_R\left(1 - (1 + A_T T)^4\right) - B_\lambda\,\lambda_s\nabla\Theta\cdot\hat{\mathbf{n}}}{\lambda T}\end{aligned}$$

for which averaging can also be performed to give $\overline{\mathrm{Nu}}_\psi$.

Relevant Nusselt numbers will be used to analyse the natural convection flow. In the present chapter, the local Nusselt number on the boundary will be Nu_T for isothermal bodies and Nu_J for uniform heat flux on the surface. In Chapter 6, the governing equation presented in Chapter 4 will be solved and the Nusselt number Nu_ψ will be used to analyse the flow properties.

5.2 Single fuel sample

In this section, three test problems for the natural convection around a single cylinder are solved numerically, using COMSOL Multiphysics. These test problems are for the natural convection flow around (1) an isothermal horizontal cylinder (2) Uniformly heated (constant heat flux) horizontal cylinder and (3) a conducting square cylinder in an enclosure.

The first two test problems will test the the accuracy of COMSOL Multiphysics against the works of Kuehn and Goldstein [57] and Wang et al. [58] respectively. These two problems assume the Boussinesq approximation. This approximation, combined with the relatively simple heating boundary conditions, means that there are only two nondimensional parameters; Prandtl number (Pr) and Rayleigh number (Ra). The fluid medium is assumed to be air so that the Prandtl number remains as the constant $\mathrm{Pr} = 0.7$. Therefore, the only parameter in the problem is the Rayleigh number. This parameter is defined slightly differently in the two test problems due to the contrasting heating boundary conditions. For the isothermal cylinder, the temperature of the body is known and the Rayleigh number can be defined as [57]

$$\mathrm{Ra}_T = \frac{g\beta l^3 \left(T_{\mathrm{B}} - T_0\right)}{\nu_0 \kappa_0}$$

where l is the cylinder diameter, T_{B} is the temperature of the body, and β is the thermal coefficient of volumetric expansion ($\beta = 1/T_0$). The subscript for the Rayleigh number is to highlight that this definition is for the constant temperature cylinder. For a uniformly heated cylinder, the Rayleigh number is defined as [58]

$$\mathrm{Ra}_J = \frac{g\beta l^4 J_{\mathrm{B}}}{\nu_0 \lambda_0 \kappa_0}$$

where J_{B} is the constant heating rate received on the surface of the cylinder. This version of Ra is referred to as the modified Rayleigh number [58]. The subscript for the Rayleigh number is to highlight that this definition is for the constant heating rate problem. Numerical results are obtained for a range of Rayleigh numbers.

Solid conduction is not modelled in either of these natural convection problems. This is the reason why the test problem explored by House et al. [68] is also solved. The natural convection problem is quite different to the previous two. The geometry of the body is a square cylinder. The fluid domain is still air so that Prandtl number still remains constant. However, rather than the body being placed in an infinite medium, it is now centred in an enclosure. The body receives heat from a hot enclosure wall. The ratio of solid and air thermal conductivities B_λ is an additional parameter (Rayleigh number being the other) of the model which arises due to the solid conduction in the cylinder.

These three test problems are solved using COMSOL Multiphysics for variations in the Rayleigh number and results are compared with the literature.

5.2.1 Natural convection flow around an isothermal horizontal cylinder

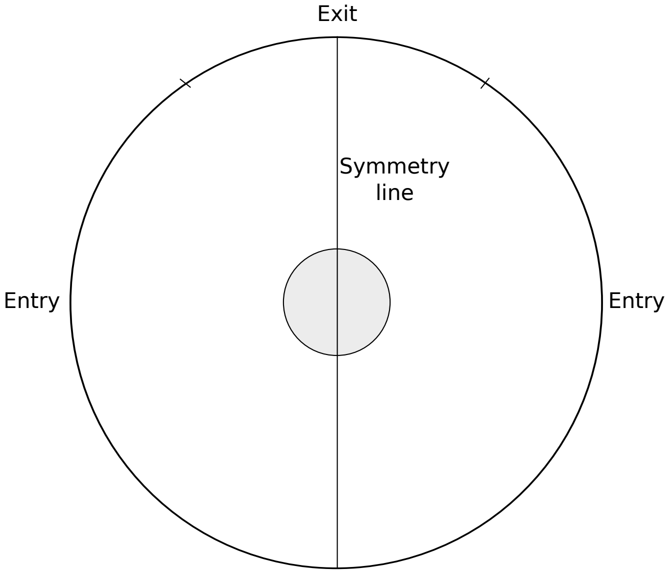

Figure 5.1: Schematic of natural convection around an isothermal cylinder. The problem is symmetric about the vertical y-axis. Outer boundary conditions are dealt in two parts; flow coming into the domain (entry) and flow leaving the domain (exit). The change from entry/exit is located at the points $(r, \theta) = (D/2, \pm\pi/6)$.

The first test problem to verify the validity of COMSOL Multiphysics is modelling the natural convection around an isothermal horizontal cylinder in an infinite domain (Figure 5.1). Kuehn and Goldstein [57] numerically solve the Navier-Stokes equations coupled with the energy equation (using the Boussinesq approximation) for a wide range of Rayleigh numbers for which they found good agreement with experimental results. Saitoh et al. [59] presented benchmark solutions to this problem which were compared with Wang et al. [58] as well as Kuehn and Goldstein [57]. The aim is to reproduce the results obtained in Saitoh et al. [59] using COMSOL in order to validate the solvers capabilities in solving natural convection problems.

The natural convection flow around an isothermal cylinder is symmetric about the vertical y-axis. The infinite air domain is dealt with using the inflow/outflow boundary conditions. The change from flow entry to exit is located at the points $(r, \theta) = (D/2, \pm\pi/6)$, where D is the diameter of the domain [57].

Assuming that the flow is steady and flow properties are constant then using the Boussinesq approximation the nondimensional governing equations reduce to

$$\nabla \cdot \mathbf{u} = 0 \tag{5.1}$$

$$\mathbf{u} \cdot \nabla \mathbf{u} + \nabla P = \mathrm{Pr}\, \nabla^2 \mathbf{u} + \mathrm{Pr}\, \mathrm{Ra}\, T\, \mathbf{j} \tag{5.2}$$

$$\mathbf{u} \cdot \nabla T = \nabla^2 T \tag{5.3}$$

where the Rayleigh number Ra is a parameter of the problem and $\mathrm{Pr} = 0.7$ corresponds to the Prandtl number of air. The cylinder has diameter l and the domain has diameter D. There is no solid conduction equation as the circular cylinder is assumed to be isothermal. The boundary conditions on the solid boundary are the no slip and constant temperature conditions

$$\mathbf{u} = 0, \qquad T = 1, \qquad \text{at } \partial\Omega_{\text{Solid}}$$

where $\Omega = \Omega_{\text{Air}} + \Omega_{\text{Solid}}$ is the whole computation domain and ∂ denotes the boundary of the domain. In order to model the infinite air domain in COMSOL Multiphysics, a fictitious outer boundary concentric to the circular cylinder is assumed. A similar approach to Ma et al. [73] is used for the outer boundary where it is treated in two parts. A part where the fluid (air) enters the domain and a part which allows the flow to exit. It is assumed that the tangential velocity on the outer boundary is zero since the fluid is either coming in (entry) to the domain or going out (exit) (Figure 5.1). In other words, the flow is normal to the outer boundary. The boundary conditions for the entry and exit are

$$\mathbf{u}\cdot\mathbf{t}=0 \qquad T=0 \qquad \boldsymbol{\tau}\cdot\mathbf{n}=\mathbf{0}$$

$$\mathbf{u}\cdot\mathbf{t}=0 \qquad \nabla T\cdot\mathbf{n}=0 \qquad \boldsymbol{\tau}\cdot\mathbf{n}=\mathbf{0}$$

respectively on $\partial\Omega_{\mathrm{Air}}$. Here $\mathbf{t}$ and $\boldsymbol{\tau}$ are the tangent vector and stress tensor respectively. The normal stress is zero because the outer boundary is interpreted to be a fluid-fluid boundary with no change of fluid properties. Fluid at ambient temperature enters the domain so that $T = 0$ at the entry. The temperature of the fluid leaving the domain is unknown, however it can be imposed that the change in the temperature of the fluid arriving at the exit and the temperature at the exit is zero so that $\nabla T \cdot \mathbf{n} = 0$.

Solutions to the governing equations (Equations 5.1–5.2) have been obtained for the range $0.37 \leq \mathrm{Ra} \leq 10^5$ using COMSOL Multiphysics. The outer boundary is assumed to be 40 times the solid cylinder diameter so that $D = 40l$. Rayleigh number Ra is the parameter in the problem which is defined to be $\mathrm{Ra} = g\beta l^3 \left(T_c - T_0\right)/\kappa\nu$.

Figure 5.2 shows the isotherms and streamlines around the circular horizontal cylinder for Rayleigh numbers $\mathrm{Ra} = [0.37, 10, 10^3, 10^5]$. At $\mathrm{Ra} = 0.37$ (as studied numerically and experimentally by Fujii et al. [74]) and $\mathrm{Ra} = 10$ the flow is upward with heat being convected away from the cylinder and upwards into the plume. At large Rayleigh numbers ($\mathrm{Ra} = 10^3$ and $\mathrm{Ra} = 10^5$) a boundary layer forms around the cylinder, the thickness of which decreases as the Rayleigh number is increased.

Table 5.1: Local and average Nusselt numbers for isothermal circular cylinder compared with the benchmark results of Saitoh et al. [59].

Ra		$\theta = 0°$	90°	180°	$\overline{\mathrm{Nu}}$
10^3	Present	3.782	3.363	1.217	3.011
	Saitoh et al. [59]	3.813	3.374	1.218	3.024
10^4	Present	5.960	5.389	1.533	4.809
	Saitoh et al. [59]	5.995	5.410	1.534	4.826
10^5	Present	9.752	8.813	1.984	7.939
	Saitoh et al. [59]	9.675	8.765	1.987	7.898

Table 5.1 shows the local and averaged Nusselt numbers from the present method compared to the benchmark solutions of Saitoh et al. [59]. The local Nusselt number is

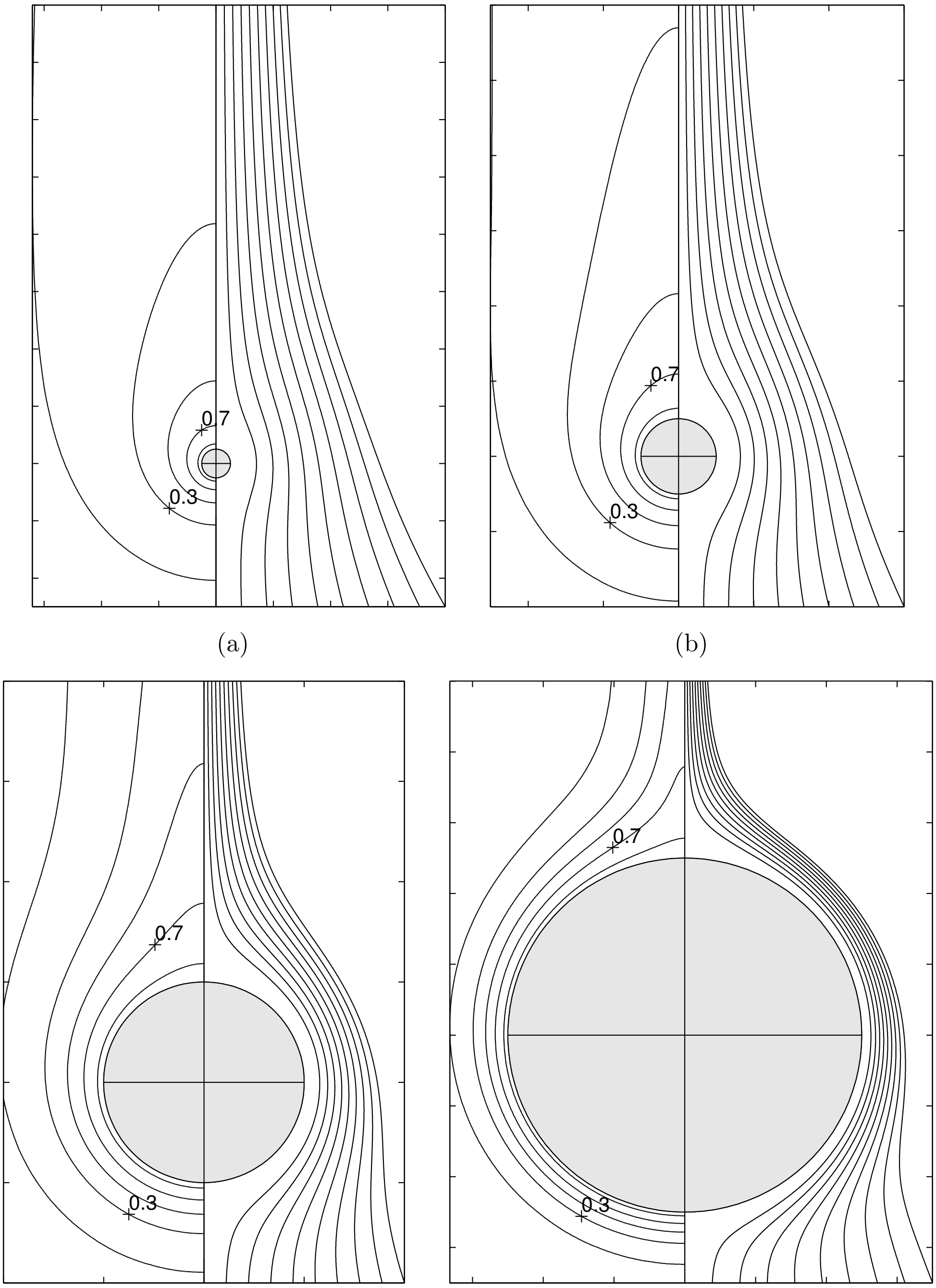

(a) (b)

(c) (d)

Figure 5.2: Isotherms (*left*) and streamlines (*right*) for (a) Ra = 0.37, (b) Ra = 10, (c) Ra = 10^3, and (d) Ra = 10^5. The Prandtl number remains constant (Pr = 0.7).

the ratio of the convective heat transfer to the conductive heat transfer at a point on the boundary. The average Nusselt number is simply the integral of the local Nusselt numbers on a boundary divided by the length of the boundary. In the case of the isothermal cylinder the local and average Nusselt numbers on the cylinder boundary are

$$\mathrm{Nu} = -\nabla T \cdot \mathbf{n}$$
$$\overline{\mathrm{Nu}} = \frac{1}{\pi d} \oint \mathrm{Nu}\, \mathrm{d}S$$

where S is measured around the surface of the cylinder. The calculated local and average Nusselt numbers (Table 5.1) are in good agreement with those of Saitoh et al. [59] as the maximum relative error is below 1%.

5.2.2 Uniform heat flux and the importance of modelling the solid conduction

Consider again the natural convection problem but this time the circular cylinder is taken to inject a constant heat flux J_0 W/m^2. Solid conduction is not included in the model so that the nondimensional heat flux boundary condition is

$$\nabla T \cdot \mathbf{n} = 1 \qquad \text{on } \partial\Omega_{\text{Solid}}$$

is the nondimensional boundary condition on the surface of the solid horizontal cylinder. The governing equations are the same as the isothermal cylinder test problem (Equations 5.1–5.3) with Prandtl number Pr = 0.7 and the modified Rayleigh number

$$\mathrm{Ra}^* = \frac{g\beta J_0 l^4}{\nu_0 \lambda_0 \kappa_0}$$

is a parameter of the problem. Recall that the Rayleigh number was defined to be

$$\mathrm{Ra} = \frac{g l^3}{\nu\kappa} \frac{T_c - T_0}{T_0}$$

in the isothermal cylinder problem [57]. Taking the characteristic temperature to be

$$T_c = \frac{l J_0}{\lambda_0} + T_0$$

gives the modified Rayleigh number as above. Solid conduction is not modelled.

This case is explored by Wang et al. [58] (as well as the isothermal cylinder case) for $\mathrm{Ra}^* = [10^6, 10^7, 10^8]$.

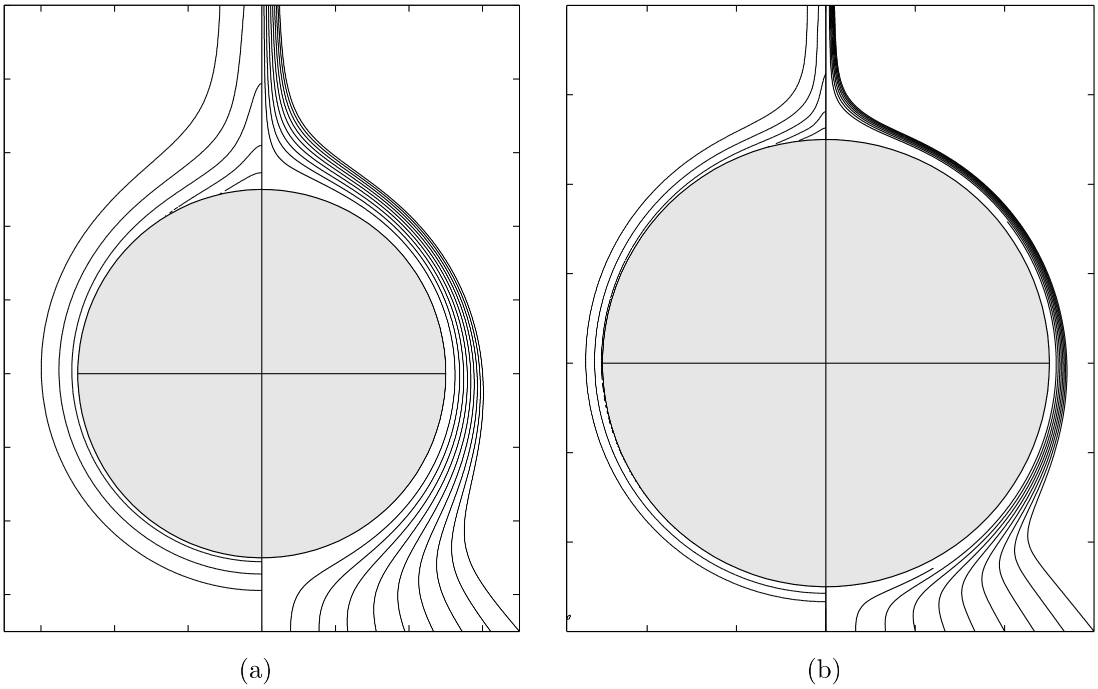
(a) (b)

Figure 5.3: Isotherms (*left*) and streamlines (*right*) for (a) $\mathrm{Ra}^* = 10^6$ and (b) $\mathrm{Ra}^* = 10^8$. The Prandtl number remains constant ($\mathrm{Pr} = 0.7$).

Streamlines and isotherms for $\mathrm{Ra}^* = 10^6$ and $\mathrm{Ra}^* = 10^8$ are plotted in Figure 5.3. As with the case of the isothermal cylinder the boundary layer thickness reduces as the modified Rayleigh number Ra^* is increased.

The local nusselt number on a point on the solid body is defined to be [72, 75]

$$\mathrm{Nu} = \frac{hl}{\lambda_0}$$

where, rather than using the earlier arguments, the local heat transfer coefficient on the solid surface is

$$h = \frac{J_0}{T - T_0},$$

and since all the quantities are dimensional and taking the characteristic temperature as

$$T_c = \frac{lJ_0}{\lambda_0} + T_0$$

the Nusselt number reduces to

$$\mathrm{Nu} = \frac{1}{\overline{T}}$$

which is the same as the earlier formula for $\overline{\mathrm{Nu}}_J$.

Local and average Nusselt numbers are listed in Table 5.2. It should be noted that the results presented in Wang et al. [58] are not benchmark results. Having

Table 5.2: Local and average Nusselt numbers.

Ra^*		$\theta = 0°$	90°	180°	$\overline{\mathrm{Nu}}$
10^6	Present	9.72	9.24	5.28	8.80
	Wang et al. [58]	9.87	9.24	5.02	8.88
10^7	Present	14.90	14.15	7.61	13.53
	Wang et al. [58]	15.02	14.04	7.23	13.56
10^8	Present	23.12	21.90	10.98	20.99
	Wang et al. [58]	23.12	21.92	10.87	21.00

said that their results for the isothermal cylinder were in good agreement with Saitoh et al. [59] so it should be expected that the uniform heat flux results are reasonable. The streamlines, isotherms, and local and average Nusselt number results are in good agreement with Wang et al. [58] .

Consider the case when solid conduction is taken into account as well as the natural convection around the conducting body. The equation for solid conduction

$$\nabla^2\Theta = 0$$

must be solved in addition to the Boussinesq equations for the air. The boundary condition on $\partial\Omega_{\mathrm{Solid}}$ is of constant heating rate and continuity of temperature

$$B_\lambda \nabla\Theta \cdot \mathbf{n} - \nabla T \cdot \mathbf{n} = 1$$

$$T = \Theta.$$

The ratio of thermal conductivities is taken to be $B_\lambda = 10$. This value is typical of wood-based fuel samples.

Figure 5.4 shows the surface temperature around the cylinder for the case when solid conduction is taken into account compared with the no solid conduction model. The angles $\theta = 0°$ and $\theta = 180°$ represent the bottom and the top of the cylinder respectively. Prandtl number $\mathrm{Pr} = 0.7$ and Rayleigh number $\mathrm{Ra} = 10^6$. The maximum solid temperature (at $\theta = 180°$) drops by about 25% when the solid conduction is modelled.

Table 5.3 shows the change in the Nusselt number and shear stress when solid

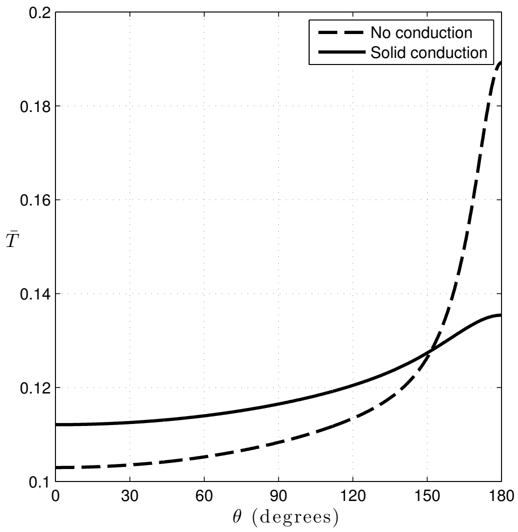

Figure 5.4: Surface temperature of the cylinder from $\theta = 0$ (bottom) to $\theta = 180°$ (top). The temperature range is significantly wider when heat conduction into the cylinder is not modelled for $\mathrm{Ra} = 10^6$ and $\mathrm{Pr} = 0.7$.

conduction is modelled. The stress tensor can be written in index notation [76] as

$$\tau_{ij} = \frac{\partial u_i}{\partial x_j} + \frac{\partial u_j}{\partial x_i} - \frac{2}{3}\frac{\partial u_k}{\partial x_k}\delta_{ij}$$

where δ_{ij} is the Kronecker delta

$$\delta_{ij} = \begin{cases} 0, & \text{if } i \neq j \\ 1, & \text{if } i = j \end{cases}$$

and the summation convention is used. Hence the nondimensional shear stress is

$$\tau_{xy} = \frac{\partial u}{\partial y} + \frac{\partial v}{\partial x}$$

so that the average shear stress around the conducting cylinder is

$$\overline{\tau}_{xy} = \frac{1}{2\pi}\int_0^{2\pi} \left|\frac{\partial u}{\partial y}\right| + \left|\frac{\partial v}{\partial x}\right|, \mathrm{d}\vartheta.$$

There is a decrease in the Nusselt number and an increase in the shear stress when the solid conduction is modelled with the largest changes occurring for large Ra. Modelling the solid conduction then affect the thermal and flow properties of natural convection, particularly for large bodies and/or strong heating rates.

5.2.3 Conducting square cylinder in an enclosure

The importance of modelling the conduction process was highlighted in the previous subsection. However, it is worth testing the solid conduction model here as well.

Table 5.3: Averaged Nusselt numbers and averaged shear stresses around the cylinder surface for Prandtl number Pr = 0.7 and Rayleigh number Ra = 10^6. Subscript c denotes values when solid conduction modelled with $B_\lambda = 10$. The average Nusselt number percentage decrease and averaged shear stress percentage increase when solid conduction is also shown.

Ra*	$\overline{\mathrm{Nu}}$	$\overline{\mathrm{Nu}}_c$	% decrease	$\overline{\tau}$	$\overline{\tau}_c$	% increase
10^{-1}	0.745	0.740	0.7	0.662	0.665	0.5
10^{0}	0.972	0.956	1.7	1.990	2.014	1.2
10^{1}	1.322	1.279	3.4	6.293	6.437	2.2
10^{2}	1.859	1.772	4.9	20.94	21.65	3.3
10^{3}	2.674	2.530	5.6	72.89	75.87	3.3
10^{4}	3.915	3.706	5.6	263.2	274.6	4.1
10^{5}	5.835	5.550	5.1	978.2	1019	4.0

House et al. [68] explore the case of the heating of a square cylinder in a finite domain (enclosure). Nevertheless, since the heat transfer rates for natural convection in an infinite domain have been verified, the problem in an enclosure can be solved to make sure that the solid conduction coupled with natural convection gives the expected results.

The governing equations in the air domain are the same as mentioned in the isothermal and uniform heating cases (Equations 5.1–5.3). The Prandtl number is slightly different (Pr = 0.71) [68] but is still representative of air. The Rayleigh number Ra is, again, a parameter of the problem but the geometry and the boundary condition are fundamentally different.

Figure 5.5 shows the new geometry and enclosure boundary conditions. The top and bottom boundaries of the enclosure are adiabatic so that $\nabla T \cdot \mathbf{n} = 0$ there. The hot and cold sides of the enclosure have $T = 1$ and $T = 0$ nondimensional temperature conditions respectively. The governing equations in the air domain are the same as those used for the isothermal and uniformly heated cylinder case but now the solid conduction is also modelled. The nondimensional energy equation in the solid body is

$$\nabla \cdot B_\lambda \nabla \theta = 0$$

where θ is the temperature in the solid domain and B_λ is the ratio of the thermal conductivity of the solid body to the air. House et al. [68] explore a variety of values for B_λ which represents a change of material of the solid body (the Prandtl number remains

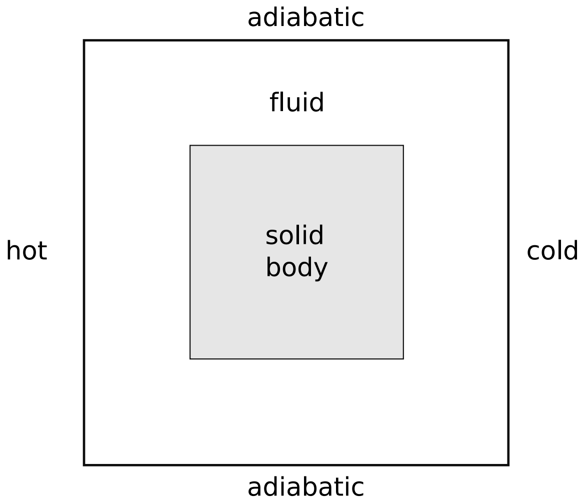

Figure 5.5: Geometry and boundary conditions for the conducting solid body in an enclosure House et al. [68].

constant at Pr = 0.71 so that the fluid is always air). Continuity of temperature and conservation of energy-flux boundary conditions are applicable on the solid boundary so that

$$T = \theta$$

and

$$\nabla T \cdot \mathbf{n} = B_\lambda \nabla \theta \cdot \mathbf{n}.$$

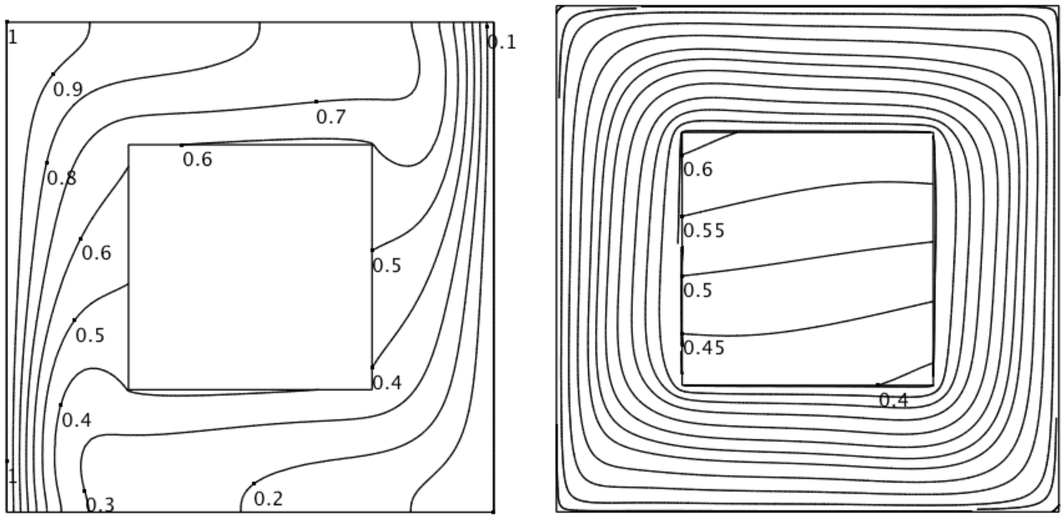

(a) (b)

Figure 5.6: Isotherms and streamlines for the solid body in an enclosure. Rayleigh number is $\mathrm{Ra} = 10^5$ and $B_\lambda = 5$.

Figure 5.6 shows the isotherms for solid and air temperature, and the streamlines for Ra $= 10^5$ and $B_\lambda = 5$. The enclosure width is twice the width of the square body. These plots are in good agreement with House et al. [68].

Table 5.4: Average Nusselt number comparison for Ra $= 10^5$ and various B_λ.

B_λ		$\overline{\mathrm{Nu}}$
0.2	Present	4.6231
	House et al. [68]	4.6257
1	Present	4.5032
	House et al. [68]	4.5061
5	Present	4.3185
	House et al. [68]	4.3221

Table 5.4 shows the comparison in the average nusselt number

$$\overline{\mathrm{Nu}} = -\int_0^1 \frac{\partial\theta}{\partial x}\,\mathrm{d}y$$

on the hot enclosure boundary. The values of $\overline{\mathrm{Nu}}$ calculated in the present study are in very good agreement with House et al. [68] with a maximum relative error of less than 0.1%.

Now that the test problems of isothermal cylinder, uniform heating rate, and solid body conduction have been verified using COMSOL Multiphysics, the problem of the natural convection around a conducting cylinder subjected to a non-uniform radiative heating rate can be studied numerically (Chapter 6). Before that though, test problems for multiple bodies will also be solved and compared to the relevant literature.

5.3 Multiple fuel samples

Test problems for the natural convection flow around multiple bodies are solved in this section. Temperature and velocity fields, with average Nusselt number values, will be compared with the relevant literature.

Experimental [77, 78] and numerical [69, 79–81] studies for the natural convection around two vertically aligned cylinders has been undertaken in recent years. Chouikh et al. [80] and Cianfrini et al. [69] study the natural convection around two vertically aligned isothermal cylinders. The natural convection heat transfer on the upstream cylinder will be affected by the downstream cylinder. This vertically aligned cylinders configuration approach can be extended. Corcione [70] presented numerical results for the natural convection flow around a vertical array of up to six cylinders. When solving the problem presented in Chapter 4, vertically aligned cylinders will present little shadowing contributions. It is the horizontal alignment of cylinders which results in a significant amount of radiative heat being blocked.

Numerical solutions to the natural convection around horizontally aligned cylinders has been solved in the literature. Cianfrini et al. [71] study the flow around two[1] isothermal cylinders set side-by-side (horizontal alignment).

These test problems for the natural convection around multiple cylinders will be solved numerically using COMSOL Multiphysics.

5.3.1 Two parallel cylinders vertically aligned

The natural convection flow around two vertically aligned parallel cylinders is explored. Numerical results are presented for isothermal cylinders so that temperature fields, velocity fields, and Nusselt numbers can be compared with numerical and experimental results in the literature.

The case of vertically aligned isothermal cylinders has been studied both experimentally and numerically in the literature. Chouikh et al. [80] study the flow around two vertically aligned horizontal isothermal cylinders of the same size. Cianfrini et al. [69] also consider isothermal cylinders and also investigate the case when the upper cylinder is adiabatic as well as exploring cylinders of unequal diameters. Isotherms, streamlines, and velocity fields are presented as well as average Nusselt numbers for both the bottom and upper cylinders.

Consider two horizontal cylinders of equal dimensions (diameter l mm) aligned vertically so that one is above the other. Let S be the vertical distance between the two cylinders. A parameter $S_L = S/l$ (S and l both measured in mm) can be defined to denote the distance between the two cylinders. For example, if $S_L = 0$ then the cylinders will be just touching each other and if $S_L = 1$ then the distance between the top of the bottom cylinder and the bottom of the upper cylinder is l mm. In order to

---

[1] Cianfrini et al. [71] consider up to a row of ten isothermal cylinders.

obtain results which are comparable to the literature, it is assumed that the cylinders are isothermal and the flow properties (viscosity, thermal conductivity, and specific heat capacity of the surrounding) are constant which is consistent with the Boussinesq approximation.

Conservation equations for mass, momentum, and energy describe the flow in the air domain along with the Boussinesq approximation so that the nondimensional fluid equations are the Boussinesq equations (Equations 5.1–5.3). The two cylinders are isothermal so that $T = 1$ everywhere in the two solid cylinders. The Prandtl number is set to $\mathrm{Pr} = 0.7$ and the Rayleigh number is a parameter of the problem. The outer boundary conditions are the same as before so that the conditions on the entry and exit are

$$\mathbf{u} \cdot \mathbf{t} = 0 \qquad\qquad T = 0 \qquad\qquad \sigma \cdot \mathbf{n} = 0$$

and

$$\mathbf{u} \cdot \mathbf{t} = 0 \qquad\qquad \nabla T \cdot \mathbf{n} = 0 \qquad\qquad \sigma \cdot \mathbf{n} = 0$$

respectively. The no slip condition is applicable on the solid isothermal cylinders so that $\mathbf{u} = \mathbf{0}$ on both the cylinders surfaces.

Figure 5.7 shows the isotherms and velocity field for $\mathrm{Ra} = 10^2$ and $\mathrm{Ra} = 10^4$ with the vertical distance between the cylinders being one cylinder diameter so that $S_L = 1$. It is clear that the boundary layer thickness is smaller for larger Rayleigh numbers. These profiles are consistent with the results obtained in Chouikh et al. [80].

The Nusselt number Nu on the solid boundaries is defined to be

$$\mathrm{Nu} = -\nabla T \cdot \mathbf{n}|_{r=0.5}$$

so that the average Nusselt number

$$\overline{\mathrm{Nu}} = \frac{1}{2\pi} \int_0^{2\pi} \mathrm{Nu}\, \mathrm{d}\theta = -\frac{1}{2\pi} \int_0^{2\pi} \nabla T \cdot \mathbf{n}|_{r=0.5}\, \mathrm{d}\theta$$

where r is measured from the centre of the cylinder and $r = 0.5$ is the surface of the cylinder.

Table 5.5 shows the Nusselt number results compared to the numerical results of Cianfrini et al. [69] and the experimental results of Sparrow and Niethammer [82]. These average Nusselt numbers show a good agreement with the literature results.

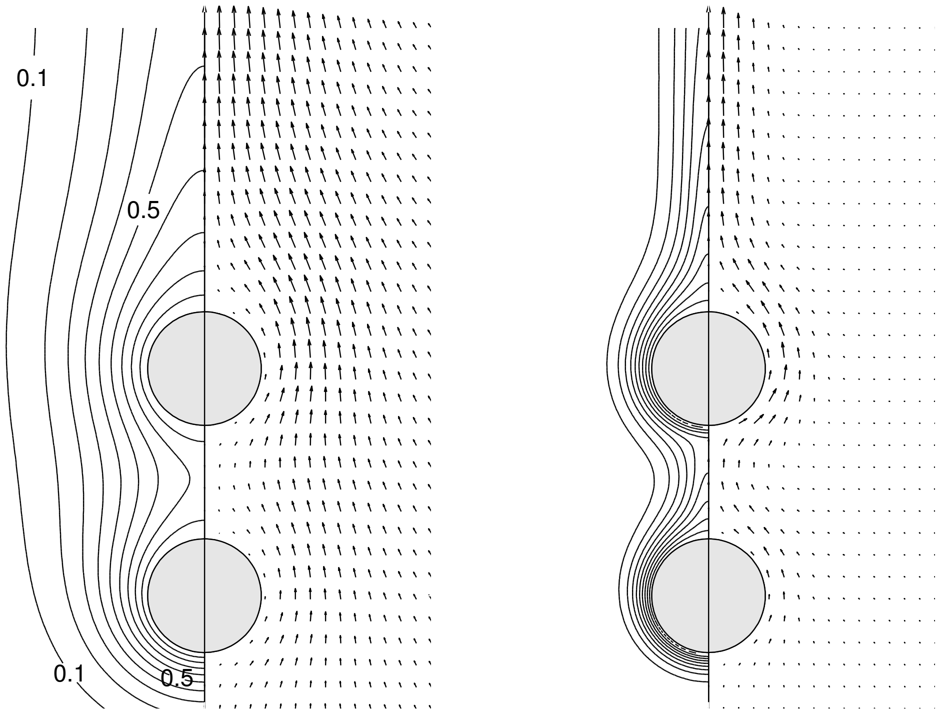

(a) Ra = 10^2 ($S_L = 1$) (b) Ra = 10^4 ($S_L = 1$)

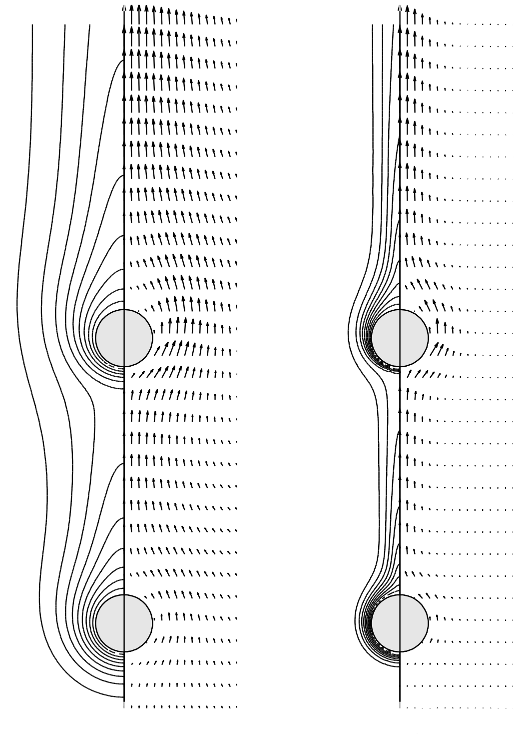

(c) Ra = 10^2 ($S_L = 4$) (d) Ra = 10^4 ($S_L = 4$)

Figure 5.7: Isotherms and velocity field for Ra = 10^2 and Ra = 10^4 for two vertically aligned horizontal cylinders of the same diameter at constant temperature. The distance between the cylinders for (a) and (b) is one cylinder diameter so that $S_L = 1$. For (c) and (d) it is four cylinder diameters ($S_L = 4$).

Table 5.5: Comparison with literature results of the ratio of average Nusselt number of the top cylinder $\overline{\mathrm{Nu}}_{\mathrm{top}}$ with the single isothermal cylinder $\overline{\mathrm{Nu}}_1$.

Ra		$\overline{\mathrm{Nu}}_{\mathrm{top}}/\overline{\mathrm{Nu}}_1(S_D = 1)$
2×10^4	Present	0.798
	Cianfrini et al. [69]	0.810
	Sparrow and Niethammer [82]	0.82
6×10^4	Present	0.832
	Cianfrini et al. [69]	0.844
	Sparrow and Niethammer [82]	0.85

5.3.2 Multiple vertically aligned cylinders

The natural convection around multiple (more than two) vertically aligned cylinders is explored here. This problem was solved numerically by Corcione [70]. The Boussinesq approximation is applied and it is assumed that the cylinders are in an infinite air domain so that Pr = 0.71. The Rayleigh number is a parameter of the problem. Hence the governing equations are again the Boussinesq equations (Equations 5.1–5.3). The cylinders are isothermal so that the temperature is constant everywhere in the cylinders so that $T = 1$ on the cylinders surfaces. Also the no slip condition is applicable on the cylinders so that $\mathbf{u} = \mathbf{0}$ on the cylinders surfaces. Conditions on the outer 'infinite' boundary depend on whether the flow enters the domain or leaves it. The conditions on entry and exit of the outer domain are

$$\mathbf{u} \cdot \mathbf{t} = 0 \qquad T = 0 \qquad \sigma \cdot \mathbf{n} = 0$$

and

$$\mathbf{u} \cdot \mathbf{t} = 0 \qquad \nabla T \cdot \mathbf{n} = 0 \qquad \sigma \cdot \mathbf{n} = 0$$

respectively. Recall that S_L was defined to be the distance between the top of the bottom cylinder and the bottom of the upper cylinder. Corcione [70] prefers to seek changes to the centre-to-centre distance D say. Define the ratio of the centre-to-centre distance D to the diameter of the cylinders (it is assumed that the cylinders are of equal dimensions) l as $D_L = D/l$. Observing the changes in the flow properties as the Rayleigh number Ra and D_L vary are of interest.

Isotherms and velocity fields are presented in Figure 5.8 and Figure 5.9 for various Rayleigh numbers Ra and cylinder spacings of $D_L = 2$ and $D_L = 8$ respectively. It is already known that the boundary layer thickness decreases for larger Ra. However

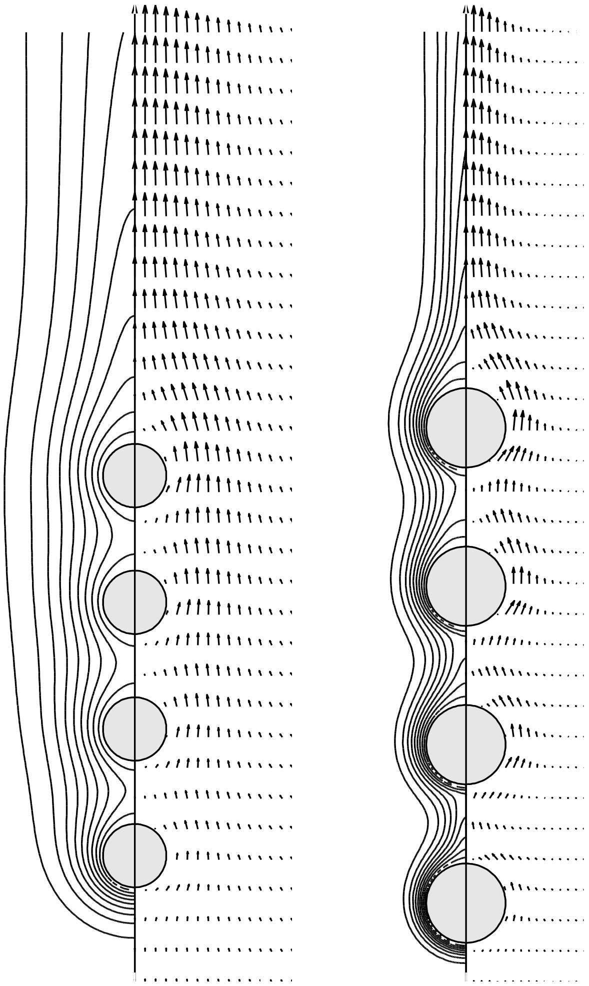

(a) Ra = 10^2. (b) Ra = 10^4.

Figure 5.8: Isotherms and velocity field for four cylinders spaced so that$D_L = 2$. Isotherms start from $T = 0.1$ up to $T = 0.9$ with a step size of 0.1 and the problem is symmetric about $x = 0$.

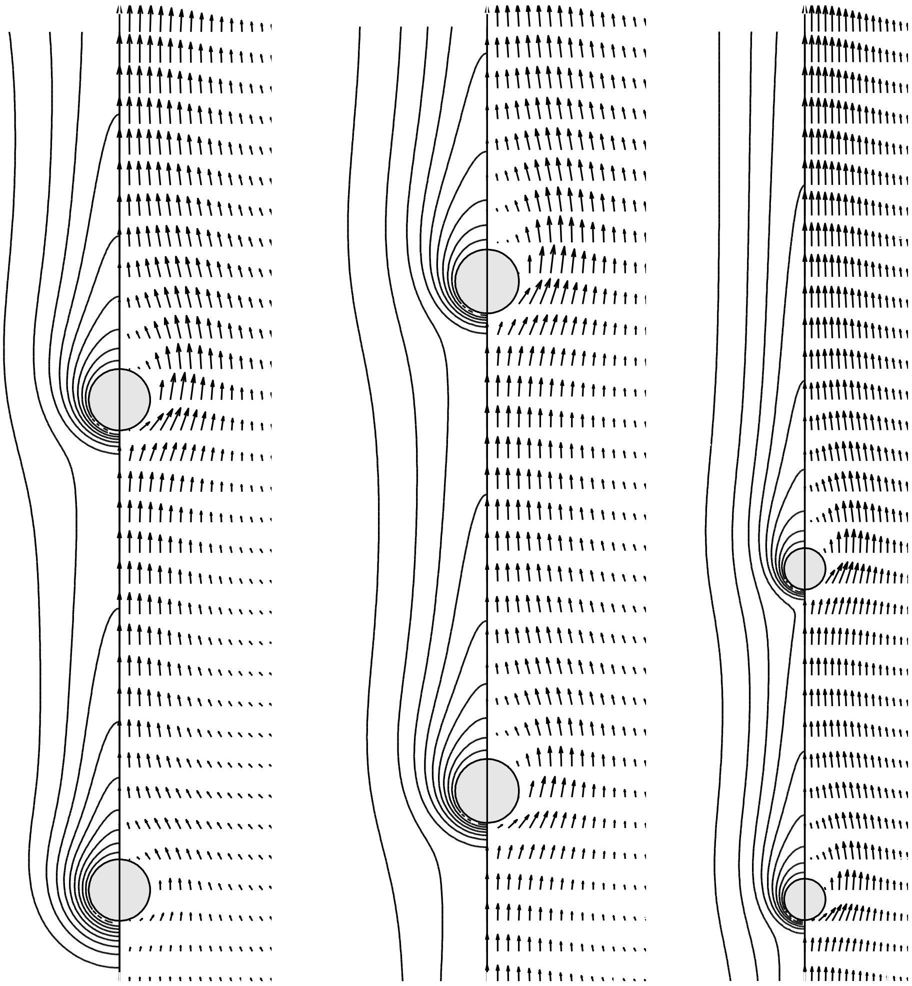

(a) $1^{\text{st}} - 2^{\text{nd}}$. (b) $2^{\text{nd}} - 3^{\text{rd}}$. (c) $3^{\text{rd}} - 4^{\text{th}}$.

Figure 5.9: Isotherms and velocity field for four cylinders spaced so that$D_L = 8$ with $\mathrm{Ra} = 10^2$. Isotherms start from $T = 0.1$ up to $T = 0.9$ with a step size of 0.1 and the problem is symmetric about $x = 0$.

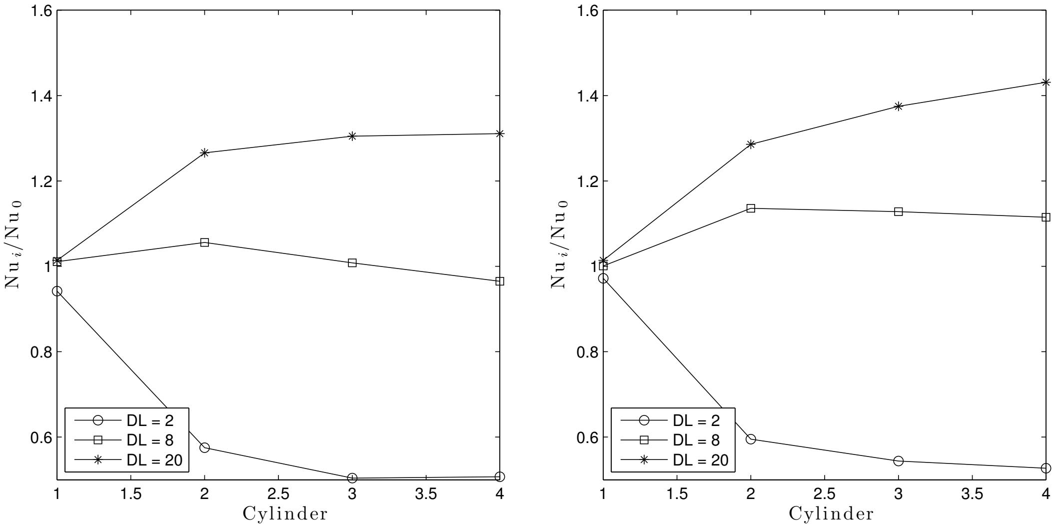

(a) Ra = 10^2

(b) Ra = 10^3

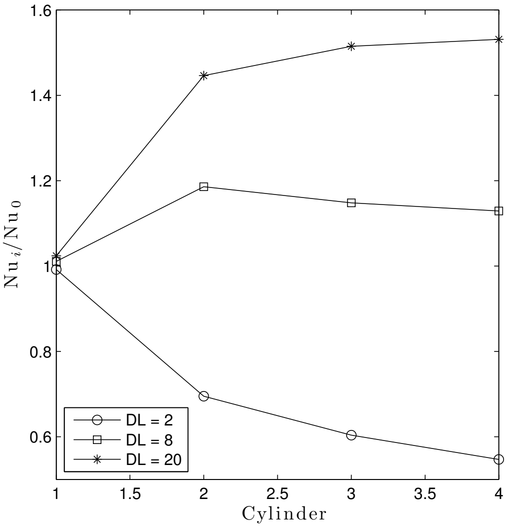

(c) Ra = 10^4

Figure 5.10: Distribution of the ratios $\mathrm{Nu}_i/\mathrm{Nu}_0$ against the cylinder number. The upstream cylinder is represented by $i = 1$ and the furthest downstream cylinder is represented by $i = 4$.

it is observed that the flow around the upper cylinders is greater than the the flow around the bottom cylinder. Plots of the Nusselt number ratios $\mathrm{Nu}_i/\mathrm{Nu}_0$, where the subscript i is the cylinder number and Nu_0 is the average Nusselt number for a single cylinder at a particular value of Ra, are shown in Figure 5.10 for $\mathrm{Ra} \in \{10^2, 10^3, 10^4\}$ and $D_L \in \{2, 8, 20\}$. This figure highlights whether the interactions of the ith cylinder with the upstream and downstream cylinders (where applicable) either enhances or degrades the heat transfer performance relative to that of the single cylinder. The heat transfer characteristics of the single isothermal cylinder is presented in section 5.2. The average Nusselt number for the bottom cylinder is approximately equal to that of the single cylinder so that

$$\mathrm{Nu}_1 \approx \mathrm{Nu}_0$$

for all Rayleigh numbers Ra and separation distances D_L considered. The largest difference between Nu_1 and Nu_0 is observed for smaller separation distances particularly when Ra is relatively low. These results are in good agreement with Corcione [70].

5.3.3 Horizontally aligned cylinders

The natural convection around horizontally aligned isothermal cylinders is explored here. Farouk and Guceri [83] and Bello-Ochende and Bejan [84] numerically solve the problem of a row of an infinite number of isothermal horizontal cylinders for laminar regimes (Farouk and Guceri [83] also solve for the turbulent regime). The Boussinesq approximation is applied and effects of varying cylinder spacing and Rayleigh number are explored. Symmetry of the flow can be exploited in order to solve the problem numerically. However this symmetry will not be present in the radiatively heated cylinders so it will be more worthwhile to consider a finite number of cylinders.

Cianfrini et al. [71] study the steady laminar free convection in air from parallel circular cylinders set side-by-side. Simulations are carried out for a row of 10 cylinders with varying centre-to-centre distances and Rayleigh numbers. The equations of motion and boundary conditions remain the same as that of isothermal vertically aligned cylinders which were stated in the beginning of this section. All that has changed is the geometry of the problem (namely the horizontal alignment instead of vertical). The governing equations are the Boussinesq equations (Equations 5.1–5.3) with the boundary conditions at the exit and entry of the outer domain as

$$\mathbf{u}\cdot\mathbf{t}=0 \qquad T=0 \qquad \sigma\cdot\mathbf{n}=0$$

and

$$\mathbf{u}\cdot\mathbf{t}=0 \qquad \nabla T\cdot\mathbf{n}=0 \qquad \sigma\cdot\mathbf{n}=0$$

respectively. The 10 cylinders are isothermal so that $T = 1$ and $\mathbf{u} = \mathbf{0}$ on the surface of the cylinders. The Prandtl number is set to $\mathrm{Pr} = 0.71$ which is consistent with air properties (this is the value used by Cianfrini et al. [71]). Let D_L be the horizontal centre-to-centre distance between the cylinders (it is assumed that the cylinders are equidistant).

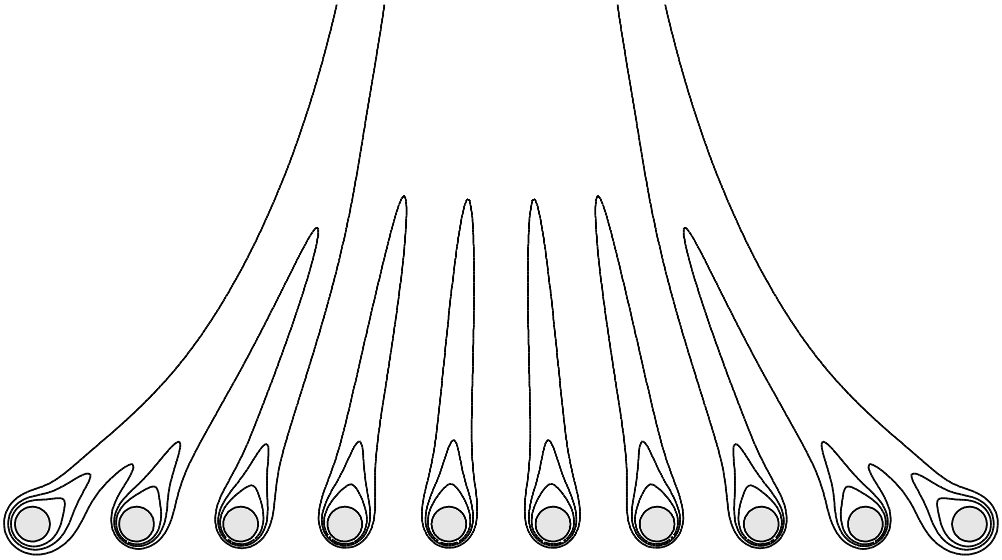

Figure 5.11: Isotherms with $T = 0.2, 0.4$, and 0.6 contours for $\mathrm{Ra} = 10^3$ and $D_L = 3$.

Isotherms for $\mathrm{Ra} = 10^3$ and $D_L = 3$ are shown in Figure 5.11 with contours $T = 0.2, T = 0.4$, and $T = 0.6$. The hot plumes from each cylinder merge into a single large plume due to the fluid flowing upwards through the array of cylinders being entrained by the plume.

The ratio of average Nusselt numbers $\overline{\mathrm{Nu}}/\overline{\mathrm{Nu}}_0$ against the Rayleigh number Ra are plotted in Figure 5.12 for $D_L = 1.4$. Here $\overline{\mathrm{Nu}}_0$ is the average Nusselt number for a single isothermal horizontal cylinder in an infinite domain at the same Rayleigh number as that for $\overline{\mathrm{Nu}}$. For medium to large Ra the heat transfer performance of the outermost cylinders (C1 and C10) is about the same as that of the single isothermal cylinder in an infinite fluid medium.

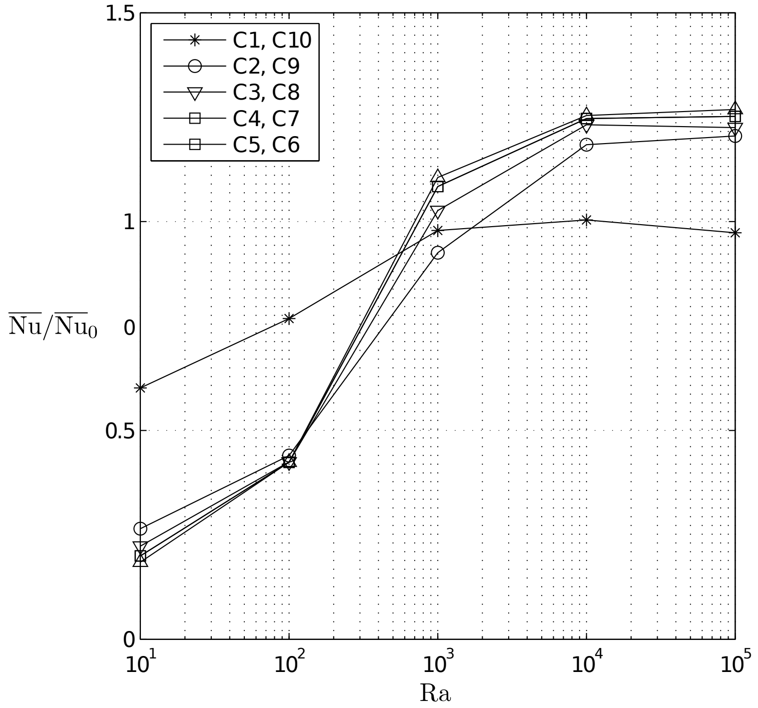

Figure 5.12: Nusselt number ratios $\overline{\mathrm{Nu}}/\overline{\mathrm{Nu}}_0$ for cylinders C1–C10 with varying Rayleigh numbers Ra with $D_L = 1.4$.

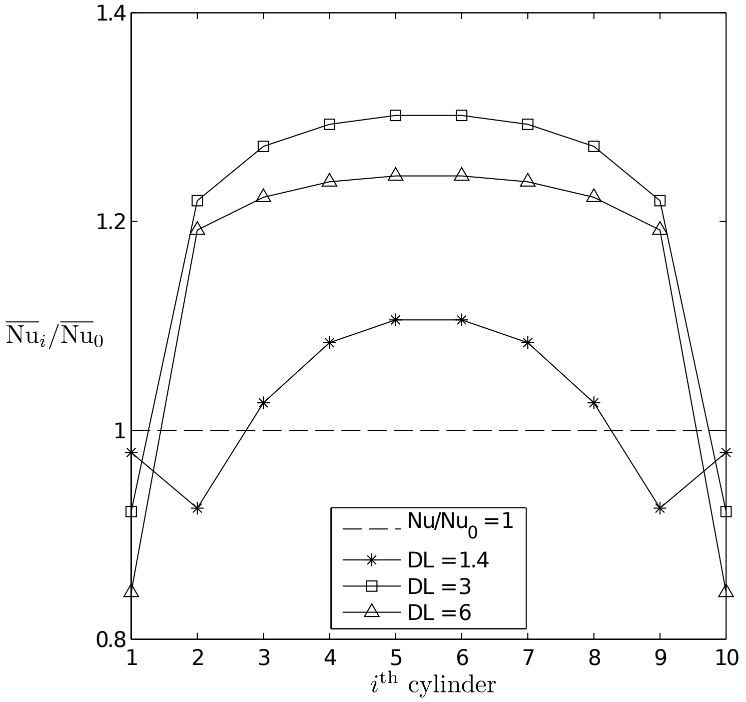

Figure 5.13: Nusselt number ratios $\overline{\mathrm{Nu}}_i/\overline{\mathrm{Nu}}_0$ for the ith cylinder and $\mathrm{Ra} = 10^3$.

The Nusselt number ratio $\overline{\mathrm{Nu}}_i/\overline{\mathrm{Nu}}_0$ for the ith cylinder is plotted for a range of centre-to-centre distances D_L and $\mathrm{Ra} = 10^3$ in Figure 5.13. The amount of heat exchanged by the inner cylinders increases for cylinders closer towards the middle of the row due to the lack of lateral entrainment into the plume above the central cylinders since the air is already hot either side of these central cylinders. These results are in good agreement with Cianfrini et al. [71].

5.4 Conclusions

Test problems for the steady natural convection around cylinders have been solved numerically using COMSOL Multiphysics. These test problems include isothermal and uniformly heated cylinders suspended in an infinite medium [57–60]. A model which includes the solid conduction, as studied by House et al. [68], is also solved. Numerical results for temperature fields, velocity fields, and average Nusselt numbers were in good with the literature for isolated cylinders.

Numerical results for multiple isothermal cylinders have also been obtained. These include problems where the cylinders have a vertical and horizontal configuration. Again, the temperature and flow profiles, as well as the average Nusselt numbers, were in good agreement with the literature for a range Rayleigh numbers of Ra and cylinder spacings.

Having found satisfactory results for the test problems, the natural convection model for the non-uniform radiant heating of fuel samples (Chapter 4) can be solved numerically using COMSOL Multiphysics.

Chapter 6

Numerical results for horizontal cylinders

The numerical procedure for solving natural convection problems has been verified for external flows around isothermal and uniformly heated bodies (Chapter 5). In this chapter the equations for natural convection around a conducting cylinder subjected to non-uniform radiative heating from an external panel is solved numerically using COMSOL Multiphysics. The governing equations, together with the boundary conditions, were presented in Chapter 4. Configurations where shadowing effects are not present is the focus of this chapter[1].

In section 6.1 the single cylinder configuration is explored. Numerical solutions for the simplified problem of constant flow properties (i.e. constant viscosity and thermal conductivity of air) without the reradiation effect are obtained and compared with the full steady problem (with variable flow properties). The sample diameter and incident heating rate are parameters of the problem.

The vertically aligned parallel cylinders configuration is explored in section 6.2. For two vertically aligned cylinders (one cylinder located directly above another) the flow from the upstream cylinder will affect the flow around downstream cylinder. The distance between the cylinders, in addition to the sample size and heating rate, is a parameter for the multiple cylinders configuration.

Temperature and velocity fields, local and average Nusselt numbers, and shear stress values are presented when analysing the heat transfer characteristics of the natural

---

[1] Chapter 7 deals with configurations where shadowing effects are present.

convection flow around the cylinders.

Details of any pyrolysis and ignition are not addressed here. Instead, the way in which natural convection can limit the degree of heating and the maximum temperature achieved at steady state are examined. Situations in which temperatures stay well below that for pyrolysis at flammability conditions (about 300°C) are unlikely to lead to ignition. Situations in which surface temperatures are significantly higher are more likely to lead to flammability conditions.

6.1 Flow around a horizontal cylinder

In this section the equations for natural convection around a conducting cylinder subjected to radiative heating derived in section 4.2 are solved numerically using COMSOL Multiphysics. The ability of COMSOL Multiphysics to solve natural convection problems has been verified by solving test problems of constant temperature (isothermal) and uniform heat flux for the circular cylinder as well as a case of solid conduction (Chapter 5) where a good agreement with the literature [57–59, 68] was found.

In deriving the governing equations (Chapter 4) the geometry of the natural convection problem was arbitrary. However, in this chapter, it is imposed that the body is a horizontal circular cylinder. This geometry is analogous to that of the problem presented in Kuehn and Goldstein [57] as well as in much of the literature on natural convection around a solid in an infinite domain [58, 59].

The case of constant flow properties, together with the Boussinesq approximation, is solved before the case of variable flow properties is explored in order to compare changes in the heat transfer rate around the horizontal cylinder. The importance of modelling the reradiation is also highlighted. This heat transfer effect is found to be particularly influential for larger Rayleigh numbers.

The temperature and velocity profiles for a range of sample sizes and heating rates are of interest in order to analyse when a fuel sample can pilot ignite. Nusselt number and shear stress values will also be analysed as they too give an insight to the heat transfer and flow properties.

6.1.1 Constant flow properties (reradiation neglected)

The steady nondimensional governing equations for the radiant non-uniform heating around a horizontal cylinder for constant fluid properties (except for the density in the buoyancy term) together with the heat flux boundary condition on the solid cylinder surface are

$$\mathbf{u} \cdot \nabla T = \nabla^2 T$$

$$\mathbf{u} \cdot \nabla \mathbf{u} + \nabla P = \mathrm{Pr} \nabla^2 \mathbf{u} + \mathrm{Pr}\,\mathrm{Ra}\, T\, \mathbf{j}$$

$$\nabla \cdot \mathbf{u} = 0$$

$$\nabla^2 \Theta = 0$$

$$B_\lambda \nabla \Theta \cdot \hat{\mathbf{n}} - \nabla T \cdot \hat{\mathbf{n}} = \psi(\vartheta).$$

These are the Boussinesq equations together with solid conduction and an anisotropic heating rate with heat loss through conduction into the air. The reradiation of heat into the air from the cylinder is neglected for now in order to reduce the number of problem parameters. This natural convection problem is similar to that of the uniformly heated cylinder studied by Wang et al. [58] except that in this case the cylinder is subjected to non-uniform heating determined by the $\psi(\vartheta)$ term in the heat flux boundary condition and, clearly, cylindrical symmetry is not maintained. The view factor ψ is defined for a panel which is located 100 mm away, in the x-direction, from the horizontal cylinder and is 500 mm wide and 400 mm high emitting an incident radiation heat flux of J_0 W/m^2. A similar configuration is used in the experiments of Cohen and Finney [64]. Their experimental configuration subjected wood-based sample (1mm and 12 mm thickness) to a radiant heating rate of $J_0 = 41$ kW/m^2 from a panel.

The Prandtl number is assumed to be constant so that Pr = 0.7 (corresponding to air) and the ratio of thermal conductivities of wood and air is $B_\lambda = 10$ [66]. Only the modified Rayleigh number

$$\mathrm{Ra} = \frac{g\beta J_0 l^4}{\nu_0 \lambda_0 \kappa_0}$$

remains as a parameter of the problem. Large Ra implies that the cylinder diameter l is large and/or the heating rate J_0 is large.

Table 6.1 lists the the average Nusselt number and shear stress around the conducting horizontal cylinder for a range of Ra. There are about 8×10^3 mesh elements in the

Table 6.1: Average Nusselt number $\overline{\mathrm{Nu}}$ and shear stress $\overline{\tau}_{xy}$ around a conducting horizontal cylinder.

Ra	Domain radius L/l	$\overline{\mathrm{Nu}}$	$\overline{\tau}_{xy}$
10^{-1}	20	0.662	0.392
10^{-1}	30	0.663	0.400
10^{-1}	60	0.665	0.402
10^{-1}	80	0.663	0.405
10^{0}	30	0.842	1.181
10^{1}	30	1.109	3.681
10^{2}	30	1.514	12.09
10^{3}	30	2.135	41.59
10^{4}	30	3.095	148.3
10^{5}	20	4.579	543.8
10^{5}	30	4.589	543.7
10^{5}	40	4.590	543.6

domain where the grid is refined near the cylinder. A range of domain radii L mm are explored for $\mathrm{Ra} = 10^{-1}$ and $\mathrm{Ra} = 10^{5}$. Good accuracy (i.e. less than 1% relative change when increasing the domain size) is observed when the nondimensional air domain radius is $L/l = 30$ for $\mathrm{Ra} = 10^{-1}$ and $L/l = 20$ for $\mathrm{Ra} = 10^{5}$. It is useful to use a fixed value for the nondimensional domain size for computation purposes. It seems that $L/l = 30$ is a good choice as it gives consistent results for heat transfer and shear stress when compared to results at larger outer domain radii.

Recall that the Nusselt number is $\mathrm{Nu}_{\psi} = -\nabla T/T$ so that the average Nusselt number is

$$\overline{\mathrm{Nu}}_{\psi} = \frac{1}{2\pi}\int_{0}^{2\pi} \mathrm{Nu}\, d\vartheta.$$

The Nusselt number gives a measure of the importance of convection compared to conduction in the heat transfer problem. A large Nusselt number means that convective heat transfer is the dominant form of heat transfer [72]. The flow is unsteady when the Nusselt number approaches about 100 [4]. Clearly convective heat transfer becomes more dominant for larger Rayleigh numbers Ra as is shown in the results from Table 6.1. Also recall from Chapter 4 (section 4.2) that the nondimensional shear stress tensor is defined as

$$\boldsymbol{\tau} = \nabla \mathbf{u} + \nabla \mathbf{u}^{\intercal} - \frac{2}{3}\left(\nabla \cdot \mathbf{u}\right)\mathbb{I}\,.$$

The viscosity is not present in the definition of the shear stress since in applying the

Boussinesq approximation it is assumed that the viscosity is constant. The stress tensor can be written in index notation [76] as

$$\tau_{ij} = \frac{\partial u_i}{\partial x_j} + \frac{\partial u_j}{\partial x_i} - \frac{2}{3}\frac{\partial u_k}{\partial x_k}\delta_{ij}$$

where δ_{ij} is the Kronecker delta

$$\delta_{ij} = \begin{cases} 0, & \text{if } i \neq j \\ 1, & \text{if } i = j \end{cases}$$

and the summation convention is used. Hence the nondimensional shear stress is

$$\tau_{xy} = \frac{\partial u}{\partial y} + \frac{\partial v}{\partial x}$$

so that the average shear stress around the conducting cylinder is

$$\overline{\tau}_{xy} = \frac{1}{2\pi}\int_0^{2\pi} \left|\frac{\partial u}{\partial y}\right| + \left|\frac{\partial v}{\partial x}\right| \,\mathrm{d}\vartheta.$$

Table 6.1 shows that the average shear stress around the cylinder increases for larger Ra. Again this is to be expected as the flow speed around the cylinder will increase for hotter cylinders.

Isotherms and streamlines are plotted in Figure 6.1 for selected values of modified Rayleigh numbers Ra. The asymmetry about the vertical y-axis results from the non-uniform radiative heating of the cylinder due to the radiating panel being located to the right of the horizontal cylinder sample. Both the isotherms and streamlines move closer to the cylinder for larger Ra. This means that the thermal boundary layer thickness becomes relatively small for larger Rayleigh numbers causing the shear stress to increase. This results in a larger rate of heat loss into the stronger flow around the cylinder at larger Rayleigh numbers.

6.1.2 Effects of reradiation

The heat flux boundary condition is now modified in order to take into account the reradiation of heat from the cylinder into the air. The boundary condition now becomes

$$B_\lambda \nabla\Theta \cdot \hat{\mathbf{n}} - \nabla T \cdot \hat{\mathbf{n}} = \psi(\vartheta) - D_R\left((1 + A_T T)^4 - 1\right).$$

Assuming that the incident heat flux from the radiating panel J_0 is constant at 40 kW/m^2 then

$$D_R = \frac{\epsilon\varsigma T_o^4}{J_0} \approx \frac{2}{5J_0} = \frac{1}{100}$$

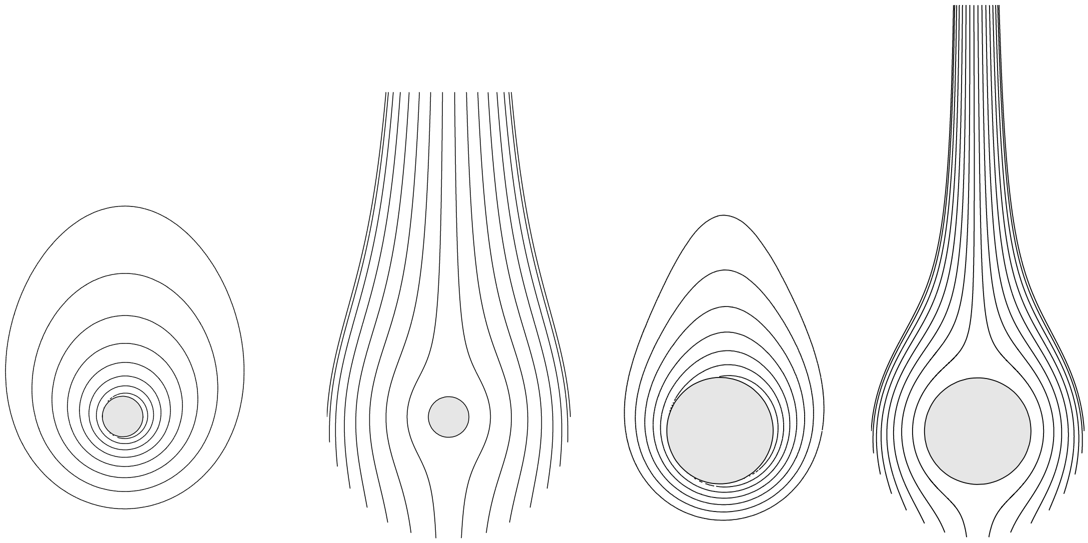

(a) $\mathrm{Ra} = 10^{-1}$ (b) $\mathrm{Ra} = 10^{-1}$ (c) $\mathrm{Ra} = 10^{2}$ (d) $\mathrm{Ra} = 10^{2}$

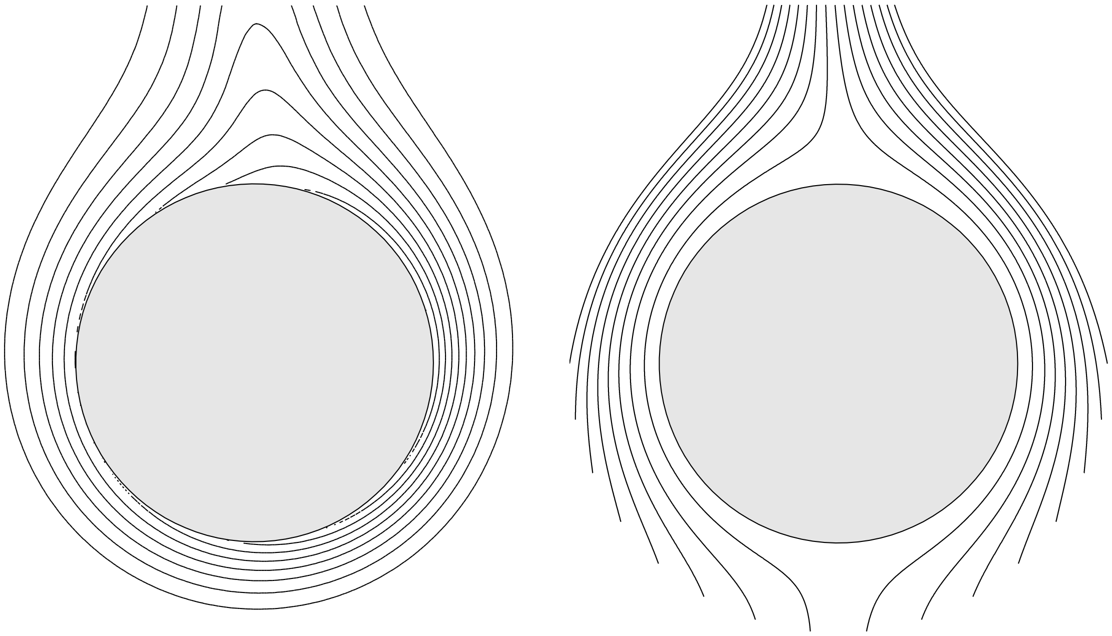

(e) $\mathrm{Ra} = 10^{5}$ (f) $\mathrm{Ra} = 10^{5}$

Figure 6.1: Isotherms (figures (a), (c), and (e)) and streamlines (figures (b), (d), and (f)) for various modified Rayleigh numbers Ra.

$$A_T = \frac{T_c - T_0}{T_0} = \frac{l J_0}{\lambda_0 T_0} \approx \frac{2\, l J_0}{15} \approx 1.54 \times \mathrm{Ra}^{1/4}.$$

The relative error in approximating A_T with $1.54 \times \mathrm{Ra}^{1/4}$ is less than 0.03% when $J_0 = 40$ kW/m^2. Hence the boundary condition on the cylinder can be approximated as

$$B_\lambda \nabla\Theta \cdot \hat{\mathbf{n}} - \nabla T \cdot \hat{\mathbf{n}} = \psi(\vartheta) - \frac{1}{100}\left(\left(1 + 1.54 \times \mathrm{Ra}^{1/4}\, T\right)^4 - 1\right).$$

Writing the boundary condition in this way ensures that the modified Rayleigh number Ra is still the only parameter of the problem since J_0 is held constant. A change in Ra can be then interpreted as a change in the size of the cylinder only, since the heating rate has been imposed ($J_0 = 40$ kW/m^2).

Table 6.2: Average Nusselt number and shear stress for selected values of Ra with $J_0 = 40$ kW/m^2.

		No Reradiation		Reradiation Included		Relative Difference (%)	
Ra	l (mm)	$\overline{\mathrm{Nu}}$	$\overline{\tau}_{xy}$	$\overline{\mathrm{Nu}}$	$\overline{\tau}_{xy}$	$\overline{\mathrm{Nu}}$	$\overline{\tau}_{xy}$
10^{-1}	0.194	0.662	0.400	0.657	0.383	1	4
10^{0}	0.381	0.842	1.181	0.828	1.101	2	7
10^{1}	0.772	1.109	3.681	1.076	3.276	3	11
10^{2}	1.605	1.514	12.09	1.439	10.10	5	16
10^{3}	7.243	2.135	41.59	1.978	32.16	8	23
10^{4}	15.53	3.095	148.3	2.775	105.0	12	29
10^{5}	33.40	4.589	543.7	3.957	349.5	16	36

Table 6.2 lists the average Nusselt numbers $\overline{\mathrm{Nu}}$ and shear stresses $\overline{\tau}_{xy}$, to four significant figures, for a range of modified Rayleigh numbers Ra. A comparison, listing the relative percentage difference (nearest %), is made between the results obtained with and without the reradiation of heat into the surrounding air being modelled. It can be seen that reradiation increases the average Nusselt number and decreases the shear stress rate.

The effect of reradiation is of course to reduce the net rate of heat absorption and so, in turn, the heat transfer to the air, thus lowering the temperature of the cylinder. With $\overline{\mathrm{Nu}}_\psi$ defined as the average value of $-\nabla T \cdot \mathbf{n}$ this causes an increase in $\overline{\mathrm{Nu}}_\psi$.

Reduced temperature also reduces the effects of buoyancy so that one would expect the shear stress to decrease around the cylinder due to the reduced temperature difference. This is evident from the results in Table 6.2. Clearly reradiation has a significant role in the heating and flow profile of the cylinder and must be included in the model in order to produce meaningful results.

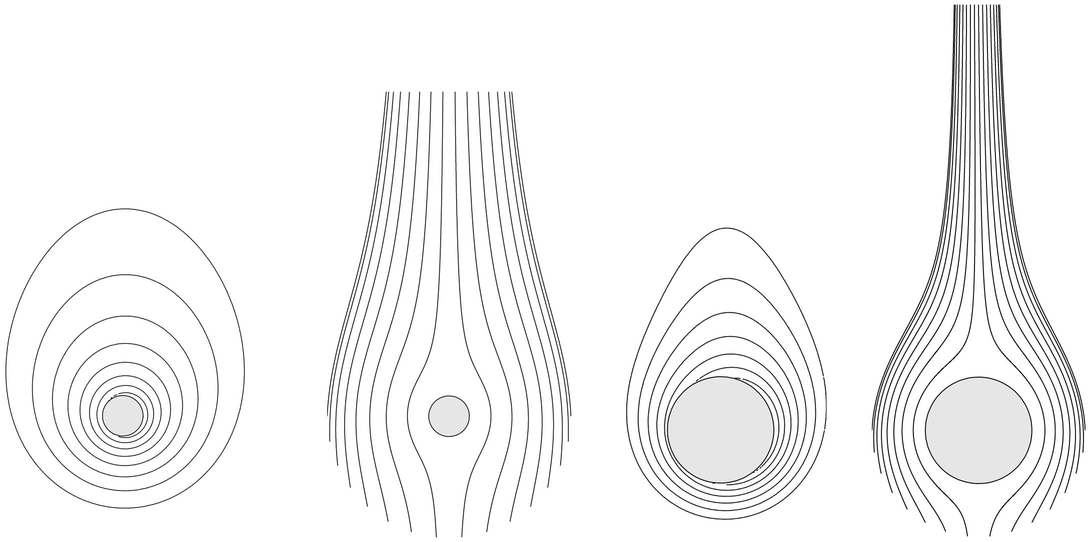

(a) Ra = 10^{-1} (b) Ra = 10^{-1} (c) Ra = 10^{2} (d) Ra = 10^{2}

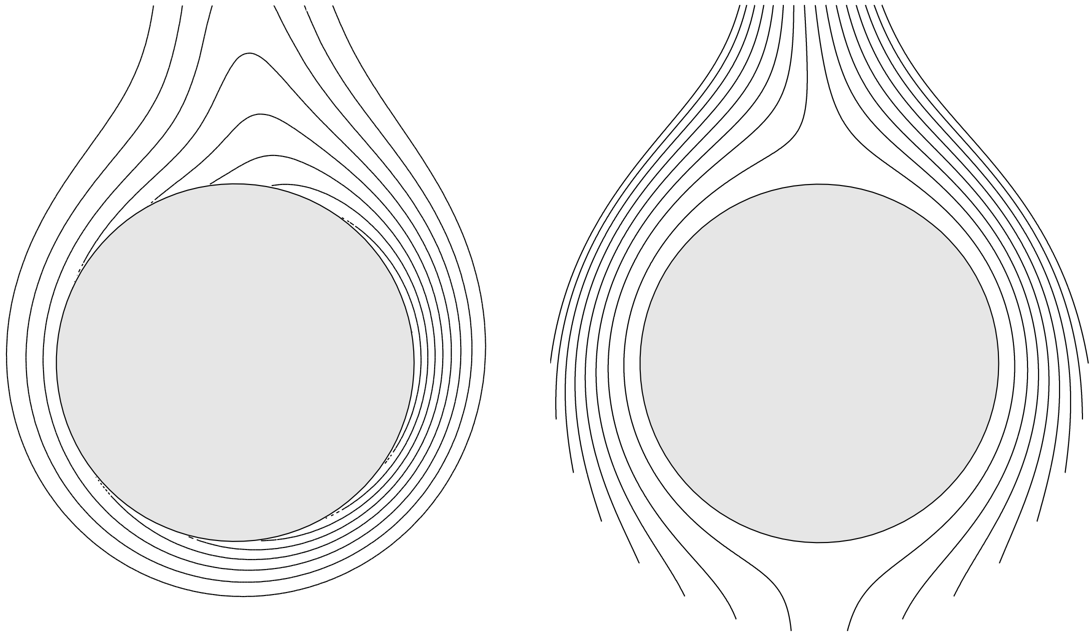

(e) Ra = 10^{5} (f) Ra = 10^{5}

Figure 6.2: Isotherms (figures (a), (c), and (e)) and streamlines (figures (b), (d), and (f)) for various modified Rayleigh numbers Ra. Effects of reradiation are modelled and the heating rate is assumed to be constant ($J_0 = 40$ kW/m^2).

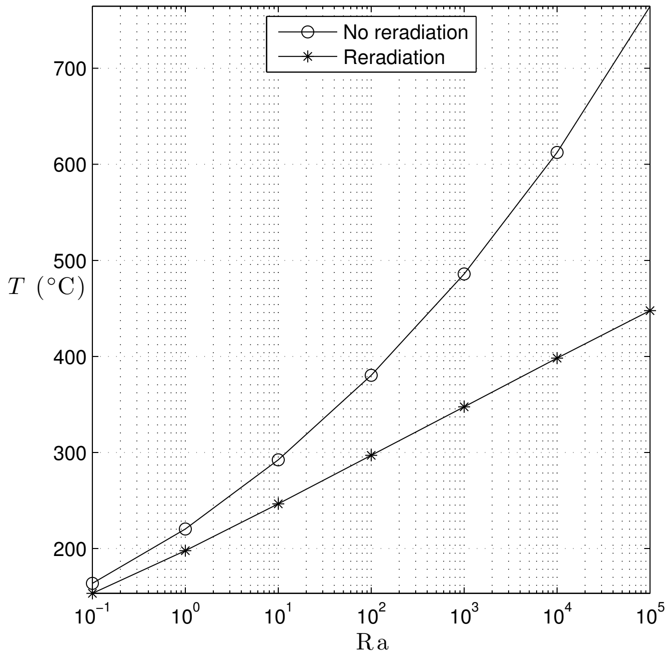

Figure 6.3: Surface temperature T (°C) at $\theta = 90°$ (the point on the cylinder most exposed to the heating from the radiant panel) for different modified Rayleigh numbers Ra. Comparison between modelling with and without reradiation is made. Heating rate is fixed at $J_0 = 40$ kW/m^2.

Figure 6.2 shows the isotherms and streamlines for various modified Raleigh numbers Ra for the case when reradiation is modelled. These profiles do not seem to differ much, in a visual sense, compared to those of the constant flow properties case presented in Figure 6.1 although some differences can be seen. The isotherms are normalised to the range of temperatures so that they are not the same as those used in Figure 6.1. The temperature difference is more clearly represented in Figure 6.3. This plot shows the temperature at the surface of the cylinder at the point $\theta = 90°$, which is the point most exposed to the radiant panel, against the modified Rayleigh number Ra. It is assumed that the heating rate is constant so that $J_0 = 40$ kW/m^2. Modelling the reradiation gives rise to significantly lower surface temperatures obtained compared with the case when reradiation is not modelled. Changes in the temperature are small for small Ra (e.g. about 10°C for Ra = 1) but become more significant for large Ra (e.g. about 300°C for Ra = 10^5). Assuming that significant pyrolysate vapour is produced when $T \approx 300$°C then results for the case when reradiation is not modelled (Figure 6.3) suggest that the circular cylinder could ignite when Ra $\approx 10^1$. However when the reradiation is modelled it is suggested that Ra $\approx 10^2$ before the cylinder can support a flame.

6.1.3 Temperature dependent flow properties

The results obtained so far assume constant flow properties except for variations in density in the buoyancy term which is a requirement for there to be any flow. However most fluids (like air) have temperature dependent properties such as viscosity η, thermal conductivity λ, and specific heat capacity c_p as well as the density itself. Therefore when the temperature differences in the fluid domain are large, assuming constant flow properties could lead to considerable errors. It is suggested in Gray and Giorgini [85] that the Boussinesq approximation is valid for temperature differences of up to 28.8°C where the ambient temperature is 15°C. This range is restrictive so it is worth examining the effects of temperature dependent flow properties in the natural convection around a horizontal cylinder.

Recall from section 4.2 that the steady nondimensional equations with variable flow properties are

$$\rho c_p \mathbf{u} \cdot \nabla T = \nabla \cdot \lambda \nabla T$$

$$\rho \mathbf{u} \cdot \nabla \mathbf{u} + \nabla P = \mathrm{Pr} \left(\nabla \cdot \boldsymbol{\tau} + \mathrm{Ra}\, \rho T \mathbf{j} \right)$$

$$\nabla \cdot \rho \mathbf{u} = 0$$

$$\rho = \frac{1}{1 + A_T T}$$

$$\nabla \cdot \lambda_s \nabla \Theta = 0$$

with the heat flux boundary condition

$$B_\lambda \, \lambda_s \nabla \Theta \cdot \hat{\mathbf{n}} - \lambda \nabla T \cdot \hat{\mathbf{n}} = \psi(\vartheta) + D_R \left(1 - (1 + A_T T)^4 \right).$$

Assuming that the thermal conductivity of the solid cylinder is constant, so that $\lambda_s = 1$, then the solid conduction equation reduces to Laplace's equation for the solid phase temperature Θ

$$\nabla^2 \Theta = 0$$

and the heat flux boundary condition reduces to

$$B_\lambda \nabla \Theta \cdot \hat{\mathbf{n}} - \lambda \nabla T \cdot \hat{\mathbf{n}} = \psi(\vartheta) + D_R \left(1 - (1 + A_T T)^4 \right).$$

Also recall that the stress tensor is

$$\boldsymbol{\tau} = \eta \left(\nabla \mathbf{u} + \nabla \mathbf{u}^{\mathsf{T}} - \frac{2}{3} \left(\nabla \cdot \mathbf{u} \right) \mathbb{I} \right).$$

The flow properties of density, viscosity, thermal conductivity, and specific heat capacity are assumed to vary with temperature so that

$$\rho = \rho(T) \qquad \eta = \eta(T) \qquad \lambda = \lambda(T) \qquad c_p = c_p(T).$$

The flow density is $\rho = 1/(1 + A_T T)$. It is suggested in Hernández and Zamora [86] that the temperature dependant functions for viscosity and thermal conductivity can be approximated as

$$\eta = \frac{(1 + A_T T)^{3/2}}{1 + A_T T / (1 + C_1/T_0)}$$
$$\lambda = \frac{(1 + A_T T)^{3/2}}{1 + A_T T / (1 + C_2/T_0)}$$

where $C_1 = 0.36\,T_0$ and $C_2 = 0.66\,T_0$ are constants chosen in such a way as that λ and η correspond to the properties of air. The ambient temperature is $T_0 = 300$ K.

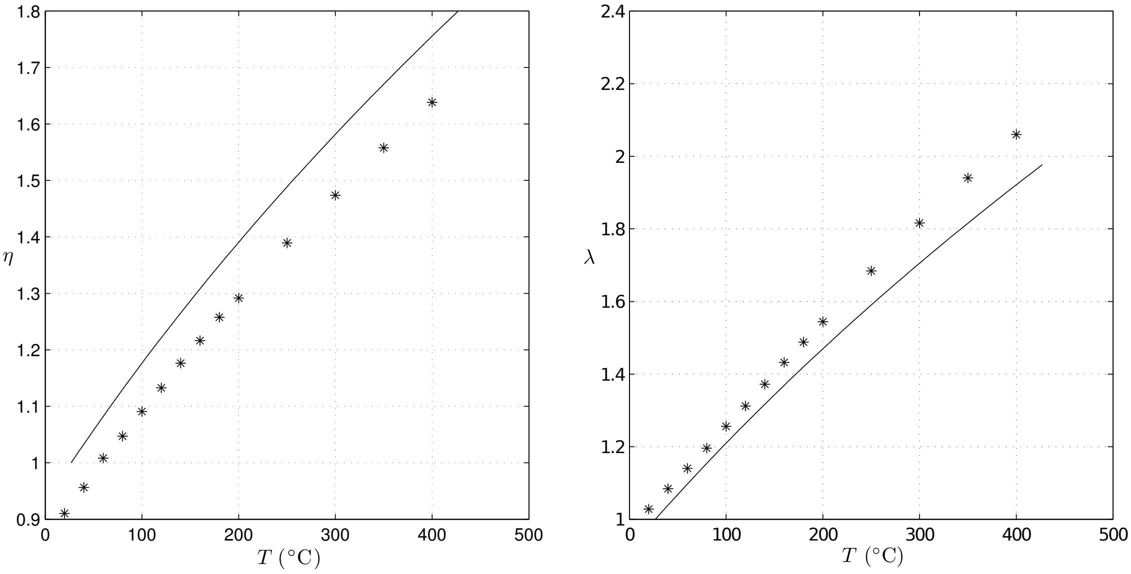

(a) $\eta = \frac{(1+A_T T)^{3/2}}{1+A_T T/(1+C_1/T_0)}$ (b) $\lambda = \frac{(1+A_T T)^{3/2}}{1+A_T T/(1+C_2/T_0)}$

Figure 6.4: Temperature dependant functions for viscosity (η) and thermal conductivity (λ) compared with data, shown as asterisks, from The Engineering Toolbox [87]. The ambient temperature is $T_0 = 300$ K.

Figure 6.4 shows the functions $\eta(T)$ and $\lambda(T)$ against the temperature together with data points from The Engineering Toolbox [87] which shows that the functions are in fairly good agreement with the data. The specific heat capacity c_P varies by less than 7% between the temperature range of 20°C to 400°C. Therefore it is a sufficient approximation to assume that the specific heat remains constant, taking $c_P = 1$ everywhere.

The parameters of the problem are the Raleigh number $\mathrm{Ra} = \mathrm{Ra}(l, J_0)$, heating intensity $A_T = A_T(l, J_0)$, and reradiation number $D_R = D_R(l, J_0)$ where l is the length scale and J_0 is the heating rate. Prandtl number Pr is also, strictly speaking, a parameter of the problem. However, it is the heating rate and sample size that will vary in the present study and the Prandtl number does not depend on either l or J_0 ($\mathrm{Pr} = \nu_0/\kappa_0$). Therefore, for the present study, the Prandtl number Pr will remain constant.

The only parameter of the Boussinesq problem without reradiation was the Rayleigh number Ra which can be interpreted as a change in the cylinder size and/or the heating rate. However when assuming variable flow properties and reradiation the nondimensional temperature range A_T and reradiation factor D_R are introduced. Therefore when analysing the numerical results it would be more meaningful, and manageable, if changes in l and J_0, which lead to changes in Ra, A_T, and D_R, are explored.

The approximate physical properties of solid wood and air at ambient temperature (300 K) are [18, 46, 66]

$$c_{s0} \approx 2.500 \text{ J/(kg K)} \qquad \rho_{s0} \approx 1,000 \text{ kg/m}^3 \qquad \kappa_{s0} \approx 10^{-7} \text{ m}^2\text{/s}$$

$$\lambda_{s0} \approx 1/4 \text{ W/(m K)} \qquad c_{p0} \approx 1,000 \text{ J/(kg K)} \qquad \rho_0 \approx 1.2 \text{ kg/m}^3$$

$$\kappa_0 \approx 2.2 \times 10^{-5} \text{ m}^2\text{/s} \qquad \lambda_0 \approx 1/40 \text{ W/(m K)} \qquad \nu_0 \approx 1.6 \times 10^{-5} \text{ m}^2\text{/s}$$

$$\eta_0 \approx 1.8 \times 10^{-5} \text{ Pa s} \qquad \epsilon \approx 6/7 \qquad \varsigma \approx 5.67 \times 10^{-8} \text{ J/(m}^2\text{ K}^4\text{ s)}.$$

After applying these approximations to wood and air properties at ambient temperature conditions, the nondimensional parameters of the natural convection model can be approximated as (see section 4.2)

$$\mathrm{Pr} = \frac{\nu_0}{\kappa_0} \approx 0.7, \quad B_\lambda = \left[\frac{\lambda_{s0}}{\lambda_0}\right] \approx 10, \quad D_R = \left[\frac{\epsilon\varsigma T_0^4}{J_0}\right] \approx \frac{400}{J_0}$$

$$A_T = \frac{T_c - T_0}{T_0} = \frac{l J_0}{\lambda_0 T_0} \approx \frac{40\, l J_0}{T_0}$$

$$\mathrm{Ra} = \frac{gl^3\left(T_c - T_0\right)}{\nu_0 \kappa_0 T_0} = \frac{gl^3}{\nu_0 \kappa_0} A_T \approx \left(3000\, l\right)^3 A_T.$$

Comparison with constant flow properties model

Table 6.3: Average Nusselt numbers $\overline{\mathrm{Nu}}$ ($\overline{\mathrm{Nu}}_{\mathrm{const}}$ corresponds to constant η and λ) for various sized cylinders (diameter l mm) for constant heating rate $J_0 = 40$ kW/m^2. The approximate percentage change is also tabulated.

l (mm)	Ra (2 S.F.)	$\overline{\mathrm{Nu}}$	$\overline{\mathrm{Nu}}_{\mathrm{const}}$	% difference
1	1.4×10^2	1.044	1.359	30
2	2.3×10^3	1.432	1.932	35
4	3.7×10^4	2.050	2.841	39
8	5.9×10^5	3.050	4.495	47
12	3.0×10^6	3.911	6.021	54
16	9.4×10^6	4.707	7.365	56

Table 6.4 shows the average Nusselt numbers for the temperature dependent viscosity and thermal conductivity model compared with the constant flow properties model. Particularly for large cylinders (corresponding to large Rayleigh numbers Ra) the difference is significant (over 50% for Ra $\sim 10^6$). The average Nusselt number is always larger for the constant viscosity and thermal conductivity model. This suggests that there is a greater convective heat transfer so that the cylinder is losing heat more readily compared to the temperature dependent flow properties model. A model which incorporates temperature dependent flow properties then would predict ignition conditions for smaller samples.

This highlights the importance of considering temperature dependent flow properties, particularly for larger Rayleigh numbers Ra, in order to obtain more accurate results. Since both the viscosity and thermal conductivity of the surrounding air increase with temperature, the cylinder loses heat more readily compared to the case when it is assumed that η and λ as constant (taking the values for viscosity and thermal conductivity at ambient air temperature). The average surface temperature on the cylinder therefore is less than that predicted by the constant flow properties model. Both viscosity and thermal conductivity increase monotonically as the air temperature increases from its ambient value (Figure 6.4). The increased viscosity at larger temperatures suggest that the convective flow will be reduced (since the air 'thickness' is reduced [65]).

Comparison with experimental study [64]

Experiments in [64] indicated that a 1 mm sample did not ignite when exposed to a 41 kW/m^2 heating rate from a radiating panel but a 12 mm sample subjected to the same heating rate did ignite. The numerical simulation based on the fuller model just outlined helps to show the reason for this.

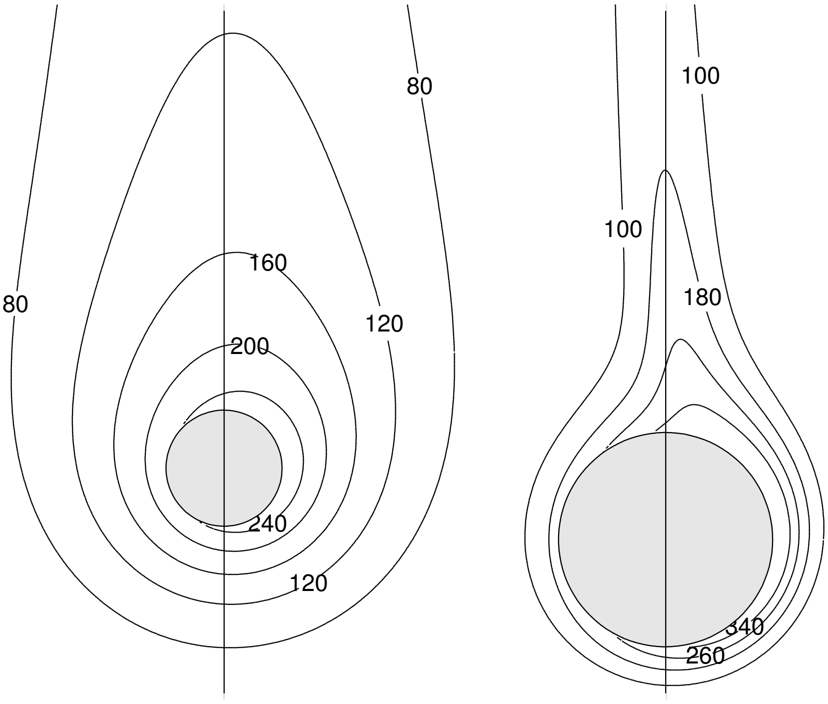

(a) $l = 1$ mm (b) $l = 12$ mm

Figure 6.5: Isotherms (°C) at heating rate $J_0 = 41$ kW/m^2 for (a) $l = 1$ mm and (b) $l = 12$ mm.

Figure 6.5 shows the isotherms for the 1 mm and 12 mm samples with an incident heating rate of $J_0 = 41$ kW/m^2. Clearly the surrounding air around the 12 mm sample is considerably (over a 100°C) hotter than the air surrounding the 1 mm sample. Typically a wooden sample produces enough pyrolysate vapour to support a flame when the surface temperature is around 350–550°C (Chapter 3).

Figure 6.6 shows the surface temperature in °C of the the 1 mm and 12 mm samples, with $J_0 = 41$ kW/m^2, for varying angle θ which is measured from the cooler side of the sample in an anticlockwise direction. This means that $\theta = \pi/2$ is the bottom of the cylinder and $\theta = 3\pi/2$ is the top of the cylinder. The average surface temperature $\overline{T}_s$

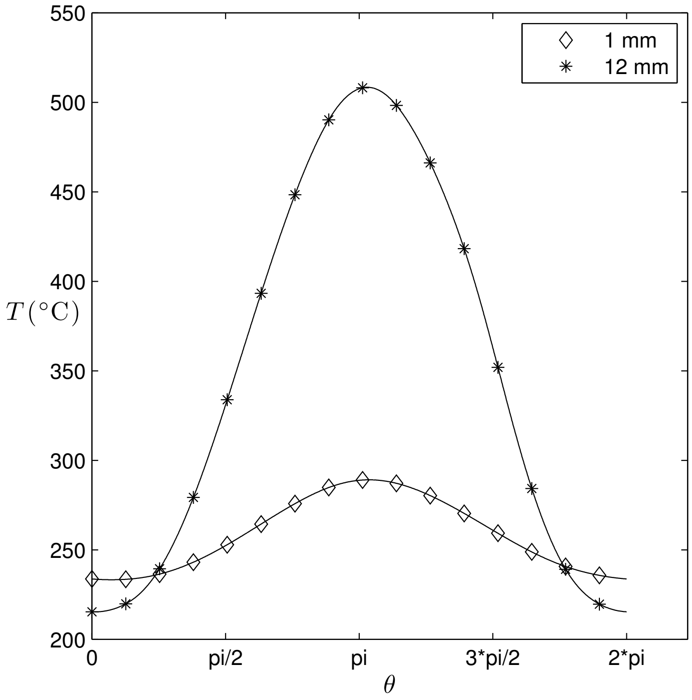

Figure 6.6: Surface temperature around the 1 mm and 12 mm samples, with $J_0 = 41$ kW/m^2, in °C. The angle θ is measured from the cooler side of the sample in an anticlockwise direction so that $\theta = \pi/2$ is the bottom of the cylinder and $\theta = 3\pi/2$ is the top of the cylinder.

can be calculated as

$$\overline{T}_s = \frac{1}{\pi l}\int_0^{\pi l} T|_{r=0.5}\,\mathrm{d}\theta.$$

Hence $\overline{T}_s|_{l=1\mathrm{mm}} = 258.8$°C and $\overline{T}_s|_{l=12\mathrm{mm}} = 352.0$°C to one decimal place. These are steady state calculations, but they do indicate that the 1 mm sample would not be heated sufficiently to pyrolyse while the temperature of the 12 mm sample would rise above 350°C so that significant pyrolysis should be expected.

Table 6.4: Average Nusselt numbers $\overline{\mathrm{Nu}}$ ($\overline{\mathrm{Nu}}_{\mathrm{const}}$ corresponds to constant η and λ) for various sized cylinders (diameter l mm) for constant heating rate $J_0 = 40$ kW/m^2. The approximate percentage change is also tabulated.

l (mm)	Ra (2 S.F.)	$\overline{\mathrm{Nu}}$	$\overline{\mathrm{Nu}}_{\mathrm{const}}$	% difference
1	1.4×10^2	1.044	1.359	30
2	2.3×10^3	1.432	1.932	35
4	3.7×10^4	2.050	2.841	39
8	5.9×10^5	3.050	4.495	47
12	3.0×10^6	3.911	6.021	54
16	9.4×10^6	4.707	7.365	56

Results for single cylinder in an infinite air domain

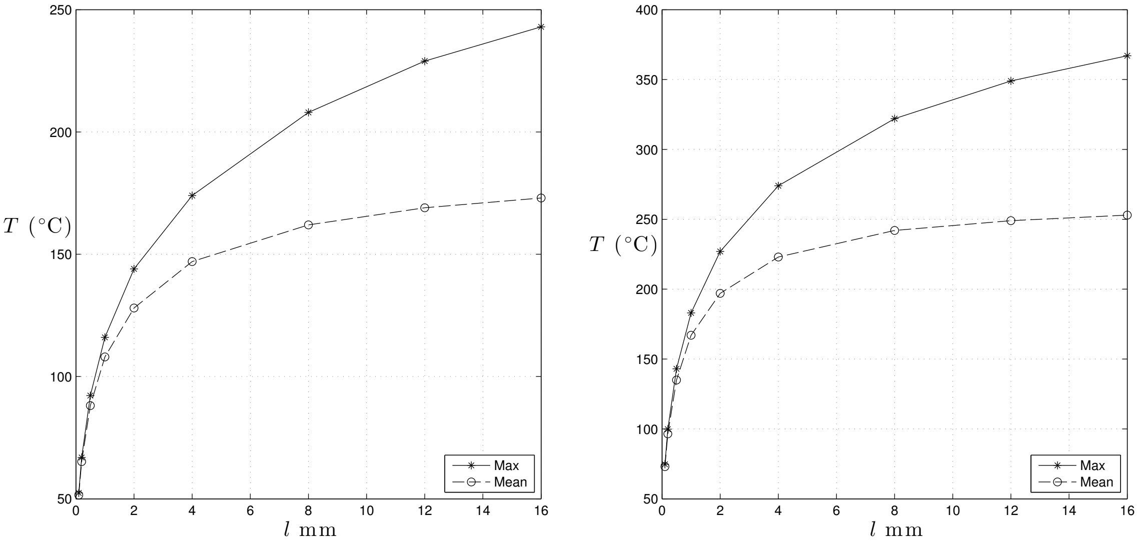

(a) $J_0 = 10$ kW/m^2 (b) $J_0 = 20$ kW/m^2

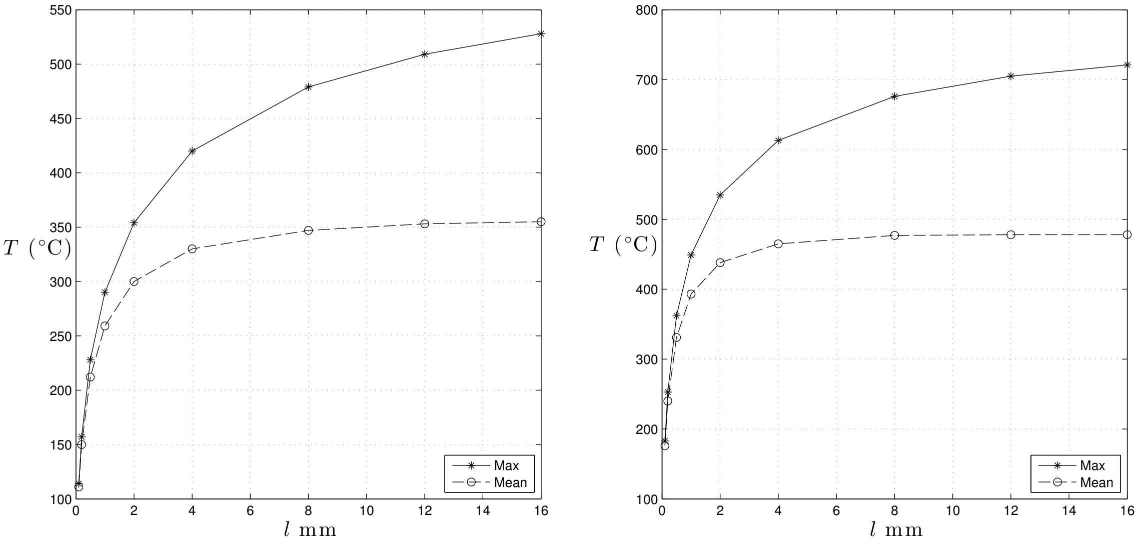

(c) $J_0 = 40$ kW/m^2 (d) $J_0 = 80$ kW/m^2

Figure 6.7: Maximum and average surface temperatures T (°C) around a horizontal cylinder against a range of sample sizes l for various heating rates J_0.

Figure 6.7 shows the maximum and average surface temperatures T (°C) around a horizontal cylinder against a range of sample sizes l for various heating rates J_0 (10 kW/m^2, 20 kW/m^2, 40 kW/m^2, and 80 kW/m^2). This range of heating rates is typical of a wildfire flame front as well as the fuel sample thickness l. For relatively small heating rates (about 10 kW/m^2) both the maximum and average surfaces temperatures are below 250°C regardless of the sample size. Assuming that significant pyrolysate vapour is produced when the temperature of any part of a fuel sample exceeds about

300°C, this suggests that a heating rate of around 10 kW/m^2 is too weak for a fuel sample to produce enough vapour for ignition to take place. At moderate heating rates ($J_0 = 40$ kW/m^2) the maximum temperature exceeds 350°C when the sample diameter is greater than 2 mm. The average surface temperature is less than 300°C for small sample sizes ($l < 2$ mm). The experiments conducted by Cohen and Finney [64] suggest that a small fuel sample ($l = 1$ mm) would not produce enough pyrolysate vapour whereas a larger fuel sample ($l = 12$ mm) subjected to the same heating rate ($J_0 = 41$ kW/m^2 in their experiments) did pilot ignite. The present numerical results are consistent with their findings.

Figure 6.8 shows the temperature profiles, velocity field, and streamlines for $l = 2$ mm, $J_0 = 20$ kW/m^2 and $l = 4$ mm, $J_0 = 40$ kW/m^2. Solid temperature profiles have a similar pattern although they differ significantly in magnitude with a difference between the maximum temperature of almost 200°C. The difference between the maximum and minimum solid temperature is larger for the larger sample which is exposed to a stronger heating rate. The exposed side of the cylinder (right-hand side) would be expected to produce pyrolysate vapour much more quickly than the ‘hidden’ side (left-hand side) of the cylinder.

The natural convection flow entrains fluid from its surroundings and drives it upwards. Figure 6.9 shows the magnitude of the velocity $|\mathbf{u}|$ in m/s against the nondimensional vertical distance from the centre of the cylinder $\overline{y}$. The velocity is zero at the top of the cylinder surface ($\overline{y} = 0.5$) and increases monotonically.

The stronger flow around the larger and hotter cylinder would convect the pyrolysate vapour more quickly which would dilute a potentially flammable mixture with air. This would reduce the chances of the production of a flammable mixture which, in turn, would reduce the possibility of ignition, although none of these issues in the progress towards flaming are examined here. However, it is envisaged that the strongly nonlinear increase in the rate of pyrolysis with temperature is likely to dominate, compared with rising buoyant flow, the chances of the production of a flammable mixture.

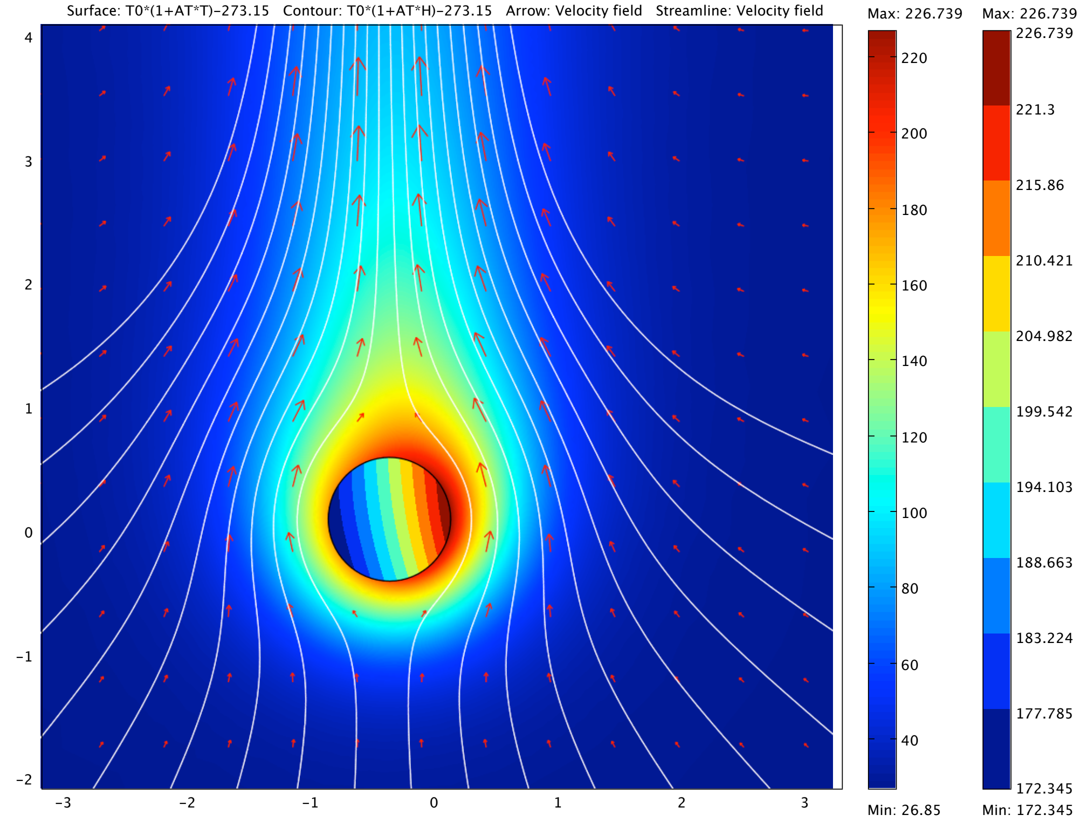

(a) $l = 2$ mm and $J_0 = 20$ kW/m^2

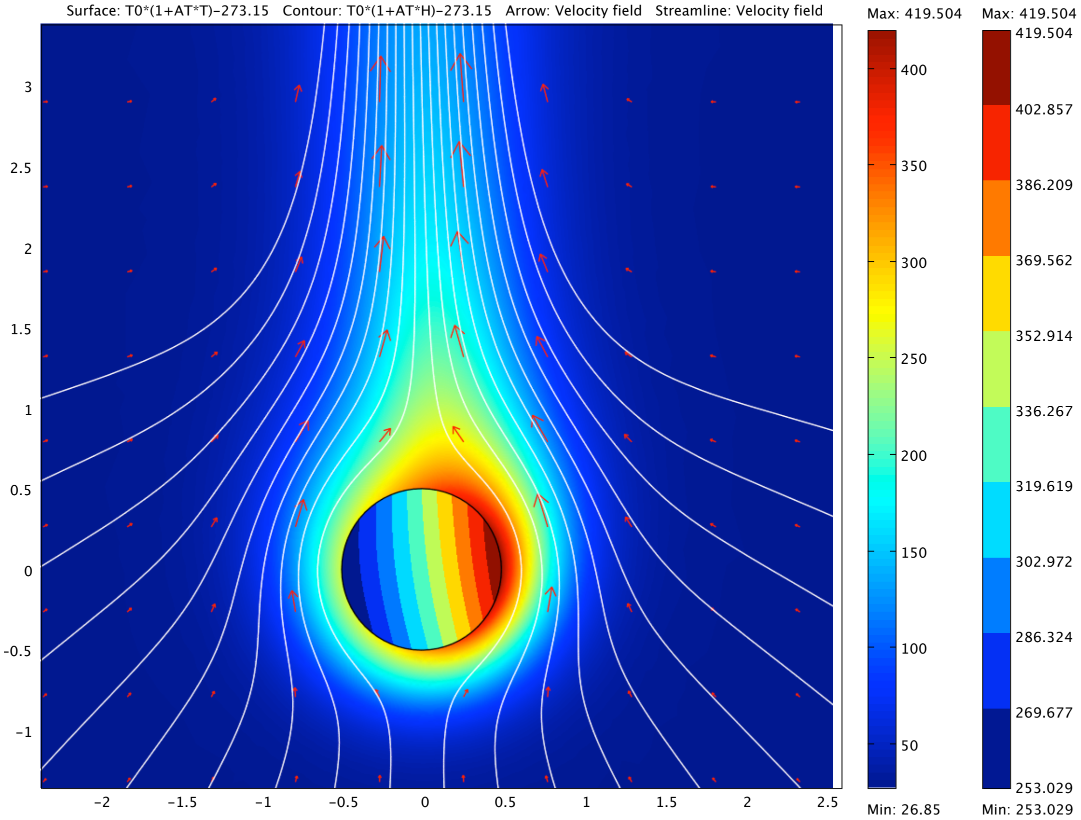

(b) $l = 4$ mm and $J_0 = 40$ kW/m^2

Figure 6.8: Temperature profiles, velocity field, and streamlines for the non-uniform heating of a single circular cylinder in an infinite air domain.

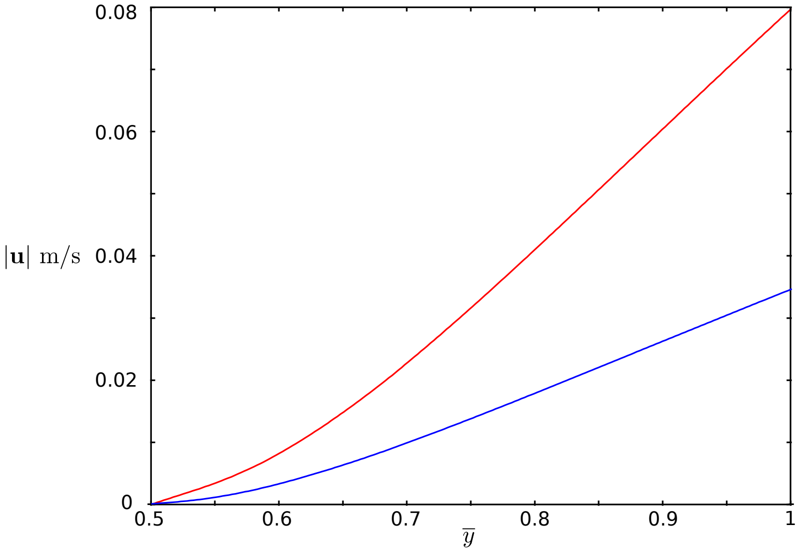

Figure 6.9: Magnitude of of velocity $|\mathbf{u}|$ m/s against the nondimensional vertical distance from the centre of the cylinder $\overline{y}$. *Blue*: $l = 2$ mm and $J_0 = 20$ kW/m^2. *Red*: $l = 4$ mm and $J_0 = 40$ kW/m^2.

6.2 Vertically aligned parallel cylinders

In this section the natural convection flow around two cylinders, heated radiatively from an external panel, is explored. The numerical results for the two isothermal cylinders configuration (Chapter 5) were found to be in good agreement with the literature [69, 80]. The geometry remains the same, namely two parallel horizontal cylinders that are vertically aligned, however they are not isothermal but subjected to a non-uniform radiant heating rate (Chapter 4). The conservation equations in the air domain are the Navier-Stokes equations and conservation of energy equations. The heat conduction equations is applicable in the two solid cylinders. It is assumed that the thermal conductivity and viscosity vary with air temperature. The specific heat capacity does not vary significantly with temperature so it is assumed to be constant. Hence the governing equations are

$$\rho\mathbf{u} \cdot \nabla T = \nabla \cdot \lambda \nabla T$$

$$\rho\mathbf{u} \cdot \nabla\mathbf{u} + \nabla P = \mathrm{Pr}\left(\nabla \cdot \boldsymbol{\tau} + \mathrm{Ra}\,\rho T\,\mathbf{j}\right)$$

$$\nabla \cdot \rho\mathbf{u} = 0$$

$$\rho = \frac{1}{1 + A_T T}$$

$$\nabla^2 \Theta_b = 0$$

$$\nabla^2 \Theta_u = 0$$

where the subscripts b and u denote the bottom (upstream) and upper (downstream) cylinders respectively. The heat flux boundary condition is applicable to both the upstream and downstream cylinder so that

$$B_\lambda \nabla \Theta_b \cdot \hat{\mathbf{n}} - \lambda \nabla T \cdot \hat{\mathbf{n}} = \psi(\vartheta) + D_R \left(1 - (1 + A_T T)^4\right)$$

$$B_\lambda \nabla \Theta_u \cdot \hat{\mathbf{n}} - \lambda \nabla T \cdot \hat{\mathbf{n}} = \psi(\vartheta) + D_R \left(1 - (1 + A_T T)^4\right).$$

Recall that the viscosity and thermal conductivity are temperature dependant and defined to be [86]

$$\eta = \frac{(1 + A_T T)^{3/2}}{1 + A_T T / (1 + C_1/T_0)}$$

$$\lambda = \frac{(1 + A_T T)^{3/2}}{1 + A_T T / (1 + C_2/T_0)}$$

where $C_1 = 0.36\, T_0$ and $C_2 = 0.66\, T_0$ are constants chosen so that η and λ correspond to air. Also the nondimensional parameters can be written as functions of sample size l mm and heating rate J_0 kW/m^2

$$\begin{aligned}
\mathrm{Pr} &= \frac{\nu_0}{\lambda_0} \approx 0.7 \\
A_T &= \left[\frac{T_c - T_0}{T_0}\right] = \frac{T_c - T_0}{T_0} = \frac{l J_0}{\lambda_0 T_0} \approx \frac{40\, l J_0}{T_0} \\
\mathrm{Ra} &= \frac{g\beta l^3 (T_c - T_0)}{\nu_0 \lambda_0} = \frac{g l^3}{\nu_0 \lambda_0} A_T \approx (3000\, l)^3 A_T \\
B_\lambda &= \left[\frac{\lambda_{s0}}{\lambda_0}\right] = \frac{\rho_{s0} c_{s0} \kappa_{s0}}{\rho_0 c_{p0} \kappa_0} \approx 10 \\
D_R &= \left[\frac{\epsilon \varsigma T_0^4}{J_0}\right] \approx \frac{400}{J_0}
\end{aligned}$$

which correspond to the properties of wood and air. Again conditions for the entry and exit of the outer boundary are

$$\mathbf{u} \cdot \mathbf{t} = 0 \qquad T = 0 \qquad \sigma \cdot \mathbf{n} = 0$$

and

$$\mathbf{u} \cdot \mathbf{t} = 0 \qquad \nabla T \cdot \mathbf{n} = 0 \qquad \sigma \cdot \mathbf{n} = 0$$

respectively.

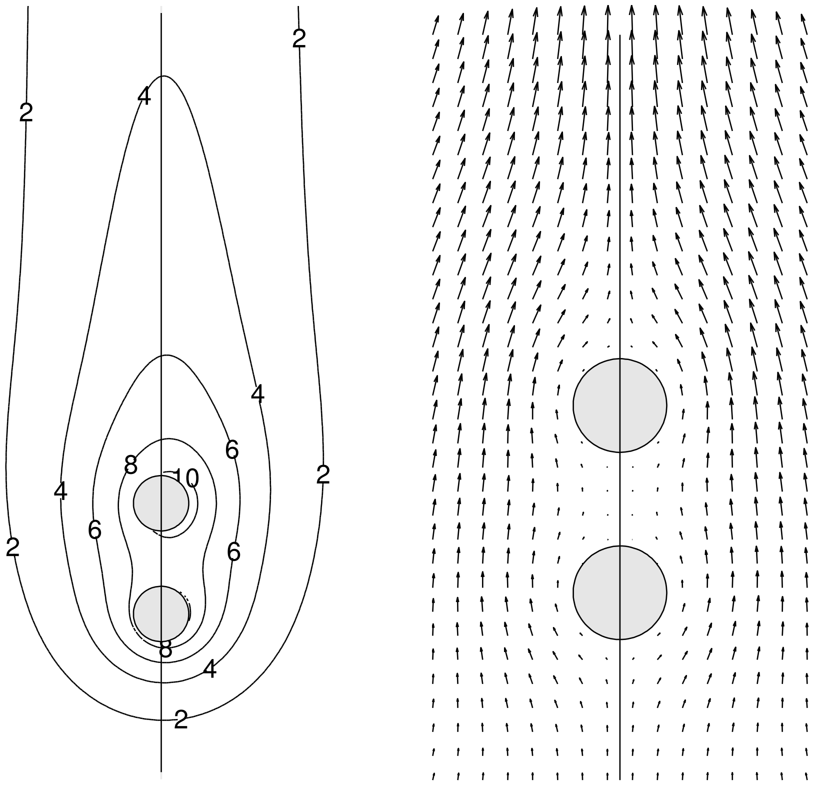

(a) $l = 1$ mm (b) $l = 1$ mm

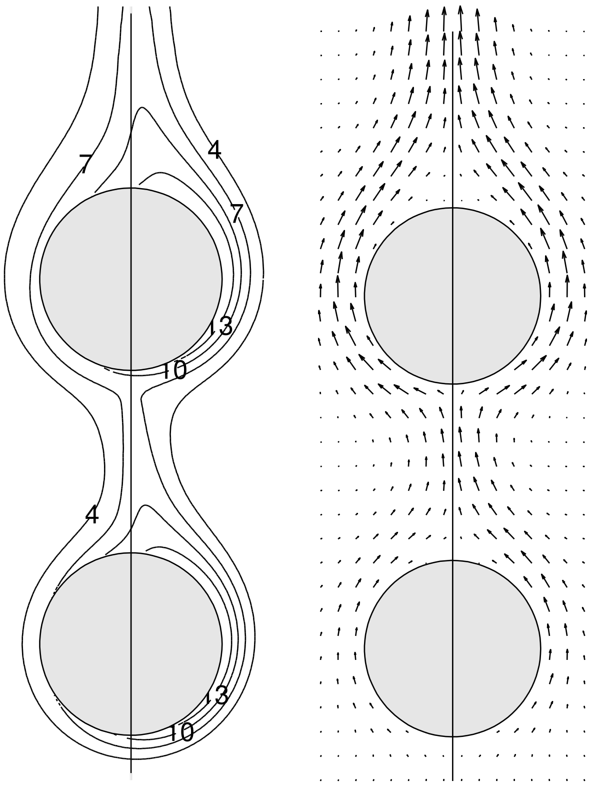

(c) $l = 16$ mm (d) $l = 16$ mm

Figure 6.10: Isotherms and velocity field for the case of $l = 1$ mm and 16 mm with $J_0 = 40\text{kW/m}^2$. Distance between the cylinders is l mm so that $S_D = 1$.

Figure 6.10 shows isotherms and the velocity field for the case when the length scale is $l = 1$ mm and $l = 16$ mm with the heating rate $J_0 = 40$ kW/m^2. The range of sample sizes and the heating rate are representative of typical wildfire vegetation and fire intensities [2, 88]. Isotherms for constant values of T/T_0 are shown where the units for both T and T_0 are °C, so that $T/T_0 = 1$ corresponds to $T = 26.85$°C, since the ambient temperature

$$T_0 = 300 \text{ K} = (300 - 273.15)^\circ\text{C}.$$

The isotherms together with the velocity field show that the downstream cylinder is hotter than the upstream cylinder. This is due to the downstream cylinder being surrounded by air which has been entrained primarily from the air which has passed over the upstream cylinder. A thin boundary layer is observed for $l = 16$ mm where the effects of the non-uniform heating term $\psi(\theta)$ are evident from the asymmetry of the isotherms near the cylinders. Higher temperatures are attained for the larger cylinders.

Figure 6.11 shows the temperature and velocity profiles for sample size $l = 8$ mm and distance between the cylinders $S_D = 1$ for (a) $J_0 = 20$ kW/m^2 and (b) $J_0 = 80$ kW/m^2. The maximum temperature obtained occurs around the downstream cylinder with temperatures around 610 K and 962 K for a heating rate of $J_0 = 20$ kW/m^2 and $J_0 = 80$ kW/m^2 respectively. The flow field appears to be the same. However, the magnitude in the velocity is larger when the samples are exposed to a stronger incident heat flux. This feature is illustrated in Figure 6.12 where the vertical velocity v m/s is plotted against the nondimensional horizontal distance $\overline{x}$ from the centre of the downstream cylinder. The velocity is zero on the boundary of the cylinder (no-slip condition) and tends to zero as $\overline{x} \to 0$. However, for cylinders subjected to a strong heating rate the vertical component of velocity is greater than that of cylinders exposed to more modest heating rates.

Table 6.5 shows the average Nusselt numbers (three decimal places) for the upper (downstream) and bottom (upstream) cylinders. These numbers are divided by the average Nusselt number for the solitary cylinder scenario. The distance between the two cylinders is l mm. Hence the distance between the cylinders increases as the length scale l increases. For every l the corresponding Rayleigh number Ra is also listed (2 significant figures) as Ra only depends on the length scale l and heating rate, which

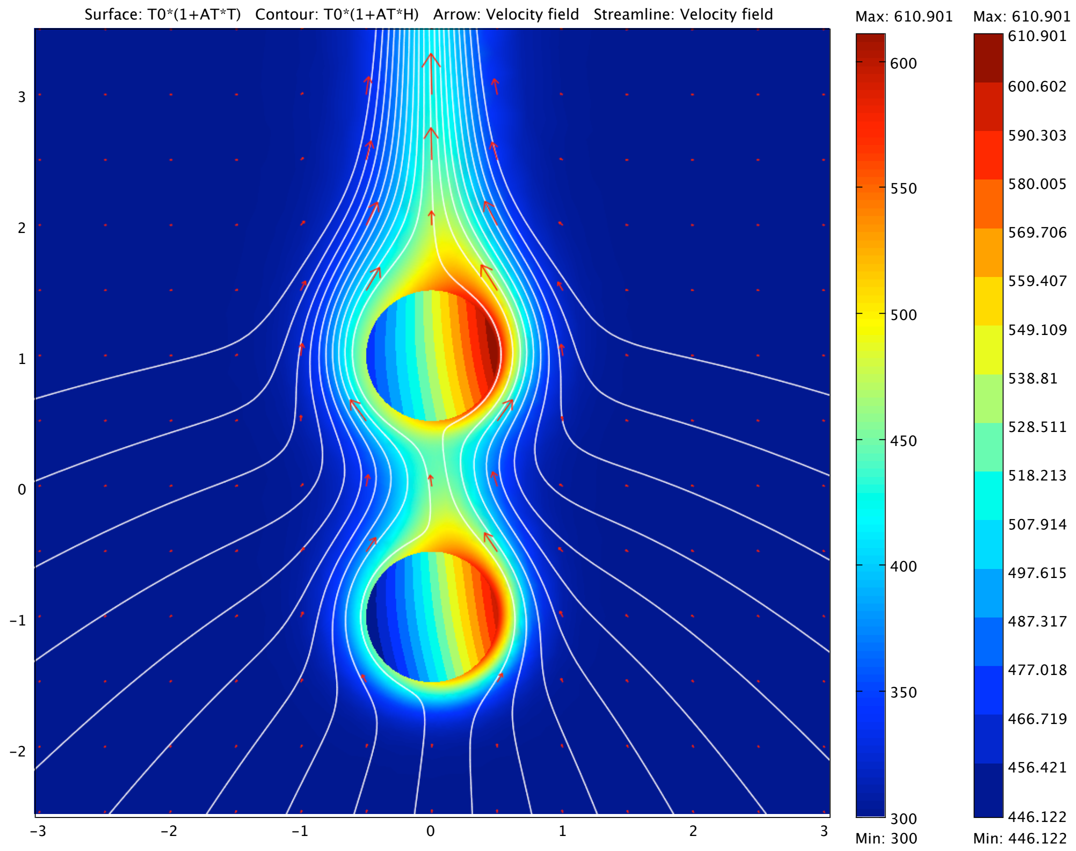

(a) $l = 8$ mm and $J_0 = 20$ kW/m^2.

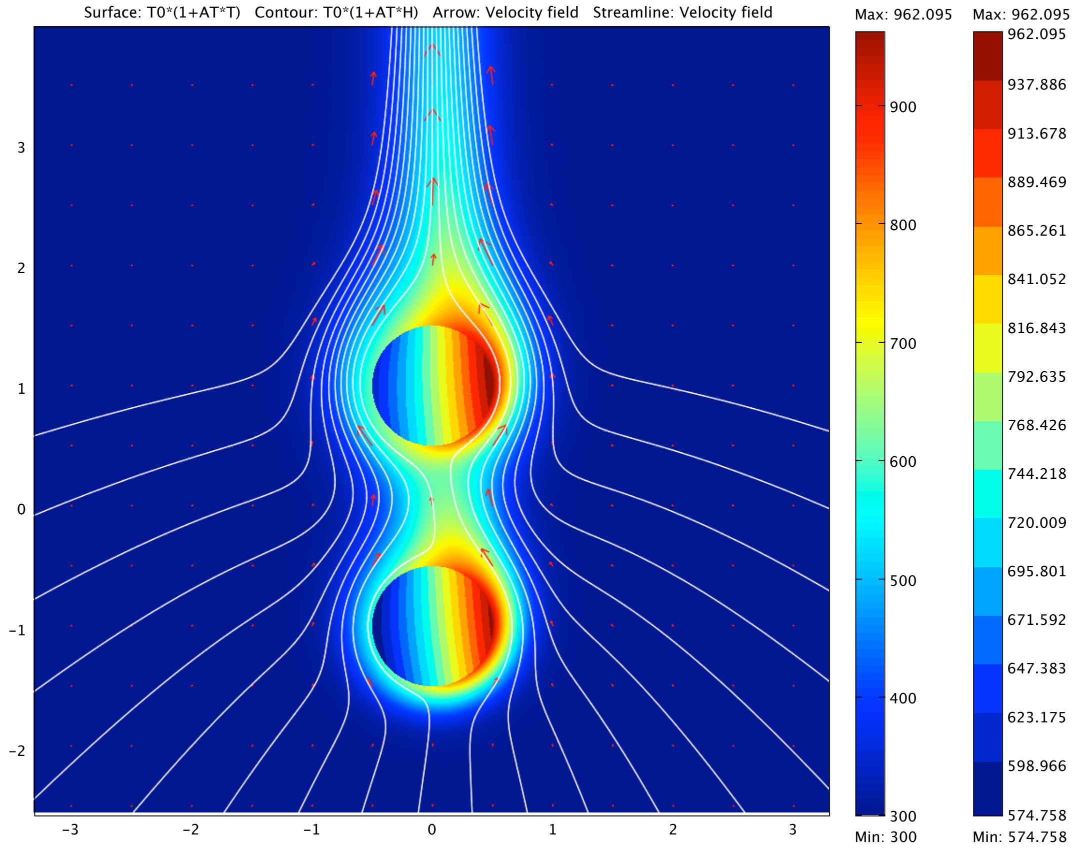

(b) $l = 8$ mm and $J_0 = 80$ kW/m^2.

Figure 6.11: Temperature profiles, velocity fields, and streamlines for two vertically aligned cylinders with $S_D = 1$.

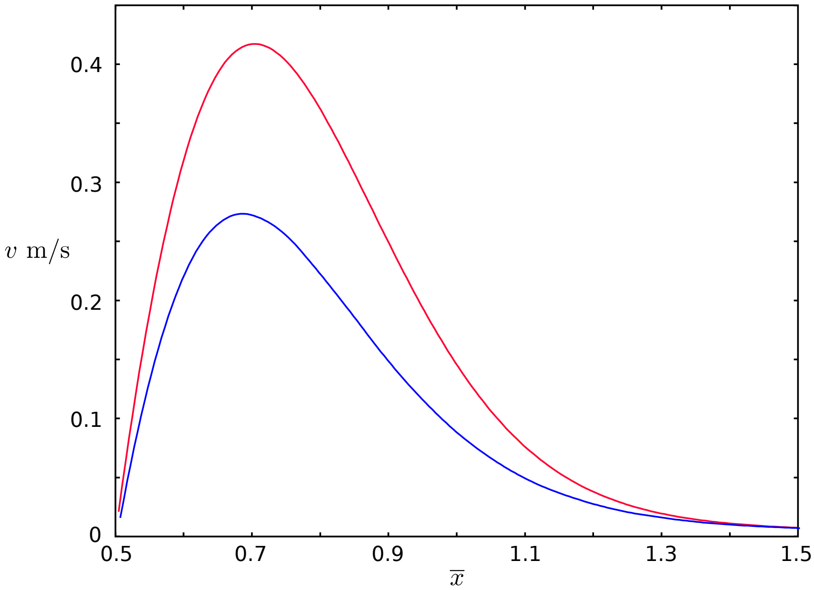

Figure 6.12: Vertical velocity v [m/s] against the nondimensional distance $\overline{x}$ from the centre of the downstream cylinder. Heating rates considered are $J_0 = 20$ kW/m^2 (*blue*) and $J_0 = 80$ kW/m^2 (*red*).

Table 6.5: Ratio of Nusselt number for bottom cylinder and single cylinder ($\overline{\text{Nu}}_b/\overline{\text{Nu}}_1$), and the upper cylinder with the single cylinder ($\overline{\text{Nu}}_u/\overline{\text{Nu}}_1$) with $J_0 = 40$ kW/m^2.

l (mm)	Ra (2 S.F.)	$\overline{\text{Nu}}_b/\overline{\text{Nu}}_1$	$\overline{\text{Nu}}_u/\overline{\text{Nu}}_1$
1	1.4×10^2	0.872	0.627
2	2.3×10^3	0.905	0.641
4	3.7×10^4	0.953	0.659
8	5.9×10^5	0.983	0.679
12	3.0×10^6	0.992	0.691
16	9.4×10^6	0.994	0.694

is constant, J_0. Conductive heat transfer is more dominant at smaller length scales l with convective heat transfer being dominant at larger length scales.

Figure 6.13 shows the temperature profiles, velocity field, and streamlines for (a) $S_D = 0.5$ and (b) $S_D = 2$. The samples size and heating rate remain constant at $l = 2$ mm and $J_0 = 40$ kW/m^2 respectively. For close cylinder spacings, the downstream cylinder is more exposed to the wake of the upstream cylinder. The upstream cylinder acts as a forced convection field [4] for the cylinder above it, resulting in stronger convection currents. The close cylinder spacing means that the temperature difference between the bottom cylinder and the air above it is reduced.

This means that the heat transfer between the cylinders is dominated by convection

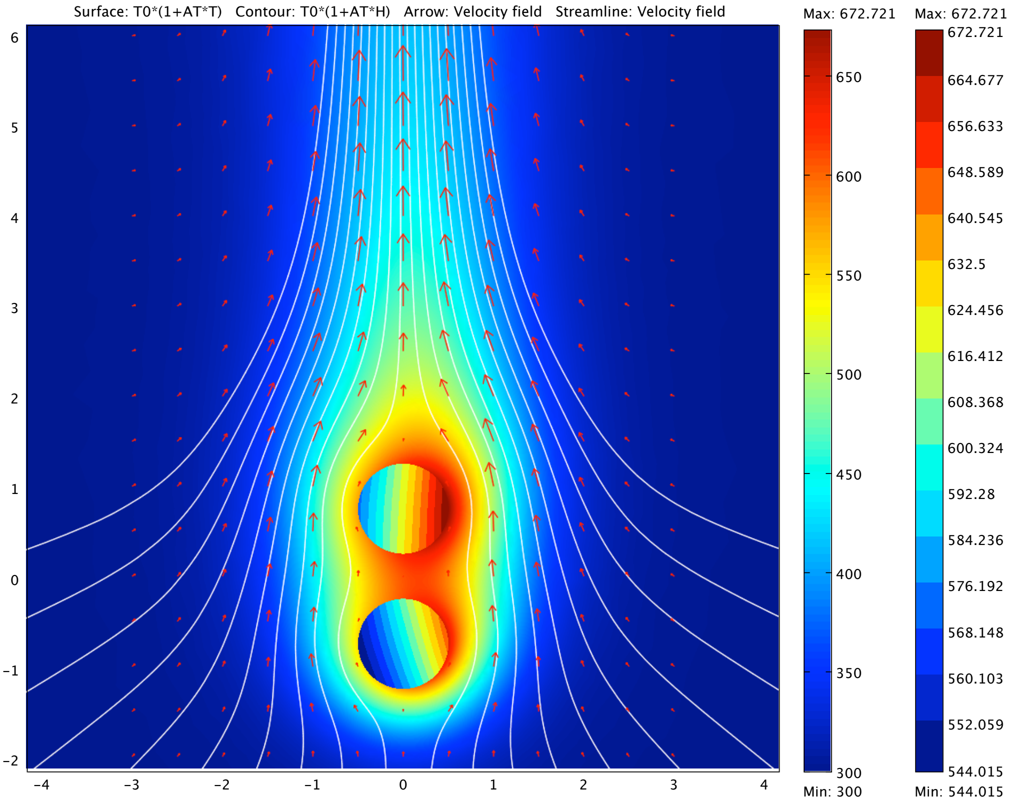

(a) $l = 2$ mm, $J_0 = 40$ kW/m^2, and $S_D = 0.5$.

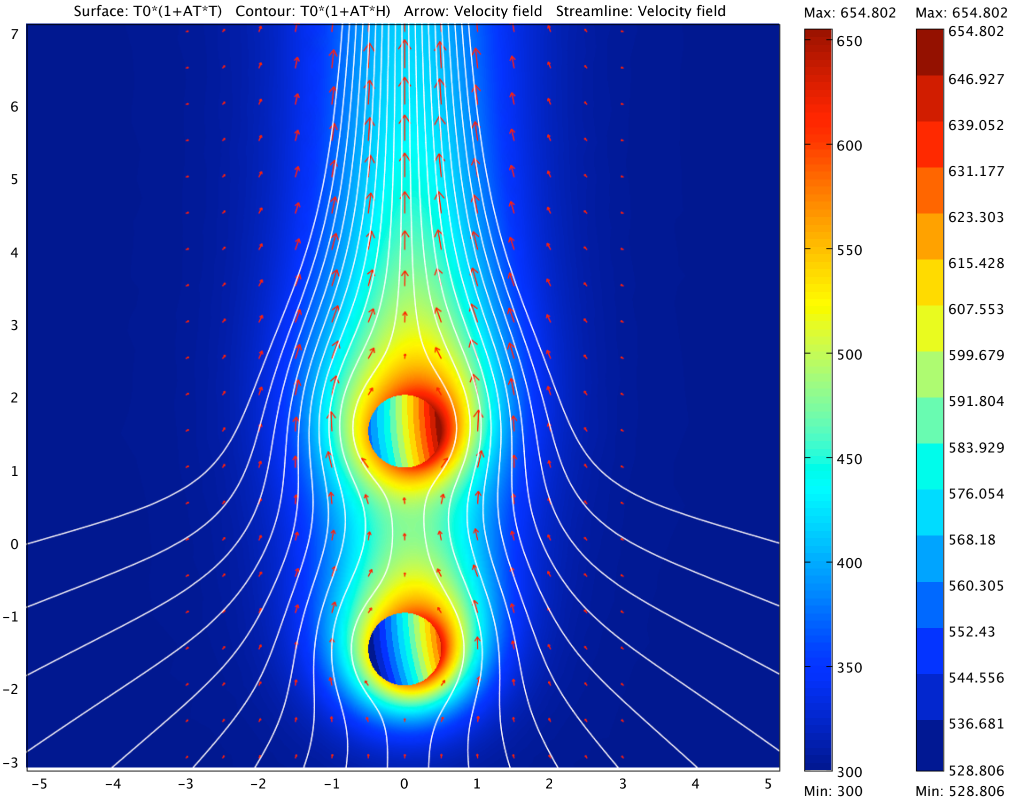

(b) $l = 2$ mm, $J_0 = 40$ kW/m^2, and $S_D = 2$.

Figure 6.13: Temperature profiles, velocity fields, and streamlines for two vertically aligned cylinders. Heating rate and sample size are fixed. Distance between the samples is (a) $S_D = 0.5$ and (b) $S_D = 2$.

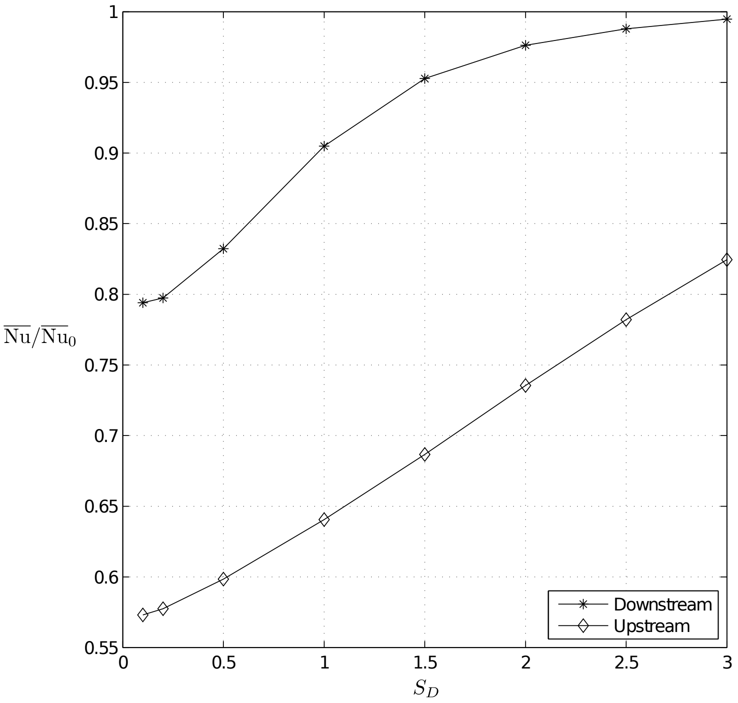

Figure 6.14: Average Nusselt number ratios against distance S_D between the upstream and downstream cylinders. Cylinder diameter and heating rate are $l = 2$ mm and $J_0 = 40$ kW/m^2 respectively.

which is evident from the reduced average Nusselt number at close cylinder spacings (Figure 6.14). At larger cylinder spacings, the heat transfer performance of the upstream cylinder approaches that of the single isolated cylinder (section 6.1.3). The temperatures attained by the cylinders is increased when they are closer together with a maximum temperature of about 672 K when $S_D = 0.5$ and 654 K when $S_D = 2$, a relative increase of about 3%.

6.3 Conclusions

Steady solutions for the natural convection around cylinders subjected to a non-uniform heating rate have been obtained. The governing equations for mass, momentum, and energy, presented in Chapter 4 were solved using COMSOL Multiphysics for non-shadowing configurations.

Variable flow properties and reradiation effects are found to have an appreciable effect on the temperature and flow around an isolated cylinder in an infinite domain. Therefore, it is argued that reradiation effects, together with variable air thermal conductivity and viscosity, need to be included in the model.

Numerical simulations are carried out for a similar configuration to that of the experimental studies of Cohen and Finney [64]. The experimental setup involved exposing wood-based particles to an incident heating rate of $J_0 = 41$ kW/m^2 from a radiating panel. The pyrolysis model results (Chapter 3) suggest that a wooden sample produces enough pyrolysate vapour to support a flame when the surface temperature is around 350–550°C. The present natural convection model suggests that the temperature around a 1 mm sample is well below this threshold. The surface temperature for much of the 12 mm sample exceeds 350°C and reaches a maximum temperature of over 500°C. This suggests that a 12 mm sample, receiving radiant heating of 41 kW/m^2, will produce enough pyrolysate vapour to support a flame. However, for the 1 mm sample, the surface temperature is too low for pyrolysis reactions to take place.

For the single isolated cylinder, the surface temperature increases as the sample size and heating rate increase. Surface temperatures remain well below 350°C at a heating rate of 10 kW/m^2 even when the sample diameter is relatively large ($l = 16$ mm). For large fuel samples the difference between the maximum and minimum temperatures is large. Therefore, it is expected that the side exposed to the radiating panel[2] will produce pyrolysate vapour much more quickly than the unexposed side. Larger fuel samples also have a stronger flow around them compared to smaller samples exposed to the same heating rate. This suggests that the pyrolysate vapour around large fuel samples would convect more quickly which would dilute a potentially flammable mixture with air, thus reducing the possibility of ignition.

Numerical results have also been obtained for two vertically aligned cylinders exposed to a radiant heat flux. These results show that, for close cylinder spacings, the downstream cylinder is hotter than the upstream cylinder. This is due to the downstream cylinder being surrounded by air which has been entrained primarily from the air which has passed over the upstream cylinder. For close cylinder spacings, the downstream cylinder is more exposed to the wake of the upstream cylinder. This is analogous to the upstream cylinder acting as a forced convection field for the cylinder above it which results in stronger convection currents. It is expected, from the solid temperature profile results of the natural convection model, that close sample

---

[2] This is the side of the cylinder where the maximum surface temperature is located.

spacings would increase the chances of flammability, particular for the cylinder which is downstream of the rising buoyant flow. However, the flow is stronger around hotter cylinders which would dilute a potentially flammable mixture with air. This would reduce the possibility of the production of a flammable mixture. However, it is envisaged that the strongly nonlinear increase in the rate of pyrolysis with temperature is likely to dominate in affecting the chance of flammability conditions.

Chapter 7

Numerical results for shadowing effects

The mathematical procedure for calculating the amount of radiation blocked from one cylinder in reaching another was presented in Chapter 4 (section 4.3). For multiple cylinders in arbitrary locations it is possible that one cylinder might block some of the radiation from the panel from reaching another cylinder. Any point (x, y) on a cylinder, for which the tangent angle is ϑ, needs to be considered in relation to any other cylinder $\mathcal{C}_k$ with centre (x_k, y_k) and radius a (Figure 7.1).

The blocked radiation is expressed as a negative radiative contribution arriving at the point (x, y) and can therefore be expressed as

$$\tilde{J}_k = -J_0 \times \frac{2}{\pi} \left(\frac{\tilde{\zeta}_k}{1 + \tilde{\zeta}_k} + \arctan(\tilde{\zeta}_k) \right) \times \tilde{\psi}_k(\vartheta)$$

with

$$\tilde{\zeta}_k \approx \frac{1}{6} \left(\frac{z_{\mathrm{B}}/x_{\mathrm{B}}}{\left(1 + \tan^2 \gamma_{\mathrm{A}}\right)^{1/2}} + \frac{4 z_{\mathrm{B}}/x_{\mathrm{B}}}{\left(1 + \tan^2\left(\left(\gamma_{\mathrm{A}} + \gamma_{\mathrm{B}}\right)/2\right)\right)^{1/2}} + \frac{z_{\mathrm{B}}/x_{\mathrm{B}}}{\left(1 + \tan^2 \gamma_B\right)^{1/2}} \right)$$

and

$$\tilde{\psi}_k(\vartheta) = \frac{1}{2} \left[\cos\left(\min\left\{\pi, \max\left[0, \gamma_{\mathrm{A}} - \vartheta\right]\right\}\right) - \cos\left(\max\left\{0, \min\left[\pi, \gamma_{\mathrm{B}} - \vartheta\right]\right\}\right)\right).$$

The cylinder $\mathcal{C}_k$ blocks radiation from the panel between the angles

$$\gamma_{\mathrm{A}} = \min\left\{\theta_{\mathrm{B}}, \max\left[\theta_{\mathrm{A}}, \beta - \alpha\right]\right\} \quad \text{and} \quad \gamma_{\mathrm{B}} = \max\left\{\theta_{\mathrm{A}}, \min\left[\theta_{\mathrm{B}}, \beta + \alpha\right]\right\}$$

for which the angles γ_{A} and γ_{B} are equal if there is no shadowing. Angles γ_{A} and γ_{B}, as well as ϑ will, in general, vary for different points (x, y) on the surface of the cylinder.

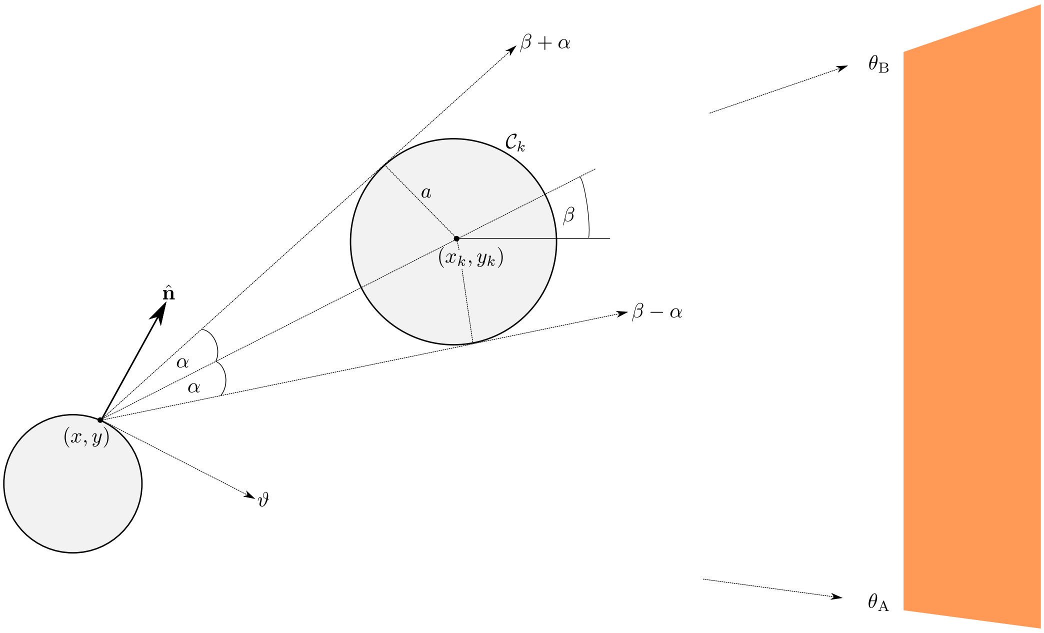

Figure 7.1: Shadowing effect for a point (x, y) on a cylinder due to the presence of cylinder $\mathcal{C}_k$ which blocks some of the radiation from the panel. Figure is not to scale as the radiating panel is assumed to be much further away from cylinder $\mathcal{C}_k$ when modelling the heat transfer.

If there is blocking by multiple cylinders (for, say, $k = 1, 2$, etc.) then additional contributions will arise for each corresponding value of k. However particular care must be taken not to double up the effect when one of these cylinders already partly falls within the shadow of another. It is worth exploring whether this approach of taking the blocking of radiation into account gives results significantly different to when shadowing effects are neglected. The most simple case of shadowing is when one cylinder blocks some of the radiation from the panel from reaching another.

7.1 Single cylinder shadowing

Consider the case of a cylinder $\mathcal{C}$ receiving a reduced heating rate from a radiating panel due to the presence of cylinder $\mathcal{C}_1$. The cylinders, with equal nondimensional radii a, are assumed to be aligned in a row with a centre-to-centre distance of D (Figure 7.2). Recall that $l = 2a$ mm is the cylinder diameter. Let $S_D = D/l$ be the nondimensional centre-to-centre distance between the two cylinders $\mathcal{C}$ and $\mathcal{C}_1$. The two cylinders are in contact when $S_D = 1$. Varying the parameter S_D would alter the degree of radiation which is blocked by $\mathcal{C}_1$ from reaching cylinder $\mathcal{C}$ as described by the mean inclination angle $\tilde{\zeta}_1$ and the view factor $\tilde{\psi}_1(\vartheta)$ (Chapter 4). Let x_B, y_B,

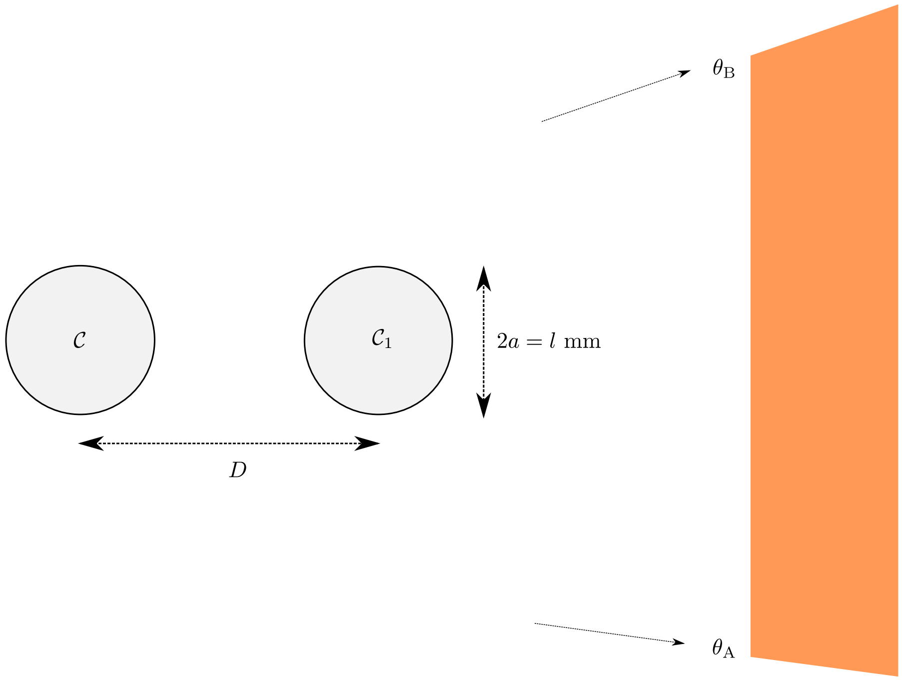

Figure 7.2: Cylinder $\mathcal{C}_1$ blocks some of the radiation from the panel from reaching cylinder $\mathcal{C}$. The centre-to-centre distance between the cylinders is D and the diameter is $2a = l$ mm.

and z_B be the lengths, in mm, of the cylinder $\mathcal{C}$ to the radiating panel, the radiating panel half-height and the cylinder half-width respectively. For now let $x_B = 100$ mm, $y_B = 200$ mm, and $z_B = 250$ mm, dimensions which are similar to the panel used in the experiments of Cohen and Finney [64]. Any panel in which each of the lengths x_B, y_B, and z_B increase by some factor generates the same radiative field around the cylinders. The importance of assuming variable, as opposed to constant, flow properties was established in Chapter 4. Therefore it will be assumed that the viscosity and thermal conductivity vary with temperature

$$\eta = \frac{(1 + A_T T)^{3/2}}{1 + A_T T / (1 + C_1/T_0)}$$

$$\lambda = \frac{(1 + A_T T)^{3/2}}{1 + A_T T / (1 + C_2/T_0)}$$

with $C_1 = 0.36\,T_0$ and $C_2 = 0.66\,T_0$ constants which correspond to air [86], and T_0 is the ambient temperature (300 K). Recall that the heating intensity is

$$A_T = (T_c - T_0)/T_0 = lJ_0/\lambda_0 T_0.$$

The radiating panel is assumed to be composed of four segments as before but the negative contribution due to the shadowing is modelled as a single negative contribution.

This approach is favoured in order to simplify the reconciliation of the overlap between the shadowing angles and the panel angles.

The total radiation received at a point (x, y) on the surface of cylinder $\mathcal{C}$ is

$$J_{\text{Total}} = J + \tilde{J}_1$$

where J denotes radiation received as though cylinder $\mathcal{C}_1$ does not shadow $\mathcal{C}$ and $\tilde{J}_1$ is the negative contribution due to the presence of $\mathcal{C}_1$ which blocks some of the radiation reaching $\mathcal{C}$.

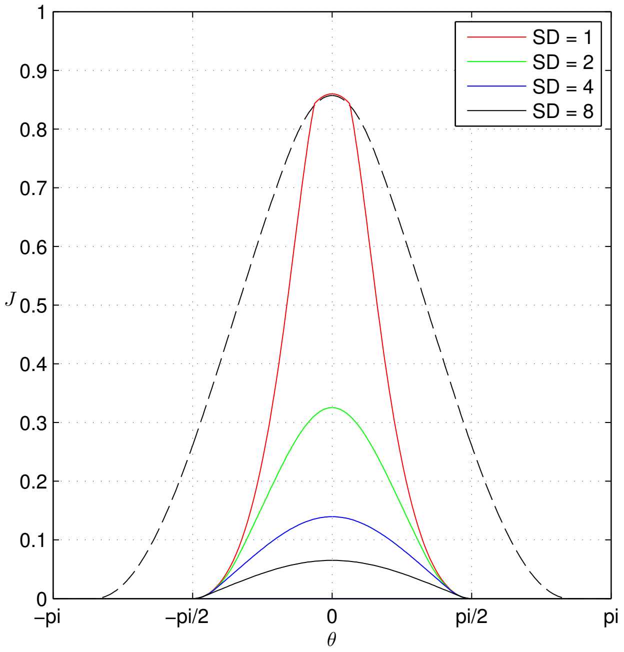

Figure 7.3: Full radiation J (*solid*) and negative radiation $-\tilde{J}_1$ (*dashed*) normalised with incident heat flux J_0 kW/m^2 around cylinder $\mathcal{C}$ with $S_D = 2$.

Figure 7.3 is a plot of the functions J and $-\tilde{J}_1$ which shows the significance of the shadowing contribution for the nondimensional centre-to-centre distance $S_D = 2$. For large values of S_D the shadowing effects become negligible. However as $S_D \to 1$ the shadowing becomes more pronounced.

Figure 7.4 shows a comparison between the isotherms, in °C, when shadowing effects are, and are not, taken into account $(S_D = 2)$ as well as the isotherms for the single cylinder case. The surrounding air is hotter when cylinders are closer together due to the increased drag on the flow around and in between the cylinders. This reduces the cooling effect of the surrounding air flow. When shadowing effects are included

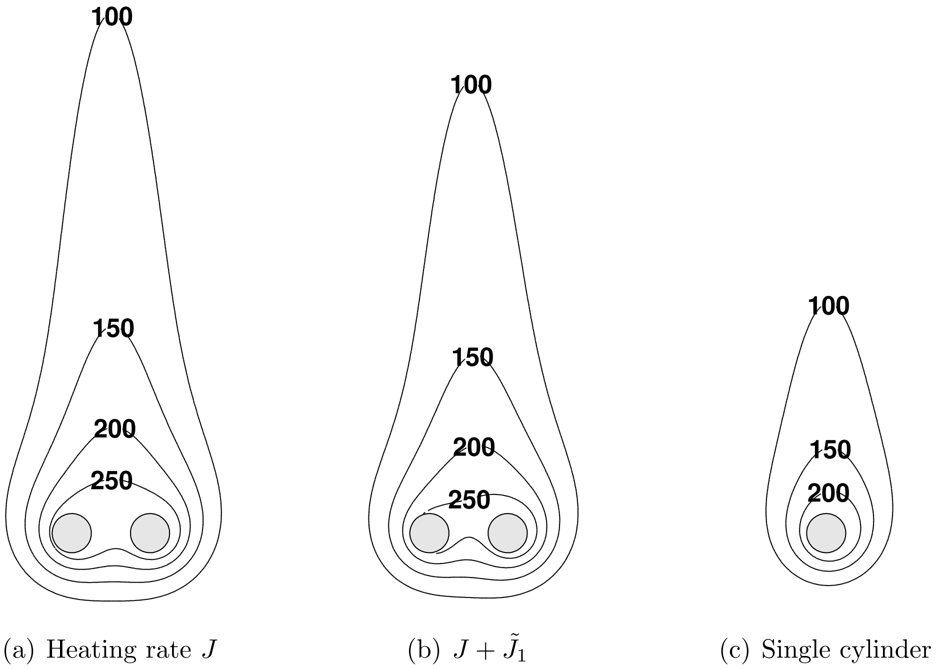

(a) Heating rate J (b) $J + \tilde{J}_1$ (c) Single cylinder

Figure 7.4: Isotherms (°C) (a) without shadowing effects, (b) with shadowing effects modelled, and (c) for the single isolated cylinder. The length scale is $l = 1$ mm with $S_D = 2$. The incident heating rate is $J_0 = 40$ kW/m^2.

a reduced surrounding air temperature is visible, particularly around the shadowed cylinder $\mathcal{C}$.

Figure 7.5 gives a comparison of the surface temperature. A significant reduction in temperature is observed around cylinder $\mathcal{C}$ when shadowing effects are taken into account. The surface temperature around cylinder $\mathcal{C}_1$ is reduced only slightly when shadowing effects are taken into account even though the heating rate for $\mathcal{C}_1$ is unchanged as the cylinder receives the full radiation from the panel. The reduction is due to the decreased heat transfer between cylinders $\mathcal{C}$ and $\mathcal{C}_1$ (Figure 7.6) since the temperature around $\mathcal{C}$ is significantly reduced when shadowing effects are modelled.

These numerical results which model the blocking of radiation from reaching a cylinder suggest that significant changes in the temperature and velocity profile are observed. The shadowing contribution is more pronounced when the cylinder bodies are closer together ($S_D \to 1$). These results suggest that shadowing effects need to be taken into account particularly for small values of S_D.

Figure 7.7 shows the local Nusselt number for two horizontally aligned cylinders, of diameter $l = 1$ mm, subjected to an incident heat flux of $J_0 = 40$ kW/m^2, with

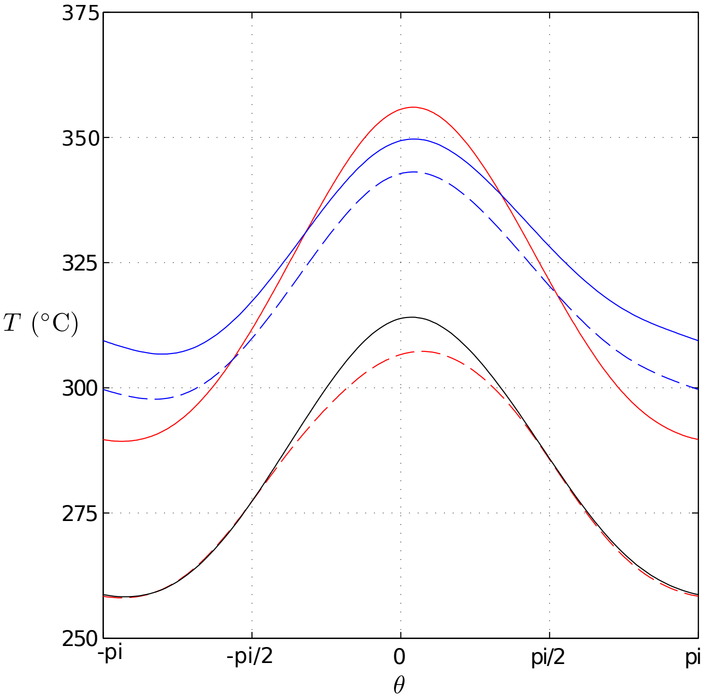

Figure 7.5: Comparison of surface temperature T in °C around $\mathcal{C}$ (*red*), $\mathcal{C}_1$ (*blue*) and the single cylinder (*black*) when shadowing effects are (dashed) and are not (solid) modelled. The length scale $l = 1$ mm and the incident heating rate $J_0 = 40$ kW/m^2.

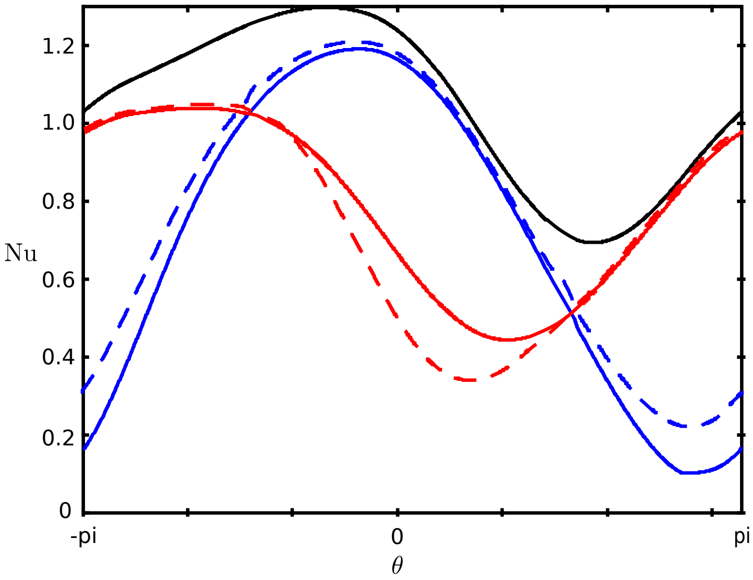

Figure 7.6: Comparison of local Nusselt number around $\mathcal{C}$ (*red*), $\mathcal{C}_1$ (*blue*) and the single cylinder (*black*) when shadowing effects are (dashed) and are not (solid) modelled. The length scale is $l = 1$ mm and the incident heating rate is $J_0 = 40$ kW/m^2.

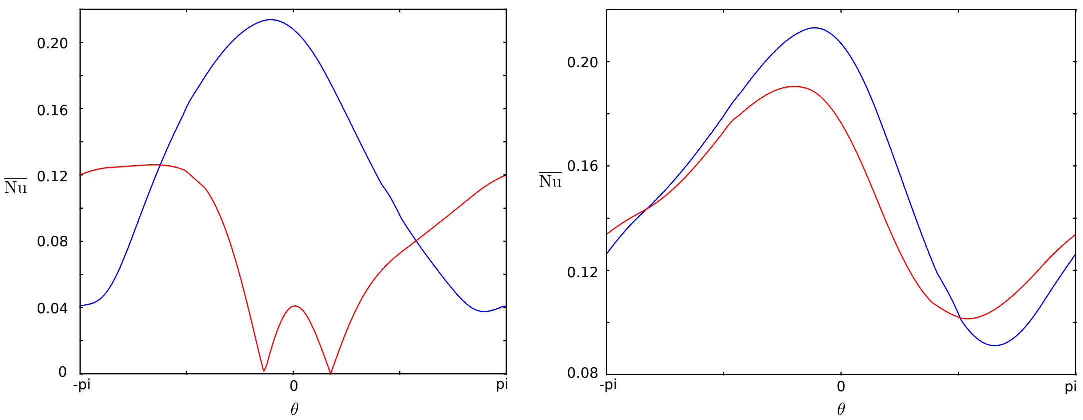

(a) $S_D = 1.2$. (b) $S_D = 5$.

Figure 7.7: Local Nusselt number for two horizontally aligned cylinders $\mathcal{C}$ (*red*) and $\mathcal{C}_1$ (*blue*). Heating rate and sample size are fixed ($l = 1$ mm and $J_0 = 40$ kW/m^2). Distance between the samples is (a) $S_D = 1.2$ and (b) $S_D = 5$.

nondimensional centre-to-centre distance of (a) $S_D = 1.2$ and (b) $S_D = 5$. Figure 7.8 shows the corresponding temperature and velocity profiles.

It is clear that for close cylinder spacings the heat transfer between the cylinders is dominated by conduction. For cylinder $\mathcal{C}$ the local Nusselt number drops significantly (Figure 7.7) around the region that is shadowed from cylinder $\mathcal{C}_1$. This suggests that the flow and temperature in that particular shadowed region are reduced. This behaviour could be conducive for ignition purposes. The reduced flow, with the close cylinder spacing, would allow pyrolysates from both cylinders $\mathcal{C}$ and $\mathcal{C}_1$ to mix with air close to the surface without being strongly diluted by the air.

The surface temperature around cylinder $\mathcal{C}_1$ is increased by about 50°C when the cylinder spacing is reduced to $S_D = 1.2$ from $S_D = 5$ (Figure 7.9). Such a large change in the temperature around the sample can make a large difference in the rate at which pyrolysate vapour is produced (Chapter 3). At large cylinder spacings, the heat transfer is dominated by convection. This means that the cylinders are mostly losing heat due to the flow around them rather than heat being conducted to the surrounding air.

Figure 7.10 shows the vertical velocity v m/s measured along a horizontal line moving right from the centre of cylinder $\mathcal{C}_1$. This is the cylinder which is fully exposed to the radiating panel. This flow is stronger when the cylinders are close together.

This reveals a mixed set of conditions affecting the chance of ignition. The should act to increase the rate of pyrolysate production while the increased flow rate would

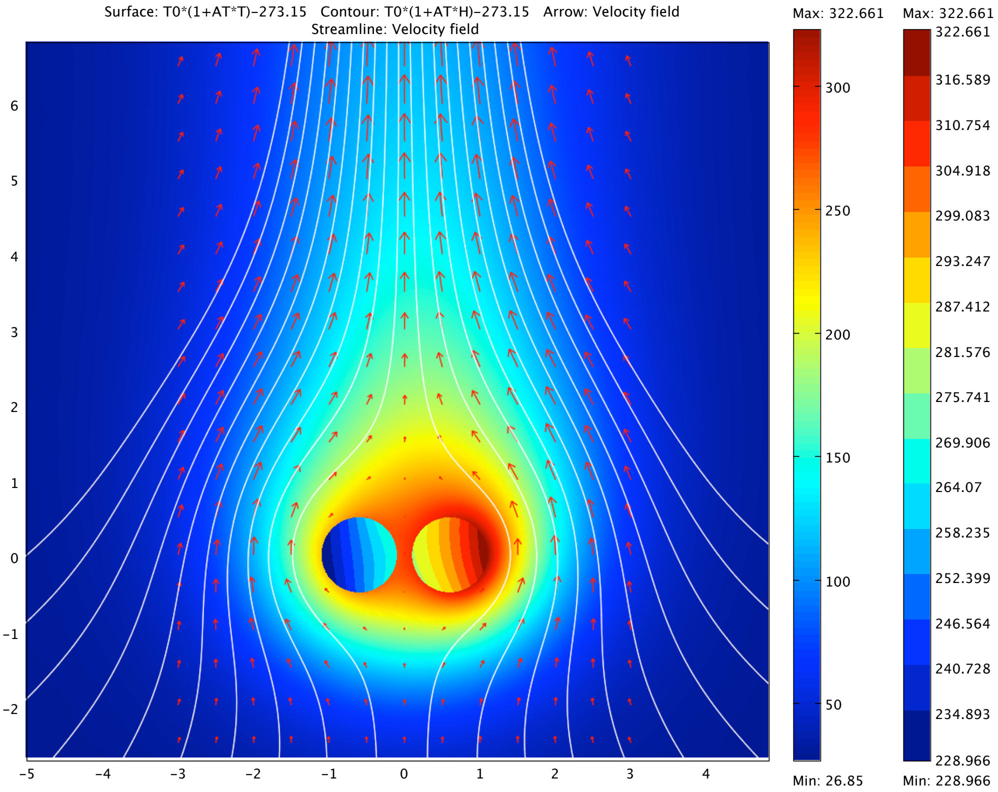

(a) $l = 1$ mm, $J_0 = 40$ kW/m^2, and $S_D = 1.2$.

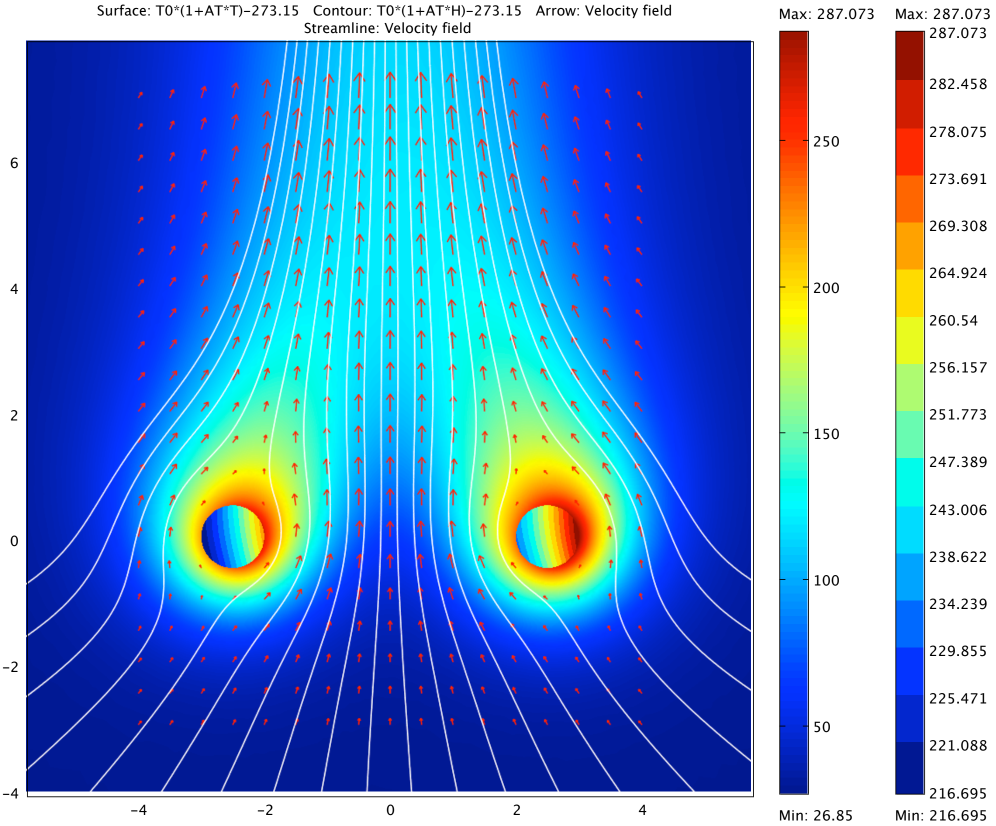

(b) $l = 1$ mm, $J_0 = 40$ kW/m^2, and $S_D = 5$.

Figure 7.8: Temperature profiles, velocity fields, and streamlines for two horizontally aligned cylinders. Heating rate and sample size are fixed. Distance between the samples is (a) $S_D = 1.2$ and (b) $S_D = 5$.

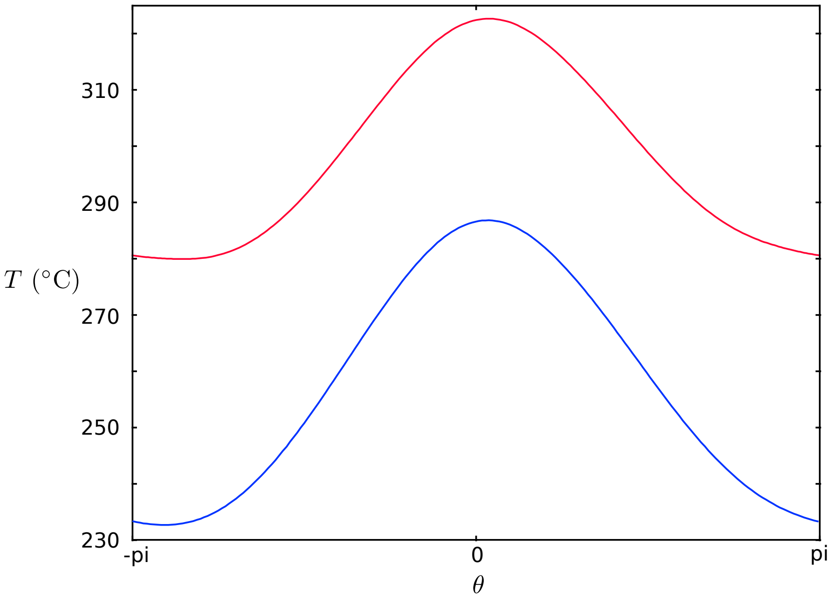

Figure 7.9: Surface temperature around cylinder $\mathcal{C}_1$ for $S_D = 1.2$ (*red*) and $S_D = 5$ (*blue*). Heating rate is $J_0 = 40$ kW/m^2 and sample diameter is $l = 1$ mm.

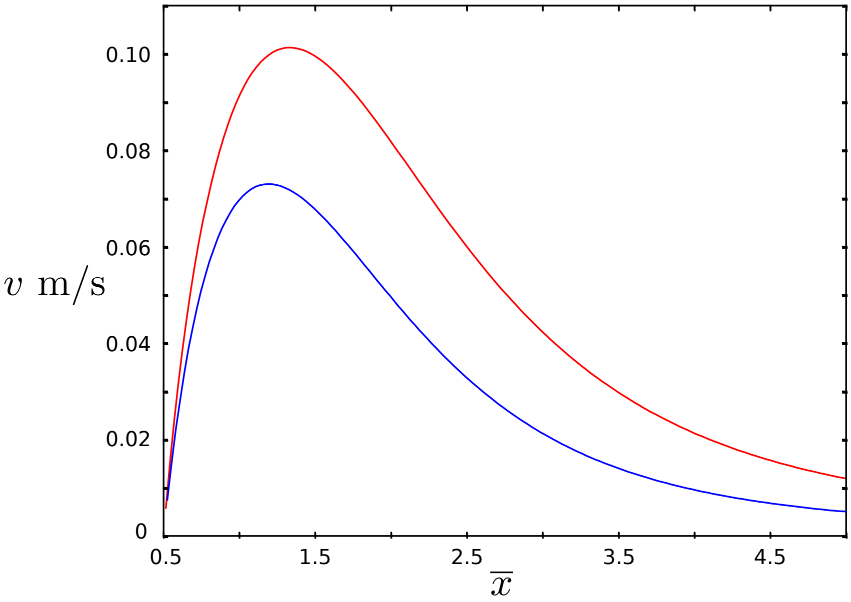

Figure 7.10: Vertical velocity v against horizontal distance from the centre of cylinder $\mathcal{C}_1$ for $S_D = 1.2$ (*red*) and $S_D = 5$ (*blue*). Heating rate is $J_0 = 40$ kW/m^2 and sample diameter is $l = 1$ mm.

tend to dilute the pyrolysates more strongly. Of these two effects, the strongly nonlinear increase in the rate of pyrolysis with temperature is likely to dominate.

7.2 Regular grid of cylinders

In the previous section, shadowing effects were explored when one cylinder blocks some of the radiative heat, from the panel, in reaching an adjacent cylinder. The effect of radiation being blocked by more than one cylinder from reaching another is modelled in this section. As a starting point, the heating of a regular square 2×2 grid of cylinders is explored (see Figure 7.11) for various nondimensional centre-to-centre distances S_D.

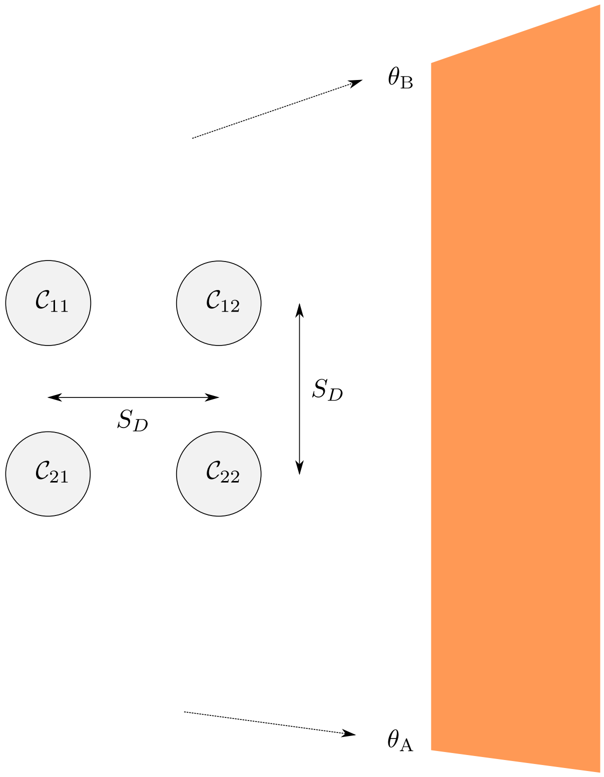

Figure 7.11: A 2×2 array of cylinders. The cylinders are labelled analogously to the entries of a matrix [89].

In a 3×3 array, or larger, the added problem of overlapping shadowing contributions is present when the cylinders are sufficiently close together.

7.2.1 2 × 2 array

Cylinders $\mathcal{C}_{11}$ and $\mathcal{C}_{21}$ receive a reduced heating rate from the radiating panel due to the presence of cylinders $\mathcal{C}_{12}$ and $\mathcal{C}_{22}$ which block some of the radiation from the panel. The nondimensional centre-to-centre distance between orthogonally arranged adjacent cylinders on a square grid is S_D and the maximum and minimum angles from a cylinder to the panel are θ_A and θ_B respectively. It is assumed that the size of the array is small compared to the distance between the radiating panel and array of cylinders. Numerical results for a panel with dimensions 200 mm × 250 mm and a distance 100 mm from the array of cylinders have been obtained.

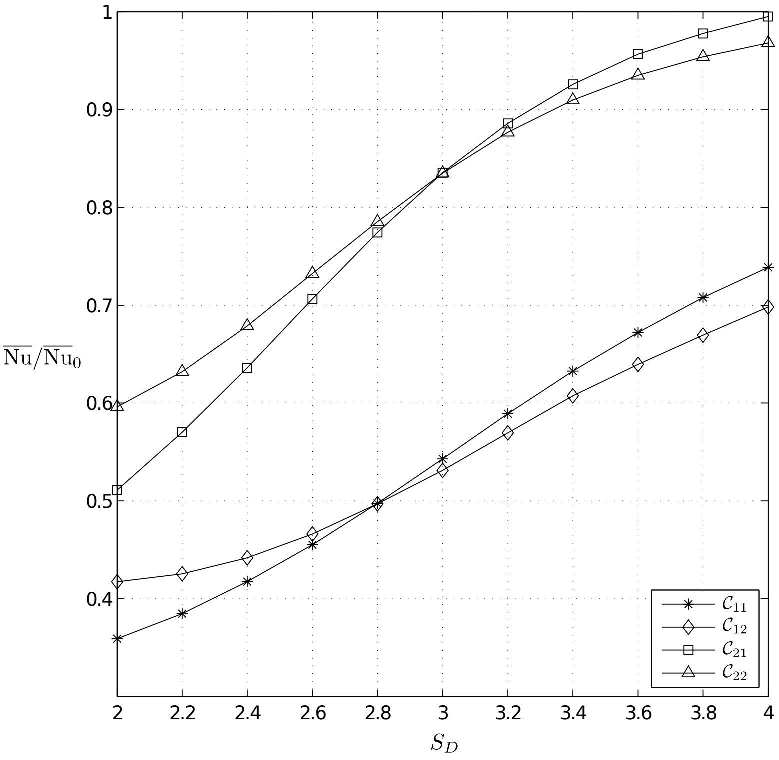

Figure 7.12: Average Nusselt number ratios against the nondimensional centre-to-centre distance S_D. Sample size is $l = 1$ mm and the heating rate is $J_0 = 40$ kW/m^2.

Figure 7.12 shows the average Nusselt number ratios $\overline{\text{Nu}}/\overline{\text{Nu}}_0$ against the centre-to-centre nondimensional distance S_D. The sample size and heating rate are $l = 1$ mm and $J_0 = 40$ kW/m^2 respectively. Recall that the Nusselt number for the non-uniform heating rate used in the present study is

$$\begin{aligned}\mathrm{Nu}_\psi &= -\frac{\nabla T\cdot\hat{\mathbf{n}}}{T}\\ &= \frac{\psi(\vartheta)+D_R\left(1-(1+A_T T)^4\right)-B_\lambda\,\lambda_s\nabla\Theta\cdot\hat{\mathbf{n}}}{\lambda T}.\end{aligned}$$

In order to compare results with the natural convection around a single cylinder, the average Nusselt number around a cylinder $\mathcal{C}_{ij}$, where $i, j \in \{1, 2\}$ is normalised by the average Nusselt number of the single cylinder $\overline{\mathrm{Nu}}_0$.

Figure 7.13 shows temperature profiles, velocity fields, and streamlines for $S_D = 2$ and $S_D = 4$. The heating rate is $J_0 = 40$ kW/m^2 and the sample size is $l = 1$ mm. Cylinder $\mathcal{C}_{12}$ attains the largest temperature mainly due to the hot buoyant air that has flowed over cylinder $\mathcal{C}_{22}$. It also, like cylinder $\mathcal{C}_{22}$, receives the full radiation from the panel. Larger solid and air temperatures are obtained for smaller values of S_D which suggests that closer sample spacings better encourage ignition conditions.

Figure 7.14 shows the vertical velocity v plotted against the horizontal distance measured to the right from the centre of cylinders $\mathcal{C}_{22}$ and $\mathcal{C}_{12}$ for $S_D = 2$ and $S_D = 4$. The vertical flow on the hotter side of the downstream cylinder ($\mathcal{C}_{12}$) is stronger compared to that of the upstream cylinder ($\mathcal{C}_{22}$). The vertical flow is also stronger for $S_D = 2$ compared with $S_D = 4$. To some extent this stronger flow would act to dilute any pyrolysate vapours produced. This would inhibit the production of a flammable mixture.

Figure 7.15 shows the vertical velocity v against horizontal distance from the centre of cylinders $\mathcal{C}_{21}$ and $\mathcal{C}_{11}$ for $S_D = 2$ and $S_D = 4$. Again, the heating rate is $J_0 = 40$ kW/m^2 and sample diameter is $l = 1$ mm. At $\overline{x} = 0.5$ there is no flow as a consequence of the no slip boundary condition. For $S_D = 2$, at $\overline{x} = 1.5$ there is also no flow. This is due to the presence of cylinders $\mathcal{C}_{12}$ and $\mathcal{C}_{22}$ so that the no slip condition is again imposed. Similarly, for $S_D = 4$, the presence of cylinders$\mathcal{C}_{12}$ and $\mathcal{C}_{22}$ means that there is no flow at $\overline{x} = 3.5$. Vertical flow in-between the cylinders is much stronger at $S_D = 4$ as is the flow between the downstream cylinders. The vertical flow between the downstream cylinders for $S_D = 4$ is actually stronger than the flow on the hotter side of cylinder $\mathcal{C}_{12}$ at $S_D = 2$.

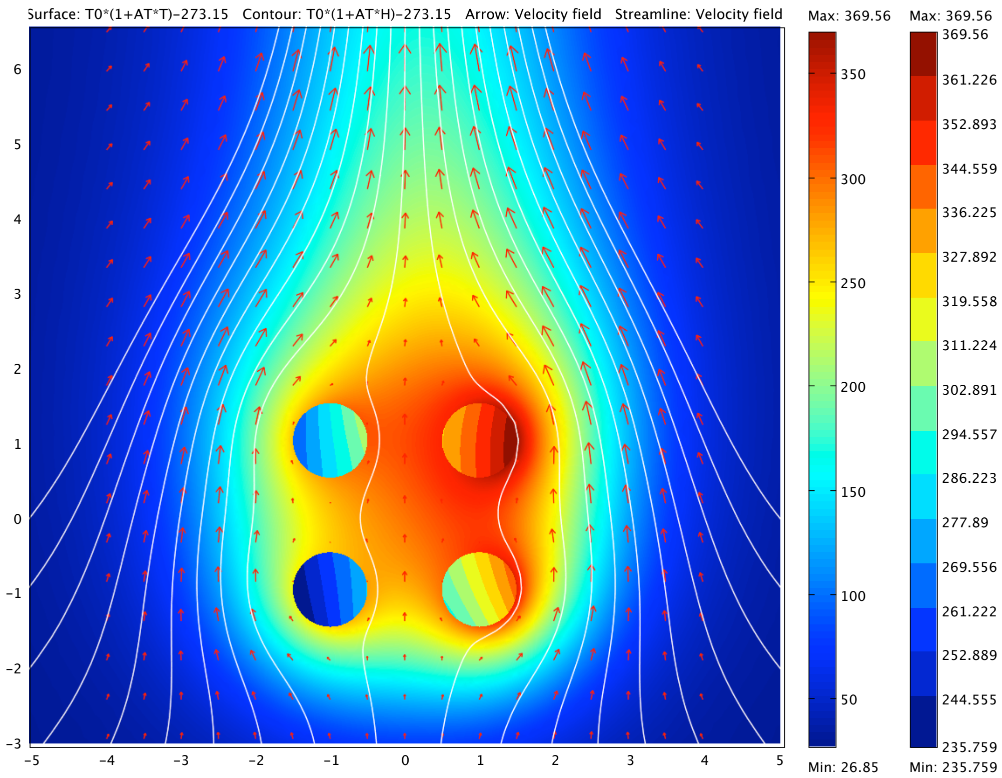

(a) $S_D = 2$.

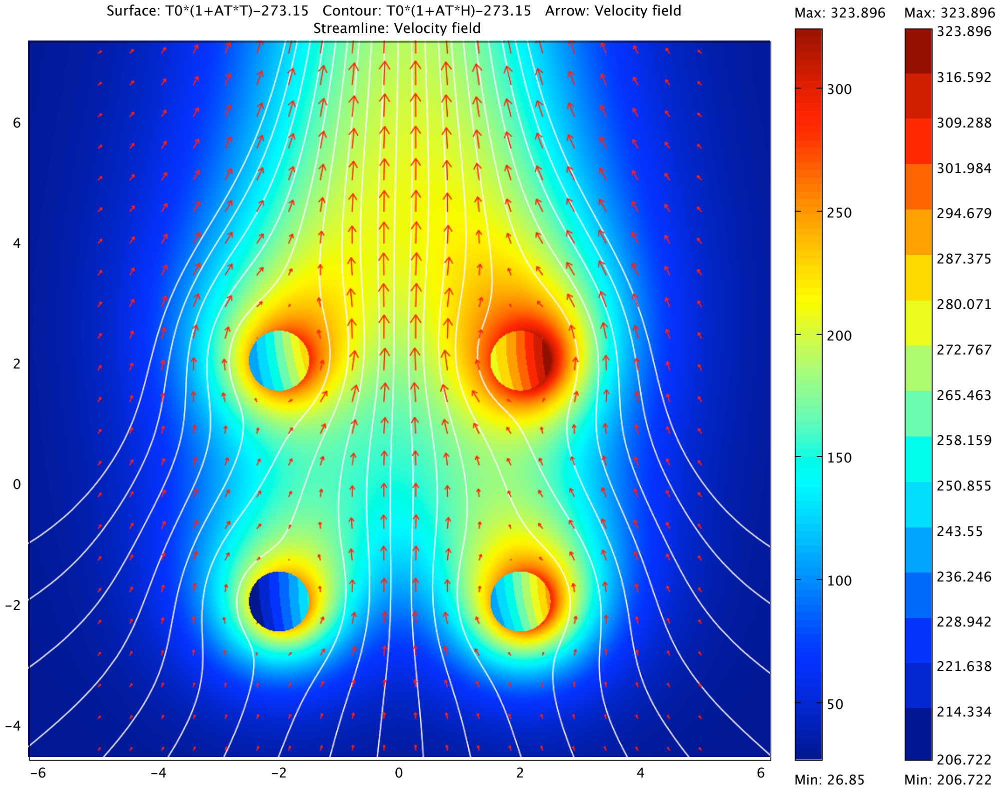

(b) $S_D = 4$.

Figure 7.13: Temperature profiles, velocity fields, and streamlines for a 2×2 array of horizontally aligned cylinders. Heating rate is $J_0 = 40$ kW/m^2 and sample size is $l = 1$ mm.

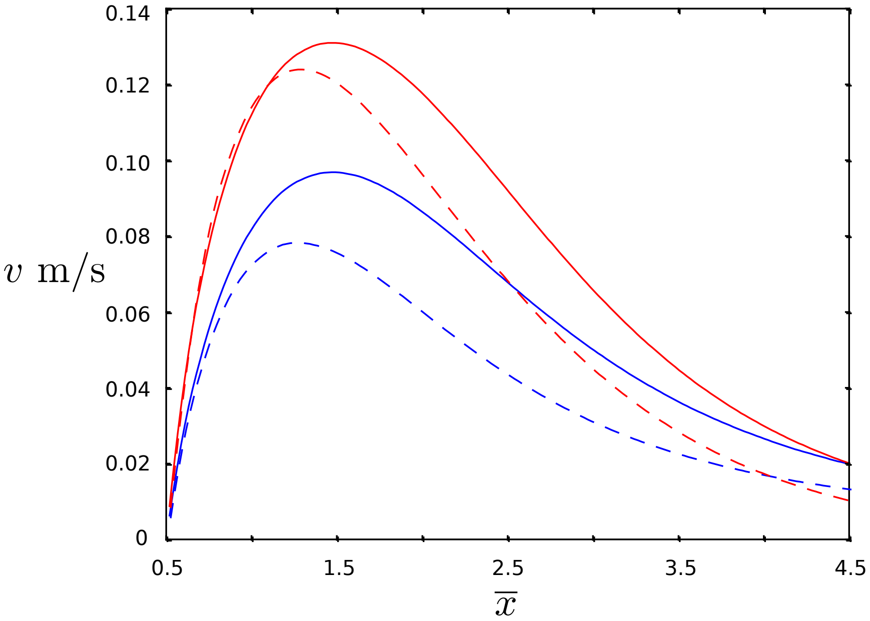

Figure 7.14: Vertical velocity v against horizontal distance from the centre of cylinders $\mathcal{C}_{22}$ (*blue*) and $\mathcal{C}_{12}$ (*red*) for $S_D = 2$ (*solid*) and $S_D = 4$ (*dashed*). Heating rate is $J_0 = 40$ kW/m^2 and sample diameter is $l = 1$ mm.

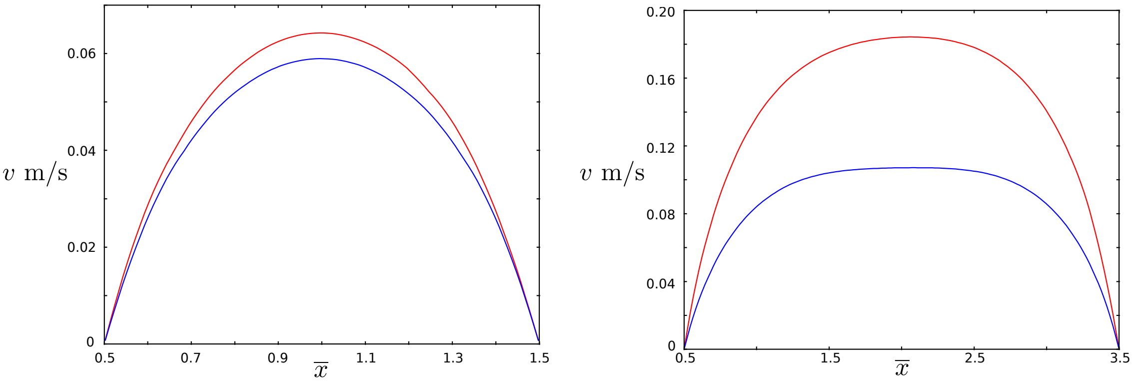

(a) $S_D = 2$.

(b) $S_D = 4$.

Figure 7.15: Vertical velocity v against horizontal distance from the centre of cylinders $\mathcal{C}_{21}$ (*blue*) and $\mathcal{C}_{11}$ (*red*) for $S_D = 2$ (*solid*). Heating rate is $J_0 = 40$ kW/m^2 and sample diameter is $l = 1$ mm.

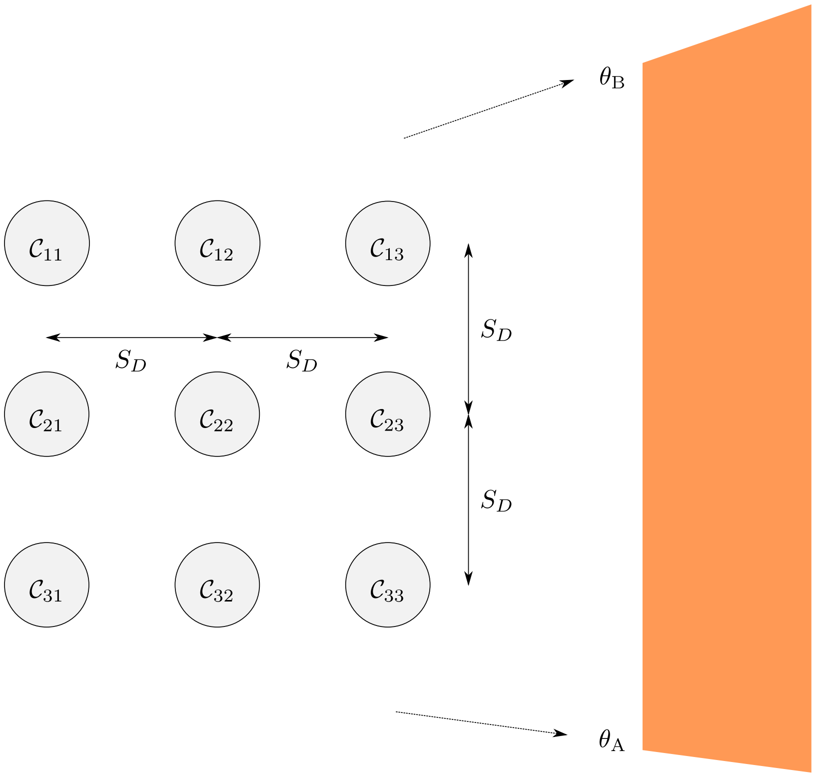

Figure 7.16: A 3 × 3 square array of cylinders. The cylinders are labelled analogously to the entries of a matrix [89].

7.2.2 3 × 3 array

A regular square grid of nine cylinders (Figure 7.16) with a centre-to-centre distance of S_D receiving heat from a radiating panel is solved numerically. The same labelling convention used for the 2×2 array is applied. In this scenario, there could be as many as five cylinders blocking radiation from the panel and potentially a doubling up effect when one of the cylinder already falls within the shadow of another.

Cylinders $\mathcal{C}_{i3}$, for $i = 1, 2, 3$, will receive the full radiation from the panel as there are no cylinders blocking the path from the panel to the cylinders. Cylinders $\mathcal{C}_{i2}$ will receive a reduced heating rate because of the presence of cylinders $\mathcal{C}_{i3}$ which is analogous to the 2×2 array case. However, for cylinders $\mathcal{C}_{i1}$ there will be some overlap of radiation contributions.

Recall that Figure 4.8 showed the shadowed regions on cylinders $\mathcal{C}_{i1}$ with $i = 1, 2, 3$ and $S_D = 3$. This is much easier to implement as the overlap regions are complete, there is no partial overlapping, so that it is easy to simply omit the blocking contribution of a cylinder. The critical value of S_D for which there is no partial overlapping in the blocking is $S_{Dc} \approx 2.2$.

Results have been obtained for a range of nondimensional orthogonally arranged centre-to-centre distances S_D on a square lattice. The Navier-Stokes equations coupled with the energy equation are solved assuming variable flow properties (variable density, viscosity, and thermal diffusivity).

Figure 7.17 (a) shows the temperature, in °C, of the cylinders and the surrounding air, together with the velocity vector field and streamlines. The heating rate is $J_0 = 40$ kW/m^2 and sample diameter is $l = 1$ mm. Cylinder $\mathcal{C}_{13}$ is the hottest whereas $\mathcal{C}_{31}$ attains the coolest temperatures. Recall that cylinders $\mathcal{C}_{i3}$, with $i \in \{1, 2, 3\}$, will receive the full radiation from the panel differing from the rest of the cylinders which receive reduced heating due to shadowing effects. In addition to the full radiation impinging $\mathcal{C}_{13}$, additional convective heating is present due to the hot buoyant air rising from cylinders $\mathcal{C}_{33}$ and $\mathcal{C}_{23}$. Cylinder $\mathcal{C}_{31}$ receives reduced heating due to shadowing and does not have the assistance of convective heating from below. Cylinder $\mathcal{C}_{21}$ benefits from the buoyant heating from $\mathcal{C}_{31}$ but receives even less radiation from the panel as the shadowed regions are more prominent compared to $\mathcal{C}_{31}$. This results in a more uniform temperature distribution around cylinder $\mathcal{C}_{21}$.

For comparison Figure 7.17 (b) shows the temperature, velocity field, and streamlines for $S_D = 4$. The heating rate is $J_0 = 40$ kW/m^2 and sample diameter is $l = 1$ mm. The cylinders have the same dimensions as before but the distance between them is now greater. The maximum and minimum temperatures achieved by the cylinders are reduced due to the cylinder spacing giving rise to a reduction of heat transfer between the cylinders. Cooling air from below is also able to flow more freely through the array. However cylinders which are shadowed receive a larger amount of radiation due to the cylinder spacing allowing more radiation to impinge on the partially shadowed cylinders. This is most clearly evident when observing the solid temperature profiles of $\mathcal{C}_{11}$ comparing with the $S_D = 2$ configuration.

Figure 7.18 shows the average Nusselt number ratios for cylinders $\mathcal{C}_{i3}$, where $i \in \{1, 2, 3\}$. The average Nusselt number is normalised with that of the single cylinder case at the same Rayleigh number Ra in order to show the extent to which the interaction between the surrounding cylinders degrades the heat transfer performance relative to the single cylinder case [71]. Cylinder $\mathcal{C}_{33}$ is almost unaffected by the

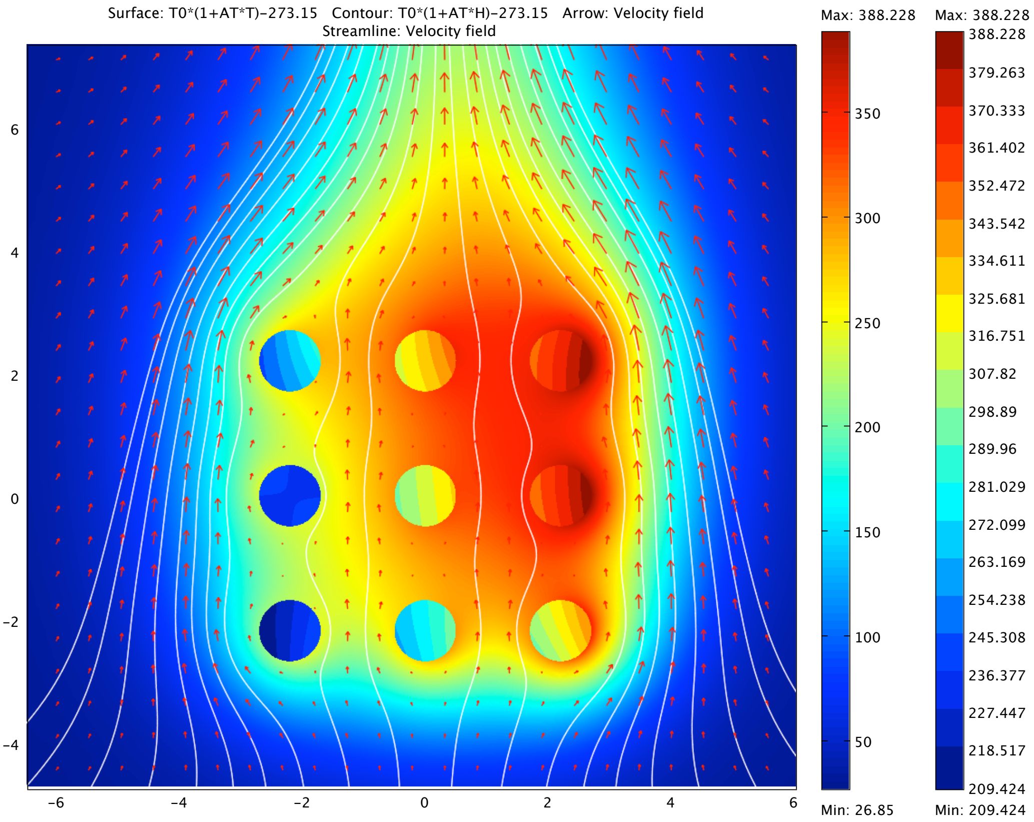

(a) $S_D = 2.2$.

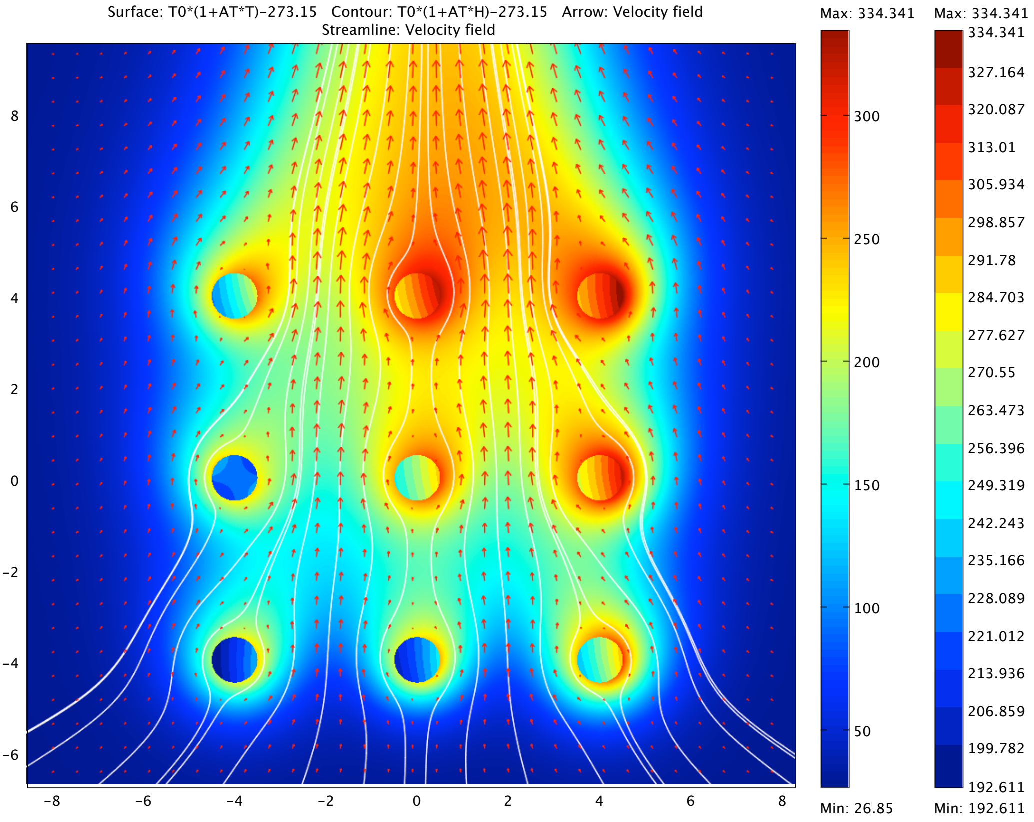

(b) $S_D = 4$.

Figure 7.17: Temperature profiles, velocity fields, and streamlines for an array of 3×3 horizontally aligned cylinders. Heating rate is $J_0 = 40$ kW/m^2 and sample size is $l = 1$ mm.

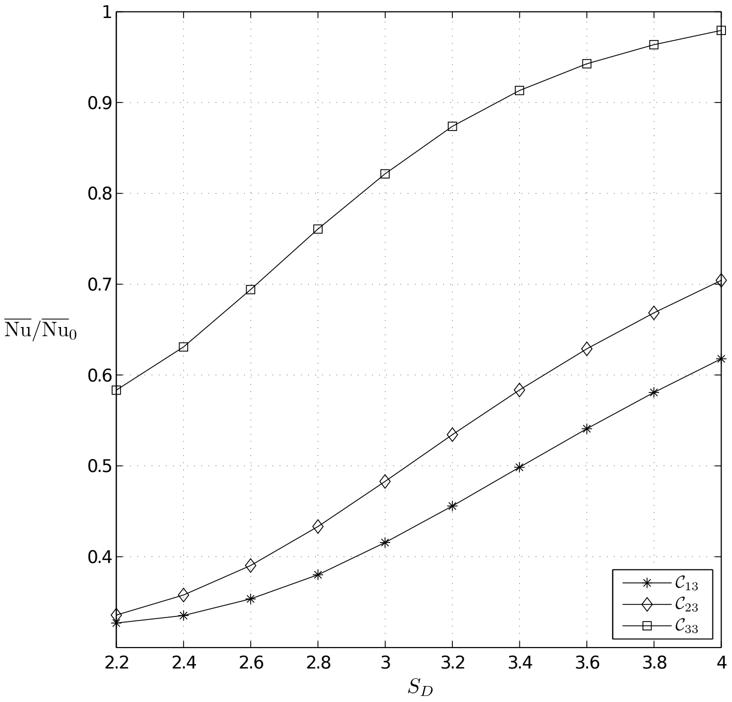

Figure 7.18: Average Nusselt number ratios for cylinders $\mathcal{C}_{i3}$, where $i \in \{1, 2, 3\}$. Sample diameter is $l = 1$ mm and heating rate is $J_0 = 40$ kW/m^2.

surrounding cylinders for large cylinder spacings which is evident from the fact that $\bar{\mathrm{Nu}}_{33}/\bar{\mathrm{Nu}}_0 \to 1$ for large S_D. For smaller S_D the heat transfer rate reduces as the buoyant flow cannot completely pass the narrow spaces above resulting in a larger stagnation region at the bottom of a cylinder [69].

Figure 7.19 shows the vertical velocity v against the horizontal distance to the right from the centre of a particular cylinder. Again the heating rate is $J_0 = 40$ kW/m^2 and the sample diameter is $l = 1$ mm. The vertical velocity is measured between the cylinders. These results suggest that flow is significantly stronger for larger cylinder spacings. Buoyant flow is slightly increased around cylinders $\mathcal{C}_{12}$ and $\mathcal{C}_{22}$ compared the flow around cylinders $\mathcal{C}_{11}$ and $\mathcal{C}_{21}$. This can be attributed to the additional reduction in heating around cylinders $\mathcal{C}_{11}$ and $\mathcal{C}_{21}$ due shadowing effects. This means that the solid temperature around these cylinders is reduced which means the flow around them will also tend to be reduced.

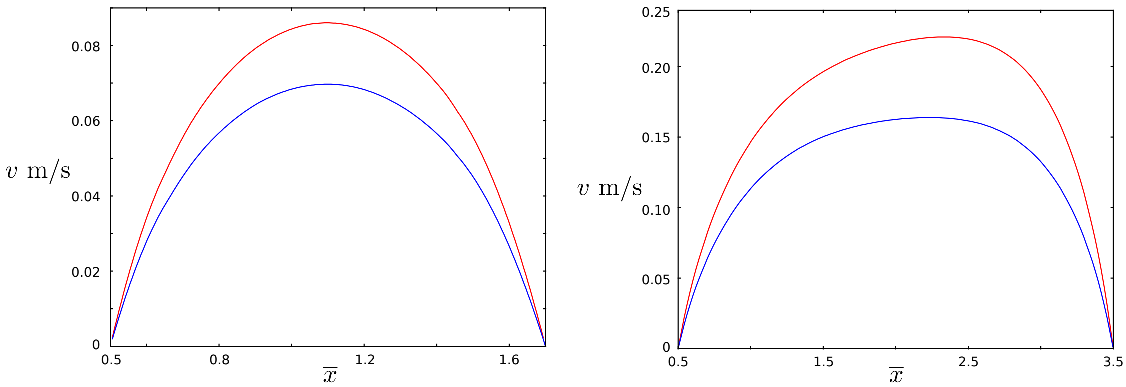

(a) $\mathcal{C}_{11}$ (*red*), $\mathcal{C}_{21}$ (*blue*), and $S_D = 2.2$.

(b) $\mathcal{C}_{11}$ (*red*), $\mathcal{C}_{21}$ (*blue*), and $S_D = 4$.

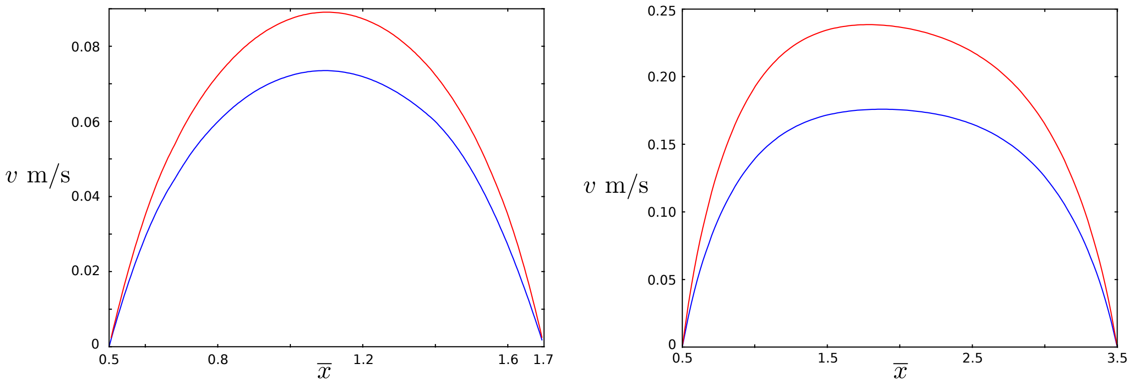

(c) $\mathcal{C}_{12}$ (*red*), $\mathcal{C}_{22}$ (*blue*), and $S_D = 2.2$.

(d) $\mathcal{C}_{12}$ (*red*), $\mathcal{C}_{22}$ (*blue*), and $S_D = 4$.

Figure 7.19: Vertical velocity v against horizontal distance from the centre of a particular cylinder. Heating rate is $J_0 = 40$ kW/m^2 and sample diameter is $l = 1$ mm.

7.3 Conclusions

The effects of reduced heating due to surrounding cylinders blocking radiation from the panel has been analysed. Geometrical arguments have been used together with an effective 'negative' panel to quantify the extent of shadowing on a particular cylinder.

For a 2×2 array only adjacent cylinders can potentially block incoming radiation from the panel. For larger arrays, however, there can be a doubling up effect on the shadowing contribution so a suitable minimum cylinder spacing is required to avoid this situation in the numerical simulations. Larger cylinder temperatures and surrounding air temperatures are achieved for smaller cylinder spacings. This can be attributed to the surrounding cylinders having a greater insulating effect when they are closer together. For larger cylinder spacings there is less shadowing. This results in larger heating rates for partially blocked cylinders. However the cylinders lose heat more readily due to the increased cylinder spacing.

This insulating effect is increased for larger arrays of cylinders. Cylinders closest to the radiating panel receive the full radiative heat. Cylinders far away from the panel receive less radiative heat from the panel since, potentially, up to five cylinders can block radiation from reaching these cylinder for a 3×3 array. Close cylinder spacings gives rise to an increase in the conductive heat transfer between the cylinders. For larger cylinder spacings the heat transfer between the cylinders is dominated by convection.

For the two vertically aligned cylinders (Chapter 6) a close cylinder spacing results in an increase of the temperature and flow around the cylinders. However, this may not be the case in arrays of cylinders since an increase in the distance between the samples allows more radiation from the panel to reach cylinders that are partially shadowed. There is also strong vertical flow between the cylinders when the centre-to-centre distance is large. Therefore, there is a complicated interaction between solid temperature and buoyant flow speed which would affect the production of a potentially flammable mixture.

Chapter 8

Conclusions

Two important physical phenomena, the pyrolysis process and natural convection, which occur when solid vegetal fuels are exposed to radiative heating have been examined. A one-dimensional time dependent model is presented for the pyrolysis process and a two-dimensional steady model for the natural convection phenomenon.

A simplified model for the fuel pyrolysis, gaseous mixing, and conditions for flammability, the onset of ignition in vegetal fuels, of slab, cylinder, and sphere geometries, has been presented. Numerical results, using the finite element software COMSOL Multiphysics, are obtained for varying external radiant heating rates, fuel sample sizes, and initial fuel moisture contents. Drying, charring, and fast pyrolysis processes have been included in order to estimate when and where a flammable mixture is formed. The geometry of the vegetal fuel sample plays a crucial role in its thermal degradation when exposed to radiant heating on its surface. Cylinder and sphere like fuels heat up more rapidly than slab like fuels due to their larger surface-area-to-volume ratio. The larger external volume in these geometries also speeds up the process of gaseous mixing which leads to a more rapid generation of a flammable mixture. Initial fuel moisture content delays the flash point time. The evaporated moisture dilutes the oxygen and fuel in the external gas mixture and can push away the location of the flash point. Char production is dominant at lower temperatures/heating rates. The temperature at the flash point time is found to be around 350°C–550°C for the range of parameters that have been explored. This large temperature range suggests that using a fixed value of ignition temperature, which is the approach typically adopted in integral based models [29], is an oversimplification. There are, however, limitations in the applicability of the pyrolysis model as studied here towards wildfire flammability conditions. For a typical wildfire an isolated vegetal fuel would not be encountered. It is more common to have a line, or array, of fuels and vapour mixing from multiple sources would act together in a buoyant two or three dimensional flow field. The heating rate would not be uniform as it would depend on the geometry of the fuel sample and radiative source.

A two-dimensional natural convection model has been presented which takes into account non-uniform heating, multiple fuel samples, and shadowing effects. Pyrolysis processes have been neglected in this natural convection model in order to focus on temperature and flow behaviour. The suitability of COMSOL Multiphysics in solving simpler natural convection problems [57–60, 68–71] was explored prior to solving the full problem presented in this thesis. Numerical results were found to be in good agreement with the literature for isothermal and uniform heating conditions.

For the full natural convection problem, variable flow properties and reradiation effects are found to have an appreciable influence on the temperature and flow around an isolated cylinder in an infinite domain. Numerical simulations were carried out for a similar configuration to that of the experimental studies of Cohen and Finney [64]. The experimental setup involved exposing wood-based particles to an incident heating rate of $J_0 = 41$ kW/m^2 from a rectangular radiating panel. The numerical results for the pyrolysis model (Chapter 3) suggest that a wooden sample can produce enough pyrolysate vapour to support a flame if the surface temperature rises above about 350°C. The natural convection model used here suggests that the temperature around a 1 mm sample is cooled by the induced airflow to well below this threshold temperature. The surface temperature for much of a 12 mm sample exceeds 350°C, reaching a maximum temperature of over 500°C. This suggests that a 12 mm sample, receiving radiant heating of 41 kW/m^2, will, almost certainly, produce the necessary pyrolysate vapour to support a flame. However, for the 1 mm sample, the surface temperature remains too low for pyrolysis reactions to take place.

For the single isolated cylinder, the surface temperature increases as the sample size and heating rate increase. Surface temperatures remain well below 350°C at a heating rate of 10 kW/m^2 even when the sample diameter is relatively large ($l = 16$ mm). For large fuel samples the difference between the maximum and minimum temperatures is large. Therefore, it is expected that the side exposed to the radiating panel will produce pyrolysate vapour much more quickly than the unexposed side. Larger fuel samples also have a stronger flow around them compared to smaller samples exposed to the same heating rate. This suggests that the pyrolysate vapour around large fuel samples would be convected away more quickly which would tend to dilute the concentration of fuel vapour thus reducing the possibility of ignition. Therefore, there is a complicated interaction between solid temperature and buoyant flow speed which would affect the production of a potentially flammable mixture. However, the strongly nonlinear increase in the rate of pyrolysis with temperature is likely to dominate in affecting the chance of flammability conditions, ensuring that a flame could be created at some stage as the heating rate or sample size is increased.

Numerical results have also been obtained for two vertically aligned cylinders exposed to a radiant heat flux. These results show that, particularly for close cylinder spacings, the downstream (or uppermost) cylinder is hotter than the upstream (or lower) cylinder. This is due to the downstream cylinder being surrounded by hotter air which has been entrained primarily from the air which has passed over the already heated upstream cylinder. For close cylinder spacings, the downstream cylinder is more exposed to the wake of the upstream cylinder. It is expected, from the solid temperature profile results of the natural convection model, that close sample spacings would increase the chances of flammability, particular for the cylinder which is downstream of the rising buoyant flow, even though the flow is stronger around hotter cylinders which again would tend to dilute a potentially flammable mixture with air.

The effects of reduced heating due to surrounding cylinders blocking radiation from the panel is also incorporated in the natural convection model. Geometrical arguments have been used together with an effective ‘negative’ radiant panel to quantify the extent of shadowing on a particular cylinder. For a 2×2 array only adjacent cylinders can potentially block incoming radiation from the panel. For larger arrays, however, there can be a doubling up effect on the shadowing contribution so that a suitable minimum cylinder spacing has restricted the range of calculations carried out in order to avoid this situation in the numerical simulations. Larger cylinder temperatures and surrounding air temperatures are observed for smaller cylinder spacings. This can be attributed to the more restricted airflow due to the surrounding cylinders having a greater insulating effect when they are closer together. For larger cylinder spacings there is less shadowing. This results in larger heating rates for partially blocked cylinders. However the cylinders lose heat more readily due to the increased convective heat transfer. Cylinders far away from the panel receive less radiative heat from the panel since, potentially, up to five cylinders can block radiation from reaching these cylinder in a 3×3 array. Close cylinder spacings give rise to an increase in the conductive heat transfer through the air between the cylinders. For larger cylinder spacings the heat transfer between the cylinders is dominated by buoyant convection. For the two vertically aligned cylinders (Chapter 6) a close cylinder spacing results in an increase in the temperature and flow around the cylinders. However, this may not be the case in arrays of cylinders since an increase in the distance between the samples allows more radiation from the panel to reach cylinders that are partially shadowed. There is also stronger vertical flow between the cylinders when the centre-to-centre distance is larger. This suggests that, for larger fuel arrays packed closer together, flammable conditions are more likely to occur than for smaller arrays of fuel cylinders of the same diameter.

The pyrolysis process and natural convection flow have been dealt with separately in this thesis. An extension to this research could be made by combining these two models. This would take the form of a two-dimensional time dependent pyrolysis model which incorporates buoyant fluid flow, non-uniform heating, and shadowing effects. A model which incorporates both the pyrolysis and natural convection processes has been studied by Kwon et al. [90]. However, their work focuses on closed domains and a single dry fuel sample. The study could also be extended by managing the doubling up effect on the shadowing contribution for close cylinder spacings so that temperature and flow results for more closely-spaced cylinders could be analysed. Finally, the study could also be extended to radiant heating of fuel samples of non-circular cross sections, such as square, rectangular, or any other relevant shape that represents vegetal fuel samples.

Bibliography

[1] Stephen J. Pyne, Patricia L. Andrews, and Richard D. Laven. *Introduction to Wildland Fire*. John Wiley and Sons, Inc., 1996.

[2] Andrew L. Sullivan. Wildland surface fire spread modelling, 1990–2007. *International Journal of Wildland Fire*, 18:349–403, 2009.

[3] Dougal Drysdale. *An Introduction to Fire Dynamics*. Wiley, 1998.

[4] FP Incropera and DP Dewitt. *Introduction to Heat Transfer*. Wiley: New York, 1985.

[5] Kenneth P. Davis. *Forest Fire: Control and Use*. McGraw-Hill Book Company, 1959.

[6] Richard C. Rothermel. A mathematical model for predicting fire spread in wildland fuels. Reasearch paper int-115, USDA forest dervice, Intermountain Forest and Range Experimental Station, 1972.

[7] R. O. Weber. Modelling fire spread through fuel beds. *Progress in Energy and Combustion Science*, 17:67–82, 1991.

[8] L M McCaw. *Predicting fire spread in Western Australia mallee-heath shrubland*. PhD thesis, University of New South Wales, Canberra, 1997.

[9] H.G. Pearce, R.W. Hamilton, and R.I. Millman. Fire behaviour and firefighter safety implications associated with the bucklands crossing fire burnover of 24 march 1998. *Forest and Rural Fire Scientific and Technical Series*, 4, 2004.

[10] Guan Heng Yeoh and Kwok Kit Yuen. *Computational Fluid Dynamics in Fire Engineering*. Butterworth-Heinemann, 2009.

[11] J W Dold and A Zinoviev. Fire eruption through intensity and spread rate interaction mediated by flow attachment. *Combustion Theory and Modelling*, 13: 763–793, 2009.

[12] Adrian Bejan. *Heat Transfer.* John Wiley and Sons, Inc., 1993.

[13] Hans Dieter Baehr and Karl Stephanson. *Heat and Mass Transfer.* Springer, 2 edition, 2006.

[14] G. S. H. Lock. *Latent Heat Transfer.* Oxford Science Publications, 1994.

[15] Hermann Schlichting and Klaus Gersten. *Boundary-Layer Theory.* Springer, 8th edition, 2000.

[16] E. R. G. Eckert. *Introduction to the Transfer of Heat and Mass.* McGraw-Hill Book Company, 1950.

[17] N. Boonmee and J. G. Quintiere. Glowing ignition of wood: the onset of surface combustion. *Proceedings of the Combustion Intstitute*, 30:2303–2310, 2005.

[18] Columba Di Blasi. Modeling chemical and physical processes of wood and biomass yrolysis. *Progress in Energy and Combustion Science*, 34:47–90, 2008.

[19] K. J. Laidler. *Chemical Kinetics.* Harper & Row, third edition, 1987.

[20] D. A. Nield and A. Bejan. *Convection in Porous Media.* Springer-Verlag, 1992.

[21] Benjamin Gebhart, Yogesh Jaluria, Roop L. Mahajan, and Bahgat Sammakia. *Buoyancy-induced flows and transport: Reference edition.* Hemisphere Publishing Corporation, 1988.

[22] Robert Siegal and John R. Howell. *Thermal Radiation Heat Transfer.* Taylor and Francis, 2002.

[23] *COMSOL Multiphysics Modelling Guide.* COMSOL AB, November 2008.

[24] Werner C. Rheinboldt. Numerical continuation methods: a perspective. *Journal of Computaional and Applied Mathematics*, 124:229–244, 2000.

[25] Desmond J. Higham and Nicholas J. Higham. *Matlab Guide*. SIAM, 2 edition, 2005.

[26] Columba Di Blasi. Multi-phase moisture transfer in the high-temperature drying of wood particles. *Chemical Engineering Science*, 53(2):353–366, 1998.

[27] Behdad Moghtaderi. The state-of-the-art in pyrolysis modelling of lignocellulosic solid fuels. *Fire Mater.*, 30:1–34, 2006.

[28] AM Kanury. Combustion characteristics of biomass fuel. *Combust. Sci. and Tech.*, 7:87–98, 1994.

[29] M. J. Spearpoint and J. G. Quintiere. Predicting the piloted ignition of wood in the cone calorometer using an integral method - effect of species, grain orientation and heat flux. *Fire Safety Journal*, 36:391–415, 2001.

[30] Edward A. Johnson and Kiyoko Miyanishi. Strengthening fire ecology's roots. *Behavior and Ecological Effects*, pages 1–9, 2001.

[31] Micheal Jerry Antal Jr. and Gabor Varhegyi. Cellulose pyrolysis kinetics: The current state of knowledge. *Ing. Eng. Chem. Res.*, 34(703-717), 1995.

[32] A. Broido and M. Weinstein. Low temperature isothermal pyrolysis of cellulose. *Proc. 3rd Int. Conf. on Thermal Analysis*, pages 285–296, 1971.

[33] A. Broido and Maxine A. Nelson. Char yield on pyrolysis of cellulose. *Combustion and Flame*, 24:263–268, 1975.

[34] A. Broido. *Kinetics of solid-phase cellulose pyrolysis.* Thermal uses and properties of carbohydrates and lignins. New York, NY: Academic Press, 1976.

[35] Allan G. W. Bradbury, Yoshio Sakai, and Fred Shafizadeh. A kinetic model for pyrolysis of cellulose. *J. Appl. Polym. Sci.*, 23:3271–3280, 1979.

[36] F. Shafizadeh. Alternative pathways for pyrolysis of cellulose. *American Chemical Society*, 28(5), 1983.

[37] Gabor Varhegyi and Emma Jakab. Is the broido-shafizadeh model for cellulose pyrolysis true? *Energy and Fuels*, 8:1345–1352, 1994.

[38] Hong Lu, Elvin Ip, Justin Scott, Paul Foster, Mark Vickers, and Larry L. Baxter. Effects of particle shape and size on devolatilization of biomass particle. *Fuel*, 89: 1156–1168, 2010.

[39] S. Raji, Y. Jannot, P. Lagiere, and J. R. Puiggali. Thermophysical characterization of a laminated solid-wood pine wall. *Contr Buil Mater*, 23:3189–3195, 2009.

[40] J. B. Henderson and T. E. Wiecek. A numerical study of the thermally-induced response of decomposing, expanding polymer composites. *Warme- und Stoffubertragung*, 22:275–284, 1988.

[41] C. A. Zaror and D. L. Pyle. *Models for Low Temperature Pyrolysis of Wood.* Butterworths & Co. Pub. Ltd, London, 1984.

[42] W. C. R. Chan, M. Kelbon, and B. Krieger. Modeling and experimental verification of physical and chemical processes during pyrolysis of large biomass particle. *Fuel*, 64:1505–1513, 1985.

[43] Jaakko Saastamoinen and Jean-Robert Richard. Simultaneous drying and pyrolysis of solid fuel particles. *Combustion and Flame*, 106:288–300, 1996.

[44] S. S. Alves and J. L. Figueiredo. A model for pyrolysis of wet wood. *Chemical Engineering Science*, 44(12):2861–2869, 1989.

[45] R. Bilbao, J. F. Mastral, J. Ceamanos, and M. E. Aldea. Modelling of the pyrolysis of wet wood. *Journal of Analytical and Applied Pyrolysis*, 36:81–97, 1996.

[46] J. F. Siau. *Transport Process in Wood.* Springer, Berlin, 1984.

[47] Judy A Libra, Kyoung S Ro, Claudia Kammann, Axel Funke, Nicole D Berge, York Neubauer, Maria-Magdalena Titirici, Christoph Fühner, Oliver Bens, Jürgen Kern, and Karl-Heinz Emmerich. Hydrothermal carbonization of biomass residuals: a comparative review of the chemistry, processes and applications of wet and dry pyrolysis. *Biofuels*, 2(1):89–124, 2011.

[48] A. M. Kanury and P. L. Blackshear. Some considerations pertaining to the problem of wood-burning. *Combust. Sci. and Tech.*, 1:339–355, 1970.

[49] M. A. Stanish, G. S. Schajer, and F. Kayihan. A mathematical model of drying for hygroscopic porous media. *A.I.Ch.E*, 32(8), 1986.

[50] J. A. Goff. Saturation pressure of water on the new kelvin temperature scale. *Transactions of the American Society of Heating and Ventilating Engineers*, pages 347–354, 1957.

[51] NIST-JANAF. Nist-janaf thermochemical tables. Online, 2000. URL `http://kinetics.nist.gov/janaf/`.

[52] Irvin Glassman. *Combustion*. ACADEMIC PRESS, INC., 1987.

[53] D. K. Shen, M. X. Fang, Z. Y. Luo, and K. F. Cen. Modeling pyrolysis of wet wood under external heat flux. *Fire Safety Journal*, 42:210–217, 2007.

[54] V. T. Morgan. The overall convective heat transfer from smooth circular cylinders. *Adv. Heat Transfer*, 11:199–264, 1975.

[55] I. Pop and D. B. Ingham. *Convective Heat transfer*. Elsevier Science & Technology Books, 2001.

[56] T. F. Smith, C. Beckermann, and S. W. Weber. Combined conduction, natural convection, and radiation heat transfer in an electronic chassis. *ASME*, 113: 382–391, 1991.

[57] T H Kuehn and R J Goldstein. Numerical solutions to the navier-stokes equations for laminar natural convection about a horizontal isothermal circular cylinder. *International Journal of Heat and Mass Transfer*, 23:971–979, 1980.

[58] P. Wang, R. Kahawita, and T. H. Nguyen. Numerical computation of the natural convection flow about a horizontal cylinder using splines. *Numerical Heat Transfer*, 1990.

[59] T. Saitoh, T. Sajiki, and K. Marauhara. Bench mark solutions to natural convection heat transfer problem around a horizontal circular cylinder. *International Journal of Heat and Mass Transfer*, 1993.

[60] R. Chouikh, A. Guizani, and M. Maâlej. Numerical study of the laminar natural convection flow around horizontal isothermal cylinder. *Renewable Energy*, 13(1): 77–88, 1998.

[61] L. Elliott. Free convection on a two-dimensional or axisymmetric bodu. *Quarterly Journal of Mechanics and Applied Mathematics*, 23:153–162, 1970.

[62] J. H. Merkin. Free convection boundary-layer on an isothermal horizontal cylinder. *ASME - AIChE Heat Transfer Conference*, 76-HT-16:1–4, 1976.

[63] A. S. Gupta and I. Pop. Effects of curvature on unsteady free convection past a circular cylinder. *Physics Fluid*, 20:162–163, 1977.

[64] Jack D. Cohen and Mark A. Finney. An examination of fuel particle heating during fire spread. In *VI Internation Conference on Forest Fire Research*, 2010.

[65] G. K. Batchelor. *An Introduction to Fluid Dynamics.* Cambridge University Press, 1967.

[66] Roger M. Rowell. *Handbook of wood chemistry and wood composites.* CRC Press, 2005.

[67] Kendall E. Atkinson. *An Introduction to Numerical Analysis.* John Wiley & Sons, 2 edition, 1989.

[68] John M. House, Christoph Beckermann, and Theodore F. Smith. Effect of a centered conducting body on natural convection heat transfer in an enclosure. *Numerical Heat Transfer*, 18:213–225, 1990.

[69] Claudio Cianfrini, Massimo Corcione, and Emanuele Habib. Free convection heat transfer from a horizontal cylinder affected by a downstream parallel cylinder of different diameter. *International Journal of Thermal Sciences*, 45:923–931, 2006.

[70] Massimo Corcione. Correlating equations for free convection heat transfer from horizontal isothermal cylinders set in a vertical array. *International Journal of Heat and Mass Transfer*, 48:3660–3673, 2005.

[71] C. Cianfrini, M. Corcione, and E. Habib. Free convection heat transfer from a row of horizontal cylinders. *Advanced Materials Research*, 452-453:1246–1251, 2012.

[72] William M. Deen. *Analysis of Transport Phenomenon.* Oxford University Press, 1998.

[73] Liping Ma, Jaap van der Zanden, Jan van der Kooi, and Frans T.M. Nieuwstadt. Natural convection around a horizontal circular cylinder in infinite space and within confining plates: A finite element solution. *Numerical Heat Transfer*, 1994.

[74] T. Fujii, M. Fujii, and T. Honda. Theoretical and experimental study on free convection around a horizontal wire. *Japan Society of Mechanical Engineers*, 1982.

[75] Y. Jaluria. *Natural convection heat and mass transfer.* Pergamon Press, 1980.

[76] H. M. Schey. *Div, Grad, Curl, and All That: An Informal Text on Vector Calculus.* New York: Norton, 1997.

[77] Olivier Reymond, Darina B. Murray, and Tadhg S. O'Donovan. Natural convection heat transfer from two horizontal cylinders. *Experimental Thermal and Fluid Science*, 32:1702–1709, 2008.

[78] Myeong-Seon Chae and Bum-Jin Chung. Effect of pitch-to-diameter ratio the natural convection heat transfer of two vertically aligned horizontal cylinders. *Chemical Engineering Science*, 66:5321–5329, 2011.

[79] Seong-Keun Park and Keun shik Chang. Numerical study on interactive laminar natural convection from a pair of vertically separated horizontal cylinder. *Numerical Heat Transfer*, 14:61–74, 1988.

[80] R. Chouikh, A. Guizani, M. Maâlej, and A. Belghith. Numerical study of the laminar natural convection flow around an array of two horizontal isothermal cylinders. *International Journal of Heat and Mass Transfer*, 26(3):329–338, 1999.

[81] H. Shokouhmand and S. M. A. Noori Rahim Abadi. The effect of the horizontal vibrations on natural heat transfer from an isothermal array of cylinders. *International Journal of Mechanics and Materials in Design*, 7:313–326, 2011.

[82] E. M. Sparrow and J. E. Niethammer. Effect of verticle separation distance and cylinder-to-cylinder temperature imbalance on natural convection for a pair of horizontal cylinders. *Journal of Heat Transfer*, 103:638–644, 1981.

[83] B. Farouk and S. I. Guceri. Natural convection from horizontal cylinders in interacting flow fields. *International Journal of Heat and Mass Transfer*, 26(2): 231–243, 1983.

[84] T. Bello-Ochende and A. Bejan. Constructal multi-scale cylinders with natural convection. *International Journal of Heat and Mass Transfer*, 48:4300–4306, 2005.

[85] Donald D. Gray and Aldo Giorgini. The validity of the boussinesq approximation for liquids and gases. *International Journal of Heat and Mass Transfer*, 1976.

[86] J. Hernández and B. Zamora. Effects of variable properties and non-uniform heating on natural convection flows in vertical channels. *International Journal of Heat and Mass Transfer*, 2005.

[87] The Engineering Toolbox. Air properties. Online, 2012. URL `http://www.engineeringtoolbox.com`.

[88] Andrew Lawrence Sullivan. *Competitive Thermokinetics and Non-linear Bushfire Behaviour*. PhD thesis, School of Physical Sciences and Engineering, 2007.

[89] Gene H. Golub and Charles F. Van Loan. *Matrix Computations*. The John Hopkins University Press, 1996.

[90] Gi Hun Kwon, Seung Wook Baek, and Young Min Sohn. Ignition of solid fuel by thermal radiation in a confined rectangular enclosure: Experimental and numerical analysis. *Combust. Sci. and Tech.*, 165:85–110, 2001.